UNIVERSIDADE D
COIMBRA

Carlos Alberto Pessoa Albino

Numerical Simulation of Elastic Wave Propagation in Discontinuous Media

Applications in Ultrasonic and Vibration Control

Thesis submitted in fulfilment of the requirements for the degree of Doctor of Philosophy on Steel and Composite Construction, supervised by Professor Luís Manuel Cortesão Godinho and Associate Professor Daniel Dias-da-Costa, and presented to the Department of Civil Engineering of the Faculty of Sciences and Technology of the University of Coimbra.

December 2020

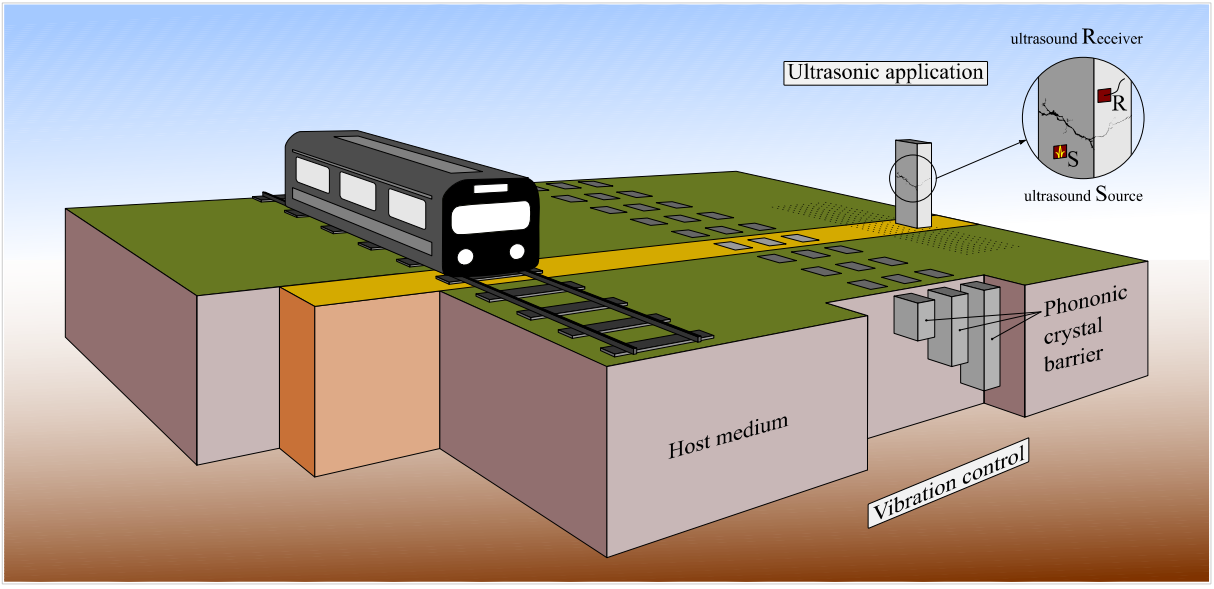

NUMERICAL SIMULATION OF ELASTIC WAVE PROPAGATION IN DISCONTINUOUS MEDIA

APPLICATIONS IN ULTRASONIC AND VIBRATION CONTROL

Thesis submitted in fulfilment of the requirements for the degree of Doctor of Philosophy on Steel and Composite Construction.

Author

Carlos Alberto Pessoa Albino

Scientific Supervisors

Luís Manuel Cortesão Godinho

Daniel Dias-da-Costa

1 2 9 0

UNIVERSIDADE D COIMBRA

Department of Civil Engineering

Faculty of Science and Technology of the University of Coimbra

Coimbra, December 2020

to my father (*in memoriam*) Adelino
to my mother Lídia
to my daughter Leonor

ACKNOWLEDGMENTS

A doctoral thesis is a rigorous work that, in addition to the candidate's effort, requires the commitment of scientific supervisors, and the support of friends and family. For this reason, I am grateful and, from now, I thank those who accompanied, supported, and motivated me on this journey.

I would like to express my sincere gratitude particularly to the supervisors, Professor Luís Godinho and Professor Daniel Dias da Costa, because it was with them that this thesis became a reality. I appreciate Professor Luís Godinho, for the suggestion of the thesis theme, for the specialized knowledge, for the scientific guidance, for the contribution in the organization of the thesis, for the patience and for the friendship established over these years. I appreciate Professor Daniel Dias da Costa, for the guidance, the knowledge transmitted, the work review, the constructive criticisms, the strength that emanates and the work capacity, reasons for which I admire him; I am grateful for the credit he gave me since I finished the integrated master; I appreciate the availability from the other side of the world.

I am grateful for the invaluable availability of Professor Paulo Amado Mendes because he has always received me with friendship in the countless times that I knocked on the door.

I would like to thank Paulo Saraiva for his practical knowledge, for his patience in listening to me at critical moments, for his motivation and friendship.

I would like to thank Bruno Pedrosa for his help, good humour, companionship and short but satisfactory debates.

I would like to thank Matheus Pereira and Matheus Veloso for their friendship, knowledge and motivation.

I would like to extend my deep thanks to Ricardo Dias, a long-time friend, for his availability, encouragement, and friendship.

I would like to thank my brothers for their support.

I am especially grateful to Susana, my life partner, who knew how to understand the reasons for my isolation. I appreciate her motivation, her patience, and her generosity. I appreciate her for believing in me. I appreciate her for the simple and unconditional love. I appreciate all the time we spent together and the wisdom of living.

I express here my deepest sense of gratitude to my mother, who has always shown me the way to be an ever-better person. I am grateful for her concern and her unconditional support throughout my life. I am grateful for the strength and courage with which she has always faced life, chasing away the pains of a difficult life. I am grateful for everything to my mother.

I am deeply grateful to Leonor, my daughter, for her unconditional love and for understanding the little time we have spent together. I appreciate her confidence and motivation, which, even though she does not know, gives me the strength I need to live.

Financial support

This work was financially supported by: Project PTDC/ECM-COM/1364/2014 – POCI-01-0145-FEDER-016783 (METASHIELD) – funded by FEDER funds through COMPETE2020 – Competitivity and Internationalization Operational Programme (PO CI) and by national funds through FCT – Foundation for Science and Technology; Project POCI-01-0145-FEDER-029577 (NVTRail) funded by FEDER funds through COMPETE2020 and by national funds through FCT/MCTES (PIDDAC). This work was also supported by FEDER funds through the Competitivity Factors Operational Programme – COMPETE and by national funds through FCT – Foundation for Science and Technology within the scope of the project (UIDP/04029/2020) (ISISE), and through the Regional Operational Programme CENTRO2020 within the scope of the project CENTRO-01-0145-FEDER-000006 (SUSpENsE).

RESUMO

A propagação de ondas é atualmente um tópico de extrema importância em diferentes áreas da engenharia, incluindo Engenharia Civil. Nesta área, existem dois temas que requerem ainda alguma investigação: o primeiro, está relacionado com a deteção de dano em estruturas através da aplicação de ultrassons e, o segundo, relacionado com o controlo e mitigação de vibrações.

As ondas ultrassónicas são caracterizadas por frequências superiores a 20 kHz e são cada vez mais utilizadas na engenharia, para medir distâncias, detetar falhas em produtos ou em estruturas. É precisamente na área da deteção de dano em estruturas de betão que, nesta tese, é apresentada uma metodologia para apoiar técnicas não destrutivas, baseada no tempo de propagação das ondas.

As vibrações produzidas por veículos rodoviários pesados e ferroviários (fonte) que se propagam pelo solo até zonas sensíveis (recetor) causam incómodo e podem danificar estruturas. Nesta tese apresenta-se uma estratégia de vanguarda, com recurso a arranjos geométricos cristalinos de elementos individuais simples, posicionados entre a fonte e o recetor, no sentido de mitigar o efeito dessas vibrações.

Como suporte às metodologias referidas, foram desenvolvidas duas ferramentas de simulação numérica: a primeira, aplicada a modelos geometricamente simples, recorrendo a soluções fundamentais do sistema, foi desenvolvida no sentido de estudar a mitigação de vibrações; a outra, com recurso a elementos finitos, foi desenvolvida para estudar a propagação de ondas em modelos geométricos mais complexos, tanto no estudo da mitigação de vibrações como no estudo do betão fissurado.

A estratégia usada para a mitigação de vibrações permitiu concluir que os cristais fonónicos têm um efeito significante na redução dos níveis de vibração. Relativamente à deteção de dano, os resultados são promissores e confirmam a viabilidade do uso de equipamentos ultrassónicos baseados em ondas primárias e secundárias para aplicação *in situ*.

Palavras-chave: barreira de estruturas enterradas periódicas, cristal fonónico, deteção de dano, método sem malha, mitigação de vibrações, modelação numérica, propagação de onda elástica, teste não destrutivo, ultrassom.

ABSTRACT

The propagation of waves is currently a topic of extreme importance in different areas of engineering, including Civil Engineering. In this area, there are two issues that still require some research: the first is related to the damage detection in structures by the application in ultrasonic, and the second, relates to control and mitigate vibrations.

Ultrasonic waves are characterised by frequencies above 20 kHz and are increasingly being used in engineering, to measure distances or to detect failures in products or structures. It is exactly in damage detection in concrete structures that, in this thesis, a methodology is presented to support non-destructive techniques, based on the propagation time of waves.

Vibrations produced by heavy road and rail vehicles (source) that propagate through the soil to sensible buildings (receiver) cause discomfort and can damage structures. This thesis presents an advanced strategy using crystalline geometric arrangements of simple individual elements, positioned between the source and the receiver, in order to mitigate the effect of these vibrations.

To support the above methodologies, two numerical simulation tools were developed: the first one, applied to geometrically simple models, using fundamental system solutions, was developed in order to study the vibration mitigation; the other, using finite elements, was applied to more complex geometric models, both in vibration mitigation and in cracked concrete analyses.

The strategy used for vibration mitigation allowed to conclude that the phononic crystals have a significant effect on vibration levels reduction. Regarding damage detection, the results are promising and confirm the feasibility of the use of ultrasonic equipment based on primary and secondary waves for *in situ* applications.

Key-words: damage detection, elastic wave propagation, meshless method, non-destructive testing, numerical modelling, phononic crystal, shielding periodic buried structures, ultrasound, vibration mitigation.

TABLE OF CONTENTS

LIST OF FIGURES

LIST OF TABLES

LIST OF SYMBOLS

Lowercases

d_H Distance between collocation point and virtual source related to the host medium

d_I Distance between collocation point and virtual source related to the inclusion

d_{VS} Distance between collocation point and virtual sources when $d_H = d_I$

f Frequency

i Unit imaginary part of complex numbers

nc Number of collocation points relating to an inclusion in MFS method

$\mathbf{u}$ Displacement vector in frequency domain

$\hat{\mathbf{u}}$ Displacement vector in time domain

Uppercases

A_p Irrotational part of the displacement

$\hat{A}_p$ Fourier transform of the irrotational part of the displacement

A_s Equivoluminal part of the displacement

$\hat{A}_s$ Fourier transform of the equivoluminal part of the displacement

E Young's modulus

E_R Relative error

G Shear modulus

I Dynamic load

NC Total number of collocation points in MFS method

NE Number of elements

T Wave period

R Inclusion radius

V Wave phase velocity

Greek letters

α	Compressional waves velocity
β	Shear waves velocity
ϕ	Dilatational potential
λ	Lamé's first parameter; Wavelength (defined in context)
μ	Lamé's second parameter
ν	Poisson's coefficient
ρ	Volumetric mass density
σ_{ij}	Elastic stress tensor
ω	Angular frequency
Ω	Body
ψ	Shear potential

Indices

$(\cdot)_0$	Initial value of $(\cdot)$
$(\cdot)_H$, $(\cdot)^H$	$(\cdot)$ related to host medium
$(\cdot)_I$, $(\cdot)^I$	$(\cdot)$ related to inclusion
$(\cdot)^{\mathrm{T}}$	Transpose of $(\cdot)$

ACRONYMS

2D	Two-dimensional space
2.5D	Two and a half dimensional space
3D	Three-dimensional space
BEM	Boundary Element Method
DSDA	Discrete Strong Discontinuity Approach
FEM	Finite Element Method
FEM-TD	Finite Element Method in Time Domain
MFS	Method of Fundamental Solutions
NDT	Non-destructive techniques
RMS	Root mean square
SBM	Singular Boundary Method
ToFD	Time of flight diffraction
uNDT	Ultrasonic non-destructive techniques
VSC	Vibration Shielding Crystals

1 INTRODUCTION

The wave propagation in elastic media is a subject studied since the first half of the nineteenth century and, currently, occupies a prominent place in medicine and engineering. As for the origin, waves can be classified in electromagnetic or mechanical. The former type is produced by varying electric and a magnetic fields. They can propagate in vacuum, in contrast with mechanical waves that are produced by a mechanical disturbance in a material medium. These waves, particularly elastic waves, which propagate without causing permanent effects in the elastic medium, are the focus of this thesis. The numerical simulation of elastic waves is a very difficult process, due to the complexity of the waves that are simultaneously present in the system. Currently, there are several methods of numerical simulation of wave propagation, both in the time and frequency domain, but they require high of computational effort. This work proposes two innovative methods applicable to important issues that are currently being investigated by the scientific community: the mitigation of vehicle-induced vibrations and damage detection in structures.

1.1 Motivation

The background and motivation of the thesis theme are presented below. Its introduction is made separately in three main topics: an introduction to numerical simulation techniques, the control of unwanted vibrations and the application of ultrasounds in damage detection in structures.

1.1.1 Numerical simulation techniques

Of all the known numerical simulation techniques, the Finite Element Method (FEM) is undoubtedly the most used in engineering. This is especially due to its advantages in certain physical systems with inhomogeneous or non-linear behaviour. FEM is part of a group of numerical techniques that require a discretised mesh of system nodes connected through finite elements to their neighbours. Other techniques, such as the finite difference or finite-volume

methods, are also within this group. It is not intended to list here all the methods or to make an exhaustive reference of them. At this point, an important distinction is made that these techniques are dependent on a finite element mesh, whereas others do not require the nodes cloud connection in the simulation domain. The latter are known as mesh free or meshless techniques and can be more efficient than mesh methods in problems with geometrically simple singularities or in open domains. Techniques like Method of Fundamental Solutions (MFS) are within this group.

As mentioned in the introductory paragraph of the section 1.1, this thesis addresses two important application areas, related to non-destructive techniques and to vibration protection devices. For efficiency reasons, numerical simulation tools are distinct for each of these topics. In this thesis, to simulate the geometrically more complex models, related to the structural damage detection, the FEM was adapted and improved to efficiently response to the proposed problems. FEM was also used in the simulation of vibration mitigation barriers, by taking advantage of vibration energy dissipative tools in order to accommodate the infinite character of the propagation medium. However, in some studies related to vibration mitigation, the geometry was fairly simple and, in those cases, MFS proved to be more efficient.

1.1.2 Mitigation of vehicle-induced vibrations

Vibrations arising from means of transport has been under discussion since the middle of twentieth century when high-speed trains, where speeds above 200 km/h emerged as regular intercity transport in several countries in Europe and Asia (Yang and Hung, 2009). These vibrations are propagated by the soil and can interfere with constructions such as dwelling houses, technological production buildings or laboratories equipped with sensitive equipment. The most common effect of these vibrations on buildings is the appearance of cracks in the plaster and paint and their subsequent fall. However, in more serious situations, cracking of structural elements or even problems with the functioning and collapse of buildings can occur (Jakubczyk-Gałczyńska and Jankowski, 2014). They can also directly interfere with ordinary people in terms of comfort, well-being and health (Croy *et al*., 2013; Smith *et al*., 2013). At European level, there are projects for implementing innovative and practical solutions by 2050

(European Commission, 2011, 2016), so that "vibrations no longer being considered a problem for the railways and its neighbours", making their levels socially and economically acceptable and allowing passenger and goods operations without time restrictions (Cheron *et al*., 2012). In this context, efficient solutions are required for vibration mitigation to achieve societal acceptance.

Scientific and technical literature reports, related to mitigation of vibrations induced by railway traffic, have been developed over the last years, proposing and analysing different solutions that can be typically grouped into three categories: those acting at the source level, those acting at the receiver, and those acting in the propagation medium (see Figure 1.1). The first category includes resilient materials that act directly at the track, such as under sleeper pads or ballast mats (Alves-Costa *et al*., 2012a; Bongini *et al*., 2011). The second category can include global base-isolation systems, globally protecting a building (Anderson, 2000; Talbot, 2016; Talbot and Hunt, 2000, 2003). The third category includes all solutions that can be introduced within the propagation medium between the source and the receiver to change the propagation patterns of elastic waves, as is the case of buried walls, trenches (empty or in-filled) and inertia blocks (Barbosa *et al*., 2015; Thompson *et al*., 2016; Yang and Hung, 2009). This last group is of particular interest, since it can help to protect groups of buildings and entire sites from traffic-generated vibrations, complementing well interventions at the source level. However, some difficulties are usually identified when using trench solutions, since their efficiency is heavily based on their depth, particularly, at low frequencies. As for in-filled trenches, recent studies by (Barbosa *et al*., 2015) and by Coulier (Coulier *et al*., 2013) show that stiff barriers provide protection mostly from a wave guiding effect due to the coupling between surface waves propagating in the ground and the bending waves propagating in the barrier. A study by Hoorickx *et al*. (2017b) analysed the effect of double buried walls, showing that in general an improvement is registered when a second buried wall is added to the system, although the resonances occurring between the two walls may originate a decrease in efficiency at some specific frequencies.

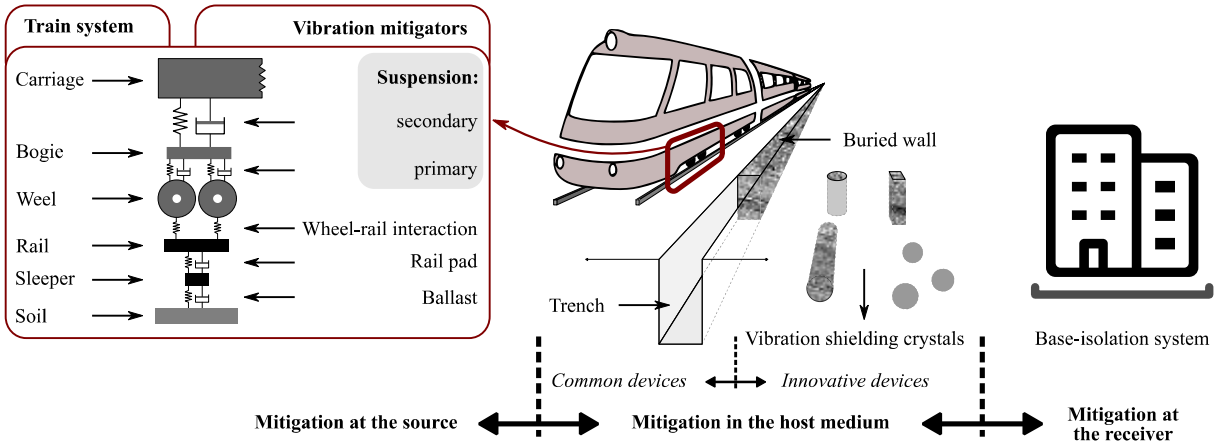

Figure 1.1 – Schematic representation of mitigation systems.

A recent trend in acoustic and vibratory protection is related to the introduction of a new paradigm based in the concept of metamaterials, which are artificial materials engineered to have properties not directly found in nature. A case of such materials is that of periodic structures, such as those usually designated as "phononic crystals", which have the property of stopping the energy passage at specific frequency bands (band gaps); some practical applications of these metamaterials can already be found for acoustic shielding as described in (Martínez-Sala *et al*., 2006; Umnova *et al*., 2006). The successful studies already developed for acoustic applications indicate that such concepts may also be extended for elastodynamic applications, in the sense of blocking vibrations at specific frequency bands. Some works concerning seismic protection by periodic structures can indeed be found in the literature. Kim and Das (2012) analysed the effect of a periodic structure in the creation of a shadow zone to seismic waves. Alagoz and Alagoz (2011) presented numerical studies concerning the effect of what they called "seismic crystals", indicating an effective attenuation of seismic waves. Brûlé *et al*. (2014) reported what is possibly the first evidence of the efficiency of such structures as a shield to seismic waves. More recently, Krödel *et al*. (2015) and Dertimanis *et al*. (2016) have shown that the use of metastructures can reflect acoustic signals with wavelengths well above the characteristic size of the internal structure of the material, opening doors for a large number of applications where low frequency band gaps are demanded.

1.1.3 Damage detection in structures

Many concrete buildings show early signs of damage and aging, which are often the result of poor design, inferior quality of materials and exposure to increasingly aggressive environments (Gomes *et al*., 2014; Maia, 2016). It is important to intervene and control the progress of degradation and to extend the life span of the structure. The early diagnosis of structural defects is essential to decide and plan effective actions that can mitigate the structural degradation at an acceptable cost. In the case of concrete cracking, the diagnosis can be particularly challenging because cracks are often not visible in the initial stage. However, it is recognised that identifying the onset of cracking, is extremely important for early interventions designed to restore the structural performance.

Strategies of inspection and evaluation of concrete structures are, in most cases, still performed by visual survey methods, with some destructive testing techniques being available to support the analysis, either *in situ* or at the laboratory. Recently, several non-destructive techniques (NDT) of damage detection have been studied and implemented. Usually, the type of damage sought dictates the type of sensor to be used (Kessler *et al*., 2002). The "Guidebook on non-destructive testing of concrete structures" (International Atomic Energy Agency, 2002) presents an extensive list of NDT and their applications, including electromagnetic methods and infrared thermography. Khazanovich *et al*. (2016) explore the heterogeneous nature of the concrete material itself, such as the presence of reinforcement and aggregates, which impose additional challenges in the damage detection. Today, other methods are object of research and with well-defined practical applications. For example, Dihoru *et al*. (2009) investigated the potential of using measured data of modal frequency for detecting the location and the size of defects in a vibrating beam using a neural network approach, and Galantucci and Fatiguso (2019) researched on damage detection in historical buildings through digital photogrammetry and 3D surface analysis. Nevertheless, the use of NDT vibration-based has shown the potential to detect and identify the location and the severity of the damage in structures (Sinou, 2009).

Ultrasounds (or ultrasonic waves) are waves whose frequency is above 20 kHz. However, the frequencies usually used in NDT are in the range between (0.5 and 25) MHz (Lohith K. S., 2009). The effectiveness is due to the high frequency that provides a good penetration ability.

In engineering, a well-known ultrasonic-based NDT used for location and size of damage detection is the Time of Flight Diffraction (ToFD) method (Manjula *et al*., 2012), which is based on the diffraction of ultrasonic waves from a crack tip and has been applied successfully, as defect sizing method in ultrasonic testing, since it uses arrival time of echoes instead of their amplitude (Honarvar and Ledari, 2016; Yeh *et al*., 2018). The principle of ultrasound testing is simple: using an ultrasonic transducer, a receiver measures the response time of a pulse generated by a transmitter (see Figure 1.2). The analysis is based on the concept that the propagation velocity of ultrasonic waves depends only on the material density and its elastic properties (Young's modulus and Poisson's coefficient). Knowing the waves velocity in the propagation medium, the time of flight can be directly related to the distance that the signal travelled. In post-processing, some information about damage can be obtained such as location and size, among others. This is the method used in this thesis for simulating damage detection of cracks in concrete structures. However, some care must be taken in the evaluation of the results, due to the interference between the various types of wave, which can accumulate energy in the receiver at a given time point.

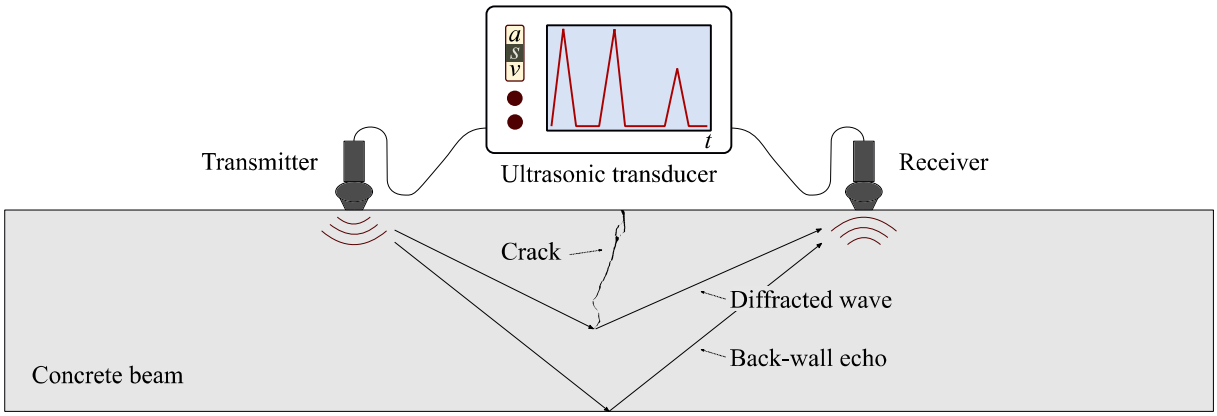

Figure 1.2 – Schematic representation of an ultrasonic transducer into operation.

1.2 Aims

As previously mentioned, this thesis aims to develop numerical tools for simulating the propagation of elastic waves in discontinuous media applied to two specific problems: the first aim focuses on the mitigation of vibrations induced by rail traffic, and the second addresses the

detection of damage in concrete structures. As mentioned before, two numerical simulation tools (FEM and MFS) are adopted, and their use is defined according to the desired result domains: time domain or frequency domain.

The first topic, focused on the vibration mitigation, has as the following main objectives:

a) study of innovative mitigation devices based on buried phononic crystals;
b) implementation of a numerical simulation model based on MFS (frequency domain);
c) implementation of a numerical simulation model based on FEM (time domain);
d) parametric study to validate the MFS model parameters;
e) parametric study to determine the influence of physical and geometric variables on the mitigation solutions efficiency.

The second topic, related to the damage detection based on non-destructive techniques, uses the Time of Flight Diffraction (ToFD) method to detect the presence of cracks, and has the following specific objectives:

a) to better understand the phenomenon of propagation of P, S and surface waves as a whole, that is, as a full wave solution;
b) implementation of a numerical simulation model based on FEM (time domain);
c) analysis of P, S and surface ultrasonic waves using the ToFD method;
d) application of the simulation model in a case study.

1.3 Thesis outline

The thesis is structured in eight main chapters. This first chapter presents generically the relevance of the proposed study by framing the theme as a response to essential and current issues, and sets the main objectives of this research work. In the second chapter, a historical review is made and the current state of the art regarding wave propagation and its application in vibration control and damage detection in concrete structures is discussed. This chapter also reviews the numerical techniques so far in the field of wave propagation. The third chapter presents the numerical models developed and used within this work. The fourth chapter presents the numerical models verification with benchmarks. The fifth chapter presents the application of MFS in frequency domain in the 2D and 2.5D study of vibration mitigation solutions. The

sixth chapter presents studies on vibrations mitigation in several scenarios of the propagation medium and the phononic crystals definition, using FEM in the time domain. The seventh chapter presents results of numerical simulation of ultrasonic waves propagation in the context of damage detection in concrete structures. Finally, the eighth chapter summarises the contributions of this work, it also presents the main conclusions and points out future developments. Outputs resulting from the research work developed under the doctoral program are also presented in this chapter.

2 BRIEF LITERATURE REVIEW

This chapter is divided into five parts. The first part deals with a generic historical introduction on elastic wave propagation, including basic definitions and concepts. In the second part, a critical review of the state-of-the-art, focusing on vibration mitigation, is made. The third part reviews the state-of-the-art related to the detection and control of damage in concrete structures. The fourth part reviews the numerical models currently used to simulate wave propagation. Finally, in the fifth part, reference is made to the technologies adopted in this thesis for the purpose of vibration mitigation, damage detection and to the numerical models used in the simulation of elastic wave propagation.

2.1 Elastic wave propagation

Historically, the interest in wave propagation arose incidentally in researches related to light propagation in the first half of the nineteenth century (Miklowitz, 1978). Around 1817, Fresnel and Thomas Young showed that two beams of light polarised in planes perpendicular to one another do not interfere with each other. Fresnel concluded that this could only be explained by transverse waves (see Figure 2.1), i.e., waves with displacements orthogonal to the direction of propagation – property that is also associated with mechanical waves. This conclusion gave the study of elasticity a powerful push, attracting great mathematicians like Cauchy and Poisson who later made significant advances in elasticity theory. By 1822, Cauchy had discovered most of the elements of elasticity classical theory, including the stress and displacement equations of motion. Later, in 1828, Poisson was the first to recognise that an elastic disturbance is in general composed of both types of fundamental displacement waves: longitudinal and transverse. After the first studies, other important findings related to elastic waves were made by Cauchy (1830) and Green (1839) who obtained equations for the propagation velocity. Stokes (1849) and Love (1903) carried out investigations related to elastic wave motion due to body forces. Rayleigh (1887) discovered surface waves that occur in a half-space and, those are currently designated by his own name. Lamb (1904) studied the propagation of a pulse in an elastic half-space. Many others, over time, had a fundamental role in the current understanding of wave propagation with

developments and applications in different branches of knowledge. Some of those researchers will be mentioned in the following sections when appropriate.

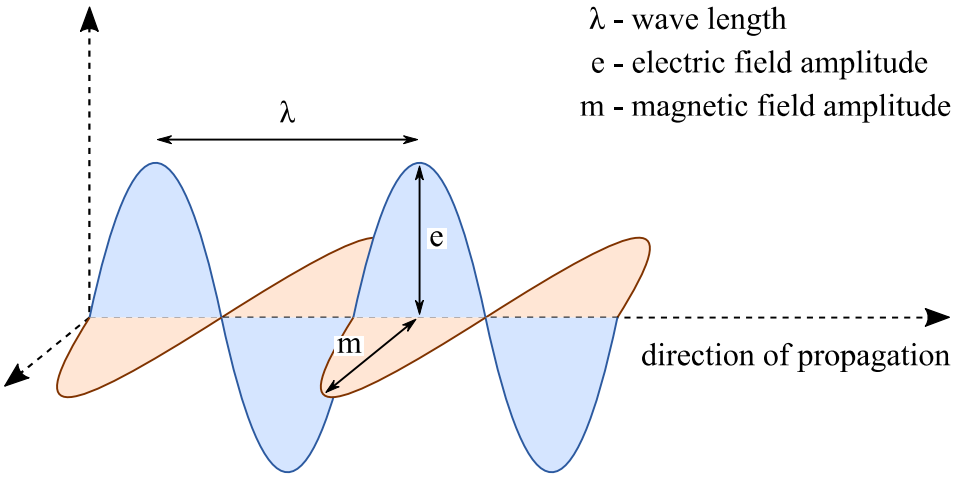

Figure 2.1 – Schematic representation of electromagnetic transverse waves.

A wave is an oscillatory perturbation of a physical quantity in space and periodic in time and, therefore, its propagation involves two different scales: a spatial scale characterised by the wavelength, λ, and a time scale characterised by the period, T. These two scales relate to each other through the velocity of the medium by the fundamental equation $V = \lambda/T$. When a medium is excited by a mechanical impulse, three distinct types of waves are generated: pressure, shear and surface waves. The first type of wave compresses and expands the medium, alternating in the same direction of propagation as shown in Figure 2.2 (a). These waves are also known as “push” and “primary” (or simply “P”) waves due to their higher speed compared to other wave motions (Milsom, 2003). The shear (“shake”, “secondary” due to the lower velocity relative to P-waves, or simply “S”) waves are transverse waves causing displacements in the medium orthogonal to the propagation direction as shown in Figure 2.2 (b). S waves propagate only in solids, since fluids (gases and liquids) do not support shear stresses. P and S waves are body waves since they expand within the medium, whereas surface waves are generated at interfaces. These waves may carry substantial energy emitted by the source, however they travel very slowly, and their amplitude decreases exponentially with the depth relatively to the interface surface. Rayleigh waves are the main type of surface waves, often called “ground roll” (Telford *et al.*, 1990), or simply “R” wave. The motion occurs mostly in

the vertical plane and describes an elliptical path with the major axis in the vertical position as shown in Figure 2.2 (c). The last type of surface waves is called Love wave, which involves transverse motion, similar to shear waves, parallel to the surface.

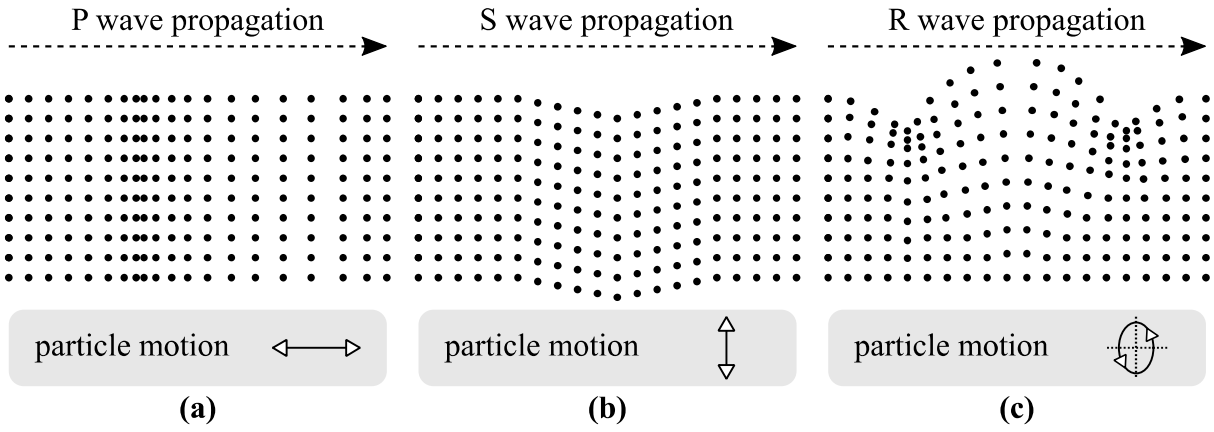

Figure 2.2 – Illustrative representation of particles motion subject to different mechanical wave propagation.

2.2 Vibration mitigation

This section addresses the vibration mitigation resulting from the activity of transport systems, with focus in rail transport. Vibration is a problem that has been discussed since the appearance of intercity trains, with speeds above 200 km/h, in several countries in Europe and Asia (Yang and Hung, 2009). Ewing (1957) discussed the wave propagation in elastic media with distinct types of sources (point or in line sources) depending on the source generator. Richart (1970) made deeper studies on the interaction between the surrounding medium and the heavy sleepers. Regarding the ground vibrations from the railways, Verhas (1979) considered trains as a point source or a line source and later, Chua (1992), and Hunt (1994), continued his study (Suhairy, 2000). In 1994, Krylov and Ferguson, developed a theoretical model of the excitation mechanism of ground vibrations generated by trains. This model, solved by Green's functions, is based on theoretical properties of the rail and train and ground parameters. Volberg (Suhairy, 2000) carried out measurements and concluded that the ground vibration generated by trains is relatively connected to the ground type and properties. Kjörling (1995) measured the ground vibrations due to the passage of trains and showed that faster and slower trains produce higher and lower frequencies, respectively (Suhairy, 2000). He concluded that vertical vibrations

arising in the railway are the most important. In addition, slow, long and heavy trains produce more vibrations at low frequencies than fast short trains. Given that those low frequency vibrations do not suffer a significant damping of the soil, they are the most difficult to mitigate. Many variables are yet to be evaluated. For example, Colaço *et al*. (2016) studied which train-related components have the most influence on ground vibrations and which may be neglected. Among several variables, they concluded that an increase in unsprung mass of the train causes a large increase in the vibration levels unlike changes in the wheel/bogie spacing and semi-sprung mass that have a minimal effect. To support and validate the studies recently being developed, experiments and measurements are being conducted across Europe to analyse track-ground vibrations (dos Santos *et al*., 2016; Kouroussis *et al*., 2016).

Vibrations induced by rail traffic do not only affect sensible buildings but also people feel their negative effects. Nowadays, with railways crossing urban areas, there has been an increase in the demand for quality and comfort, therefore increasing the complaints about noise and vibrations by passing trains (Suhairy, 2000). The noise and vibration exposure lead to increased number of awakenings and cardiac problems, with vibrations being of particular importance: combined exposure between low-vibration and high-vibration levels, might be a more pronounced alarming signal than noise alone, and the heart rate alterations endure even after the exposure has been interrupted (Croy *et al*., 2013). Studies have since been done to obtain the human response to railway-induced vibrations that were often forgotten compared to noise (Waddington *et al*., 2015). It is important to know the perception of people exposed to vibration, the annoyance caused while in their homes and the impact on sleep, so that mitigation measures can be taken. A recent study compared the annoyance caused by railway-induced noise and vibration (Ögren *et al*., 2017). The comparison provides a relationship between the ground vibration velocity and the corresponding noise level on the facade.

It should be noted that even if there were no imperfections and irregularities in the vehicle and tracks, the passing train would still produces a stress pattern in the surrounding ground (Hall, 2003). The reality, however, is that there are many particularities associated with each train and track, which may worsen the stresses by passing trains. These stresses or vibrations in general,

induced by the activity of rail transport systems, can be mitigated by reducing the vibrations from the source to the receiver.

In the source, vibrations can be strongly mitigated by acting on the train system (see "mitigation at source" in Figure 1.1, page 4), in the rail and just underneath it, using resilient materials, such as under sleeper pads and ballast mats (Alves-Costa *et al*., 2012a; Bongini *et al*., 2011; Hemsworth, 2000). Toward *et al*. (2014) examined the effect of two alternative approaches applied to soft soils: placing (continuous) concrete blocks directly under the track and impeding wave blocks positioned at a certain depth also under the track. They further concluded that jet grouting is less effective than concrete. However, it could be a viable solution for tracks on soft ground, particularly if the soil is stiffened to a greater depth. To mitigate vibrations, Feng *et al*. (2017) analysed the influence of Cement Fly-ash Gravel (CFG) piles on the soil treatment under the track. They considered an equivalent soil to simplify the model (see Figure 2.3). Among other things, the authors concluded that the effect of this soil treatment on vibration mitigation is significant but decreases rapidly with distance. However, with the soil treatment depth, the benefits on surface ground vibration isolation increase consistently and the effective zone of vibration reduction expand largely. To complement the measures that can be taken at source it should be noted that train drivers also play a key role in vibration control. They must be trained to avoid vehicle instabilities such as bouncing, rolling, pitching and yawing, thus contributing to mitigate ground disturbance.

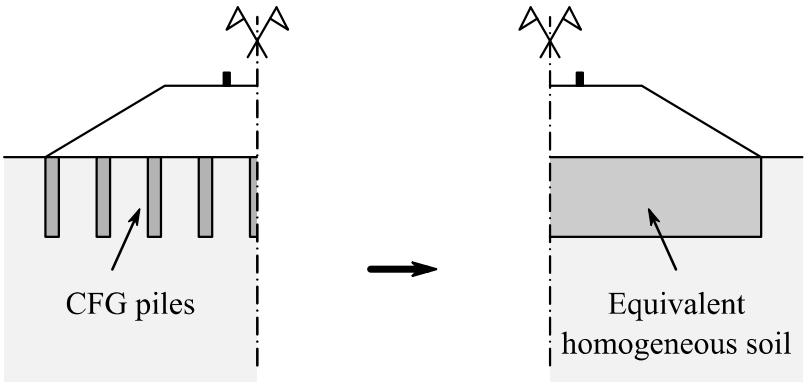

Figure 2.3 – Illustration of the equivalent model assumed by Feng et al. to simulate the CFG piles.

At the receiver, mitigation can be done using base-isolation systems to protect the whole building (Anderson, 2000; BSW-Berleburger, 2014; Talbot, 2016; Talbot and Hunt, 2000, 2003). Although the use of base isolation is frequent and, applied to a wide variety of buildings (such as apartments, offices, cinemas, concert halls, hospitals, etc.), there is a significant lack of guidance in design (Talbot, 2016). However, around the world, base-isolation technologies continue to be improved, mostly with earthquake protection as their primary objective (D'Amato *et al*., 2019; Mazza and Labernarda, 2018; Saitta *et al*., 2018). For example, Saitta *et al*. analysed the curved surface sliders and their behaviour under low-energy earthquakes (Saitta *et al*., 2018). In his PhD thesis, Tehrani investigated an innovative dual-mode rolling isolation system to protect isolated equipment, to mitigate the impacts caused by exceeding the displacement capacity and to reduce the response of the primary structure supporting the isolated equipment (Hadikhan Tehrani, 2019). Di Matteo *et al*. (2019) examined the hybrid use of three passive control strategies to mitigate the seismic response of a base-isolated structure: strategies that combine the base isolation with the Tuned Mass Damper, the New Tuned Mass Damper (New TMD) and the Tuned Liquid Column Damper. Among other aspects, the authors concluded that the New TMD can represent an effective mean to reduce the response of base-isolated structures. Although in some buildings only sensitive equipment is isolated, in general the complete building is isolated at its base by "breaking" the rigid connection to the ground. These base-isolating systems can be coupled to the building in various ways. Figure 2.4 shows examples of the most common locations of base-isolation systems in buildings.

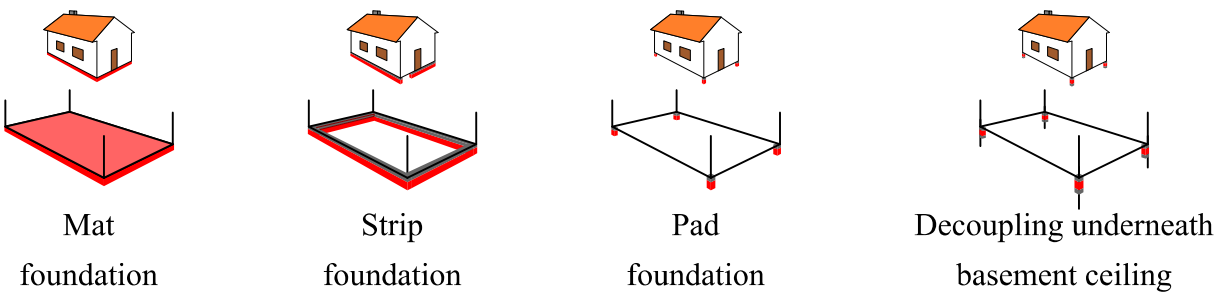

Figure 2.4 – Schematic representation of most common locations of base-isolation systems in buildings.

As discussed above, there are source and receiver mitigation systems, but even combined they are not foully efficient. Sometimes there is a need to intervene in the propagation medium, at a

certain distance, between the source and the receiver. Open or in-filled trenches (also known as buried barriers) with materials that together with the ground constitute a vibration mitigation system, have been studied and applied on large scale for mitigation of vibrations induced by trains (Jiang *et al*., 2015). Numerical simulations demonstrate that a stiff wave barrier, consisting of a material that is stiffer than the host medium, can be very effective if the contrast between the stiffnesses of barrier and medium is sufficiently large. Coulier and Hunt (2014) confirmed this by carrying out a lab experiment using gelatine instead of soil to reduce the wavelengths and thus the scale of the test setup. Full-scale tests were later performed and it was found that the buried barriers are effective in real vibration reduction (Coulier *et al*., 2014, 2015). Dijckmans *et al*. (2015), in collaboration with Coulier and others, investigated the effectiveness of heavy masses placed above the ground in a continuous row along and next to the track forming a wall (see Figure 2.5), as a measure for the reduction of railway induced ground vibration. The authors found that heavy masses become effective above the mass–spring resonance frequency, which is determined by the dynamic stiffness of the soil and the mass of the wall. They also concluded that at frequencies above resonance, masses at the surface of soil mitigate the propagation of surface waves. Later, Dijckmans *et al*. (2016) investigated the effectiveness of a sheet pile wall to reduce railway induced vibration. They concluded that the sheet pile wall acts as a stiff wave barrier and the efficacy is determined by the depth and stiffness contrast with soil.

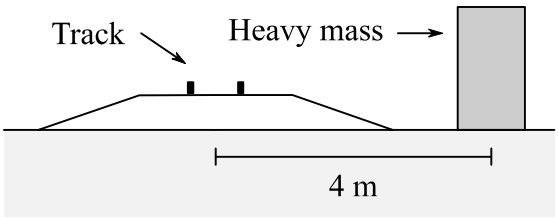

Figure 2.5 – Schematic representation of heavy mass next to and along the track to reduce railway induced ground vibrations.

Persson *et al*. (2016) investigated the effects of infiltration of water into an open trench and concluded that the effectiveness of the trench decreases when any large amount of infiltrateds water is present since water transmits P waves. For example, if a water level of 12 m in a trench 16 m deep was found, the effectiveness of the trench decreases, and vibration level reduction

decreases from 65 % to 21 %. Hoorickx *et al*. (2017a, 2017b) compared the performance of double jet-grout wall barriers with single wall barriers with the same material properties and total volume. They concluded that the double wall barrier performs slightly better than the single wall barrier at shorter distances along the barrier, and that for large walls thickness and spacing between walls, a higher insertion loss is found, especially when these measures (walls thickness and spacing between walls) are close to a quarter of the Rayleigh wavelength. Bordón *et al*. (2018) investigated the shape optimisation (position, inclination, length and thickness) of single and double walls. The authors observed that when the walls depth is less than 1.1 times the Rayleigh wavelength, the barrier topology does not lead to significant improvements. They found that by repositioning and inclining the walls, these become more effective when compared to the reference cases. Huang *et al*. (2017) proposed a layered periodic structure as wave barrier (see Figure 2.6), consisting of two different components. They concluded, among other things, that the number of periods and barrier depth have significant effect on the vibration reduction. They also concluded that greater barrier distances from the track are more effective due to the increasing content of surface waves. Still Yarmohammadi *et al*. (2019) concluded that open trenches have much higher mitigation capacities when compared with the in-filled trenches, and using double-trench barriers instead of single-trench, enhances the mitigation capacity by up to 20 %. However, triple trench barriers do not have such a large increase in mitigation level.

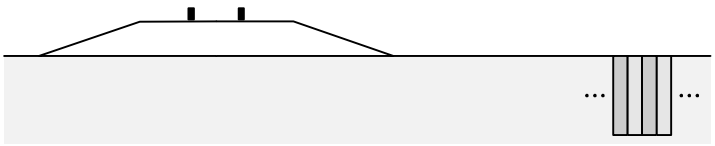

Figure 2.6 – Schematic representation of a layered periodic structure.

Up to now, studies have been presented to improve common solutions, such as trenches and buried walls, and innovative devices based on those, such as above-ground heavy masses or layered periodic structures. However, all those devices are placed along the railway at a certain distance and are built continuously. In recent years, phononic crystals also have been studied to mitigate the vibrations induced by rail traffic. These structures were initially studied within the scope of acoustic barriers, being a relatively recent innovation (Amado-Mendes *et al*., 2016;

Fard *et al*., 2015; Godinho, Soares Jr., *et al*., 2015; Morandi *et al*., 2015). The focus of these studies is the analysis of the distribution of the elements in the crystal, the properties of the materials and their shape and size. The application of this concept to vibration mitigation is a much more recent subject being still in a research phase. The above referred phononic crystals are elementary structures, periodically distributed forming a pattern similar to a macro-scale crystalline structure. The individual inclusions forming the crystal can be linear elements, such as driven piles (with cylindrical or rectangular shape), or may be more compact individual elements (as spheres or cubes at different depths) forming a 3D matrix, here named "Vibration Shielding Crystals" (VSC) – see examples in "Vibration Shielding Crystals" section of Figure 1.1, page 4. On this subject, Castanheira-Pinto *et al*. (2018) investigated the influence of continuous buried horizontal inclusions, parallel to the railway, and found that the response pattern is very complex. They also verified that the distribution of inclusions in the group that form the crystal affects its efficiency. Huang *et al*. (2019) analysed the trees as large-scale natural phononic crystals both theoretically and experimentally. Through simulation, the authors shown that effectiveness of vibration reduction increases with the number of tree lines and that they (the trees) can be observed as a large-scale natural phononic crystal.

Li *et al*. (2017) developed a small device, based on metamaterials concept, which can filter mechanical waves and harvest energy at the same time. Even though it is not a topic addressed in this research work, its importance for future work is recognised.

2.3 Damage detection

A relevant application of the analysis of wave propagation in civil engineering, is related to damage detection in concrete structures. The diagnosis and monitoring of structures in service are needed to ensure its durability and reliability (Goszczyńska *et al*., 2012). Due to the damage and ageing processes that appear increasingly earlier in modern construction (Gomes *et al*., 2014), it is important to intervene at the right moment to avoid further degradation and to extend the life span of the structure. The early detection of structural defects in this scope can indeed prevent a costly repair and retrofit at later stages. In this scope, the inspection and evaluation of concrete structures is, in most cases, still performed by visual survey methods and sometimes

with some destructive testing techniques to support the analysis, either *in situ* or at the laboratory (Gomes *et al*., 2014). Visual inspections may be insufficient for timely damage detection because cracks are often not visible in the initial stages, and destructive testing techniques cause localised damage that may not be acceptable. The non-destructive inspection may be repeated over time, without affecting the integrity and, in most cases without affecting the operability of the structure. Currently, there are several methods of inspection of concrete structures based on, e.g., digital image correlation, infrared thermography, or ultrasound (Galantucci and Fatiguso, 2019; International Atomic Energy Agency, 2002). However, new proposals have emerged to improve the performance of existing techniques and other innovative areas are being developed. Based on the image deformation approach, an efficient strategy to monitor structural integrity and crack propagation in concrete structures was applied (Dias-da-Costa *et al*., 2016). This approach could extract the global crack maps from the structure surface and detect extremely small changes occurring within a given time interval, such as the movement associated with cracks opening. This technology can be complemented by other non-destructive technique (NDT) based on ultrasonic methods, and can have several advantages, particularly in terms of the early detection of damage and cracking (Godinho, Dias-da-Costa, *et al*., 2013), both on the surface and within the structural element.

Ultrasonic non-destructive techniques (uNDT) are based on the propagation of ultrasonic waves. These techniques require the use of ultrasonic transducers, and receivers that measure the response time of the pulse generated by a source (see Figure 1.2, page 6). Since the presence of cracks and voids will affect the propagation time of ultrasonic waves, this information can be used to infer the most likely type of damage within the structure. The development of these techniques began in the mid-1930s when Sergei Y. Sokolov demonstrated a continuous transmission technique to detect metal failures. However, the resolution of the experimental devices manufactured was very weak and could not be used for practical applications. Despite this, from the 1940s onwards, the technology suggested by Sokolov, which could generate a very short pulsed sound wave needed to measure the brief time of propagation of its echoes, came to be produced. Industrial applications of ultrasonic testing apparently began at the same time in the United States, Great Britain, Germany and Japan (APC International Ltd., 2015; Woo, n.d.). Since then, the uNDTs have been developed and are very well known and widely

used in the analysis of defects in steel structures. However, the application of uNDT is not limited to steel. Ultrasonic testing can be used in concrete, wood, plastics, ceramics and composite structures (Nobile and Nobile, 2015).

More recent studies focus on non-contact tests between the object of study and both source and receiver of ultrasonic waves. This contactless is interesting because it may be used for quick scanning large surfaces, avoiding problems with wet or dry coupling between contact ultrasonic transducers and tested materials (Kaczmarek *et al*., 2015). Another recent innovation related to early detection of cracks in reinforced concrete structures, discussed by Chakraborty *et al*. (2019), proposes ultrasonic sensors embedded in concrete. According to the authors, this type of ultrasonic measurements offers significant advantages over traditional measurement techniques because it can deliver the full-field surface strain measurements, as well as be advantageous in determining crack opening and propagation. Furthermore, the ultrasonic feature can monitor small strains/cracks during loading.

Focusing now on the existing techniques that employ transmitted and received ultrasonic waves using contact transducers, it is well known that the propagation is deeply influenced by the presence of obstacles or discontinuities in the medium, which impact the different travel times observed – particularly in comparison with a homogenous medium (Medeiros, 2007). One of the most critical tasks in ultrasound testing, the signal processing, can be done using time or frequency domain responses or considering both the time and frequency domains (Xu and Wei, 2019). The most outstanding analysis methods for ultrasonic damage detection in the time domain are the Phased Array Ultrasonic Testing (using reflection) and the Time-of-Flight Diffraction (ToFD, using diffraction). ToFD has been reported as accurate in several works related to crack sizing (Capineri *et al*., 1992; Ogilvy and Temple, 1983). ToFD complemented with Time Reversal Method can be used to construct the digital image of the shape of cavities and cracks. Together, they can evaluate the surface damage severity and can identify the location and the boundary of internal cracks and voids (Kimoto *et al*., 2017; Zhao *et al*., 2018). Some authors have been studying the use of shear horizontal (SH) waves in ultrasonic propagation models (Godinho, Dias-da-Costa, *et al*., 2013; Liu and Lam, 1996; Wang and Wang, 1996). One advantage that SH waves have over some other wave types is their ability to

propagate around curved surfaces with little loss of energy (Petcher *et al*., 2014). Other types of waves have been used in damage detection. For example, guided waves such as Rayleigh and Lamb waves have shown great potential for damage detection in metallic and composite structures. Nevertheless, body waves, travelling in the bulk of the material, are, in general, easier to model than those waves (Lee and Staszewski, 2003). The presence and interaction of body (P and S) and surface (R) waves leads to the physical phenomena within the propagation media becoming quite complex, even in geometrically simple media.

2.4 Numerical simulation of wave propagation

There are two distinct approaches to modelling the wave propagation: one based on finite elements and the other based on boundary elements. It is not known with certainty when the finite elements based method arose, however, it began to have its big success even before the appearance of the first personal computer, by the 1960's (Argyris *et al*., 1964; Idelsohn and Oñate, 2006). Practically at the same time as the FEM arose, a method based on boundary elements also emerged (Ang, 2007; Idelsohn and Oñate, 2006). Nevertheless, Brebbia and Dominguez (1977) were probably the first to use the term "boundary element method" introducing the method in the engineering research community, nearly two decades later (Ang, 2007). In the last two decades, several meshless methods were developed to reduce the computational cost (Fries and Matthies, 2004; Idelsohn and Oñate, 2006). BEM, a meshless method, obtained greater interest by the researchers. However, among other constraints (Godinho, Amado-Mendes, *et al*., 2015; Tsiatas and Yiotis, 2013), the total computational cost can be high due to the fullness of the system matrix obtained. Another important constraint is related to the accuracy of the evaluation of nearly singular integrals. Gu *et al*. (2016) have recently proposed an alternative method for these integrals and found that its implementation results in reductions in the relative error of several orders of magnitude when compared to a straightforward implementation of Gaussian quadrature. Another meshless method, the Method of Fundamental Solutions, has proved to be a worthy and more efficient alternative to classic methods, such as the BEM or FEM. Recently, a considerable effort has been done to eliminate the need to create finite element meshes (Gu *et al*., 2011). In fact, it is interesting to denote the progressive shift from the term “meshless” to “meshfree” adopted in recent publications, with

both terms being used interchangeably. A recent example is due to (Gu *et al*., 2011), who developed the Singular Boundary Method (SBM) from the MFS. In the SBM, unlike the MFS, the virtual sources, coinciding with collocation points in the physical boundary of the element, are used to simulate the displacement field and an inverse interpolation technique regularises the singularity of the fundamental solution (Gu *et al*., 2011). Nonetheless, a limitation of SBM, as also in other methods, is the associated intrinsic error, which in this case can be difficult to reduce. A very interesting and accepted approach that found applications in many domains is its precursor – the MFS. In the case of wave propagation problems, the MFS displacement field is simulated by the fields superposition generated by some virtual sources located outside the domain. The errors of this method can be controlled and minimised through the right choice of the collocation points number and distances between virtual sources and those collocation points (Gu *et al*., 2011, 2014; Tadeu *et al*., 2009). This method can have improved performance compared with the BEM since it avoids integrations, although still requiring the knowledge of the fundamental solutions, which can be referred to as Green's functions. In the MFS, the response is computed based on the consideration of a set of virtual sources with initially unknown amplitude, which simulate the wave field. The final response depends only on the use of appropriate fundamental solutions, points location and material properties. To combine the advantages of both FEM and meshless methods, some researchers have come to coupling them (Gu and Zhang, 2008; Rao and Rahman, 2001). However, (Amado-Mendes *et al*., 2015; dos Santos *et al*., 2017; Germonpré *et al*., 2017; Godinho, Amado-Mendes, *et al*., 2013; Jin *et al*., 2018) have been developing the coupling for wave propagation domain induced by transport systems.

The numerical simulation methods mentioned above have advantages and disadvantages in relation to each other, and it is important to know them to evaluate and minimise their application errors, but also to define compromise between these and computational performance. With regard to wave propagation, to simulate large systems or (semi-) infinite media, meshless methods are more appropriate since they do not depend on finite elements. The elements mesh density is related to the wavelength: with six finite elements per wavelength typically required for a solution with an error between 10 % and 15 %, while a number between 7 and 10 elements per wavelength already provides an accurate solution (Langer *et al*., 2017;

Marburg, 2002). The numerical simulation of (semi-) infinite media with FEM is only possible using absorption techniques for suppressing reflections from the truncated model boundaries. Several techniques exist for modelling those edges. The most commonly used is the Perfectly Matched Layer (PML). The formulation and use of this technique can be easily found in the literature on wave propagation where the truncation of the infinite medium is necessary – as examples refer to (Colaço *et al*., 2017; Fontara *et al*., 2018; Lopes *et al*., 2013, 2014). The use of infinite elements for this purpose is not common but it is a topic being studied by some authors (Barros, 1996; Shih *et al*., 2016).

With respect to signal analysis, either of the numerical simulation methods can perform time or frequency domain analysis. Recently, Soares Jr. developed an explicit time marching algorithm based only on single-step displacement-velocity relations (Soares Jr., 2016) and is here adopted to render the numerical process more efficient. According to the author, it is a conditionally stable algorithm and exhibits high stability limits, with its critical sampling frequency varying between 3.571 and 4.0 (i.e. its upper limit is twice the central difference method).

Regarding the concrete damage detection, the use of ultrasonic wave propagation technology is not recent, although it has received particular attention from researchers in recent years. There are several conventional techniques such as Pulse Echo or Through Transmission, but these techniques are highly dependent on defect orientation (Praveen *et al*., 2013). ToFD (already discussed in section 2.3) is a method which can be used in these concrete structures and has been reported as accurate in several works related to crack size (Capineri *et al*., 1992; Ogilvy and Temple, 1983).

Still on the numerical simulation, it should be mentioned that the loading, in the case of propagation of elastic waves, must be time-varying. Several wavelets can be found, however, the simplest and most widely used in the literature – for example, (Lopes *et al*., 2013; P. G. Santos *et al*., 2014) – is the Ricker pulse (or wavelet), R_p, the second derivative of the Gaussian function. This wavelet is shown in Figure 2.7 in (a) time and (b) frequency domains which are respectively the graphs of Equations (2.1) and (2.2), for a time peak centred at 0.05 s and a central frequency of 30 Hz.

$$R_p(t) = [1 - 2(\pi f_c t)^2]\mathrm{e}^{-(\pi f_c t)^2} \tag{2.1}$$

$$R_p(f) = \frac{2}{\sqrt{\pi}}\frac{f^2}{f_c^3}\mathrm{e}^{-\left(\frac{f}{f_c}\right)^2} \tag{2.2}$$

where, f_c is the central frequency (or peak frequency), t is the time and f the frequency. The main advantage of this wavelet is that it is bounded in both time and frequency domains.

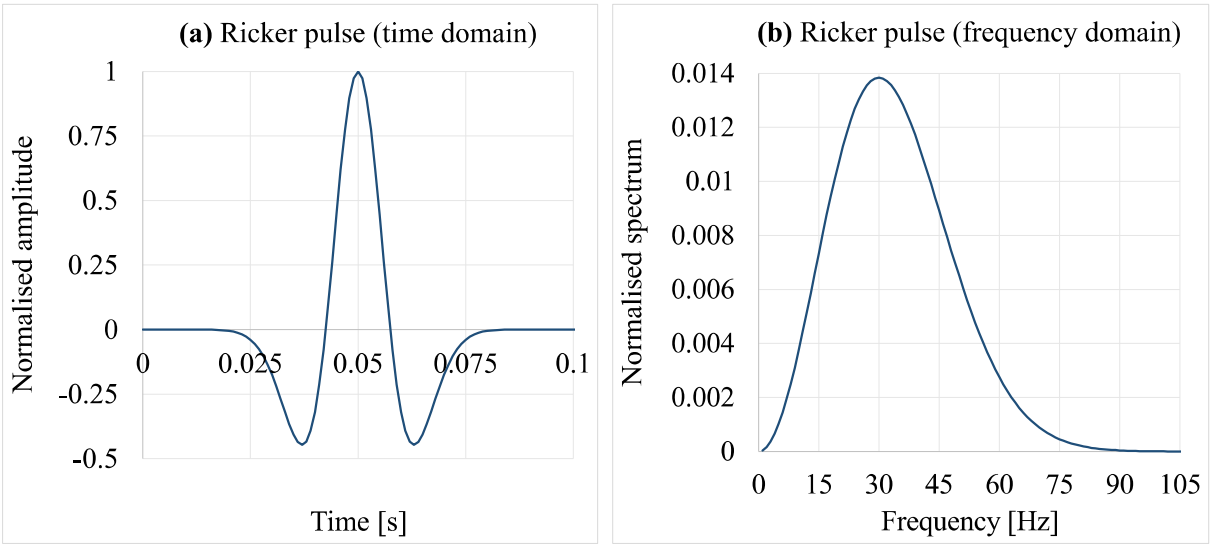

Figure 2.7 – Ricker pulse in (a) time and (b) frequency domains.

2.5 Final remarks

In this chapter, some basic definitions and concepts about elastic wave propagation were introduced. Then, some of the most important methodologies for mitigating heavy vehicle-induced vibrations, namely rail transport, were addressed. The use of ultrasound to detect damage in concrete structures was another topic mentioned. Finally, commonly used methodologies for the numerical simulation of elastic wave propagation were presented.

3 DEVELOPMENT OF NUMERICAL SIMULATION MODELS

Any wave propagation problem can be divided into three stages – generation from a source, propagation through the medium and reception of the propagated wave. On the other hand, the same problem can be approached in two distinct domains: the frequency domain and the time domain.

The first model presented – Method of Fundamental Solutions (MFS) – is used in the simulation of vibration mitigation and applied to simple geometries once it has some limitations in the presence of geometric singularities. This model is developed in the frequency domain, corresponding to practical situations where the propagation time signal of the elastic wave is not relevant but rather the energy that wave transports at specific frequencies.

The second model, the Finite Element Method in Time Domain (FEM-TD) is applied to more complex geometries. It has no geometric constraints and, in this thesis, is used both in vibration mitigation and damage detection. This model has an added benefit since detection is based on the time of flight diffraction of the ultrasonic waves. This will be further explored later.

3.1 Governing differential equations

Before presenting the computational models, the mathematical formulation for the wave propagation will be presented. For a homogeneous elastic medium and in the time domain, the wave propagation follows the equilibrium equation, where the body force term is not included, since it does not have a significant effect (Bedford and Drumheller, 1996). The equilibrium equation can be expressed relating the stress field tensor $\boldsymbol{\sigma}$ to the particle displacement u in a material of density ρ (Drozdz, 2008; Godinho, Amado-Mendes, *et al*., 2015) by:

$$\frac{\partial \sigma_{ij}}{\partial x_j} = \rho \frac{\partial^2 u_i}{\partial t^2}. \tag{3.1}$$

The stress-strain relation for an isotropic linear elastic material is given by $\sigma_{ij} = \lambda\delta_{ij}\varepsilon_{kk} + 2\mu\varepsilon_{ij}$, where $\lambda = \frac{\nu E}{(1+\nu)(1-2\nu)}$ and $\mu = \frac{E}{2(1+\nu)}$ are the Lamé's first and second parameters, respectively, δ_{ij} is the Kronecker delta function, ε_{kk} is the Lagrangian strain tensor, E is the Young's modulus and ν is the Poisson's ratio. The components of the linear strain tensor are related to the components of the displacement by $\varepsilon_{ij} = \frac{1}{2}\left(\frac{\partial u_i}{\partial x_j} + \frac{\partial u_j}{\partial x_i}\right)$. Therefore, the stress components in terms of the displacement components are $\sigma_{ij} = \lambda\delta_{ij}\frac{\partial u_k}{\partial x_k} + \mu\left(\frac{\partial u_i}{\partial x_j} + \frac{\partial u_j}{\partial x_i}\right)$. Then, by substituting these expressions into the Equation (3.1), the equation of balance of linear momentum for an isotropic linear elastic material is obtained (Bedford and Drumheller, 1996):

$$(\lambda + \mu)\frac{\partial^2 u_j}{\partial x_i \partial x_j} + \mu\frac{\partial^2 u_i}{\partial x_j \partial x_j} = \rho\frac{\partial^2 u_i}{\partial t^2}. \tag{3.2}$$

Introducing the Cartesian unit vectors, $\mathbf{i}_i$ (where the i index is a cartesian direction) this equation results in the vector equation:

$$(\lambda + \mu)\frac{\partial}{\partial x_i}\left(\frac{\partial u_j}{\partial x_j}\right)\mathbf{i}_i + \mu\frac{\partial^2 u_i}{\partial x_j \partial x_j}\mathbf{i}_i = \rho\frac{\partial^2 u_i}{\partial t^2}\mathbf{i}_i \tag{3.3}$$

that can be expressed in a vector form as (Bedford and Drumheller, 1996):

$$(\lambda + \mu)\nabla(\nabla \cdot \hat{\mathbf{u}}) + \mu\nabla^2\hat{\mathbf{u}} = \rho\frac{\partial^2\hat{\mathbf{u}}}{\partial t^2}. \tag{3.4}$$

The second term of the left side is known as vector Laplacian of $\hat{\mathbf{u}}$ and can be written in the form

$$\mu\nabla^2\hat{\mathbf{u}} = \nabla(\nabla \cdot \hat{\mathbf{u}}) - \nabla \times (\nabla \times \hat{\mathbf{u}}). \tag{3.5}$$

Substituting the last expression into Equation (3.4), the following can be written (Bedford and Drumheller, 1996)

$$(\lambda + 2\mu)\nabla(\nabla \cdot \hat{\mathbf{u}}) - \mu\nabla \times (\nabla \times \hat{\mathbf{u}}) - \rho\ddot{\hat{\mathbf{u}}} = 0, \tag{3.6}$$

where $\hat{\mathbf{u}}$ vector is the displacement of the material relative to the reference state, $\ddot{\hat{\mathbf{u}}}$ is the acceleration, and the del operator has different vector operation meanings: (∇) is the gradient (product with a scalar), $(\nabla \cdot)$ is the divergence (dot product, changes in the volume and density of the material) and $(\nabla \times)$ is the curl (cross product, which describes the infinitesimal rotation). Equations (3.2) and (3.6) are well known equations of motion because they are expressed in terms of the displacement of the material (Bedford and Drumheller, 1996).

By applying a time Fourier transform to the previous equation, the following equation is obtained that represents the elastic wave propagation in the frequency domain, for null initial conditions:

$$(\lambda + 2\mu)\nabla\nabla \cdot \mathbf{u} - \mu\nabla \times \nabla \times \mathbf{u} + \omega^2\rho\mathbf{u} = 0, \tag{3.7}$$

in which ω is the angular frequency and $\mathbf{u}$ is the displacement vector in the frequency domain.

By taking the Equation (3.6) and decomposing the displacement field into the sum of the gradient of a scalar potential ϕ ($\phi = \nabla \cdot \mathbf{u}$, representing the dilation of the material) and the curl of a vector potential $\boldsymbol{\psi}$ ($\boldsymbol{\psi} = \nabla \times \mathbf{u}/2$ representing the rotation vector), the displacement field comes as (Bedford and Drumheller, 1996; Yang and Hung, 2009):

$$\hat{\mathbf{u}} = \nabla\phi + \nabla \times \boldsymbol{\psi}, \tag{3.8}$$

and Equation (3.6) becomes (Bedford and Drumheller, 1996):

$$\nabla\left[\rho\frac{\partial^2\phi}{\partial t^2} - (\lambda + 2\mu)\nabla^2\phi\right] + \nabla \times \left[\rho\frac{\partial^2\boldsymbol{\psi}}{\partial t^2} - \mu\nabla^2\boldsymbol{\psi}\right] = 0. \tag{3.9}$$

The last equation is satisfied if the potentials ϕ and $\boldsymbol{\psi}$ satisfy:

$$\rho \frac{\partial^2 \phi}{\partial t^2} = \alpha^2 \nabla^2 \phi \tag{3.10}$$

and

$$\rho \frac{\partial^2 \boldsymbol{\psi}}{\partial t^2} = \beta^2 \nabla^2 \boldsymbol{\psi}. \tag{3.11}$$

The constants α and β are the propagation velocities, where:

$$\alpha = v_P = \sqrt{\frac{\lambda+2\mu}{\rho}} = \sqrt{\frac{E(1-\nu)}{\rho(1+\nu)(1-2\nu)}}, \tag{3.12}$$

is the velocity of propagation of dilatational (compressional) waves in an elastic medium and:

$$\beta = v_S = \sqrt{\frac{\mu}{\rho}} = \sqrt{\frac{E}{2\rho(1+\nu)}}, \tag{3.13}$$

is the velocity of propagation of rotational (shear) waves in an elastic medium.

The Rayleigh waves propagation velocity is not defined by a closed form expression, but the following relationship with the secondary waves velocity is considered a good approximation (Yang and Hung, 2009), and is used in this thesis:

$$v_R \approx \frac{0.87+1.12\nu}{1+\nu} v_S = \frac{0.87+1.12\nu}{1+\nu} \sqrt{\frac{E}{2\rho(1+\nu)}}. \tag{3.14}$$

3.2 The Method of Fundamental Solutions

To solve the vector wave equation in the frequency domain, Equation (3.7), several strategies and numerical schemes can be used. In this thesis, the MFS is used, which approximates the solution within a given elastic domain as a combination of fundamental solutions generated by

a set of virtual sources positioned outside the domain to avoid numerical singularities. In this section, the main features and the formulation of the MFS method are presented.

To formulate the numerical simulation using the MFS method, consider a solid inclusion Ω_I, with density ρ_I, where pressure (P) and shear (S) waves propagate with α_I and β_I velocities, respectively. This inclusion is embedded in an elastic host medium Ω_H, with density ρ_H which allows (P and S) waves to propagate with α_H and β_H velocities (Amado-Mendes and Godinho, 2013; Tadeu *et al*., 2009). The host medium is excited by a dynamic load I at position $P_0(x_0, y_0)$ oscillating with a frequency ω, according to the Figure 3.1.

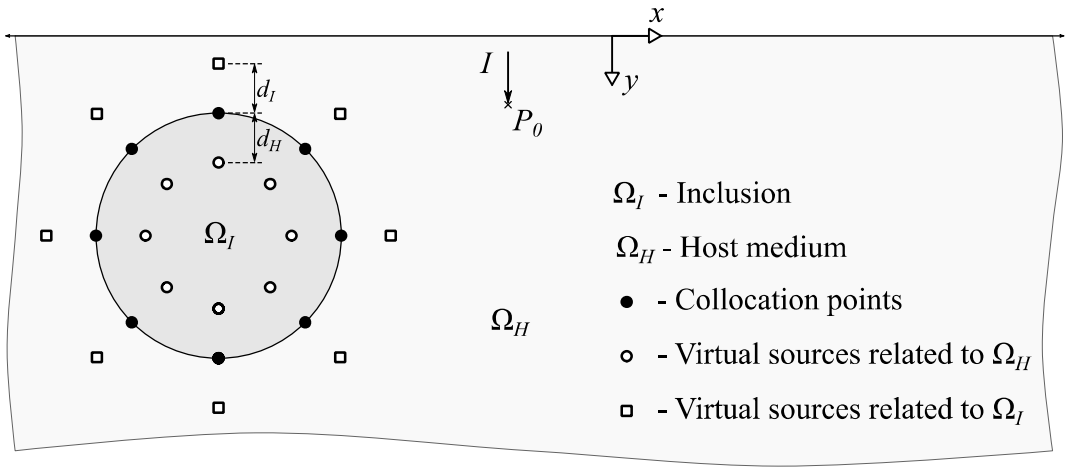

Figure 3.1 – Schematic representation of required data for the MFS model.

The computation is performed using NC collocation points distributed along the inclusion boundary and two sets of NC virtual sources placed on either side of that interface at a distance d_I and d_H, related to the inclusion and host medium, respectively. At each position, loads must be considered acting in both directions x and y. The sources inside the inclusion (related to the host medium) have unknown amplitudes P_{nj}, whereas those placed in the host medium (related to the inclusion) have unknown amplitudes Q_{nj} (n is the source order number and j is the direction in which the load acts on this source point).

To determine the unknown amplitudes, it is necessary to impose the boundary conditions of continuity of tangential and normal displacements and stresses along the interface at the NC

collocation points, therefore establishing a linear equation system with $4NC$ equations/unknowns. After solving these equations, the displacements at any point (x, y) in the propagation domain can be determined as the summation of the contribution of their respective virtual sources (Amado-Mendes and Godinho, 2013). Accordingly, in the host medium, the displacements are given by:

$$u_i^H(x,y) = \sum_{n=1}^{NC} \sum_{j=1}^{a} P_{nj} G_{ij}^H, \tag{3.15}$$

while inside the inclusion:

$$u_i^I(x,y) = \sum_{n=1}^{NC} \sum_{j=1}^{a} Q_{nj} G_{ij}^I, \tag{3.16}$$

where $G_{ij}^m = G_{ij}^m(x_n^m, y_n^m, x, y, \rho_m, \alpha_m, \beta_m)$ is the displacement at point (x, y) in the medium m, along direction i, generated by a load acting along j at position $(x_n^m,\ y_n^m)$ computed using the adequate fundamental solution (Amado-Mendes and Godinho, 2013); a, is the number of coordinates considered and takes the value of 2 (corresponding to x and y coordinates) for 2D formulation and the value of 3 (corresponding to x, y and z coordinates) for 2.5D formulation.

The aforesaid system of equations is generated from two sets of fundamental solutions: one for an elastic half-space simulating the host medium and another for an elastic full-space simulating the field within the inclusion.

3.2.1 Fundamental solutions

Both sets of fundamental solutions (also known as Green's functions), which relate the field variables (stresses or displacements) at some location in the half-space domain caused by the dynamic source placed elsewhere in the medium, are extensively described in the works by Tadeu and Kausel (2000) and Tadeu *et al*. (2001).

The fundamental solutions presented here are expressed in an explicit form and represent the Green's functions for a harmonic (steady state) line load buried in a half-space whose amplitude

varies from a sinusoidal shape in the third (i.e. z) dimension. For this purpose, consider an infinite and homogeneous space subjected, at the origin of coordinates, to a spatially varying line load in the z direction of the form $p(x,y,z,t) = \delta(x)\delta(y)\mathrm{e}^{i(\omega t - k_z z)}$ and acting in one of the three coordinate directions. In this expression, x, y and z are the three spatial directions; t, is the time variable; $\delta(x)$ and $\delta(y)$ are Dirac delta functions; e is the exponential function; $i = \sqrt{-1}$ represents the unit imaginary complex number; ω is the load frequency and k_z is the wavenumber in the z direction as represented in Figure 3.2 (a).

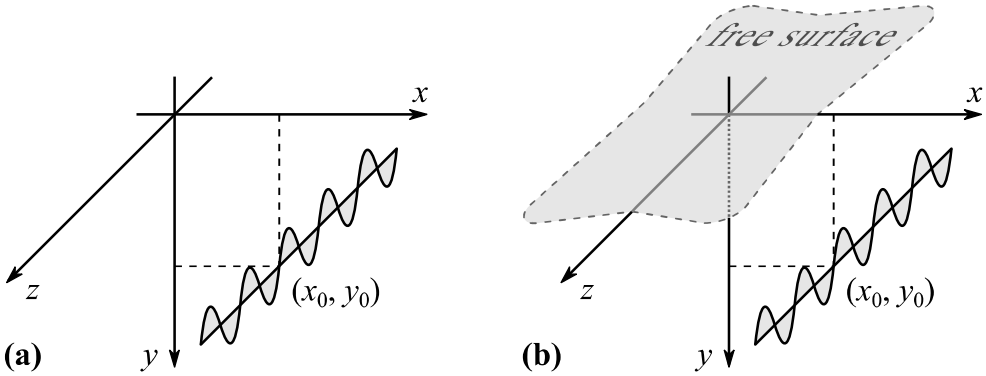

Figure 3.2 – Geometry of the (a) full space and the (b) half-space problems.

The response to this load can be obtained by applying a spatial Fourier transform in the z direction to the Helmholtz equations for a point load. To understand this transformation, see Equation 17.34.4 in (Gradshteyn and Ryzhik, 2007). In the z direction, the transformed equations are

$$\left(\frac{\partial^2 \hat{A}_p}{\partial x^2} + \frac{\partial^2 \hat{A}_p}{\partial y^2} + k_\alpha^2 \hat{A}_p\right) = \frac{-i\mathrm{H}_0^{(2)}(-ik_z r)}{4\rho\alpha^2} \tag{3.17}$$

and

$$\left(\frac{\partial^2 \hat{A}_s}{\partial x^2} + \frac{\partial^2 \hat{A}_s}{\partial y^2} + k_\beta^2 \hat{A}_s\right) = \frac{-i\mathrm{H}_0^{(2)}(-ik_z r)}{4\rho\beta^2} \tag{3.18}$$

were $k_\alpha = \sqrt{k_p^2 - k_z^2}$ with $\text{Imag}(k_\alpha) \leq 0$ and $k_p = \omega/\alpha$, $k_\beta = \sqrt{k_s^2 - k_z^2}$ with $\text{Imag}(k_\beta) \leq 0$ and $k_s = \omega/\beta$, $\alpha = \sqrt{(\lambda + 2\mu)/\rho}$ and $\beta = \sqrt{\mu/\rho}$, λ and μ are the Lamé constants, $\hat{A}_p(x, y, k_z, \omega)$ and $\hat{A}_s(x, y, k_z, \omega)$ are the Fourier transforms of the two potentials $A_p(x, y, k_z, \omega)$ and $A_s(x, y, k_z, \omega)$, respectively, for the irrotational and equivoluminal parts of the displacement vector; $\text{H}_0^{(2)}(\cdot)$ are the Hankel functions of the second kind and order 0 and $r = \sqrt{x^2 + y^2}$.

In the equilibrium condition, $\hat{A}_p$ and $\hat{A}_s$ assume the respective values,

$$\hat{A}_p = \frac{i}{4\rho\omega^2}\left[\text{H}_0^{(2)}(k_\alpha r) - \text{H}_0^{(2)}(-ik_z r)\right] \tag{3.19}$$

and

$$\hat{A}_s = \frac{i}{4\rho\omega^2}\left[\text{H}_0^{(2)}(k_\beta r) - \text{H}_0^{(2)}(-ik_z r)\right]. \tag{3.20}$$

Also, the displacements G_{ij} in direction i due to a load applied in direction j can be obtained from the relation of those two values as

$$G_{ij} = \frac{\partial^2(\hat{A}_p - \hat{A}_s)}{\partial x_i \partial x_j} + \delta_{ij}\hat{\nabla}^2\hat{A}_s, \tag{3.21}$$

where $x_j = x, y, z$ for $j = 1,2,3$ and $\partial/\partial_z = -ik_z$.

Considering the previous equations, it is possible to observe that

$$\hat{A}_p - \hat{A}_s = \frac{1}{4i\rho\omega^2}\left[\text{H}_0^{(2)}(k_\beta r) - \text{H}_0^{(2)}(k_\alpha r)\right] \tag{3.22}$$

and

$$\hat{\nabla}^2 \hat{A}_s = \frac{1}{4i\rho\beta^2} \mathrm{H}_0^{(2)}(k_\beta r) \tag{3.23}$$

and it is possible to obtain the complete set of Green's functions as:

$$\begin{bmatrix} G_{xx} & G_{xy} & G_{xz} \\ G_{yx} & G_{yy} & G_{yz} \\ G_{zx} & G_{zy} & G_{zz} \end{bmatrix} =$$

$$A \times \begin{bmatrix} k_s^2 \mathrm{H}_{0\beta} - \frac{1}{r} B_1 + \gamma_x^2 B_2 & \gamma_x \gamma_y B_2 & ik_z \gamma_x B_1 \\ \gamma_x \gamma_y B_2 & k_s^2 \mathrm{H}_{0\beta} - \frac{1}{r} B_1 + \gamma_y^2 B_2 & ik_z \gamma_y B_1 \\ ik_z \gamma_x B_1 & ik_z \gamma_y B_1 & k_s^2 \mathrm{H}_{0\beta} - k_z^2 B_0 \end{bmatrix} \tag{3.24}$$

where $A = \frac{1}{4i\rho\omega^2}$ is the amplitude; $B_n = k_\beta^n H_{n\beta} - k_\alpha^n \mathrm{H}_{n\alpha}$, $\mathrm{H}_{n\alpha} = H_n^{(2)}(k_\alpha r)$ and $\mathrm{H}_{n\beta} = \mathrm{H}_n^{(2)}(k_\beta r)$ are the Hankel function of the second kind and n$^{\text{th}}$ order; $\gamma_i = \frac{\partial r}{\partial x_i} = \frac{x_i}{r}$ for $i = x, y$.

The full set of Green's functions for the strains and stresses are given in (Tadeu and Kausel, 2000), Appendix II.

The total wave field can be expressed by considering the incident field generated by the source (source terms), and the terms generated at the surface (surface terms). The source terms can be written making use of the equations proposed by (Tadeu and Kausel, 2000), while surface terms can be represented by a set of one dilatational, ϕ, and another shear, ψ, potentials with unknown amplitude values. The continuous integrals of the effects of plane waves which express both the source and the surface terms, can be discretised into summations of discrete terms, assuming the existence of an infinite number of virtual sources placed along the x direction at equal intervals, L_x. The distance separating them is large enough to prevent the virtual loads from contaminating the response. Considering the contribution of $2N + 1$ terms, the potentials that define the surface terms for loads acting along the x direction are

$$\phi_0^x = E_a \sum_{n=-N}^{n=+N} \left(\frac{k_n}{v_n} E_{b0} A_n^x \right) E_d \tag{3.25}$$

and

$$\psi_0^x = -E_a \sum_{n=-N}^{n=+N} (E_{c0} C_n^x) E_d. \tag{3.26}$$

For loads acting along the y direction,

$$\phi_0^y = E_a \sum_{n=-N}^{n=+N} (E_{b0} A_n^y) E_d \tag{3.27}$$

and

$$\psi_0^y = E_a \sum_{n=-N}^{n=+N} \left(\frac{k_n}{\gamma_n} E_{c0} B_n^y \right) E_d, \tag{3.28}$$

were A_n^x, A_n^y, B_n^y and C_n^x, are the unknown coefficient to be determined from appropriate boundary conditions; $E_a = \frac{1}{2\rho_1 \omega^2 L_x}$; $E_{b0} = \mathrm{e}^{-iv_n y}$; $E_{c0} = \mathrm{e}^{-i\gamma_n y}$; $E_d = \mathrm{e}^{-ik_n(x-x_0)}$; $k_n = 2\pi n / L_x$ (the horizontal wavenumber along x); $k_{p1} = \omega/\alpha_1$; $k_{s1} = \omega/\beta_1$; $\gamma_n = \sqrt{k_{s1}^2 - k_n^2}$ (where $\mathrm{Imag}(\gamma_n) \leq 0$); $v_n = \sqrt{k_{p1}^2 - k_n^2}$ (where $\mathrm{Imag}(v_n) \leq 0$); ω is the excitation frequency.

Within the scope of this thesis, the fundamental solutions for the displacements are computed differently by evaluating the displacement field outside or within an inclusion. Within the inclusion, the fundamental solution for the displacements field can be simply described by the full space Green's functions (Tadeu *et al*., 2001), such that

$$G_{xx}^I(\cdot)_I = G_{xx}^{full}(\cdot)_I \tag{3.29}$$

and

$$G_{yx}^{I}(\cdot)_I = G_{yx}^{full}(\cdot)_I, \tag{3.30}$$

where $(\cdot)_I = (x_0, y_0, x, y, \rho_I, \alpha_I, \beta_I)$ and $G_{kl}^{full}(\cdot)_I$ represents the displacement generated along k direction, due to a load acting along l, by a dynamic source in an infinite elastic medium.

In the case of a half-space (outside of the inclusion), it is necessary to impose the boundary conditions: null tangential and normal stresses at the half-space free surface. Thus, the systems of equations can be established for each value of k_n that allow the unknown amplitude factors to be calculated. As an example, taking the specific case of a load acting along x, after solving the relevant equation systems for a full sequence of values of k_n, in the range $\left[-\frac{2\pi}{L_x}N;\ +\frac{2\pi}{L_x}N\right]$, the final displacements contains an additional summation – see (Amado-Mendes and Godinho, 2013; Tadeu and Kausel, 2000) – due to the influence of the surface and that satisfies the free-surface conditions:

$$G_{xx}^{H}(\cdot)_H = G_{xx}^{full}(\cdot)_H + E_a \sum_{n=-N}^{n=+N} \left(A_n^x \frac{-ik_n^2}{\nu_n} E_{b0} - i\gamma_n E_{c0} C_n^x \right) E_d \tag{3.31}$$

and

$$G_{yx}^{H}(\cdot)_H = G_{yx}^{full}(\cdot)_H + E_a \sum_{n=-N}^{n=+N} (-ik_n^2 A_n^x E_{b0} + ik_n C_n^x E_{c0}) E_d, \tag{3.32}$$

where $(\cdot)_H = (x_0, y_0, x, y, \rho_H, \alpha_H, \beta_H)$.

Note that the formulation presented above relates to the more general case of 2.5D problems, that is, considering that the propagation medium has an invariable geometry along one direction (z). For 2D, the corresponding equations can be directly obtained by setting $k_z = 0$. Once the fundamental solutions are known, the resulting system is solved.

3.2.2 MFS Equation system

The equation system must be assembled in the conventional matrix form $\mathbf{Aa} = \mathbf{b}$. Consider a generic physical system with n buried inclusions such that each inclusion i can be defined by different nc_i collocation points. The total number of collocation points is $NC = \sum_{i=1}^{n} nc_i$. By imposing the equilibrium and compatibility conditions in those collocation points, each one is defined by four unknowns: two, x and y, displacements and two, normal and tangential, stresses. Accordingly, the vector that incorporates the prescribed displacements, $\overline{\mathbf{u}}$, and stresses, $\overline{\boldsymbol{\sigma}}$, at the collocation points is defined as

$$\mathbf{b} = \begin{bmatrix} \overline{\boldsymbol{\sigma}}_{2NC} \\ \overline{\mathbf{u}}_{2N} \end{bmatrix}_{4NC}. \tag{3.33}$$

The vector of unknown amplitudes, with same dimension as $\mathbf{b}$, can be defined as

$$\mathbf{a} = [a_{1,x} \quad a_{1,y} \quad a_{2,x} \quad a_{2,y} \quad \cdots \quad a_{NC,x} \quad a_{NC,y}]^{\mathrm{T}}. \tag{3.34}$$

It remains necessary to define the $\mathbf{A}$ matrix – matrix of fundamental solutions – where each item is the contribution of a specific virtual source at a given collocation point (see Figure 3.1). This matrix can be given in a compact form,

$$\mathbf{A} = [\mathbf{A}_{\Omega_h} | \mathbf{A}_{\Omega_i}]_{4NC,4NC}, \tag{3.35}$$

where the full $\mathbf{A}_{\Omega_h}$ matrix contains the fundamental solutions that are the contributions of virtual sources related to the host medium (those which are within the inclusion) and the block-diagonal $\mathbf{A}_{\Omega_i}$ matrix contains the fundamental solutions that are the contributions of virtual sources related to the inclusions (those which are outside the inclusion). Looking to the general case and grouping the contributions of virtual sources related to the host medium through the inclusions to which they belong (see Figure 3.1), it follows that

$$\mathbf{A}_{\Omega_h} = \begin{bmatrix} \mathbf{A}_{\Omega_h}^{11} & \cdots & \mathbf{A}_{\Omega_h}^{1k} & \cdots & \mathbf{A}_{\Omega_h}^{1n} \\ \vdots & \ddots & \vdots & \ddots & \vdots \\ \mathbf{A}_{\Omega_h}^{k1} & \cdots & \mathbf{A}_{\Omega_h}^{kk} & \cdots & \mathbf{A}_{\Omega_h}^{\mathrm{kn}} \\ \vdots & \ddots & \vdots & \ddots & \vdots \\ \mathbf{A}_{\Omega_h}^{n1} & \cdots & \mathbf{A}_{\Omega_h}^{nk} & \cdots & \mathbf{A}_{\Omega_h}^{nn} \end{bmatrix}_{4N\ ,2NC}, \tag{3.36}$$

with $k = 1, \ldots, n$.

Now, grouping the contributions of virtual sources related to the inclusions, the block-diagonal matrix is obtained

$$\mathbf{A}_{\Omega_i} = \begin{bmatrix} \mathbf{A}_{\Omega_i}^{11} & & & & \\ & \ddots & & & \\ & & \mathbf{A}_{\Omega_i}^{kk} & & \\ & & & \ddots & \\ & & & & \mathbf{A}_{\Omega_i}^{nn} \end{bmatrix}_{4NC,2NC}, \tag{3.37}$$

since the set of sources around the inclusion only influence its internal field. In the two preceding equations, $\mathbf{A}_{\Omega}^{pq}$ contains the displacements, $\mathbf{u}_{pq}$, and stresses, $\boldsymbol{\sigma}_{pq}$, that are the fundamental solutions – the contributions from virtual sources of inclusion q at collocation points of inclusion p. Therefore,

$$\mathbf{A}_{\Omega}^{pq} = \begin{bmatrix} \boldsymbol{\sigma}^{pq} \\ \mathbf{u}^{pq} \end{bmatrix}_{4nc,2n}. \tag{3.38}$$

In this expression, $\boldsymbol{\sigma}^{pq}$ contains the normal, $\boldsymbol{\sigma}_n^{pq}$, and tangential, $\boldsymbol{\sigma}_t^{pq}$, components of the (fundamental) stresses. Hence,

$$\boldsymbol{\sigma}^{pq} = \begin{bmatrix} \boldsymbol{\sigma}_n^{pq} \\ \boldsymbol{\sigma}_t^{pq} \end{bmatrix}_{2nc_p,2nc_q}. \tag{3.39}$$

On the other hand, $\mathbf{u}^{pq}$ contains the x, and y components of the (fundamental) displacements, $\mathbf{u}_x^{pq}$ and $\mathbf{u}_y^{pq}$, respectively. For that

$$\mathbf{u}^{pq} = \begin{bmatrix} \mathbf{u}_x^{pq} \\ \mathbf{u}_y^{pq} \end{bmatrix}_{2nc_p,2nc_q}. \tag{3.40}$$

Normal stresses components are due to load in x direction, $\boldsymbol{\sigma}_n^{pq,x}$, and y direction, $\boldsymbol{\sigma}_n^{pq,y}$, applied in the virtual sources. Similarly, it is true for the tangential components of the stress:

$$\boldsymbol{\sigma}_n^{pq} = \left[\boldsymbol{\sigma}_{\mathrm{n}}^{\mathrm{pq,x}} \quad \boldsymbol{\sigma}_n^{pq,y}\right]_{nc_p,2nc_q} \tag{3.41}$$

and

$$\boldsymbol{\sigma}_t^{pq} = \left[\boldsymbol{\sigma}_t^{pq,x} \quad \boldsymbol{\sigma}_t^{pq,y}\right]_{nc_p,2nc_q}. \tag{3.42}$$

Also, each displacement x and y are due to loads in both directions. Thus, similarly to the stresses, it follows that

$$\mathbf{u}_x^{pq} = [\mathbf{u}_x^{pq,x} \quad \mathbf{u}_x^{pq,y}]_{nc_p,2nc_q} \tag{3.43}$$

and

$$\mathbf{u}_y^{pq} = \left[\mathbf{u}_y^{pq,x} \quad \mathbf{u}_y^{pq,y}\right]_{nc_p,2nc_q}. \tag{3.44}$$

Finally, each element of matrices defined in Equations (3.41) to (3.44) is a $nc_p \times nc_q$ submatrix which assigns the contributions of each isolated component of fundamental solution from virtual sources of inclusion q to the collocation points of inclusion p. Taking as an example the components of the normal stress in the collocation points of inclusion p due to loading of the virtual sources of inclusion q, it follows that

$$\boldsymbol{\sigma}_n^{pq,x} = \begin{bmatrix} \sigma_n^{11,x} & \cdots & \sigma_n^{1j,x} \\ \vdots & \ddots & \vdots \\ \sigma_n^{i1,x} & \cdots & \sigma_n^{ij,x} \end{bmatrix}_{nc_p,nc_q} ; i = 1,\dots,p; j = 1,\dots,q, \tag{3.45}$$

where $\sigma_n^{ij,x}$ is a fundamental solution, i is an individual collocation point and j is an individual virtual source. The same procedure can be used for the other three components.

In terms of computational effort, the algorithm can be optimised when the inclusions have the same dimensions and the same material properties. In this situation, the $\mathbf{A}_{\Omega_i}$ diagonal submatrix has repeated $\mathbf{A}_{\Omega_i}^{kk}$ blocks that need to be calculated only once.

This system of equations is valid for the 2D spatial problems. To address 2.5D problems, the third direction should be considered, and the system of equations is

$$\mathbf{Aa} = \mathbf{b} \Leftrightarrow \left[\mathbf{A}_{\Omega_{h_{6NC,3N}}} \left|\mathbf{A}_{\Omega_{i_{6NC,3NC}}}\right.\right]_{6N\ ,6NC} \times \mathbf{a}_{6N} = \begin{bmatrix} \overline{\boldsymbol{\sigma}}_{3NC} \\ \overline{\mathbf{u}}_{3N} \end{bmatrix}_{6N} . \tag{3.46}$$

3.3 Models for complex configurations

For complex geometric configurations, the strategy of making a time domain analysis was adopted, together with a more general numerical method, able to address all necessary geometric complexities. In this section, the computational model based on the FEM in the time domain is briefly described since can easily be found in a variety of publications and reference books, e.g. Bathe (2014) and Zienkiewicz *et al*. (2000). The purpose is to present a recently developed and innovative time-marching algorithm, in the context FEM models, which will be used for some of the simulations.

3.3.1 The finite element method for static problems

Keeping in mind the traditional FEM, consider an undisturbed body, Ω, delimited by the external boundary, Γ, that is fixed in a subdomain of the external boundary, Γ_u, where the

essential boundary conditions, the displacements $\bar{\mathbf{u}}$, are prescribed (see Figure 3.3). Now consider that a small load increment of a given total loading is applied, such that the response remains quasi-static, and is composed of body forces, $\bar{\mathbf{b}}$, and natural boundary conditions, the imposed tractions $\bar{\mathbf{t}}$, the latter distributed on part of the external boundary, Γ_t, being $\Gamma = \Gamma_u \cup \Gamma_t$ and $\Gamma_u \cap \Gamma_t = \emptyset$. The unit vector n is defined as orthogonal and pointing outwards to the boundary surface.

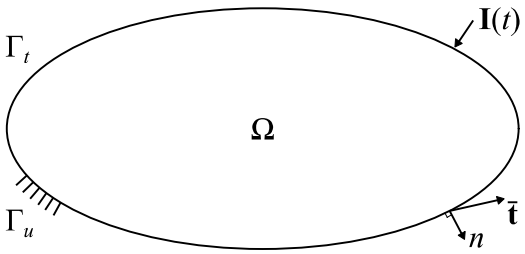

Figure 3.3 – Schematic representation of the domain.

The governing field equations and the boundary conditions can be expressed as

$$\nabla \cdot \boldsymbol{\sigma} + \bar{\mathbf{b}} = \mathbf{0} \text{ in } \Omega, \tag{3.47}$$

$$\boldsymbol{\varepsilon} = \nabla^s \mathbf{u} \text{ in } \Omega \text{ (for small displacements)}, \tag{3.48}$$

$$\boldsymbol{\sigma} = \boldsymbol{\sigma}(\boldsymbol{\varepsilon}) \text{ in } \Omega, \tag{3.49}$$

$$\mathbf{u} = \bar{\mathbf{u}} \text{ at } \Gamma_u, \tag{3.50}$$

$$\boldsymbol{\sigma} \cdot \mathbf{n} = \bar{\mathbf{t}} \text{ at } \Gamma_t, \tag{3.51}$$

where $\boldsymbol{\sigma}$ is the stress field, $\boldsymbol{\varepsilon}$ is the total strain field and $\mathbf{u}$ is the total displacement field; ∇ denotes the gradient operator and $(\cdot)^s$ is the symmetric part of $(\cdot)$.

By the principle of virtual work, the work done by the internal stress in the virtual deformation of the body (δW_I) is equal to the work done by the external forces in the virtual displacements of its points of application (δW_E). Equation (3.52) translates this equality:

$$\delta W_I = \delta W_E \tag{3.52}$$

For the continuous body shown in Figure 3.3, the principle of virtual work can be written as

$$\int_\Omega \delta\boldsymbol{\varepsilon}^{\mathrm{T}} \cdot \boldsymbol{\sigma} d\Omega = \int_\Omega \delta\mathbf{u}^{\mathrm{T}} \cdot \bar{\mathbf{b}} d\Omega + \int_{\Gamma_t} \delta\mathbf{u}^{\mathrm{T}} \cdot \bar{\mathbf{t}} d\Gamma, \tag{3.53}$$

where $\delta\boldsymbol{\varepsilon}$ and $\delta\mathbf{u}$ are the virtual strain and the virtual displacement fields, respectively. In the FEM formulation, the strain field is interpolated from nodal displacements as

$$\boldsymbol{\varepsilon} = \mathbf{B}\mathbf{a}, \tag{3.54}$$

where $\mathbf{B} = \mathbf{L}\mathbf{N}$ is the deformation matrix and $\mathbf{a}$ is the nodal displacements vector. $\mathbf{L}$ contains the differential operators and $\mathbf{N}$ contains the usual element shape functions. For Ω belonging to 2D space, $\mathbf{L}$ becomes

$$\mathbf{L}^{2\mathrm{D}} = \begin{bmatrix} \frac{\partial}{\partial x_1} & 0 \\ 0 & \frac{\partial}{\partial x_2} \\ \frac{\partial}{\partial x_2} & \frac{\partial}{\partial x_1} \end{bmatrix} \tag{3.55}$$

and for Ω belonging to 3D space, $\mathbf{L}$ becomes

$$\mathbf{L}^{3\mathrm{D}} = \begin{bmatrix} \frac{\partial}{\partial x_1} & 0 & 0 \\ 0 & \frac{\partial}{\partial x_2} & 0 \\ 0 & 0 & \frac{\partial}{\partial x_3} \\ \frac{\partial}{\partial x_2} & \frac{\partial}{\partial x_1} & 0 \\ 0 & \frac{\partial}{\partial x_3} & \frac{\partial}{\partial x_2} \\ \frac{\partial}{\partial x_3} & 0 & \frac{\partial}{\partial x_1} \end{bmatrix}, \tag{3.56}$$

where x_1, x_2 and x_3 correspond to x, y and z Cartesian coordinates, respectively. For Ω belonging to 2D space and 3-node elements (triangular elements) are considered, $\mathbf{N}$ becomes

$$\mathbf{N}^{\mathrm{Tri}} = \left[\begin{array}{cc|cc|cc} N_1 & 0 & N_2 & 0 & N_3 & 0 \\ 0 & N_1 & 0 & N_2 & 0 & N_3 \end{array}\right] \tag{3.57}$$

In this case, the nodal basis functions are

$$N_1 = 1 - \xi - \eta \tag{3.58}$$

$$N_2 = \xi \tag{3.59}$$

$$N_3 = \eta \tag{3.60}$$

where ξ and η are the coordinates of the integration domain (normalised coordinate system, always in the $[-1, 1]$ range).

For Ω belonging to 3D space and 4-node elements (tetrahedral elements) are considered, $\mathbf{N}$ becomes

$$\mathbf{N}^{\mathrm{Tet}} = \left[\begin{array}{ccc|ccc|ccc|ccc} N_1 & 0 & 0 & N_2 & 0 & 0 & N_3 & 0 & 0 & N_4 & 0 & 0 \\ 0 & N_1 & 0 & 0 & N_2 & 0 & 0 & N_3 & 0 & 0 & N_4 & 0 \\ 0 & 0 & N_1 & 0 & 0 & N_2 & 0 & 0 & N_3 & 0 & 0 & N_4 \end{array}\right], \tag{3.61}$$

where the nodal basis functions in the normalised coordinate system are given by

$$N_1 = 1 - \xi - \eta - \varsigma \tag{3.62}$$

$$N_2 = \xi \tag{3.63}$$

$$N_3 = \eta \tag{3.64}$$

$$N_4 = \varsigma \tag{3.65}$$

where ς is the third normalised coordinate.

The stresses (for an isotropic material with elastic linear behaviour) can be obtained by the following constitutive relationship:

$$\boldsymbol{\sigma} = \mathbf{D}\boldsymbol{\varepsilon} = \mathbf{DBa}, \tag{3.66}$$

where **D** is the elasticity matrix given by

$$\mathbf{D}^{2\mathrm{D}} = \begin{bmatrix} \frac{E}{1-\nu^2} & \frac{E\nu}{1-\nu^2} & 0 \\ \frac{E\nu}{1-\nu^2} & \frac{E}{1-\nu^2} & 0 \\ 0 & 0 & \frac{E}{2(1+\nu)} \end{bmatrix}, \tag{3.67}$$

if a 2D space and a plane stress state is considered and, if a 3D space is considered, **D** becomes

$$\mathbf{D}^{3\mathrm{D}} = \frac{E}{(1+\nu)(1-2\nu)}\begin{bmatrix} 1-\nu & \nu & \nu & 0 & 0 & 0 \\ \nu & 1-\nu & \nu & 0 & 0 & 0 \\ \nu & \nu & 1-\nu & 0 & 0 & 0 \\ 0 & 0 & 0 & \frac{1-2\nu}{2} & 0 & 0 \\ 0 & 0 & 0 & 0 & \frac{1-2\nu}{2} & 0 \\ 0 & 0 & 0 & 0 & 0 & \frac{1-2\nu}{2} \end{bmatrix}. \tag{3.68}$$

From nodal displacements, the displacement field interpolation is performed with the expression

$$\mathbf{u} = \mathbf{N}\mathbf{a}. \tag{3.69}$$

When Equations (3.54) and (3.69) refer to virtual displacements, they can be written, respectively, as follows

$$\delta\boldsymbol{\varepsilon} = \mathbf{B}\delta\mathbf{a} \Leftrightarrow \delta\boldsymbol{\varepsilon}^{\mathrm{T}} = \delta\mathbf{a}^{\mathrm{T}}\mathbf{B}^{\mathrm{T}}, \tag{3.70}$$

$$\delta\mathbf{u} = \mathbf{N}\delta\mathbf{a} \Leftrightarrow \delta\mathbf{u}^{\mathrm{T}} = \delta\mathbf{a}^{\mathrm{T}}\mathbf{N}^{\mathrm{T}}. \tag{3.71}$$

Replacing Equations (3.66), (3.70) and (3.71) in the Equation (3.53), and after some algebraic simplifications, the principle of virtual work is expressed by the following equation:

$$\int_{\Omega} \mathbf{B}^{\mathrm{T}}\mathbf{D}\mathbf{B}d\Omega\,\mathbf{U} = \int_{\Omega} \mathbf{N}^{\mathrm{T}}\bar{\mathbf{b}}d\Omega + \int_{\Gamma_t} \mathbf{N}^{\mathrm{T}}\bar{\mathbf{t}}d\Gamma. \tag{3.72}$$

This equation can be written in matrix format:

$$\mathbf{F}_E = \mathbf{F}, \tag{3.73}$$

where $\mathbf{F}_E = \mathbf{K}\mathbf{U}$ is the elastic force and $\mathbf{F}$ is the applied static load; $\mathbf{K}$ is stiffness matrix and $\mathbf{U}$ is the vector of (unknown) displacements.

3.3.2 The finite element method for dynamic problems

Consider now the influence of time on one of the load increments on body shown in Figure 3.3. At time $t = 0$ s an impulsive load, $\mathbf{I}(t)$, represented in Figure 3.3, time dependent and with a certain frequency, is imposed, on part of the external boundary, Γ_t. To understand the behaviour of the structure over time due to that impulsive (dynamic) load, a time-history analysis of the structure is performed. In this case, inertia should be included as a contribution of body forces (the latter being neglected for dynamic study). On the other hand, at any given time instant, only the effect of impulsive loading is considered. Thus, in order to contemplate the dynamics and assuming that velocities and accelerations are approximated as displacements, the Equation (3.72) can be written as follows:

$$\int_{\Omega} \mathbf{B}^{\mathrm{T}}\mathbf{D}\mathbf{B}d\Omega\,\mathbf{U} + \int_{\Omega} \mathbf{N}^{\mathrm{T}}\rho\mathbf{N}d\Omega\,\ddot{\mathbf{U}} = \int_{\Gamma_t} \mathbf{N}^{\mathrm{T}}\mathbf{I}(t)d\Gamma \tag{3.74}$$

or in matrix format

$$\mathbf{F}_E + \mathbf{F}_I = \mathbf{F} \tag{3.75}$$

where $\mathbf{F}_I = \mathbf{M}\ddot{\mathbf{U}}$ is the force of inertia, $\mathbf{M}$ is the mass matrix and $\ddot{\mathbf{U}}$ is the acceleration. Note that all terms of Equation (3.75) are time dependent. Equation (3.75) is integrated using an innovative step-by-step procedure developed by Soares Jr. (Soares Jr., 2016). This specific procedure is briefly presented in the next section.

3.3.3 Specific finite element method in the time domain (FEM-TD)

Consider now that the body shown in Figure 3.3 represents a dynamic, multidimensional and damped system. Applying that principle to this system, the Equation (3.74) can be written in weak form:

$$\int_{\Omega} \mathbf{B}^{\mathrm{T}}\mathbf{D}\mathbf{B}d\Omega\,\mathbf{U} + \int_{\Omega} \mathbf{N}^{\mathrm{T}}c\mathbf{N}d\Omega\,\dot{\mathbf{U}} + \int_{\Omega} \mathbf{N}^{\mathrm{T}}\rho\mathbf{N}d\Omega\,\ddot{\mathbf{U}} = \int_{\Gamma_t} \mathbf{N}^{\mathrm{T}}\mathbf{I}(t)d\Gamma \tag{3.76}$$

or in compact form

$$\mathbf{F}_E + \mathbf{F}_D + \mathbf{F}_I = \mathbf{F} \tag{3.77}$$

were $\mathbf{F} = \mathbf{I}(t)$ is the applied dynamic load, $\mathbf{F}_I = \mathbf{M}\ddot{\mathbf{U}}(t)$ is the force of inertia, $\mathbf{F}_D = \mathbf{C}\dot{\mathbf{U}}(t)$ is the damping force and $\mathbf{F}_E = \mathbf{K}\mathbf{U}(t)$ is the elastic force. $\mathbf{M}$ and $\mathbf{K}$, are, respectively, the mass and stiffness matrices; $\mathbf{C} = \alpha_c\mathbf{M} + \beta_c\mathbf{K}$ is the proportional (Rayleigh) damping matrix, with α_c and β_c calculated so that the required damping factor ζ is attained at desired frequencies. $\ddot{\mathbf{U}} = \ddot{\mathbf{U}}(t)$, $\dot{\mathbf{U}} = \dot{\mathbf{U}}(t)$ and $\mathbf{U} = \mathbf{U}(t)$, are respectively the acceleration, velocity and displacement vectors dependent on time. Once $\mathbf{M}$, $\mathbf{C}$ and $\mathbf{K}$ matrices are obtained, the time integration is performed with the algorithm developed by Soares Jr. and presented in (Soares Jr., 2016), where the basic aspects and the main parameters of the time-marching formulation are described.

The algorithm is based only on single-step displacement-velocity relations and it requires no system of equations to be dealt with (once lumped mass matrices are considered). It is second-order accurate and allows the dissipation of spurious modes, which makes it very effective and able to provide accurate analyses with relatively large time steps. Moreover, since the algorithm has high stability limits, it minimises the main drawback of explicit procedures, allowing time-steps that are only usual in accurate implicit analyses, rendering good results at reduced computational costs – see (Soares Jr., 2016; Soares Jr. *et al*., 2007). The equations used for the analysis of the proposed complex geometric configurations, read as follows:

- *the velocity equation,*

$$\mathbf{E}\dot{\mathbf{U}}^{n+1} = \Im_{\mathbf{F}}^{n+\frac{1}{2}} + \mathbf{M}\dot{\mathbf{U}}^{n} - \frac{1}{2}\Delta t\mathbf{C}\dot{\mathbf{U}}^{n} - \mathbf{K}\left(\Delta t\mathbf{U}^{n} + \frac{1}{2}\Delta t^{2}\dot{\mathbf{U}}^{n}\right) \tag{3.78}$$

- *and the displacement equation,*

$$\mathbf{E}\mathbf{U}^{n+1} = \mathbf{E}\left(\mathbf{U}^{n} + \frac{1}{2}\Delta t\dot{\mathbf{U}}^{n} + \frac{1}{2}\Delta t\dot{\mathbf{U}}^{n+1}\right) - \frac{1}{2}\Delta t^{2}\mathbf{C}\dot{\mathbf{U}}^{n+1} - \mathbf{K}\left[(\beta b_1 b_2)\Delta t^{3}\dot{\mathbf{U}}^{n} + \left(\frac{1}{16} + \beta b_1\right)\Delta t^{3}\dot{\mathbf{U}}^{n+1}\right] \tag{3.79}$$

where $\mathbf{E} = \mathbf{M} + \frac{1}{2}\Delta t\mathbf{C}$ is the effective matrix; n and $\Delta t = 3.571/\sqrt{\max\left(\text{eig}(\mathbf{K},\mathbf{M})\right)}$ are the time-step number and time-step length, respectively; $\beta = 1$, $b_1 = 8.567 \times 10^{-3}$ and $b_2 = 8.590 \times 10^{-1}$ are the time integration parameters of the Soares Jr. method; $\Im_{\mathbf{F}}^{n+1/2} = \beta_1 \Delta t\mathbf{F}^{n} + \beta_2 \Delta t\mathbf{F}^{n+1}$, with $\beta_1 = \beta_2 = 1/2$, using trapezoidal quadrature rule or $\beta_1 = 1$ and $\beta_2 = 0$, extending the explicit feature of the technique to the load term. More details can be seen in (Soares Jr., 2016).

The time integration parameters, b_1 and b_2, defined above, are pre-established to optimise the performance of the method and the β parameter ($0 \leq \beta \leq 1$) is selected to control the algorithm dissipative features of the technique. In this context, if $\beta = 0$, no numerical dissipation is introduced into the analysis and if $\beta = 1$, maximal dissipation is considered, resulting in a null value for the bifurcation spectral radius. For this reason, the value $\beta = 1$ was assumed in this thesis.

The two equations and the parameters here presented completely describe the new model of time marching proposed by Soares Jr. From the above, it can be concluded that the model is very simple, and it is essentially depending on β. Both mass and damping matrices must be diagonal to avoid systems of equations to be solved within each time step of the analysis.

The main features of this model, among others, can be outlined: the method is based only on single-step displacement-velocity relations and, therefore, stands as truly self-starting; it may require no system of equations to be dealt with in the analysis; it provides reduced period elongation errors; it allows numerical dissipation of spurious high-frequency modes (for $\beta > 0$); it exhibits extended stability limits; it may be stated as second-order accurate, etc. This model is very effective, being able to provide accurate analyses considering relatively large time steps. Moreover, since it has high stability limits, it minimises the main drawback of explicit procedures, allowing time-steps that are usually observed in accurate implicit analyses,

rendering good results at reduced computational costs (Soares Jr., 2016). For example, if its critical time-step is adopted (ensuring stability), the proposed time-marching method will only require around 56 % of the number of time steps of the (very popular) Central Difference Method to reach the solution at a given time instant, for $\beta = 1$, and 50 % for $\beta = 0$; this saving can be quite important in large problems such as the ones analysed in this thesis.

3.3.4 Absorbent layer to simulate (semi-)infinite media

To simulate infinite or semi-infinite media, it requires demanding computational resources and numerical tools when traditional numerical techniques as FEM are chosen. It is important to remember that vibration mitigation structures are in an (semi-)infinite medium and, therefore, to be able to model them, it is necessary to use numerical techniques that reduce the degrees of freedom of the problem. The absorbent layer allows using only a part of the (semi-)infinite medium – the Analysis zone – plus the absorbent layer (see Figure 3.4). This layer has the function of dissipating the propagated wave energy minimising the spurious reflections of the geometric model bounds that represent the infinite part of the modelled medium.

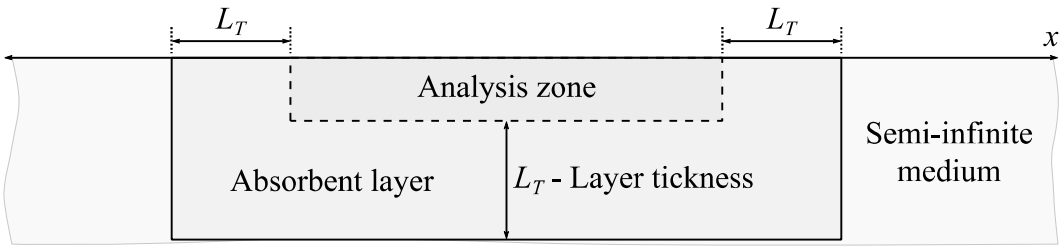

Figure 3.4 – Schematic representation of the absorbent layer in a semi-infinite medium.

Next, two absorption layer techniques used in the simulations of this thesis are presented.

Initially, an efficient, position-dependent and normalized function has been created in order to absorbing unwanted vibration reflections. Equation (3.80) gives a multiplication factor, f_{al}, as function of x position – a relative position within the layer and its value varies linearly between 0, next to the Analysis zone and 1, on the edge of the layer furthest from the Analysis zone.

$$f_{al}(x) = 1 - \left(\mathrm{e}^{0.025x^2} - 1\right) \times 10. \tag{3.80}$$

This function is easy to implement in the time integration process and it works well only in the frequency range of about 10 kHz. In fact, these function parameters are individually adjusted for a certain frequency range or, at the limit, for each frequency. Figure 3.5 shows the graph of this function.

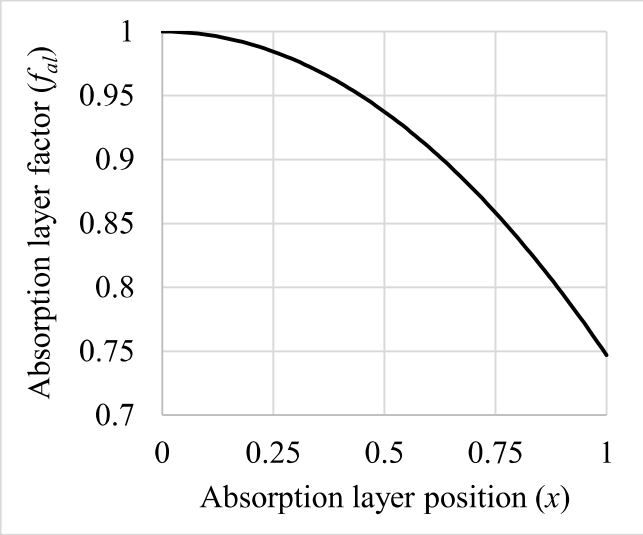

Figure 3.5 – Position-dependent function for a frequency range of about 10 kHz.

3.3.4.1 Forced decay absorbent layer

To automate the technique for absorbing unwanted vibration reflections, a forced decay function has been developed from the function (3.80).

$$f_{al}(x) = 1 - \left(\mathrm{e}^{\left[0.025+1.811\times10^{-6}\{f-10\times10^{3}\}\right]x^2} - 1\right) \times 10 \tag{3.81}$$

where f is the frequency under analysis.

Figure 3.6 shows the normalised graphs of this function for an absorbent layer with a propagation frequency of 60 Hz and 10 kHz.

This function was applied on a frequency range between 1 Hz and 200 kHz, using different materials, yielding the desired result, i.e., no reflection for the domain under analysis. This technique is also easy to implement in the time integration process.

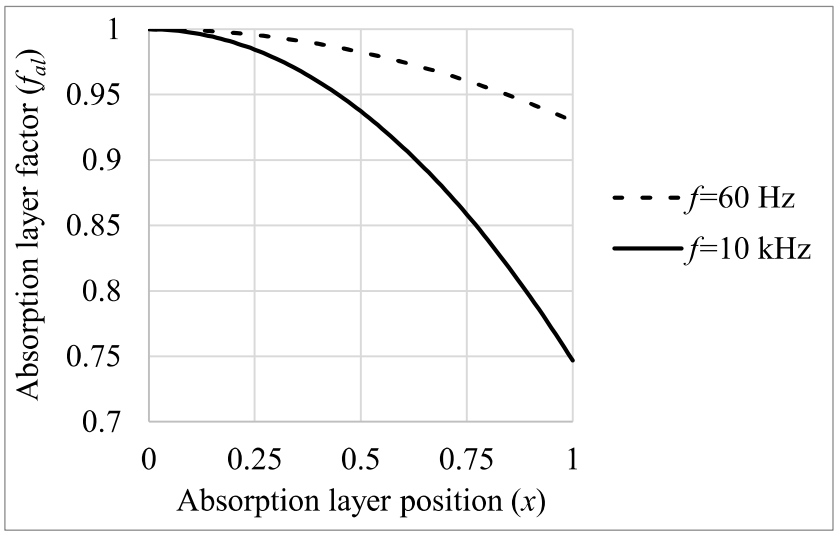

Figure 3.6 – Forced decay function.

Once this technique is implemented in the time integration process, there is the disadvantage of slowing down the time marching, since this computation has to be done in each time step. On the other hand, damping is unchanged throughout the process and the effort due to the formation of the matrices of the regular meshes (often used) is reduced.

3.3.4.2 Variable damping absorbent layer

In order to avoid the computation overload in the time integration process, another technique was created and applied when assembling the dynamic matrix. In this case, absorption acts as a material property associated with damping, i.e., in the absorption layer width, the damping increases to the outer edge of the absorption layer. The equation expressing the amount of absorption, p_{al}, associated with the damping is:

$$p_{al}(x) = D_{max} x^2 \tag{3.82}$$

where D_{max} is the maximum damping (generally, 70 % gives good results). p_{al} is then added to α_c – see description of Equation (3.77), page 46 – to compute the damping matrix. This equation produces the normalized graph shown in Figure 3.7.

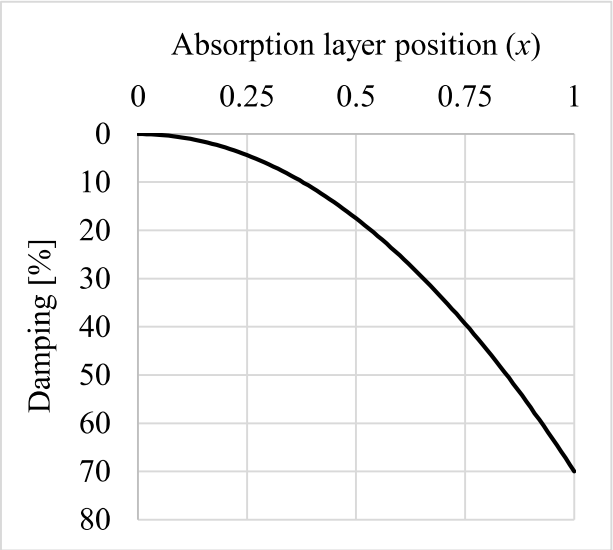

Figure 3.7 – Variable damping function.

This technique is the most efficient since the computation is performed only once and does not interfere with the time marching process. Although it makes the computation of the damping matrix a little slower, the time integration is faster, reducing often the total time.

An important note to mention at this point is related to the models used to reach those functions. Since the absorbent layers are essentially used to modelling (semi-)infinite models, their application is intrinsically linked to vibration mitigation. In this sense, the values are related to the material in this propagation medium: the soil.

4 IMPLEMENTATION AND VERIFICATION OF NUMERICAL SIMULATION MODELS

This chapter describes the implementation and verification of the numerical simulation models presented in the previous chapter. Indeed, the implementation of the Method of Fundamental Solutions in the numerical simulation of elastic waves propagation requires a detailed analysis, for example in what concerns the number of colocation points needed for a good simulation, the distance from virtual sources to the border and errors related to analytical solutions. Regarding the Finite Element Method in the time domain, the implemented step-by-step analysis in the numerical simulation of elastic waves propagation, also needs to be carefully studied and should be verified against other methodologies before application. In this case, a comparison is made with the analytical solution transformed from the frequency domain.

4.1 The Method of Fundamental Solutions

4.1.1 Implementation and verification

To analyse the implementation process of the MFS, consider a single inclusion buried in a propagation medium as shown in Figure 4.1. The location of the receiver where the displacement field is computed must be considered. If the receiver is outside of the inclusion, Equation (3.15) must be used, whereas if the receiver is inside the inclusion, Equation (3.16) must be used. If the receiver is on the edge of the inclusion, any of the equations can be used. The computing process of displacement amplitude is shown in Figure 4.1, where an inclusion with four collocation points (for simplicity) and the respective virtual sources are represented. Figure 4.1 (b) shows the virtual sources that intervene in computing the amplitudes in a receiver inside an inclusion – see Equations (3.29) and (3.30); Figure 4.1 (a) shows the virtual sources that intervene in computing the amplitudes in a receiver outside an inclusion and the incident field that directly affects the amplitude in that receiver – see Equations (3.31) and (3.32).

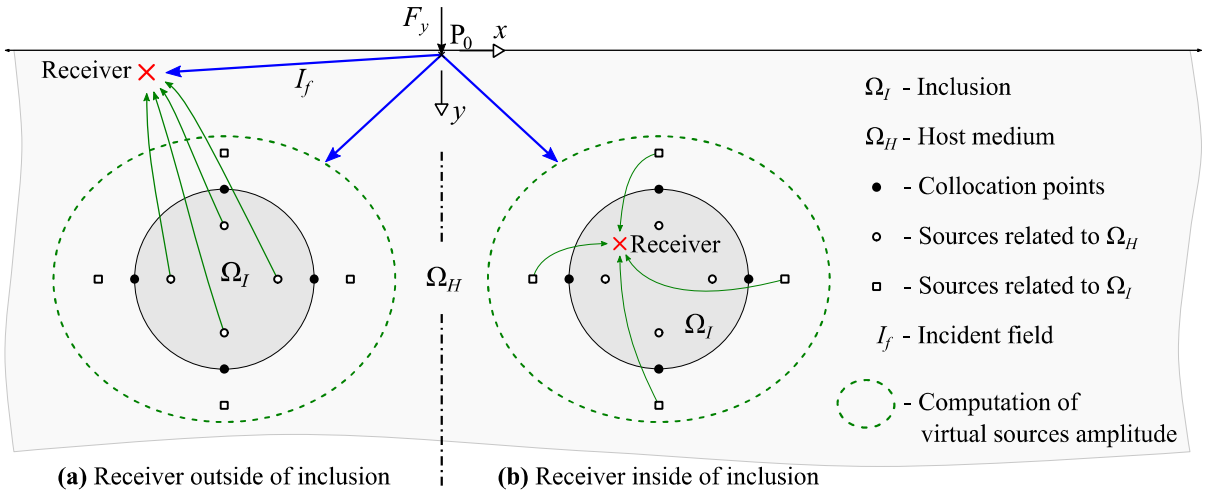

Figure 4.1 – Schematic representation of displacement computation (a) outside and (b) inside an inclusion.

It is important to note that the full discretization of the system is only possible using simplified approaches to introduce a small numerical damping that ensures convergence in the computation of the Green's functions of half space domain (Tadeu *et al*., 2001). In this thesis, the complex angular frequency with a small imaginary part is used for this purpose (Tadeu *et al*., 2001):

$$\omega_c = 2\pi f - i\eta \tag{4.1}$$

where f is the frequency, $i = \sqrt{-1}$ and $\eta = 0.7(2\pi/T)$.

For MFS verification, a comprehensive study was made using firstly, a single inclusion and then, several inclusions. In what follows, this study will be described.

Single inclusion

Consider a circular inclusion of radius 0.5 m centred at point $(-10, 2)$ m, embedded in an elastic medium that is excited by a dynamic vertical load $F_y = 1$ N, acting at point $(0, 0.1)$ m, according to Figure 4.2. The inclusion is made as the same material as the host medium, with density $\rho = 1700$ kg/m^3, shear modulus $G = 43.52 \times 10^6$ Pa and Poison's ratio $\nu = 0.33$. The response, in

terms of horizontal (x) and vertical (y) displacements, is computed for a specific frequency of 20 Hz over a set of 10 receivers evenly distributed along the border of the inclusion.

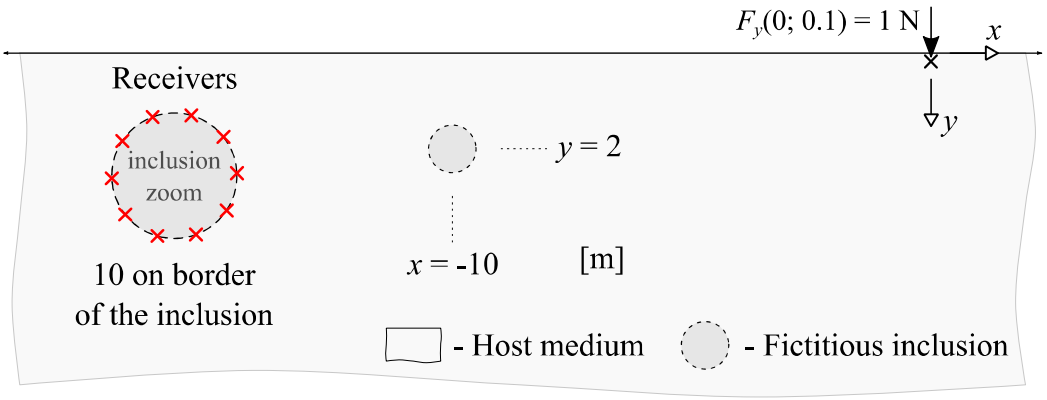

Figure 4.2 – Schematic representation of a fictitious circular inclusion embedded in an elastic medium.

The computation was performed using the MFS model, with 40 collocation points evenly distributed along the inclusion boundary and with two sets of 40 virtual sources placed to either side of that interface at a distance of 0.25 m. Receivers are displaced of the collocation points, where the responses should be the same in both implementations. The response (displacement) values are shown in Figure 4.3 in both (a) x and (b) y directions as well as the relative error, E_R, logarithmically scaled, with respect to the analytical values resulting from the Green's functions, also in (c) x and (d) y directions. In all receivers, the relative error is smaller than 1×10^{-5}, validating the response. The response is schematically represented in Figure 4.4, where 'O-filled' markers are receivers on the original position; 'O' markers represent the analytical response computed directly with the Green's functions; '×' markers represent the result computed as if the receivers were inside the inclusion using Equation (3.16); and '+' markers, highlights results computed as if the receivers were in the host medium and calculated using the fundamental solution corresponding to the half-space Green's functions depicted in Equation (3.15).

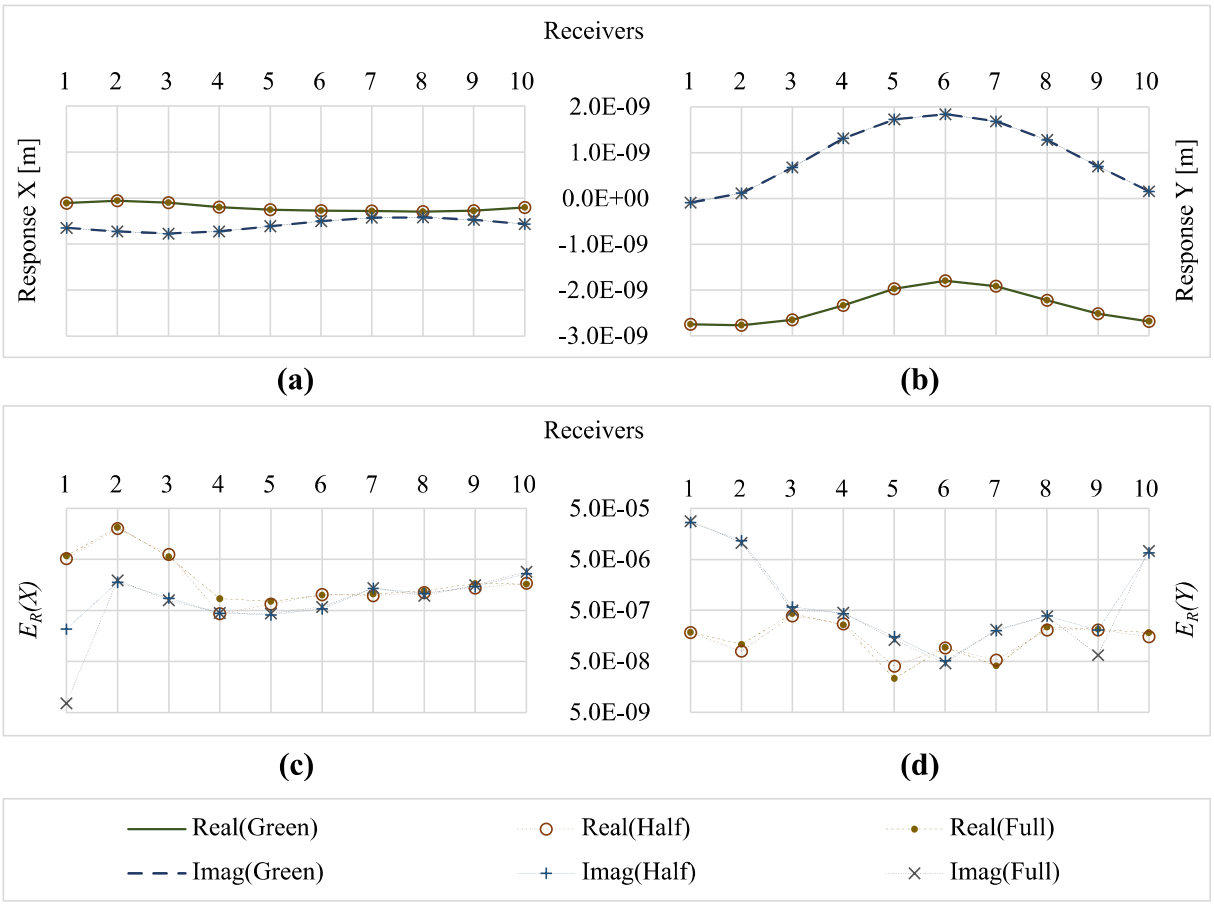

Figure 4.3 – Response (displacement) in the (a) x and (b) y directions and error in (c) x and d) y directions relative to the analytical (Green) response.

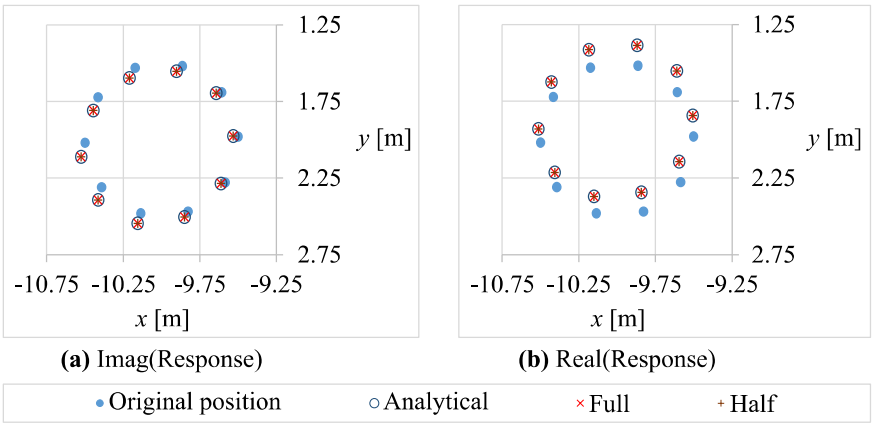

Figure 4.4 – Displaced positions of the receivers: (a) imaginary and (b) real parts of the response, amplified by a factor of 5×10^7.

Multiple inclusions

A comprehensive study was also made using more than one inclusion. Here a test case is analysed considering $NE = 6$ solid circular inclusions with radius $R = 0.5$ m. For the study a varying number of collocation points in the set $NC = \{20, 30, 40, 50, 60, 70, 80\}$ along each inclusion border was considered, as well as a frequency of either (20 or 100) Hz and a shear modulus in the set $G_I = \{G_H/2, G_H, 2G_H\}$ Pa. For the host medium, a shear modulus $G_H = 43.52 \times 10^6$ Pa was considered. Both host medium and inclusion had a density $\rho_H = \rho_I = 1700\ \text{kg/m}^3$ and Poisson's ratio $\nu_H = \nu_I = 0.33$. The centre of the upper inclusions was placed at a depth of 2 m and spaced from each other 2 m, either vertically or horizontally, as shown in Figure 4.5.

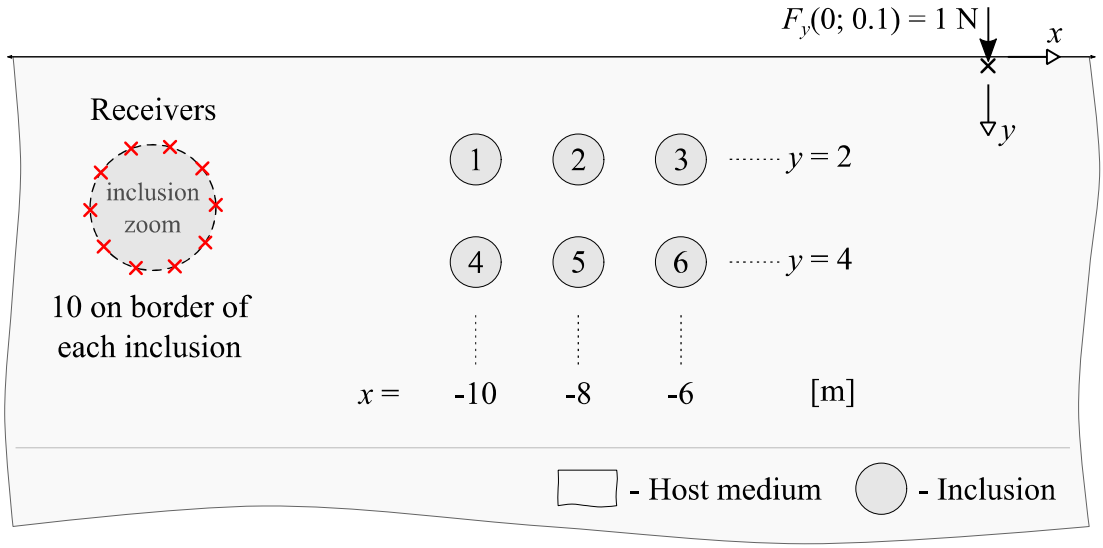

Figure 4.5 – Schematic representation of multiple inclusion model.

The response, in terms of horizontal (x) and vertical (y) displacements, is computed in NE sets of 10 receivers evenly distributed along each inclusion border. Since receivers are placed on the border of the inclusions, the computation is performed by two possible ways: first using the result of Equation (3.15), as if receivers were in the host medium, and then the result of Equation (3.16), as if receivers were inside the inclusion.

Preliminary studies were carried out to assess the effect of the number of collocation points and of the distance of virtual sources to the inclusion border in the accuracy of the computations. The analysis of these effects is presented at the end of this verification.

Of the set of cases evaluated, only one is presented for illustrative purposes. In all other cases, satisfactory results were also obtained. Therefore, only the analysis of the computed response for six inclusions with the same material properties of the host medium and excited by a frequency of 20 Hz is presented. For this model (shown in Figure 4.5) different collocation points were considered. For the case of 40 collocation points and the virtual sources positioned at $d_{VS} = d_H = d_I = 0.5R$, the (a) imaginary and (b) real parts of the response, amplified by a factor of 1.5×10^8, are schematically represented in Figure 4.6, where "O-filled" markers are receivers on the original position; "O" markers represent the analytical response computed directly with the Green's functions; '×' markers represent the result computed as if the receivers were inside the inclusion using Equation (3.16); and '+' markers highlights results computed as if the receivers were in the host medium and calculated using the fundamental solution corresponding to the half-space Green's functions depicted in Equation (3.15).

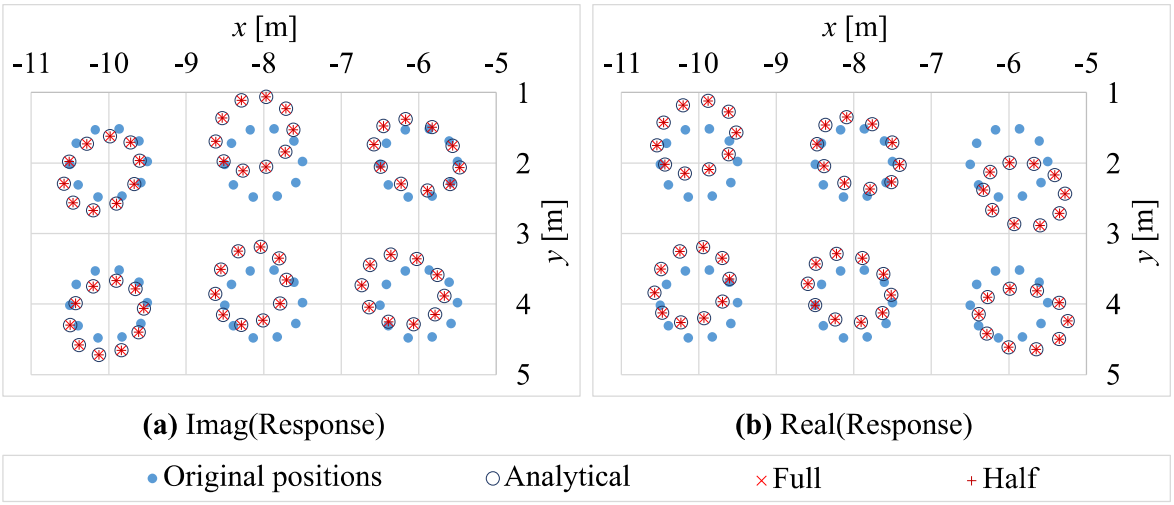

Figure 4.6 – Deformed shape of the inclusions: (a) imaginary and (b) real parts of the response, amplified by a factor of 1.5×10^8.

As can be seen in the previous figure, the numerical results match very well those calculated analytically, using the half-space Green's functions. The relative error, E_R, with respect to the

analytical response are shown, logarithmically scaled, in Figure 4.7 which presents the (a) imaginary and (b) real parts of relative errors for all studied collocation points in range $NC = \{20, 30, 40, 50, 60, 70, 80\}$, using $d_{VS} = 0.5R$. In this figure "Full" means the computation was performed using Equation (3.16) and "Half" means the computation was performed using Equation (3.15); "-X" and "-Y" relate to directions x and y, respectively. Observing the presented plots it can be concluded that the relative error tends to decrease with increasing numbers of collocation points, indicating a progressive convergence to the correct solution. Using 40 collocation points the relative error is already lower than 1×10^{-5}, indicating excellent solution accuracy.

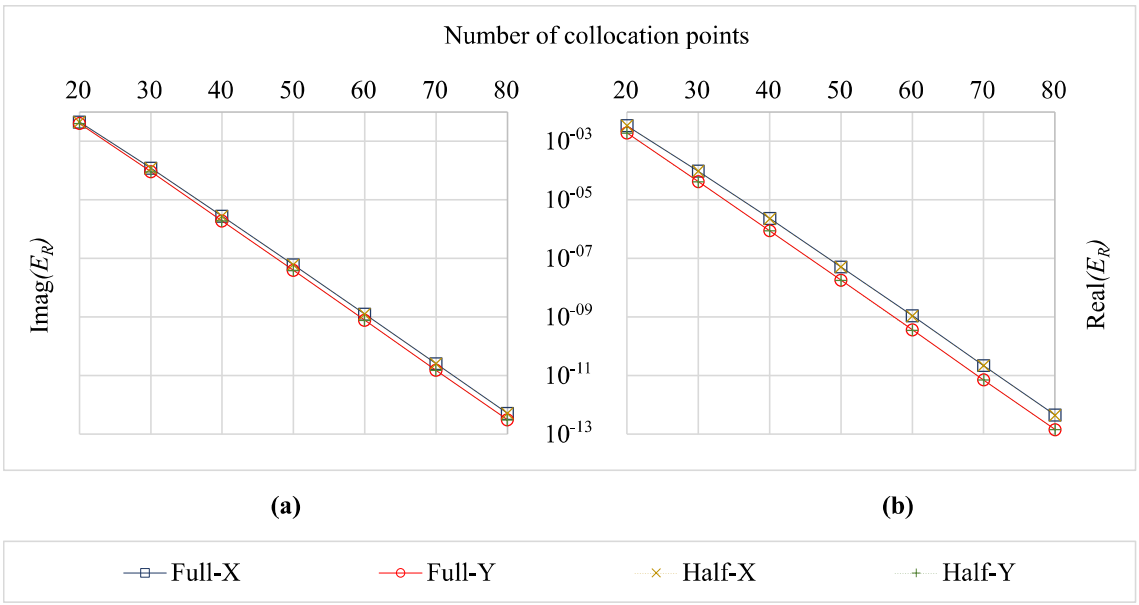

Figure 4.7 – (a) imaginary and (b) real parts of relative errors related to collocation points number.

The same type of analysis was performed for the distance of virtual sources. For the previously presented study, with 40 collocation points, Figure 4.8 shows the relative error, logarithmically scaled, related to the distance of the virtual sources where (a) imaginary and (b) real parts for the range $d_{VS} = \{0.1, 0.15, 0.2, 0.25, \ldots, 0.9\} \times R$, are presented. In addition, as in the case of collocation points, it can be concluded that the relative error tends to decrease with increasing the virtual sources distance. Using $d_{VS} = 0.5R$ the relative error is lower than 1×10^{-5}, indicating excellent solution accuracy.

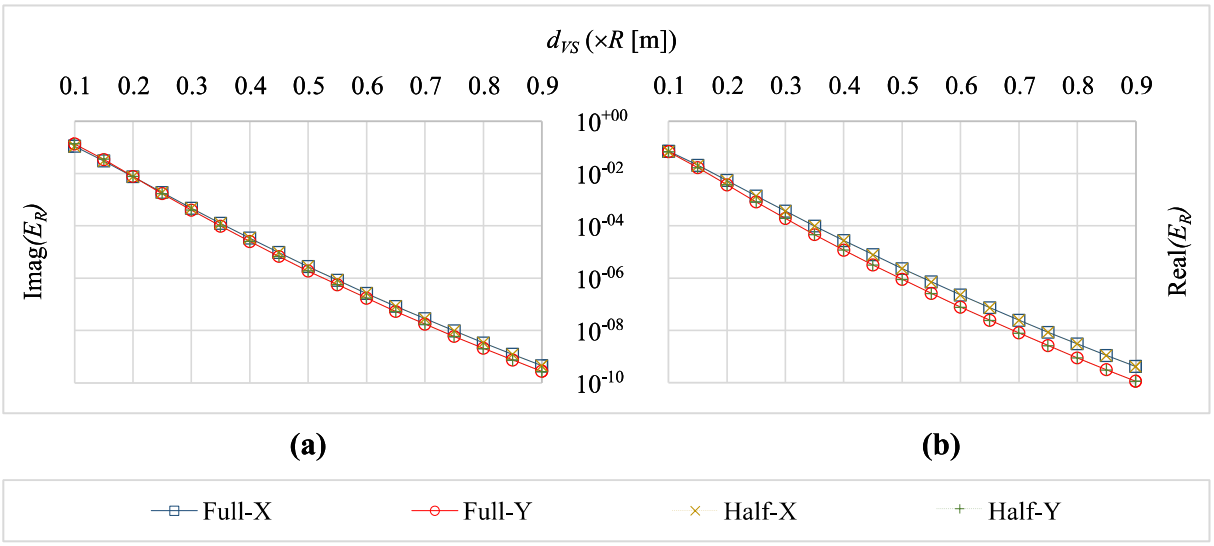

Figure 4.8 – (a) imaginary and (b) real parts of relative errors related to virtual sources distance.

Observing Figure 4.9, it can be seen that the system matrix becomes progressively more ill-conditioned with the increase of the number of collocation points and the distance of the virtual sources, although the quality of the calculations does not seem to be degraded due to this issue. However, it is considered that this parameter should be monitored to avoid numerical errors due to badly conditioned matrices.

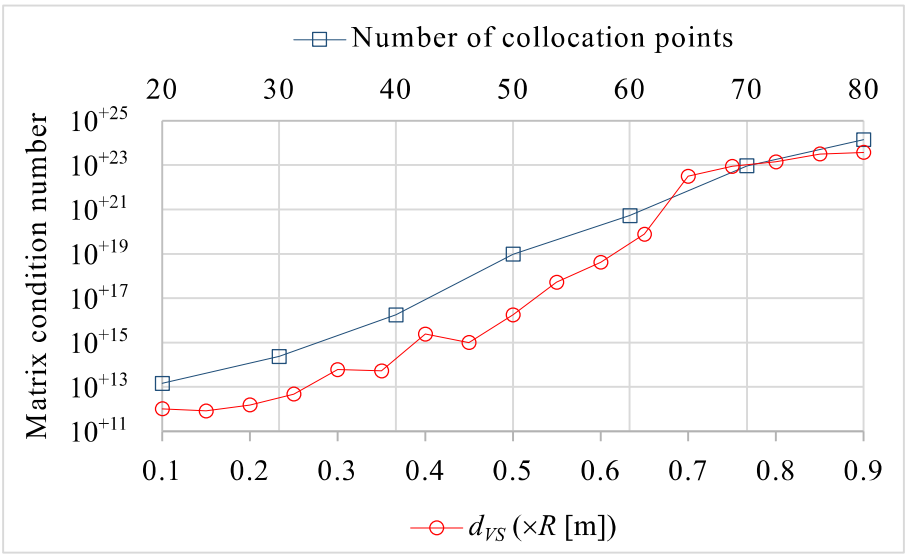

Figure 4.9 – System matrix condition number.

The effect of the inclusion stiffness relative to the host medium is shown in Figure 4.10 through the representation of the deformed shape of the inclusion with the same stiffness ("O" markers), half stiffness ("×" markers) and twice the stiffness ("+" markers) of the host medium. This figure also compares these results with those achieved using the BEM (Godinho and Tadeu, 2002) under the same conditions. As can be seen, an excellent agreement of the MFS and BEM is obtained. Although not shown here, also good results were obtained for larger sets of inclusions.

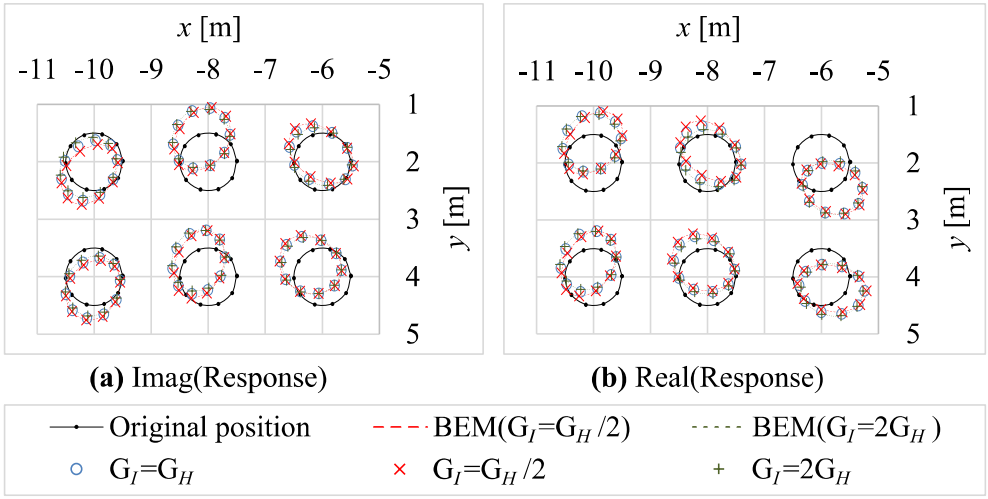

Figure 4.10 – Modified positions of receivers: (a) imaginary and (b) real parts of the responses, amplified by a factor of 1.5×10^{8}.

4.1.2 Optimal position of virtual sources

As already seen in previous cases, a higher number of collocation points leads to a better result. However, the accuracy of the result computed for each number of collocation points depends on the distance of the virtual sources to the inclusion boundary. Furthermore, a higher number of collocation points has an increased computation time. So, for a given number of collocation points, it is important to determine the best position of the virtual sources in order to obtain accurate results while minimising the computational cost. To do this, an evaluation of the result should be carried out and this evaluation should be comparable. There are several ways to compute the error, such as the:

- *average of errors computed in receivers' location (E_{RL})*:
  average of relative errors to the analytical solution computed in receivers' location;
- *average of errors computed in collocation points' location (E_{CP})*:
  average of relative errors to the analytical solution computed in collocation points' location;
- *the Integral of errors computed along the inclusion border (E_{IB})*:
  result of the integration of the difference between the computation of the full-space Green's functions and the half-space Green's functions along the inclusion border.

The first two forms of quantifying the errors consider the relative errors to the analytical solution. Therefore, they are only valid when analytical solution is known, as in the case when both host medium and inclusions have the same material characteristics. On the other hand, it was seen previously that independently of material characteristics of both media, the result on the inclusion border must be the same computed using either fundamental solution corresponding to the full-space Green's functions or fundamental solution corresponding to the half-space Green's functions. However, when this computation is made away of the collocation points, there is a difference between the two results that can be measured, and the smaller the difference, the better the result. By integrating this difference along the inclusion border a value is obtained, characteristic of the model conditions, which can be seen as representing the error of the result (Tadeu *et al*., 2009). This is the principle of the third method (E_{IB}) to estimate the error of a particular result. Some examples are presented next, considering these methods of evaluating the result error.

Both media with same characteristics

The study of the error when the inclusion has the same material characteristics of the host medium, where it is buried, is the simplest case and allows the computation of the error through the three methods previously presented, and so their differences can be established. For this purpose, consider the system depicted in Figure 4.11 where a circular inclusion of radius 0.5 m centred at point $(-10, 2)$ m, with the same material of the elastic medium in which it is embedded, that is excited by a dynamic vertical load $F_y = 1$ N, acting at point $(0, 0.1)$ m and oscillating with a frequency of 100 Hz. The elastic properties of both media are: density $\rho = 1700\,\mathrm{kg/m^3}$, shear modulus $G = 43.52 \times 10^6$ Pa and Poison's ratio $\nu = 0.33$. Consider too a set

of receivers at a depth of 0.1 m and 1 m horizontally spaced in a range of $\{-30, \dots, 30\}$ m. A system damping is introduced by means of a complex frequency with a small imaginary part.

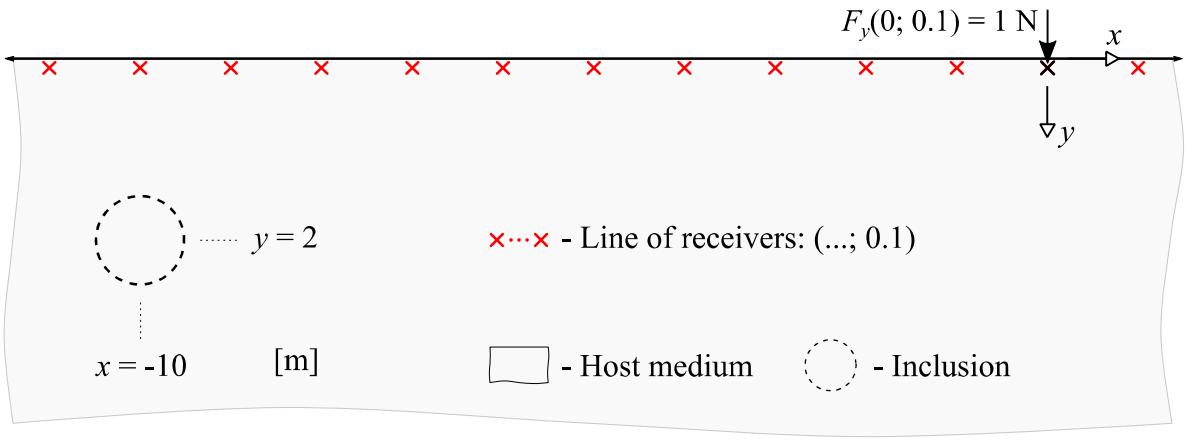

Figure 4.11 – Schematic representation of the system used for determining the model error measure.

For this case, the distances between the virtual sources and the interface tested for each number of collocation points are in the range between $0.10R$ and $0.90R$, with steps of $0.10R$. Between 10 and 60 collocation points, the distances of virtual sources were, then, evaluated in the range between $0.80R$ and $0.99R$ with steps of $0.01R$, since with the step of $0.10R$ all results were $0.90R$. With 100 collocation points the distance of $0.45R$ was also evaluated. These latest two evaluations were made to establish more detailed differences in optimal distances. Table 4.1 shows the different analyses performed to allow a better understanding. As can be seen from the results shown in the Figure 4.12 (a), all proposed methods of determining the error lead practically to the same optimal distance of the virtual sources. Indeed, the differences between methods observed when adopting 20 to 50 collocation points are irrelevant as will be seen later.

Table 4.1 – Performed analyses.

	Collocation points	d_{VS}	Δd_{VS}
1st	10 to 100	(0.10 to 0.90) R	$0.10R$
2nd	10 to 60	(0.80 to 0.99) R	$0.01R$
3rd	100	(0.40 to 0.50) R	$0.05R$

It should be noted that the errors of each optimal virtual sources distance to the respective number of collocation points shown in Figure 4.12 (b) cannot be compared in absolute terms because they have different meanings. While E_{CP} and E_{RL} are the relative errors to the analytical solution, E_{IB} is the integral of absolute errors computed along the inclusion border. Furthermore E_{CP} and E_{RL} also cannot be compared because they are computed in different receivers. Nevertheless, all methods have the same trend. So, any of them can be used for computing the optimal virtual sources distance.

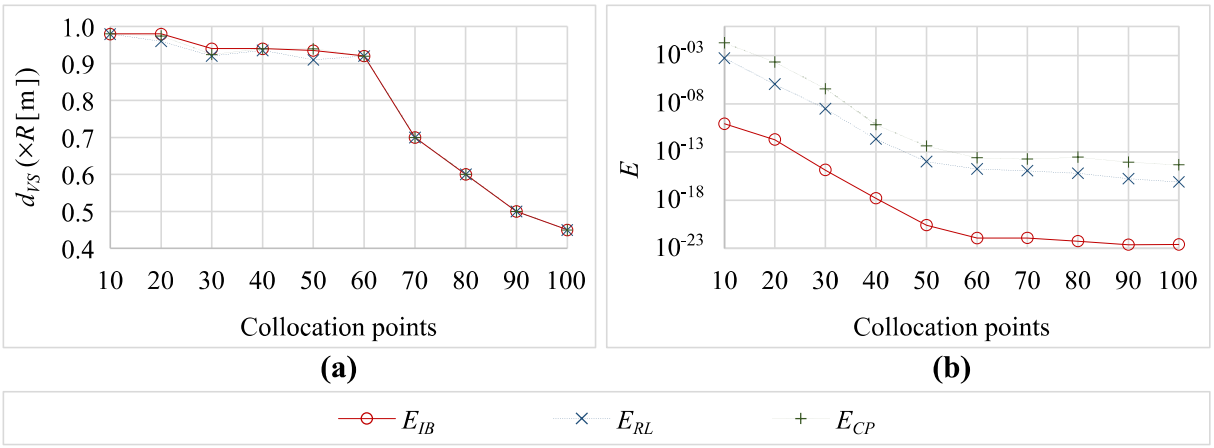

Figure 4.12 – (a) optimal distance of virtual sources and (b) associated error taking into account the number of collocation points.

In this example, the best choice would correspond to the pair $(NC, d_{VS}) = (100, 0.45)$, which exhibits the lowest error. However, the practical choice falls on $(NC, d_{VS}) = (30, 0.9)$, with excellent results and computationally much faster due to the lower number of collocation points. By analysing Figure 4.12 it can be concluded that the optimal distance of virtual sources and correspondent error decreases with increasing the number of collocation points. Increasing the collocation points improves the definition of the model's geometry, while allowing a more detailed wave-field to be reconstructed by adding the contribution of a larger number of virtual sources, leading to better results. On the other hand, the decrease of the virtual sources distance with the increase of the number of collocation points also improves the results. As already seen in Figure 4.9, both the increase in the collocation points number and in the distance of virtual sources make the system ill-conditioned. Thus, by reducing the distance of virtual sources, the

system becomes better conditioned reducing the numerical error due to instability. A similar conclusion had already been reached by (Godinho *et al*., 2012).

Inclusion with different stiffness from the host medium

Consider the model shown in Figure 4.11. A similar analysis to the one previously presented was performed for different ratios of stiffness between inclusion and host medium, and all other properties were kept constant. For a frequency of 100 Hz the optimal distance of virtual sources for each number of collocation points can be seen in Figure 4.13 (a) and the respective E_{IB} errors in Figure 4.13 (b). For any stiffness ratio between inclusion and host medium, the same previous conclusion can be drawn, i.e., the optimal distance of virtual sources and corresponding error decreases with increasing the number of collocation points. Note that, as in all cases previously seen, using 10 collocation points always leads to bad results. When considering other frequencies, the graphics are similar as will be seen later.

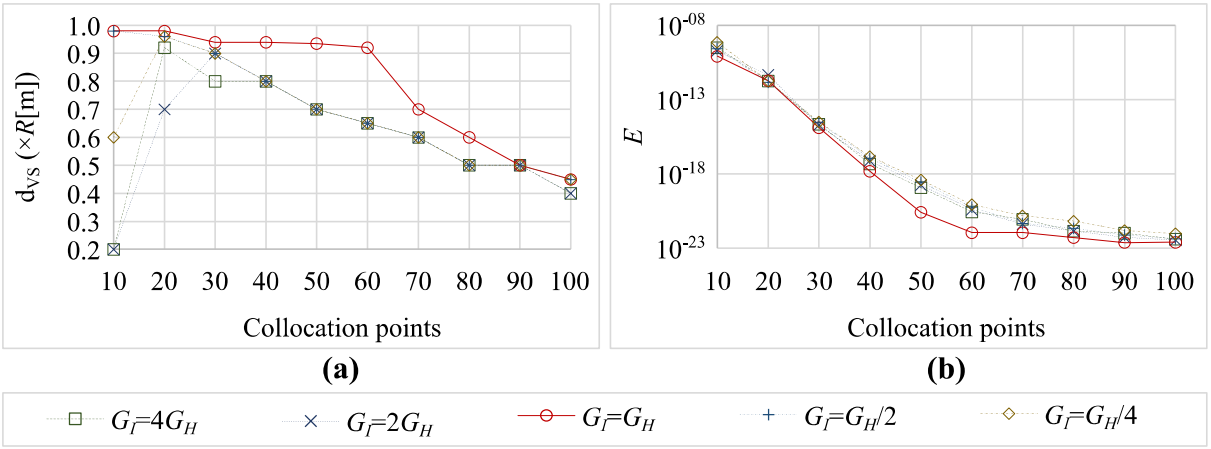

Figure 4.13 – (a) optimal distance of virtual sources and (b) associated error considering the number of collocation points for different ratios of stiffness between inclusion and host medium.

Looking at the Figure 4.13 (a), considering, for example, 60 collocation points, it can be seen that all ratios except $G_I = G_H$ have an optimal distance of $d_{VS} = 0.65R$ as opposed to the latter which is $d_{VS} = 0.92R$, all of them with an error less than 1×10^{-2} . Next, the response for the case of an inclusion four times stiffer than the host medium is analysed with those two distances from virtual sources, since if E_{CP} and E_{RL} errors are minimized, the optimal distance is $d_{VS} =$

$0.92R$. Horizontal (x) and vertical (y) displacements are shown in Figure 4.14 (a). Graphically there is no difference using $d_{VS} = 0.65R$ or $d_{VS} = 0.92R$. The absolute difference of displacements computed considering those distances is shown in Figure 4.13 (b). It can be seen, given the order of magnitude of this difference, that in practice it is irrelevant to use one or another of those distances. Identical analysis was done for the remaining ratios of stiffness, obtaining equivalent results. This means that for 60 collocation points, a distance of $d_{VS} = 0.65R$ or $d_{VS} = 0.92R$ could be used for all cases without loss of accuracy.

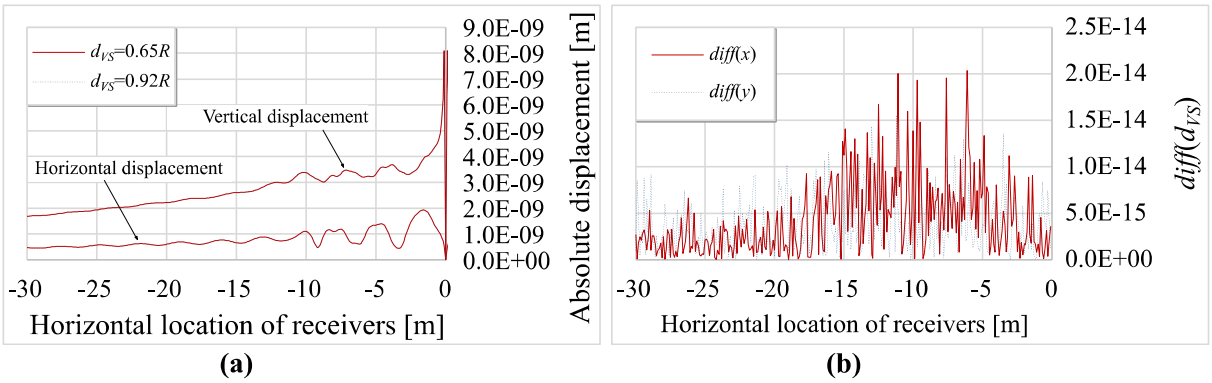

Figure 4.14 – (a) Response in terms of displacement and (b) difference between displacements (x and y directions) computed with different distances of virtual sources.

Behaviour of the method for different frequencies

This study was carried out in the same scenario presented in Figure 4.11 and taking into account a unitary vertical load oscillating with several frequencies in the range (10 to 150) Hz. Different stiffness ratios between inclusion and host medium were also considered. As it has been seen for frequency of 100 Hz, the optimal distance of virtual sources and the associated error decrease with increasing the number of collocation points (see Figure 4.12 and Figure 4.13). This conclusion cut across any frequency value and any stiffness ratio. Figure 4.15 shows this result for the inclusion four times stiffer than the host medium. Similar results are obtained for the other stiffness ratios.

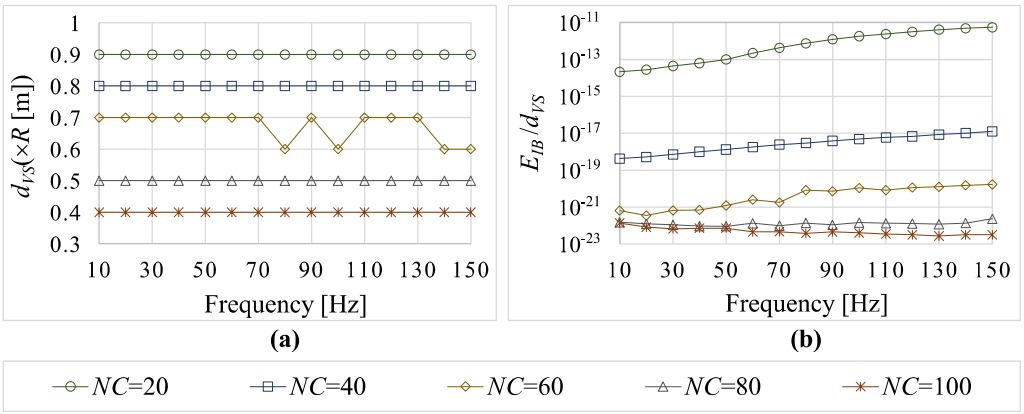

Figure 4.15 – (a) optimal distance of virtual sources and (b) associated E_{IB} error considering the number of collocation points for different frequencies.

Multiple inclusions

In this example, consider the model with 6 inclusions shown in Figure 4.5, to study the behaviour of the distance of the virtual sources and the respective error with the number of collocation points and the frequency. To study the E_{RL} error, the same receptors identified in the system of Figure 4.11 (a set of receivers at a depth of 0.1 m and 1 m horizontally spaced in a range of $\{-30, \ldots, 30\}$ m) have been considered. Figure 4.16 presents the results obtained for the frequency of 50 Hz. Howsoever, all frequencies have a similar behaviour. Comparing this image with those related to a single inclusion (Figure 4.12 and Figure 4.13), it is concluded that the multiple inclusions follow the same trend of individual inclusions.

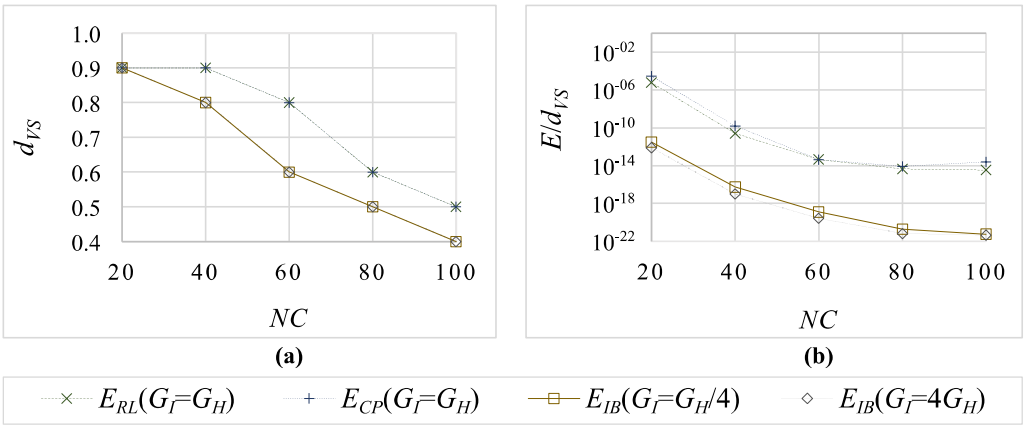

Figure 4.16 – (a) optimal distance of virtual sources and (b) associated error considering the number of collocation points for two ratios of stiffness between inclusion and host medium.

With these examples it is seen that each case is different and must be particularly evaluated. However, based on the evaluated cases, it can be stated for frequencies up to 150 Hz, the use of 25 or more collocation points and distances of virtual sources between $(0.5 \text{ and } 0.8)R$ can be obtained accurate results.

4.2 The Finite Element Method in the Time Domain

4.2.1 Implementation and verification

To verify the correct implementation of the Finite Element Time Domain algorithm, a simple verification scenario has been tested, corresponding to a half-space medium. The material properties correspond to a Young's modulus of $G = 30 \times 10^9$ Pa, a Poisson's ratio of $\nu = 0.2$ and a density of $\rho = 2400\,\text{kg/m}^3$. Calculations were performed over a grid covering an area of 0.8 m wide by 0.2 m deep where a vertical load is positioned half width at the surface of the medium, generating a Ricker pulse with a central frequency of 70 kHz. This problem has been modelled using the FEM-TD algorithm considering an element size of 0.001 m, and the time step used is 3.33×10^{-7} s (calculated automatically from the highest order eigenvalue of the equation system).

In order to obtain a reference solution for this verification, the fundamental solution for a half-space in the frequency domain has been used. Responses have been computed for the same geometric configuration and material properties indicated above for 128 frequencies, starting at 2000 Hz and with an increment of 2000 Hz, following the procedure indicated, for example, in (Godinho, Dias-da-Costa, *et al.*, 2013).

Figure 4.17 presents the calculated results for the two methods, for a time instant $t = 8.5 \times 10^{-5}$ s. Observing the results it is clearly that very similar results have been obtained, with only very small amplitude differences being registers between the two completely independent methods. This result clearly indicates that a correct prediction is provided by the FEM-TD implementation, and that it can be used reliably to analyse this type of problem.

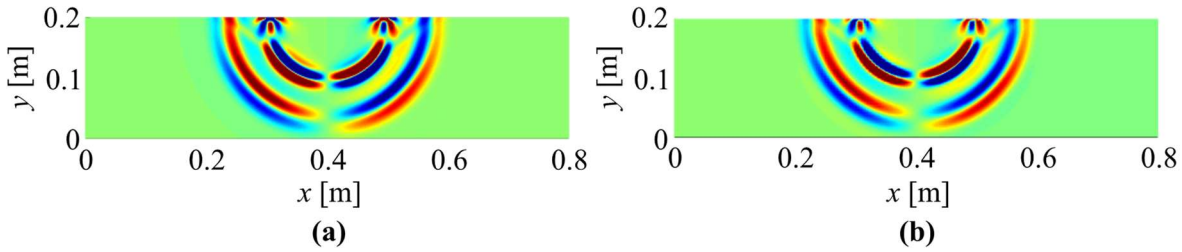

Figure 4.17 – Horizontal displacement computed over a complete grid of receivers using the (a) FEM-TD and (b) an analytical solution transformed from the frequency domain, at $t = 8.5 \times 10^{-5}$ s.

In order to show the potential of the FEM-TD algorithm, two examples of wave propagation simulation are presented next: the first, simulating the propagation in a semi-infinite medium using an absorption layer to simulate the infinite nature of the medium; and the second, simulating the propagation in a finite medium corresponding to a concrete beam.

Figure 4.18 (a) shows a slice of a semi-infinite medium 0.5 m wide, 30 m long and up to 7 m deep where the host medium has a density $\rho = 2000\ \text{kg/m}^3$, Young's modulus $E = 50 \times 10^6$ Pa, Poisson's ratio $\nu = 0.35$ and a damping factor of $\zeta = 1$ % was assumed. To simulate the infinite part of the soil a 5 m thick absorption layer was used.

Figure 4.18 (b) shows a concrete beam with $400 \times 100 \times 100\ \text{mm}^3$ which has a $5 \times 20 \times 100\ \text{mm}^3$ notch, located at the middle of the top. The material properties are: density $\rho = 2500\ \text{kg/m}^3$, Young's modulus $E = 35\ 000\ \text{N/mm}^2$, Poisson's ratio $\nu = 0.15$ and a damping factor of $\zeta = 3$ % was assumed.

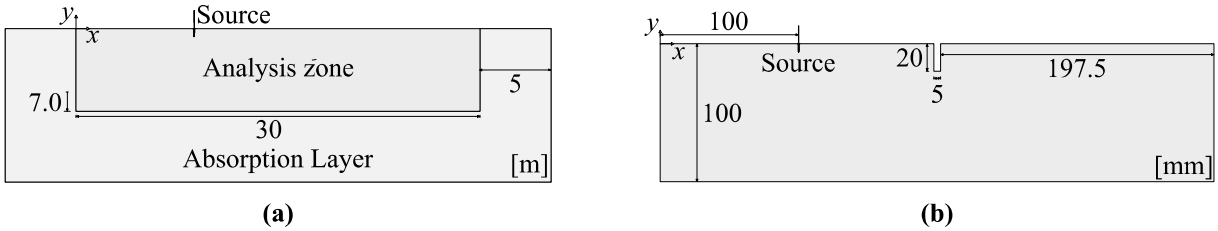

Figure 4.18 – (a) schematic representation of a soil slice and (b) schematic representation of a concrete beam.

Figure 4.19 (a) shows the time evolution of horizontal displacement due to a load generated by a Ricker pulse applied to the ground surface, 10 m from the origin of the Analysis zone (upper

left corner) with a central frequency of 100 Hz. As can be seen from these plots, the propagation is physically coherent and the absorption layer blocks the reflections of the boundaries of the geometric model, thus fulfilling its purpose.

Figure 4.19 (b) shows snapshots of the time evolution of vertical displacements due to a load generated by a Ricker pulse applied to the beam upper face, 100 mm from the origin of the beam (upper left corner), with a central frequency of 150 kHz. Reflections can be seen at the boundaries of the beam and, in later times, the reflection caused by the notch can also be seen. Once again, the main features observed in this simulation are in-line with the expected patterns, thus indicating the good results achieved with the algorithm.

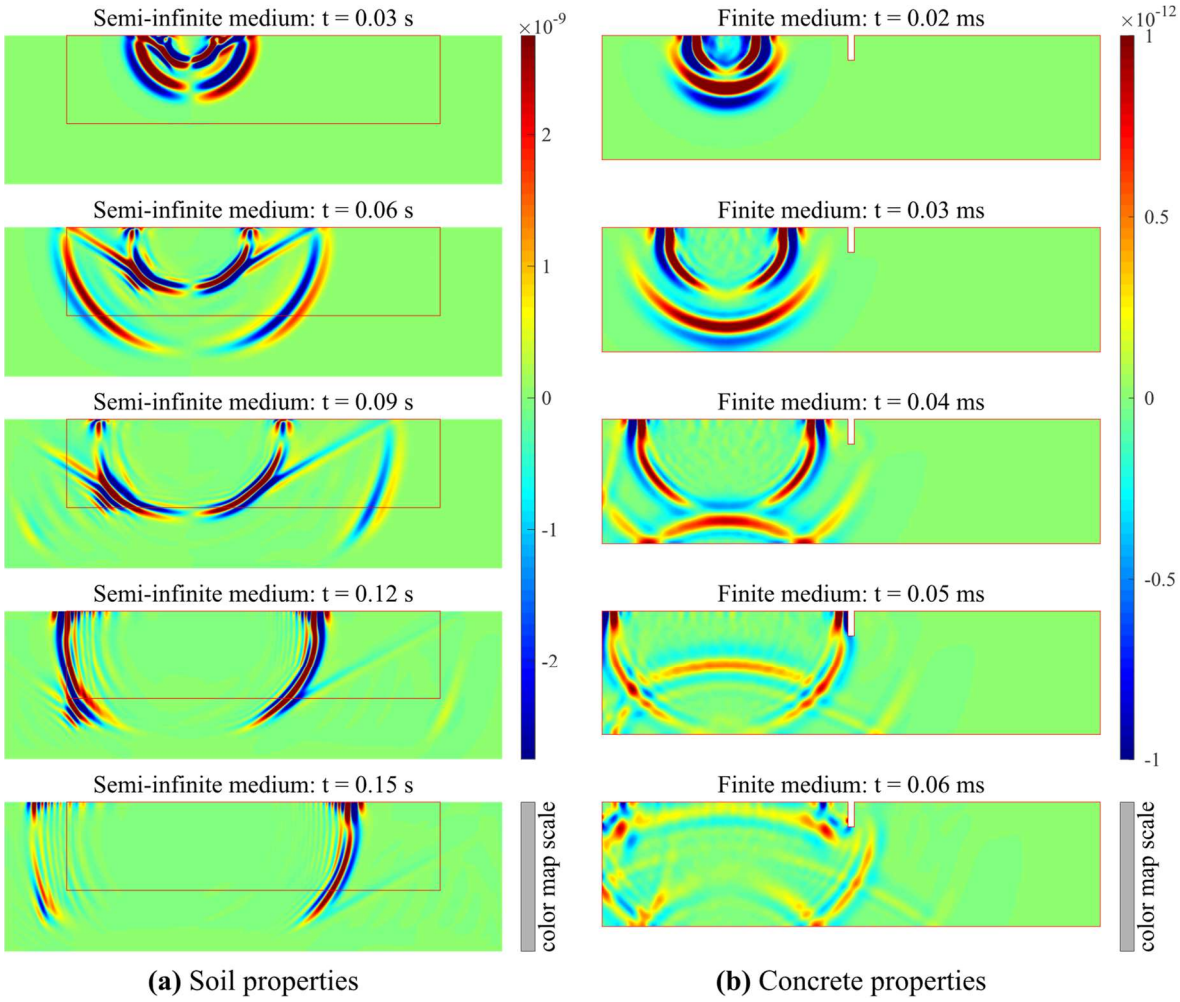

Figure 4.19 – (a) horizontal displacements in a semi-infinite medium and (b) vertical displacements in a finite medium.

It should be noted that, in the absence of a reference of the maximum element size or of the number of elements per wavelength, in the examples presented in this work, at least 8 elements per wavelength are always considered, thus ensuring the accuracy of the results.

4.2.2 Behaviour of the absorbent layer

Consider a slice ("Analysis zone") of a semi-infinite medium 0.5 m wide, 30 m long and up to 7 m deep as shown in Figure 4.20. The host medium has a density $\rho = 2000\,\mathrm{kg/m^3}$, Young's modulus $E = 50 \times 10^6$ Pa and Poisson's ratio $\nu = 0.35$.

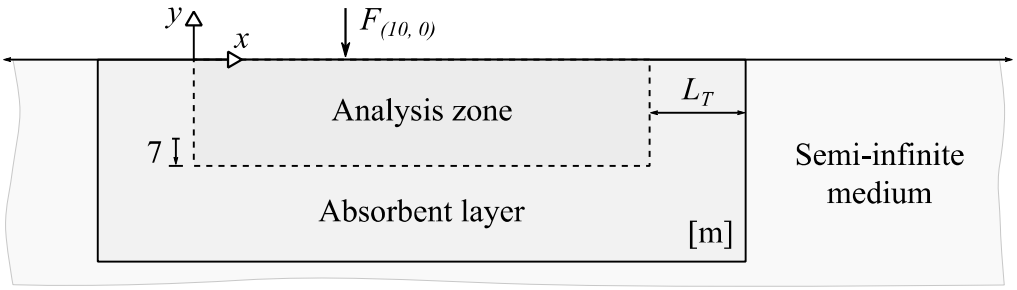

Figure 4.20 – Schematic representation of absorbent layer analysis model.

To analyse the behaviour of the absorbent layer, the frequencies of $(5, 10, 20, 50, 100$ and $250)$ Hz and the layers thicknesses of $(2, 3, 4, 5$ and $6)$ m were used. Analyses have been performed using the variable damping absorption layer (VD) and using the forced decay absorption layer (FD). For the VD analyses the value of $D_{max} = 70\,\%$ – see Equation (3.82) – was used. The results are shown in Figure 4.21. There is a big difference between the models regarding the trend of layer thickness. In the case of the FD model, there is a need for a thick layer at almost all studied frequencies. In the case of the VD model, as the frequency increases, the required layer thickness to absorb the unwanted reflected energy decreases. Taking into account the object of study (the mitigation of vibrations induced by means of transport, mainly railway) and the associated frequencies are between $(20$ and $100)$ Hz, the VD model ensures greater efficiency by modelling a narrow absorbent layer.

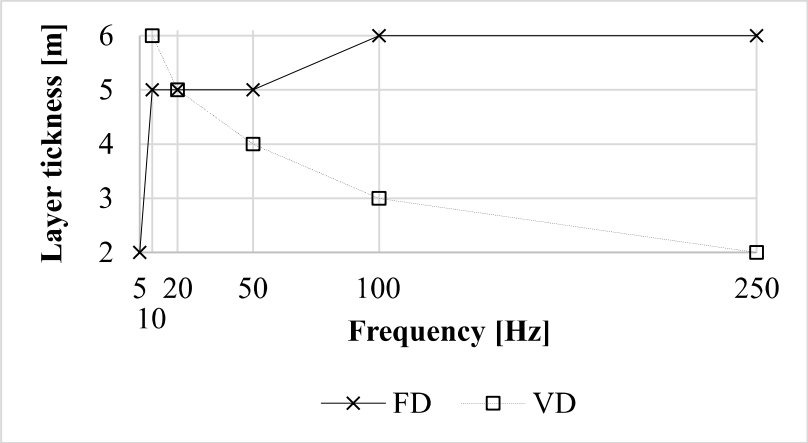

Figure 4.21 – Layer thickness against frequency in FD and VD absorbent layer models.

Using the described geometric model and for a frequency of 100 Hz, Figure 4.22 shows snapshots of wave propagation in terms of vertical displacements in the Analysis zone and the absorbent layer in the $y = 0$ m plane. In Figure 4.22 (a) the VD model with a thickness of 2 m was used; in Figure 4.22 (b) the same model with a thickness of 3 m was used; Figure 4.22 (c) shows the results of the FD model with a thickness of 3 m. In (a) and (c), in later time snapshots, reflections can be seen in the Analysis zone, while in (b), no spurious reflections from the artificial absorption layer seem to occur. This result is compatible with the graphic of the Figure 4.21.

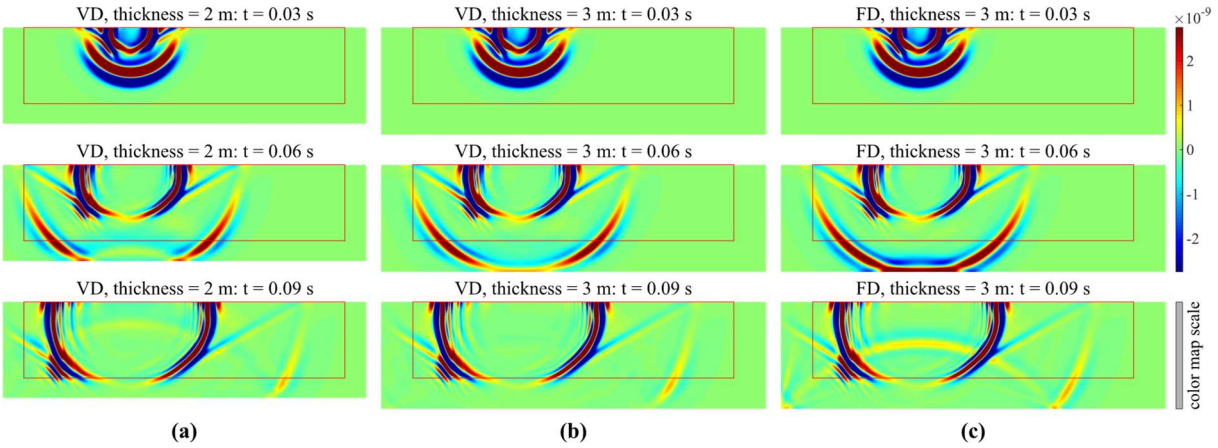

Figure 4.22 – Time evolution of wave propagation in the domain with an absorbent layer: (a) VD with 2 m thick, (b) VD with 3 m thick and (c) FD with 3 m thick.

As already mentioned at the end of the section 3.3.4, both models perfectly simulate an (semi-)infinite medium dissipating the unwanted propagated wave energy. It was also seen that the VD model is more efficient since it is computed only once before the time marching process. However, another advantage is evident: for the same system under study, a thinner absorption layer is needed (comparing with the FD model), thus reducing the number of finite elements and the respective computation time. The use of the FD model has advantages when there is a small time window or when there are relatively few time-steps.

5 APPLICATION OF THE MFS FOR THE STUDY OF VIBRATION MITIGATION SOLUTIONS

In this chapter, the main objective is to better understand the effect of introducing a set of inclusions between an emitting source and a set of receiver points, considering the scenario of wave propagation in a half-space soil. To evaluate the effect of the presence of inclusions in the vibrations registered at the set of receivers, the reduction of vibration levels is evaluated for some test cases. This reduction is computed in terms of an insertion loss, IL, that is defined as the difference between the vibration levels obtained in the presence of inclusions (L_1) and the displacement vibration levels obtained without the inclusions (L_0). This ratio is given in dB by the Equation (5.1).

$$IL_i = L_{0,i} - L_{1,i} = -20\log\frac{|u_i|}{|G_{ij}|} \tag{5.1}$$

where u_i is the displacement field, along direction i, computed at receivers in the presence of inclusions and G_{ij} represents the displacement field, along direction i and generated by a load acting along direction j, computed without the inclusions. According to Equation (5.1), positive values correspond to a reduction of the displacement vibration levels in the presence of inclusions and negative values of the insertion loss stand for losing protective solutions efficiency.

The application examples presented in this chapter are simulated based on MFS formulation that are separated into two sections: the first, based on 2D model and the second on 2.5D model of MFS numerical application.

At this point it is important to define the terminology of several zones affected by the load that will be used in this chapter. Figure 5.1 shows schematically the system divided in these zones and the terminology of each one of them. Accordingly, the Analysis zone is located between the load application point, the sensible point, and the Remaining zone in the opposite direction. The Analysis zone, in turn, is divided into three zones: the Inclusions zone, the Downstream

zone (between the sensible point and the inclusions) and the Upstream zone (between the load point and the inclusions).

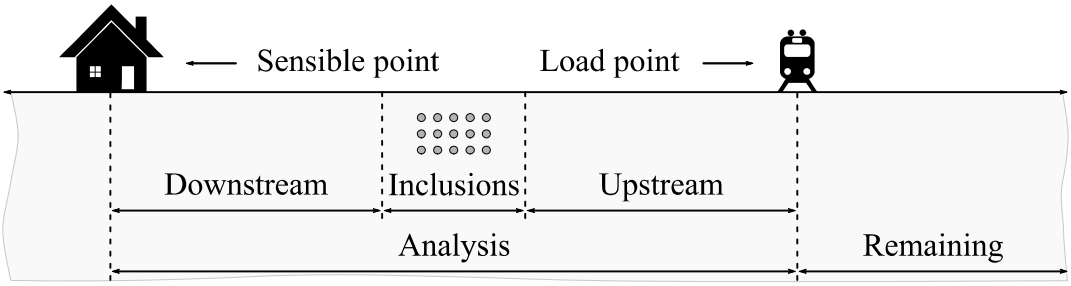

Figure 5.1 – Zones terminology.

5.1 Analysis of 2D scenarios

5.1.1 Number of inclusions and their geometric distribution

In this numerical study, four different groups of solid circular inclusions are compared. Figure 5.2 schematically shows these groups and their location in an elastic half-space where they are buried. The groups are considered with two distinct depths from the centre of the upper inclusion: (1 and 3) m. They are subjected to two frequencies, (15 and 120) Hz, resulting from the dynamic vertical load $F_y = 1$ N acting near the surface at point $(0, 0.1)$ m. All inclusions have a radius of 0.3 m and are made by a homogenous material with elastic properties of $\rho_i = 2700$ kg/m^3, $G_i = 1840 \times 10^6$ Pa and $\nu_i = 0.20$, while the hosting soil is characterised by $\rho_m = 1700$ kg/m^3, $G_m = 43.61 \times 10^6$ Pa and $\nu_m = 0.33$. The inclusions are placed along the system axes, equally spaced between them by a distance which is twice their diameter, and the centre of each group along horizontal direction is kept at $x_G = -15$ m.

The response in terms of horizontal, x, and vertical, y, displacements is computed along a line of receivers placed 0.1 m below the surface and 0.1 m horizontally spaced in a range of $\{-30, \ldots, 30\}$ m. The computations are performed using the MFS model, with 30 collocation points distributed along the boundary of each inclusion, and with two sets of 30 virtual sources placed at either side of that interface, at a distance of 0.24 m.

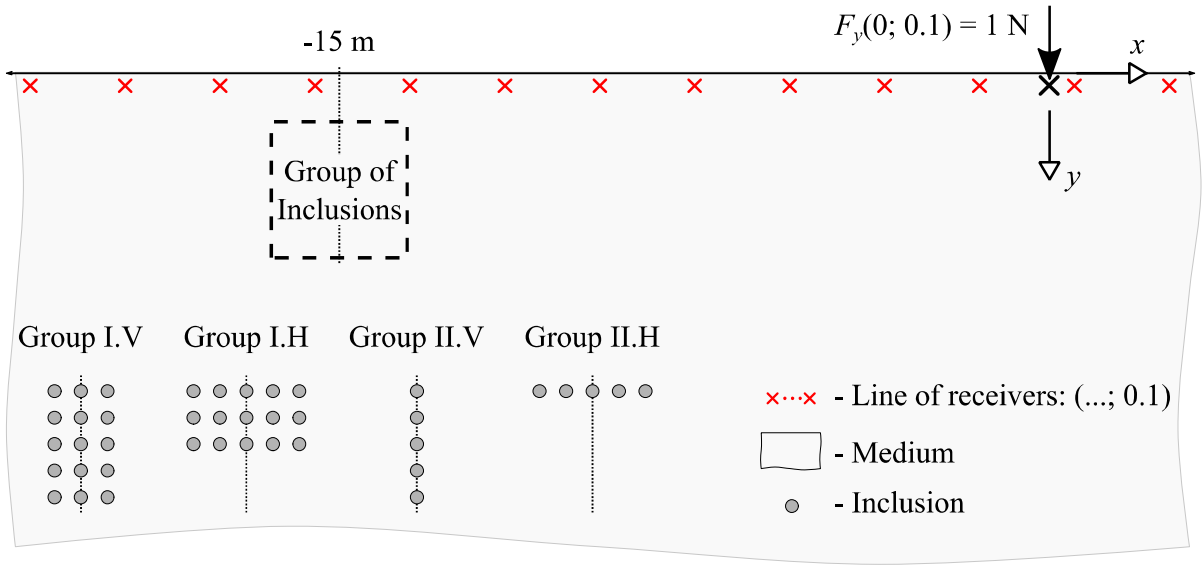

Figure 5.2 – Schematic representation of model for the numerical application related to insertion loss.

The various zones affected by the load are defined in the Table 5.1.

Table 5.1 – Zones definition.

Zones	Downstream	Inclusions	Upstream
Location [m]	$x = \{-30, \dots, -20\}$	$x = \{-20, \dots, -10\}$	$x = \{-10, \dots, 0\}$

As an example of the graphic representation of displacements, Figure 5.3 shows the horizontal and vertical displacements caused by the impulsive load, without any inclusions (G_x and G_y, respectively) and with the effect of inclusions Group I.V (D_x and D_y). The upper graphs result from the inclusions at a depth of 1 m, while the lower graphs result from their depth at 3 m from the surface. In the left-hand charts, the impulsive load has a frequency of 15 Hz, whereas in the right-hand plots the frequency is 120 Hz.

In the upper right chart (frequency of 120 Hz and depth of 1 m), the largest difference between the displacements without and with the inclusion group is evident. It is clearly seen that the inclusions group causes a decrease in the amplitude of the displacements, especially the vertical ones, in the Downstream zone. On the other hand, in the Remaining zone, there is an increase of the amplitude in the presence of that group of inclusions, evident in the vertical

displacements. Regardless of the amplitude of the displacement, the graphs of the other groups have a similar shape.

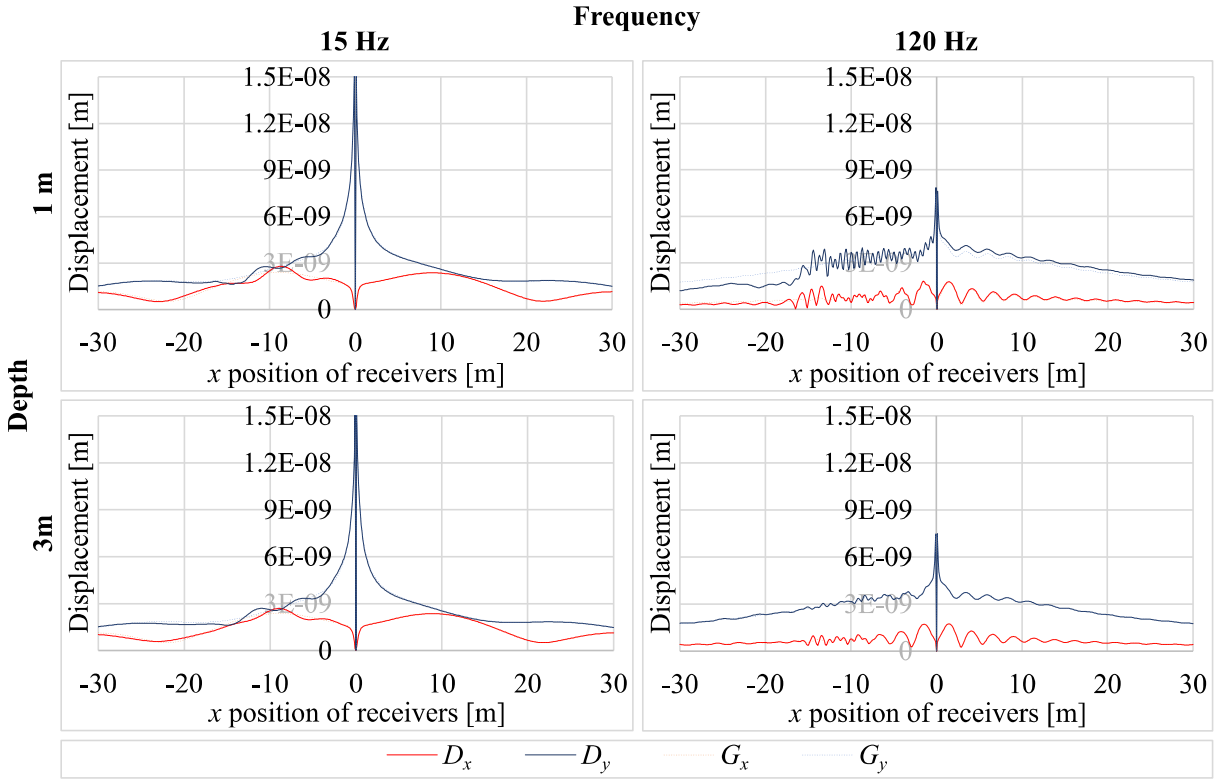

Figure 5.3 – Displacements with inclusions Group I.V (D_x and D_y) and without inclusions (G_x and G_y).

Figure 5.4 illustrates the insertion loss, in dB, along the line of receivers for x and y components of the displacements and shows the influence in the response of the depth (1 or 3) m of inclusions Group I.V (see Figure 5.2) and for frequencies of (15 and 120) Hz. Considering these results, it can be concluded that for low frequencies (15 Hz) the influence of the depth of the inclusions is not very perceptible, and low attenuation values are always registered. However, at a higher frequency (120 Hz) the effect of this geometric parameter reveals to be determinant in the effect provided by the presence of the inclusions. At receivers placed in the Downstream zone, considerable attenuation values (positive IL values) are identified, for the lowest depth values. There is also a positive evolution in the horizontal attenuation along the Inclusions zone reaching a high peak in the left border of the group ($x = -16.5$ m) evident when they are in the shallowest position (depth of 1 m). The negative effect of this group in the Remaining zone, in

the case (frequency of 120 Hz and depth of 1 m), is more evident in this graph with the negative insertion values in this zone.

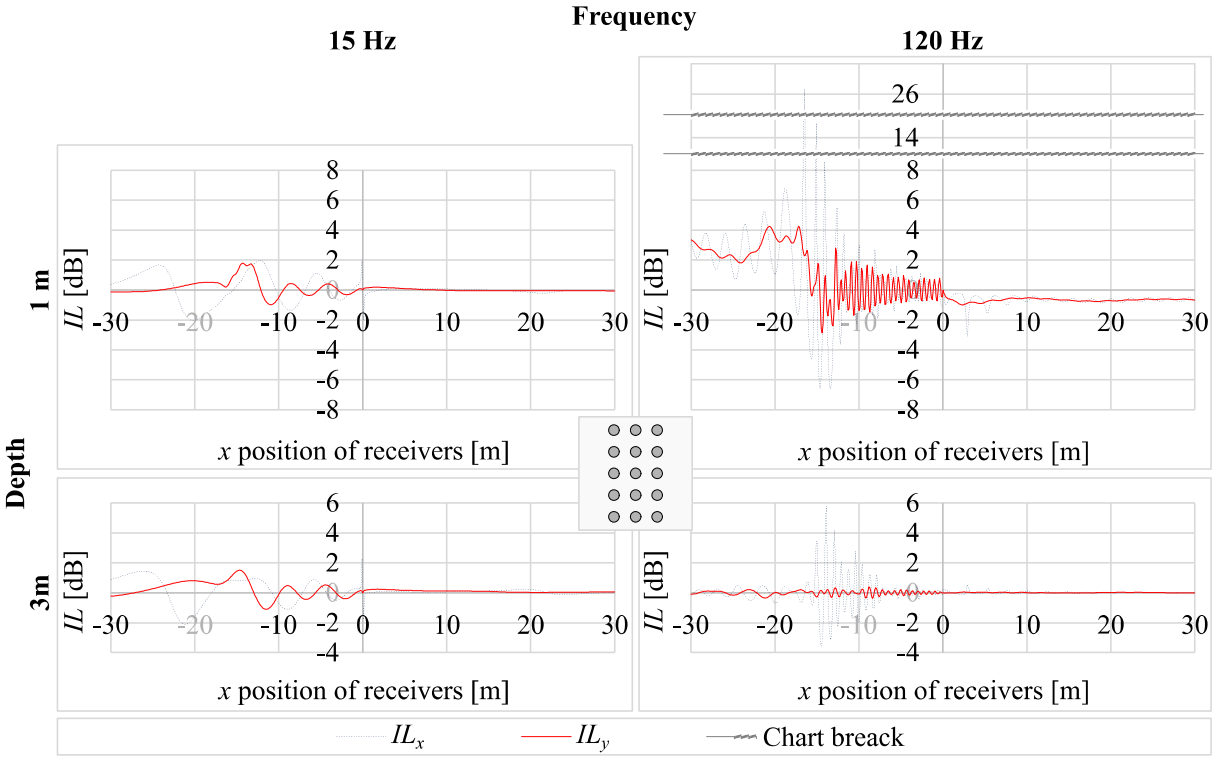

Figure 5.4 – Attenuation provided by Group I.V.

Considering now Group I.H (rotating the inclusions Group I.V by 90°), the computed results at the same line of receivers are presented in Figure 5.5. Again, for the lower frequency, with larger wavelengths, very small attenuations are registered, while a much stronger attenuation effect is seen in the Downstream zone for the higher frequency, and for inclusions closer to the surface. Comparing these results with those of Group I.V, a stronger attenuation is observed when a larger number of inclusions is distributed along the horizontal direction, thus allowing a stronger interference with waves traveling closer to the surface.

In order to identify the effect of varying number of inclusions, relative to the previous model, consider now just the presence of one column with five inclusions (Group II.V), whose results can be seen in Figure 5.6, and another case in which the group of five inclusion is arranged horizontally (Group II.H), for which the results are shown in Figure 5.7.

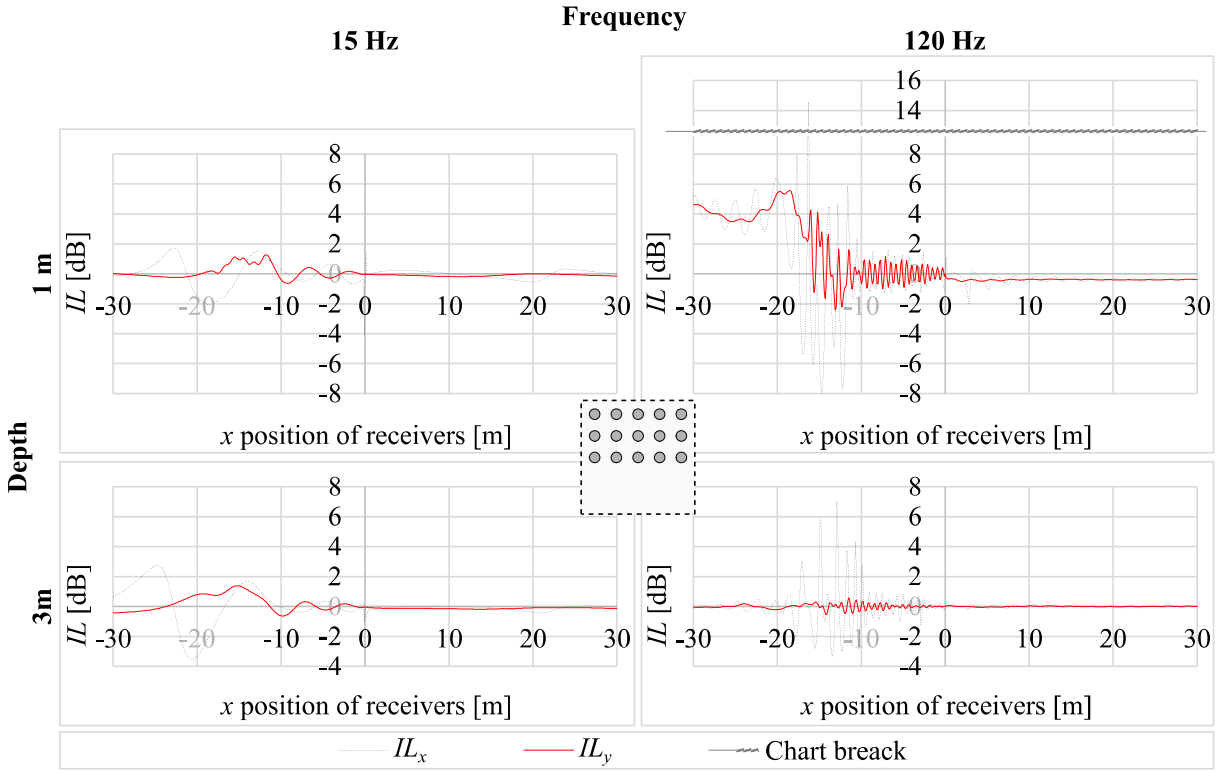

Figure 5.5 – Attenuation provided by Group I.H.

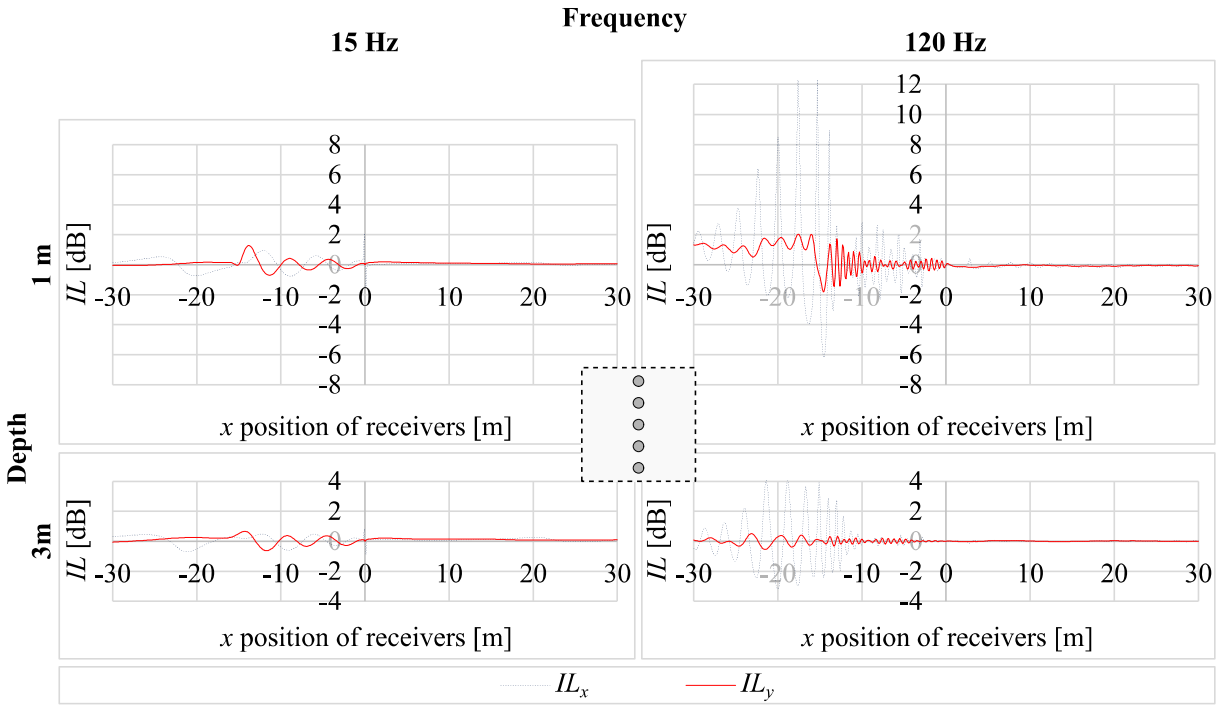

Figure 5.6 – Attenuation provided by Group II.V.

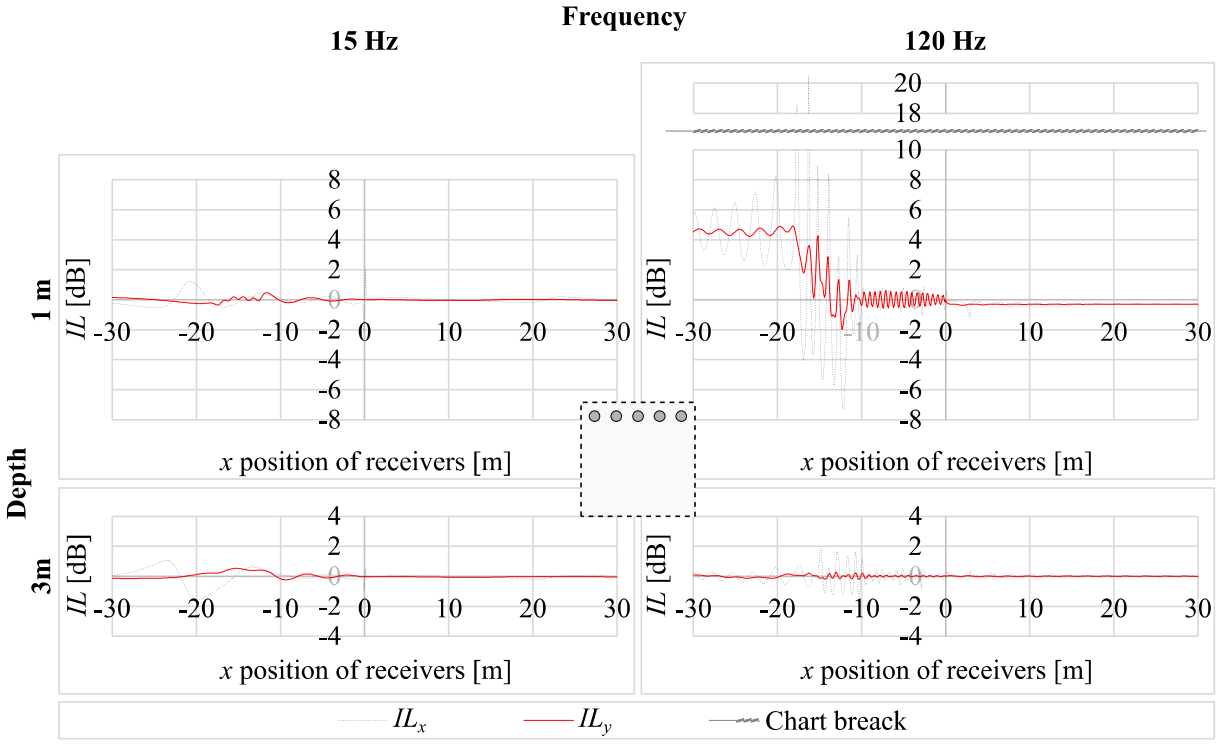

Figure 5.7 – Attenuation provided by Group II.H.

Analysing these last two sets of results it becomes clear that, horizontal distribution of inclusions (Group II.H) allows a better efficiency in reducing the vibration levels. In addition, for the higher frequency, the effect provided by just one line of inclusions is very similar to that obtained when three horizontal lines are included. When a lower frequency is considered, the larger wavelengths involved lead again to a smaller attenuation when only one line (or one column) of inclusions is used.

It should still be noted that the influence of inclusions also occurs to the right of the load application point, in the Remain zone, as a result of reflections originated at the inclusions' surfaces. In general, the insertion loss values are not significant in this zone, however, there may be increases of 3 dB (see Figure 5.4, depth of 1 m and frequency of 120 Hz) which in real applications may result in constraints.

Table 5.2 shows the RMS (Root Mean Square) insertion loss, in dB, of all inclusions groups at both depths, computed in the receivers placed on the Downstream zone, taking into account the

frequencies of (15 and 120) Hz. The results are separated in the two main directions, x and y. It can be seen, by observing this table, that all groups of inclusions at the depth of 3 m are inefficient, even amplifying the vibration levels produced, considering the highest frequency of 120 Hz. This is quite an interesting observation, which is related to the fact that for, that frequency, the smaller wavelength allows surface waves to just pass over the introduced inclusions, without interference. It is also clear that the parameter that most affects the efficiency of the system is the number of inclusions positioned in the horizontal direction, indicating, again, that this is preferred direction for distributing these buried devices.

Table 5.2 – RMS of insertion loss, in dB, in the receivers placed in Downstream zone, due to the frequencies (15 and 120) Hz for all inclusions groups in both depth of (1 and 3) m.

Group			**I.V**		**I.H**		**II.V**		**II.H**	
Frequency [Hz]			**15**	**120**	**15**	**120**	**15**	**120**	**15**	**120**
Depth [m]	**1**	***x***	**0.55**	2.58	-0.17	4.08	0.21	0.66	-0.24	**4.40**
		y	**0.03**	2.70	-0.14	4.03	0.01	1.97	-0.03	**4.52**
	3	***x***	0.62	-0.03	**0.67**	-0.03	0.23	-0.33	0.23	**-0.01**
		y	**0.32**	**-0.03**	-0.01	-0.03	0.12	-0.04	-0.09	-0.05

Table 5.3 identifies the group of inclusions which has the highest effectiveness in reducing vibration levels for the chosen scenario, in Downstream zone. As can be seen from the two tables, none of the groups produces a reduction in vibration when placed 3 m deep in case the load vibrate at a frequency of 120 Hz.

Table 5.3 – Group selection with better efficiency for each combination depth-frequency-displacement direction.

Effectiveness			**Frequency [Hz]**	
			15	**120**
Depth [m]	**1**	***x***	I.V	II.H
		y	I.V	II.H
	3	***x***	I.H	N/A
		y	I.V	N/A

The frequencies of (15 and 120) Hz may not be representative of low and high frequencies, respectively. For this reason and to better assess the attenuation provided by the different

configurations, an additional study was carried where a full range of frequencies between (12 and 112) Hz were considered. Figure 5.8 illustrates the insertion loss (in dB) for each of the inclusions' groups in one third octave bands and computed in the receivers placed on the Downstream zone. The first observation to be made is relative to the depth, being evident that the inclusions 3 m depth have a lower performance. They come even be harmful mainly in the horizontal vibration levels. Clearly, when only one vertical line of inclusions is considered very low insertion loss values are registered throughout the frequency range analysed. When more inclusions are considered along the horizontal direction, again very low attenuations are registered at lower frequencies, but starting on the 63 Hz band a much stronger insertion loss is visible. Indeed, considering the propagation velocities allowed by the host medium (around $318\ \mathrm{m/s}$ for P waves, $160\ \mathrm{m/s}$ for S waves and $150\ \mathrm{m/s}$ for R waves), this frequency band coincides with the so-called "phononic crystal effect", generated by the Bragg interference phenomenon occurring between inclusions, which occurs approximately around $c/2d$ (c being the velocity and d the spacing between inclusions) considering, in this case, the R wave velocity ($c = 150\ \mathrm{m/s}$). As more inclusions are considered along the horizontal direction, this effect becomes stronger, and leads to stronger attenuations, as is clear in the provided results. This results confirms that this type of mitigation strategy may be designed to fit a given frequency of the propagating vibration field, thus originating a good attenuation and providing effective protection for sensible structures positioned the beyond the inclusions.

Figure 5.9 shows the effectiveness, in terms of insertion loss, of each zone in the protection of the sensitive point, in the case of the Group I.H. Observing the behaviour of the two lower graphs it is found that, regardless of the amplitude, they have a similar shape. The same is to say that the effectiveness of the whole zone of study (Analysis zone) is influenced, in the majority, by the Inclusions zone. This observation is valid for all cases, although in the deeper groups, this relationship is not so evident.

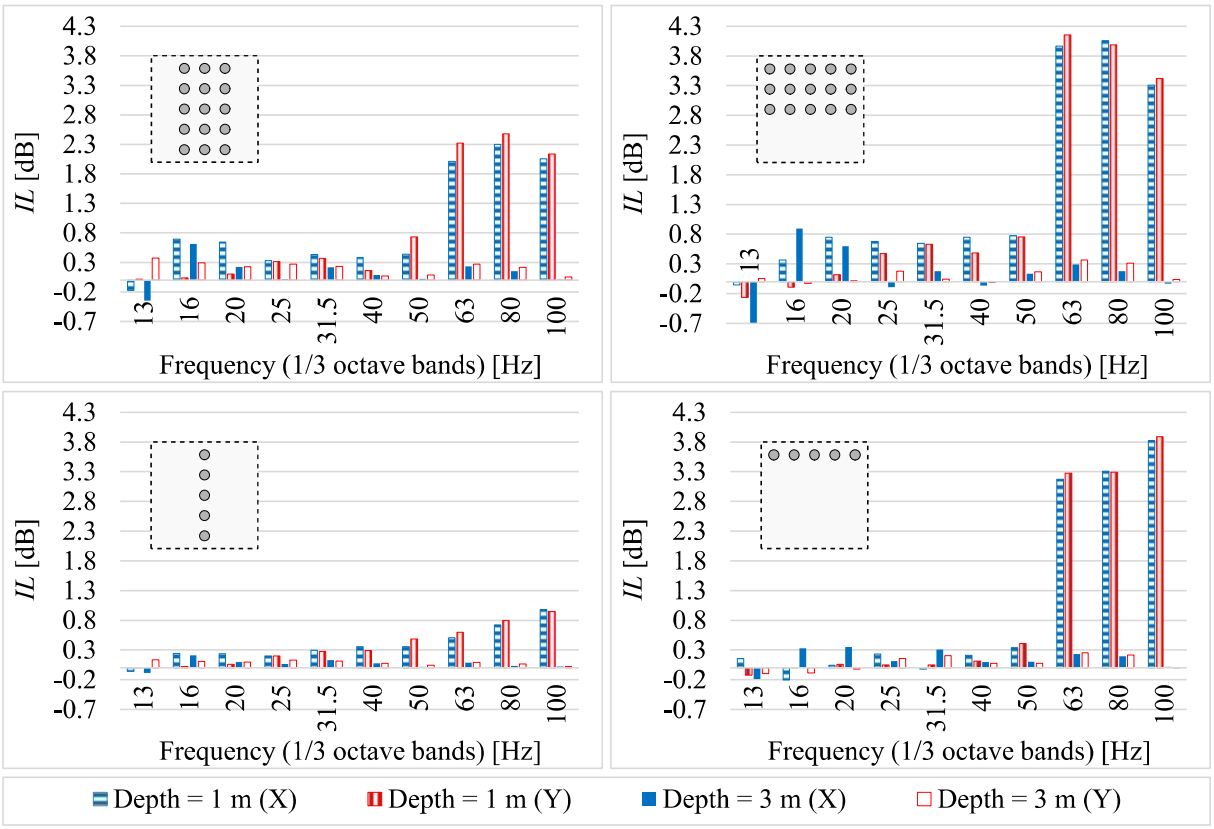

Figure 5.8 – Insertion loss in 1/3 octave bands.

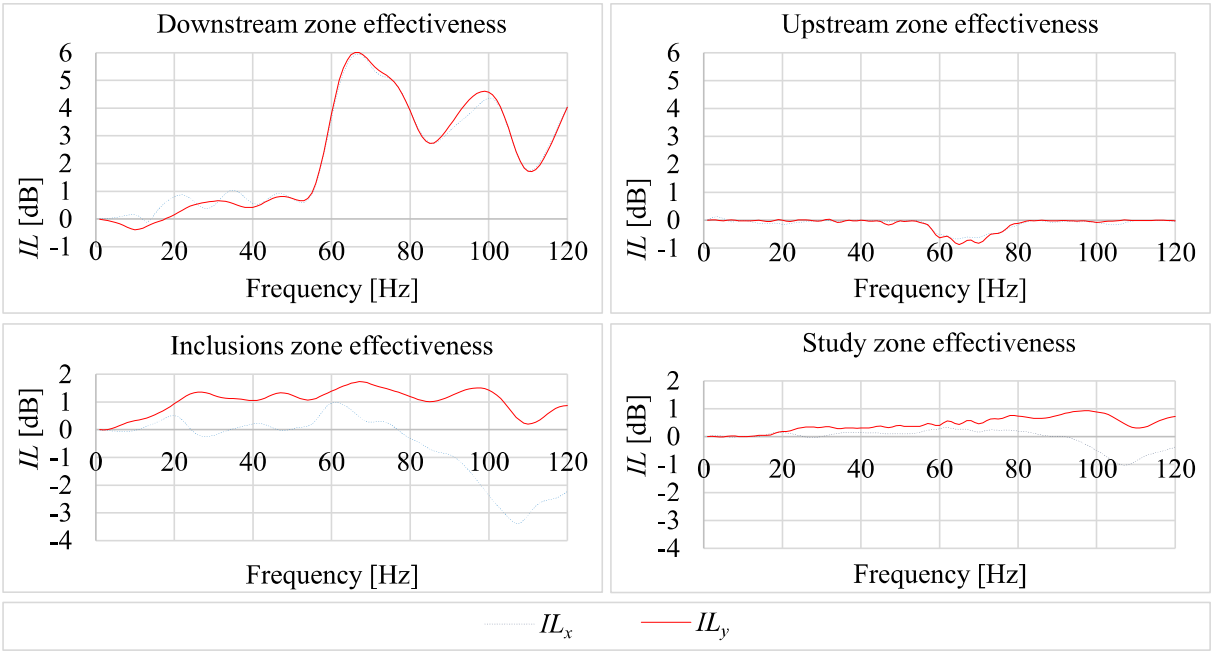

Figure 5.9 – Effective vibration levels by frequency to the inclusion Group I.H.

A small study on the influence of the inclusions radius was made for the inclusions Group II.H in the two depths of top of inclusions, (0.7 and 2.7) m. The study was performed for the frequencies of 1/3 octave band of central frequency of 100 Hz and for radius of $\{0.15, 0.30, 0.45\}$ m. As shown in Figure 5.10, the effectiveness in Downstream zone increases exponentially with the radius for depth 0.7 m. Conversely, the almost null effectiveness decreases when the inclusion group is at a depth of 2.7 m, being harmful when the inclusions have the largest radius.

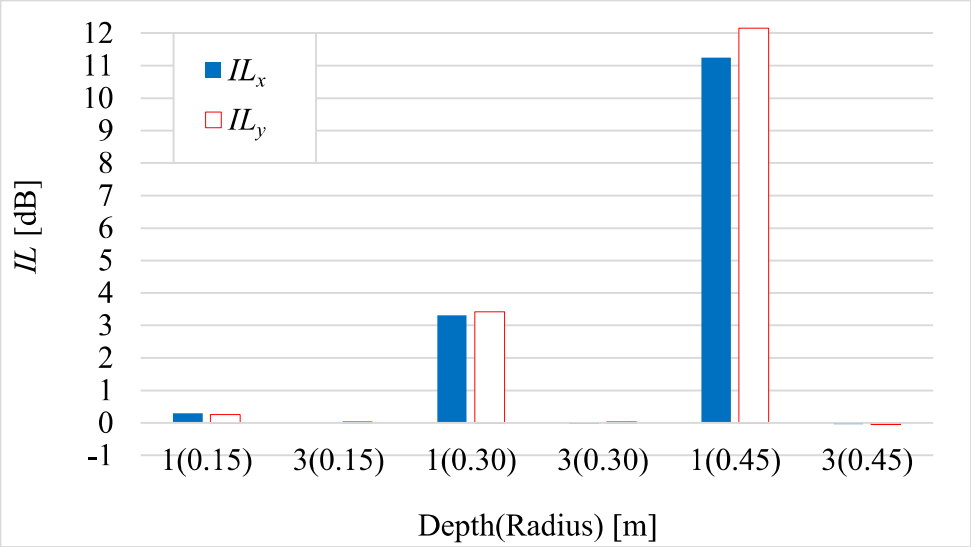

Figure 5.10 – Effective vibration levels in 1/3 octave band of 100 Hz to the inclusion Group II.H for radius study.

To assess the influence of the distance between inclusions, another study was carried out on Group II.H, where all inclusions have a diameter of $D = 0.6$ m and was performed for the frequencies of 1/3 octave band of central frequency of 100 Hz. The centre of the inclusions group was always kept at a depth of 1 m and positioned 15 m to the left of the dynamic vertical load as shown in the Figure 5.2. As it can be seen in Figure 5.11, the inclusions work better as a group when their centres are separated by $1.5D$ m. When they are separated more than $2.8D$ m it is assumed that they work alone.

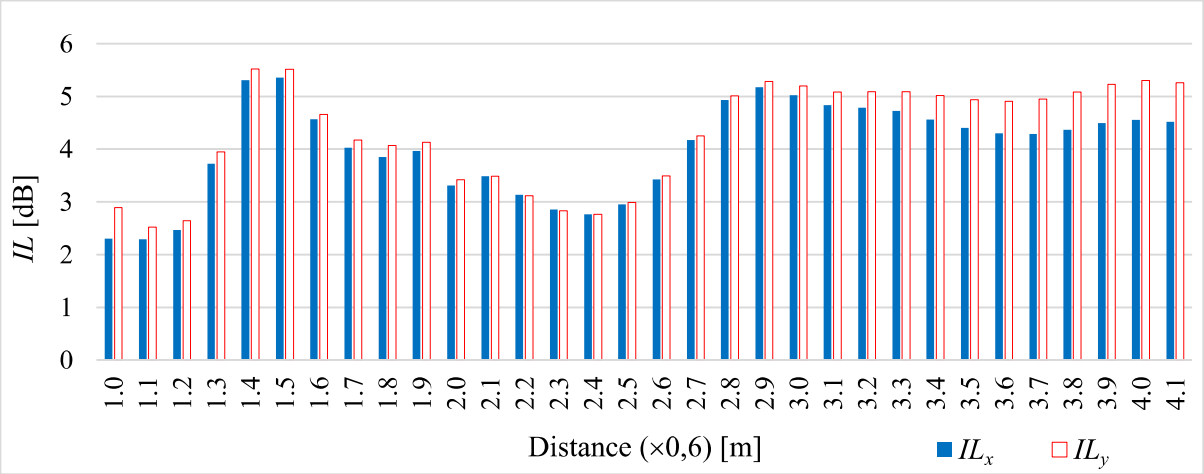

Figure 5.11 – Effective vibration levels in 1/3 octave band of 100 Hz to the inclusion Group II.H for distance study.

5.1.2 Conclusions

In this section, a general MFS strategy was presented to allow the analysis of wave propagation in the presence of buried inclusions in a half-space. The proposed strategy is general and allows the simulation of any number of inclusions filled with distinct materials. The presented numerical results evidence the stability and convergence of solutions. The accuracy of the MFS is quite good, particularly when compared with BEM results. This section only reported findings concerning the 2D case, and further in-depth studies need to be conducted to verify and improve the proposed strategy, for 2.5D and 3D cases.

Conceptually, the inclusions have a significant effect on vibration attenuation, and it was observed that their efficiency peaks at a specific frequency range, which is strongly related to the Bragg effect occurring due to the multiple interferences between reflections at the equally spaced structures.

5.2 2.5D MFS applications

In this section, a 2.5D numerical model based on the MFS is used to analyse the elastic wave propagation in the ground to help reducing the vibrations that can reach sensible structures, considering arrays of elastic inclusions buried in a homogeneous medium. In this model, the

complete elastodynamic interaction between the inclusions and the host medium is fully considered. Due to the geometric periodicity of the analysed problem, the numerical formulation can be simplified, particularly in what concerns the calculation of the system matrix, and significant computational gains can be obtained. The results of a numerical study concerning the behaviour of a sequence of embedded inclusions within an elastic material, when subject to the incidence of waves with different frequencies, is here presented, and the interpretation of the involved phenomena is described in order to clarify the main wave propagation features in the presence of multiple elastic inclusions.

Beyond the physical phenomena themselves, one of the challenges of this type of problem is related to their accurate computational simulation. Previous works in the field of wave propagation – see, for example, (Amado-Mendes and Godinho, 2013) and (Martins *et al*., 2013) – made use of a number of techniques, which can be extended and adapted to treat the problem of metamaterials in solid media. Methods such as BEM or MFS seem to be appropriate choices for that purpose. Conceptually, one way to solve this problem is related to a 2.5D analysis, in which the geometry remains constant along one direction, although with a purely 3D source. These models are very efficient (P. G. Santos *et al*., 2014) and can be of interest to study the propagation of elastic waves in the presence of arrays of scatterers; they may serve as an excellent base for understanding the underlying physics of such complex phenomena.

This section intends to provide a numerical strategy based on the use of a 2.5D MFS implementation and tries to interpret physically the wave propagation phenomena that occur around solid buried inclusions embedded in a host homogeneous soil. Due to the geometric periodicity and geometrically repetitive nature of the analysed problem, the numerical implementation can be significantly simplified, particularly in what concerns the calculation of the system matrix; indeed, a large number of repeated blocks occur in this matrix, whose calculation just needs to be performed once, and so significant computational gains can be obtained. Several numerical simulations are here used to illustrate the main features of wave propagation in this type of scenarios, using different arrays of scatterers and considering different elastic properties.

5.2.1 2.5D formulation complements

Consider an elastic medium within which a set of elastic bodies is embedded, composing a multi-domain elastic system. Based on the frequency domain wave equation defined in Equation (3.7), consider that in this physical system the solid inclusions have a constant geometry along the z direction, and the whole system is subjected to a harmonic point source, which is oscillating with an angular frequency ω. Since the system's geometry is infinite and does not change along the z direction, it is possible to apply a spatial Fourier transformation along that direction and to determine the 3D displacement field as a continuous integral of simpler bi-dimensional solutions, as

$$\mathbf{u}^{3\mathrm{D}} = \int_{-\infty}^{+\infty} \mathbf{u}^{2.5\mathrm{D}}(k)\mathrm{e}^{-ik(z-z_0)}\,dk \tag{5.2}$$

been k the axial wavenumber. Discretising this integral and rewriting this equation as a discrete summation (assuming an infinite set of virtual sources equally spaced L_{vs} along the axial direction, such that $\Delta k_z = 2\pi/L_{vs}$), the 3D displacement field may be written as

$$\mathbf{u}^{3\mathrm{D}} = \sum_{m=-\infty}^{+\infty} \mathbf{u}^{2.5\mathrm{D}}(k_z)\mathrm{e}^{-ik_z(z-z_0)}\Delta k_z \mathrm{e}^{-ik_z(z-z_0)} \tag{5.3}$$

where $k_z = m\Delta k_z$. This summation converges and can be approximated by a finite number of terms, ranging from $-M$ to $+M$. Note that, in order to avoid any spatial contamination from the virtual sources, the distance L_{vs} must be sufficiently large and that the case with $k_z = 0$ corresponds to the 2D problem (as already seen in section 3.2.1).

5.2.2 Details for periodic geometries

If a set of n inclusions is considered, equally spaced between them forming a regular matrix, the calculation of the MFS system matrix can be greatly accelerated – see Equations (3.36) and (3.37). It is important to notice that, if the inclusions are periodically placed, many of the

submatrices of $\mathbf{A}_{\Omega_h}$, in Equation (3.36), are repeated, and may only be calculated once; this can be easily realized, for example, for all diagonal submatrices. This behaviour is applied to both displacements and their derivatives, according to the corresponding constitutive law: stresses and strains. Given this observation, a practical implementation algorithm to compute $\mathbf{A}$ – see Equation (3.35) – can simply be written as (pseudocode):

```
FUNCTION compute_A (data)
  k = 0
  FOR i FROM 1 to n
    FOR j FROM 1 to n
      v = x_i^I − x_j^I    # vector connecting the centres of inclusions i and j.
      IF v = ANY(v_(0 to k−1)) THEN
        v_l = (v = v)
        # there is no need to compute the A^ij submatrix.
        A^ij = A^mn(v_l)    # the reference of previously computed submatrix is associated to A^ij.
      ELSE
        k = k + 1
        v_k = v    # v vector is added to the list of computed submatrices.
        A^ij(v_k)    # A^ij submatrix is computed and stored.
      END IF
    END FOR j
  END FOR i
  RETURN A    # with all necessary submatrices computed.
END FUNCTION
```

5.2.3 Model verification and performance

To first check the correctness of the proposed model and of its implementation, a homogeneous system is simulated, for which the analytical solution corresponds to the fundamental solutions described in section 3.2.1. Using the proposed strategy, a matrix with 3×3 elastic inclusions, with radius 0.3 m, equally spaced 1.2 m is embedded in a host medium, and the same properties are ascribed to both the host medium and to the inclusions: Young's modulus of 100 MPa, density of 2000 kg/m^3 and a Poisson's ratio of 0.2. The system is excited by a source positioned at $(x, y) = (-2.0, 0.0)$ m, vertically centred with the inclusions, and responses are computed at a receiver positioned at $(x, y) = (5.3, 1.8)$ m. Figure 5.12 illustrates the computed displacements at the receiver, originated by a vertical load, together with the analytical solution, and

considering an apparent velocity of 1336 m/s (defined as $v_z = \omega/k_z$). The presented plots clearly evidence an excellent match between the two results.

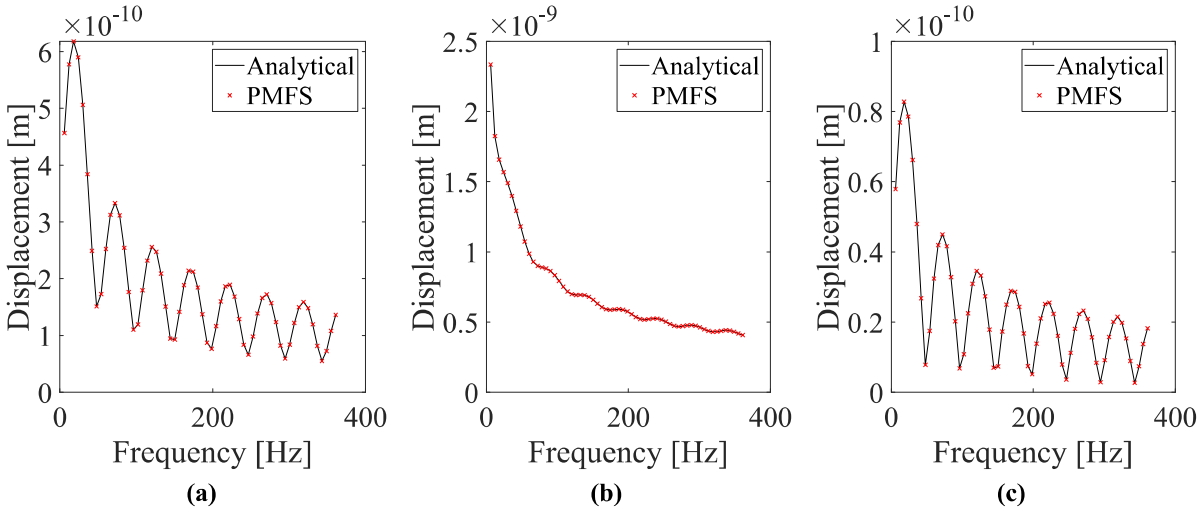

Figure 5.12 – Verification of the implemented algorithm for directions (a) x, (b) y and (c) z of displacements.

To understand the performance gain between the proposed scheme (designated by PMFS) and a traditional MFS implementation, a sequence of tests has been performed, recording the CPU runtimes required by each approach. Geometries with 4×4, 5×5, 6×6 and 7×7 inclusions are considered, with 30 collocation points describing each inclusion; a maximum MFS matrix size of 8820×8820 is thus obtained for the larger problem. The internal material of the inclusions is assumed to have a Young's modulus of 30 GPa, a density of 2500 kg/m^3 and a Poisson's ratio of 0.3. Figure 5.13 illustrates the performance of the methods using a bar chart, in which each bar is divided in two parts: the lower (dark grey) part is related to the CPU runtime required for matrix formation; the upper (lighter grey) is related to the solution of the equation system. Since the same solver is used in both cases, the required CPU runtime for the equation system solution is always the same for the two schemes. Analysing the plot it is seen that a significant reduction of the CPU runtime occurs for the proposed implementation, which is related only to the matrix formation time. Comparing the dark grey parts of the plotted bars, this reduction is very large and, in general, only (20 to 30) % of the CPU runtime is required.

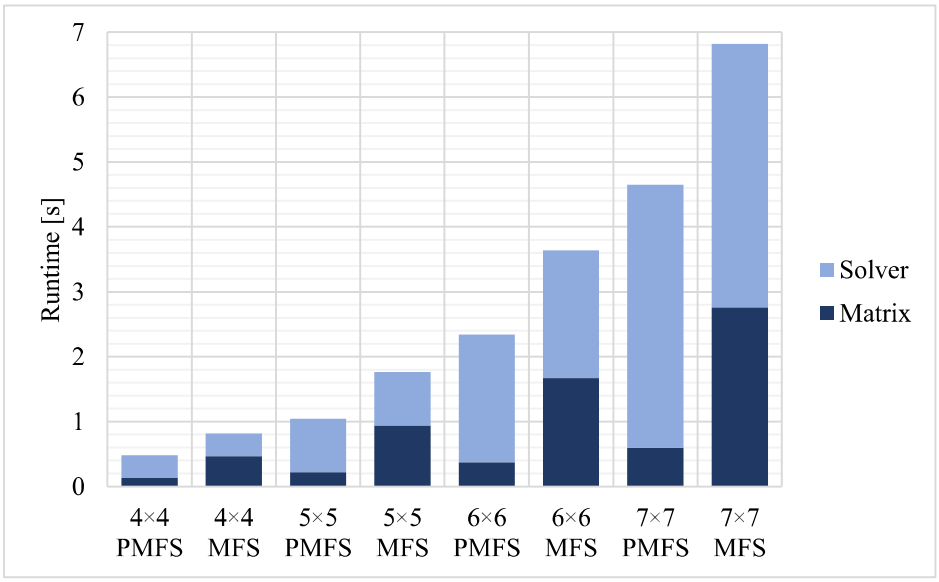

Figure 5.13 – CPU runtimes for the proposed (PMFS) and for the classical MFS implementations.

5.2.4 Numerical application

The presented model has been used to study the wave propagation patterns and the physical behaviour of a system composed by different numbers of inclusions. Several results are shown for different geometries composed of arrangements of circular cylinders. All results are presented in terms of normalized slowness and of normalized frequency (non-dimensional parameters). The normalized frequency, $\bar{f}$, is given in terms of the relation between the lattice constant of the arrangement of cylinders (spacing between consecutive centres), a, and the wavelength of the S waves, λ_S, in the solid host medium, allowing to define:

$$\bar{f} = \frac{a}{\lambda_S} = a\frac{f}{v_S} \tag{5.4}$$

The normalized slowness, $\bar{k}$, is defined as the relation of the axial wavenumber, k_z, to the S wave wavenumber, given as:

$$\bar{k} = \frac{k_z}{\omega/v_S} \tag{5.5}$$

The following material properties are used in this study:

Table 5.4 – Material properties.

Material	Density [kg/m^3]	Young [MPa]	Poisson
M1	2000	100	0.2
M2	7800	200000	0.3
M3	2500	30000	0.3

Different geometrical arrangements are analysed, including both square and triangular lattice distributions. The typical arrangement for each test case is represented in Figure 5.14, for configurations with (a) 2×5 inclusions in a rectangular lattice, and (b) 2×3 inclusions in a triangular lattice.

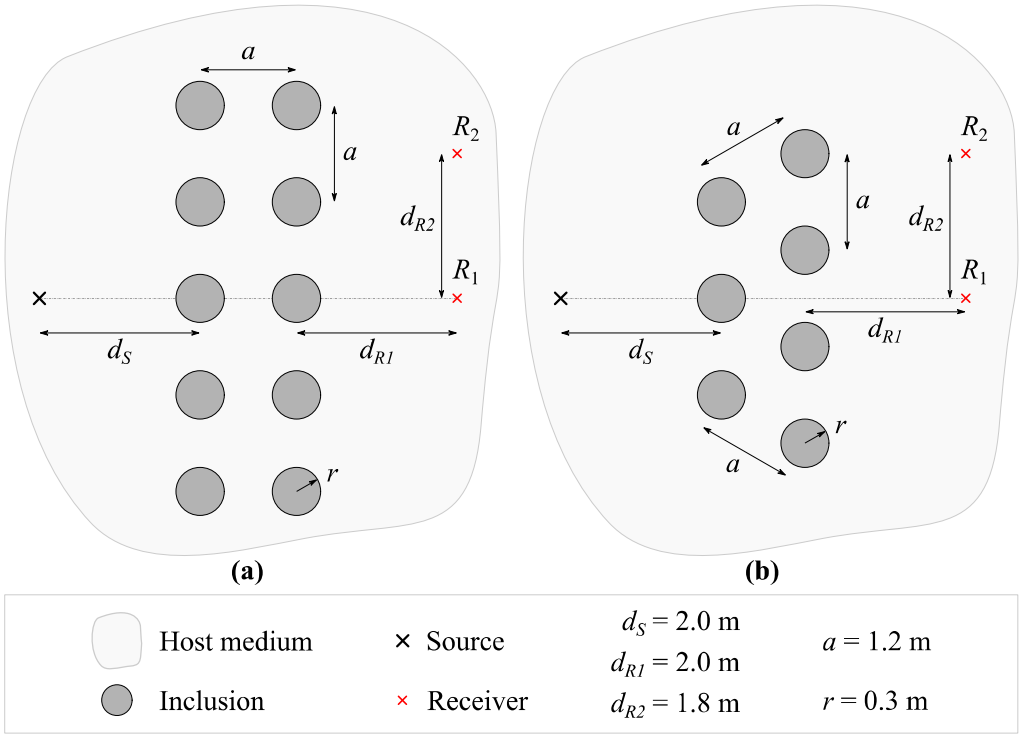

Figure 5.14 – Illustrative scheme of the tested configurations for (a) 2×5 square and (b) 2×3 triangular lattices.

The first set of examples is related to the case in which perfectly rigid and unmovable inclusions are considered, embedded in a solid medium with the properties of M1, referring to a soft soil,

where S waves propagate at 144.3 m/s, and P waves at 235.7 m/s. Although this is a conceptual scenario, it allows getting a better insight of the involved physical phenomena.

Figure 5.15 presents the amplitude level of the combined x, y and z velocities at R_1. For normalized slowness above 1, very little energy propagates in the system, and only evanescent waves exist. Bellow this slowness, since the elastic waves propagate freely, without obstacles, increasing vibration velocities are seen as the frequency increases. This scenario greatly changes in the presence of a rigid inclusion, as can be seen in Figure 5.15 (b) (where a rigid inclusion of radius 0.3 m is considered between the source and the receiver). In this case, a significant decrease in the velocity levels is observed throughout the whole analysed $\bar{f}-\bar{k}$ domain, since the presence of the obstacle blocks the direct incidence of waves at the receiver.

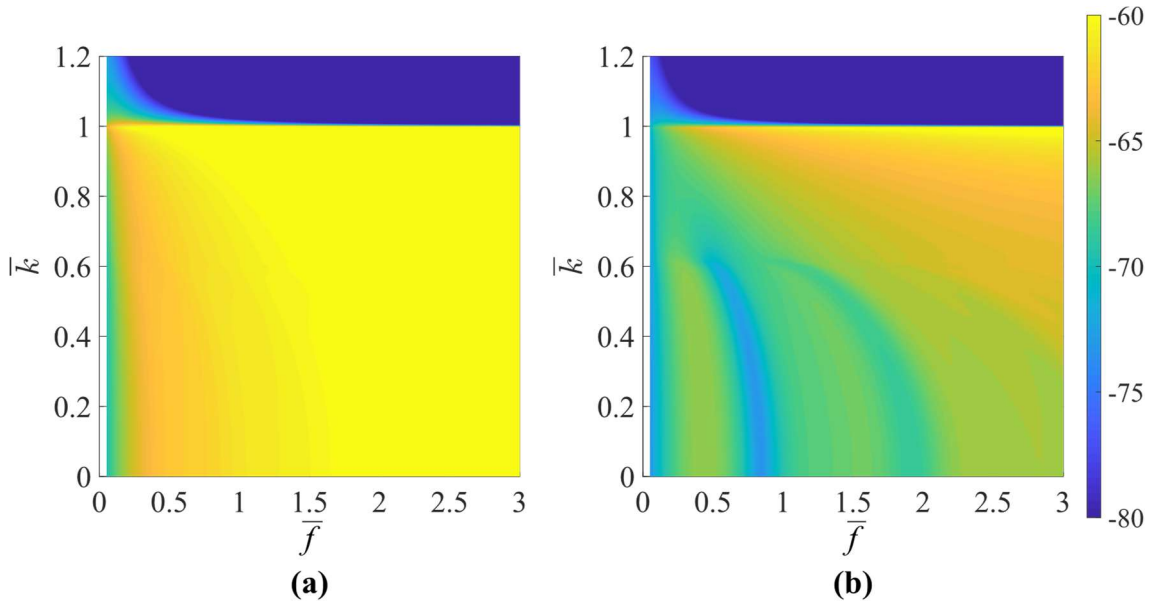

Figure 5.15 – Absolute vibration velocity levels at R_1 for (a) an homogeneous medium and (b) in the presence of a single rigid inclusion.

To understand the effect of multiple inclusions, disposed in an organized pattern defined by a lattice constant a, in the wave propagation pattern, several tests were performed for different scenarios. To facilitate the interpretation of the effect of the multiple inclusions, next examples illustrate the results in terms of insertion loss, IL, given by the difference of vibration levels registered at the receiver without and with the intermediate structures – see Equation (5.1).

Figure 5.16 shows the *IL* computed for an array of 9 inclusions (3 × 3 square lattice), disposed in a rectangular manner, considering a lattice constant $a = 1.2$ m and an inclusion radius of 0.3 m. The structure of these plots is much more complex than the previous one and includes several features. Indeed, multiple interactions occur between inclusions, originating constructive and destructive interferences. However, one feature merits special attention, particularly the presence of a high attenuation frequency range visible as a pattern of lighter shades in the presented plots. This zone occurs for the full sequence of $\bar{k}$ values and indicates that a strong attenuation is originated by the presence of the set of inclusions. This effect occurs mostly between normalized frequencies of 0.5 and 1.5, that is, between frequencies $f = 0.5v_S/a$ Hz and $f = 1.5v_S/a$ Hz (this zone is marked with "1" in the plot). Interestingly, this lower limit can be related to the theory of the acoustic attenuation by sonic crystal, in which the band gap frequency can usually be defined as $f = 0.5v_S/a$ Hz; thus, it can be inferred that, possibly, the dominant effect controlling the energy attenuation by this system is the same as that observed in acoustics. An additional effect that is also seen in the presented plots is related to a constructive interference between the multiple inclusions (these regions are marked with "2" in the plot).

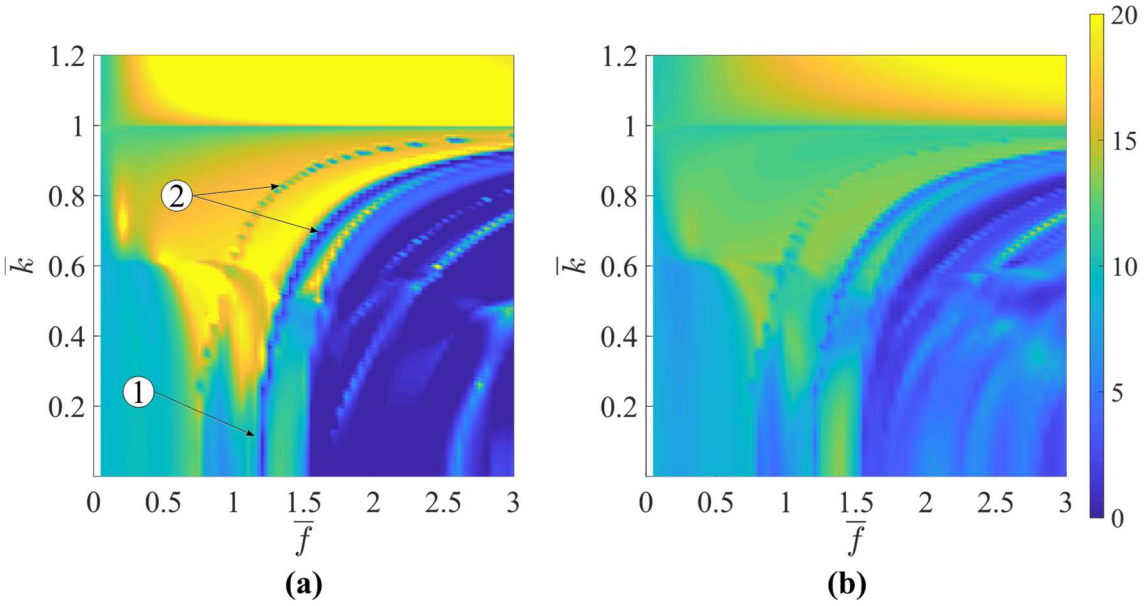

Figure 5.16 – Insertion Loss at (a) R_1 and (b) R_2 for a 3×3 square lattice system.

Figure 5.17 illustrates similar plots computed for triangular shaped inclusion distributions, considering 3×3 (total of 10) and 5×3 (total of 17) inclusions. These plots reveal a quite similar behaviour to those in Figure 5.16, although some differences can be observed. The "band gap" identified above is now more marked and narrower, even for the 3×3 case, and seems to become progressively more intense when more inclusions are added. For the case of 17 inclusions, the "band gap" effect is very well defined and corresponds to a continuous bright patch in the Figure 5.17 (b), occurring between normalized frequencies of 0.5 and 1.0. Additionally, it becomes clear that one of the constructive effects identified above – the leftmost one marked "2" in Figure 5.16 (a) – has now disappeared. That effect can be related to the diagonal distance between inclusions in the rectangular distribution, which is eliminated when triangular lattices are considered.

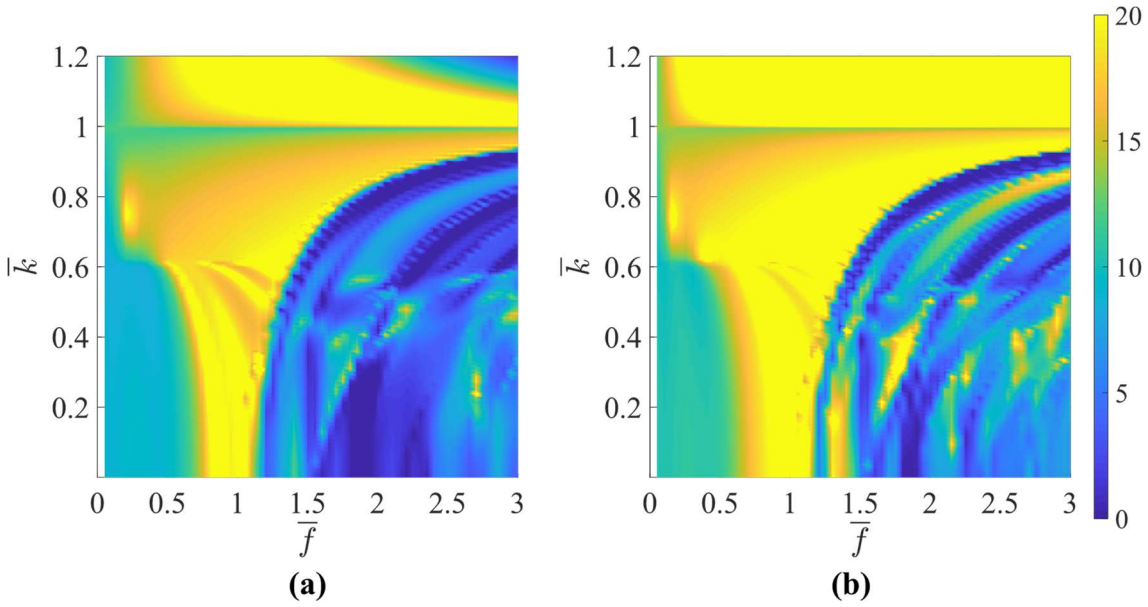

Figure 5.17 – Insertion Loss at R_1 for triangular lattices considering (a) 3×3 and (b) 5×3 groups.

To understand the effect of considering the inclusions as being made of an elastic material, simulations were performed for the geometrical configuration used in Figure 5.17 (b), i.e., 5×3 triangular lattice. The material properties M2 and M3 (see Table 5.4) for the inclusions were considered. Figure 5.18 illustrates the IL at receiver R_1 for these two materials.

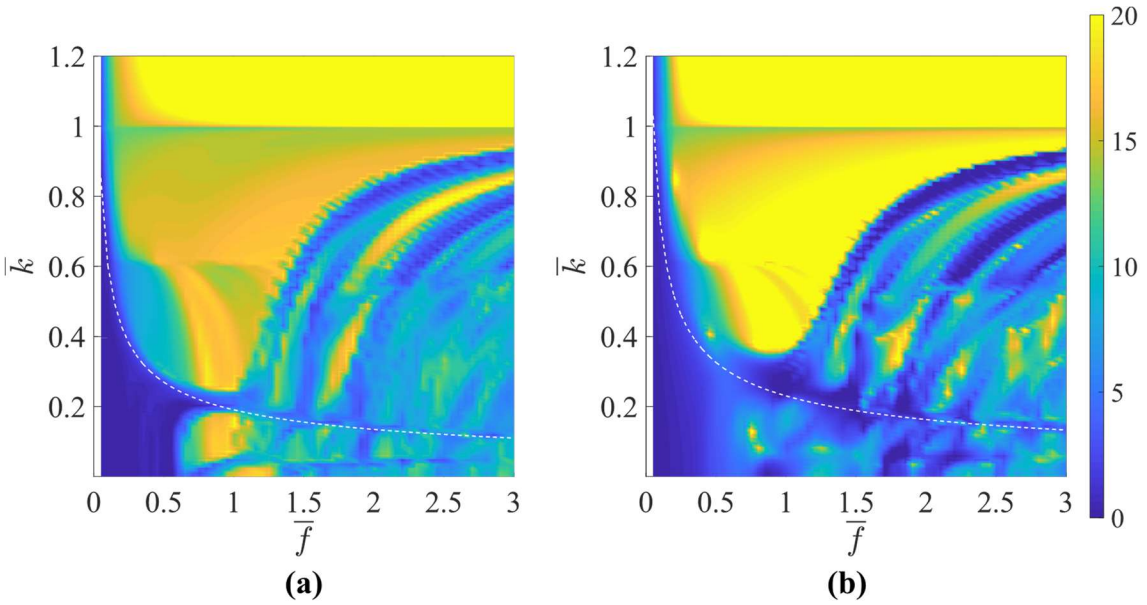

Figure 5.18 – Insertion Loss at R_1 when the inclusions are made of (a) M2 and (b) M3.

Observing the plotted results, new features due to the consideration of the elastic properties of the inclusions can be seen. Although the upper part of the plots remains essentially unchanged, there is a very distinct behaviour on the lower part. This behaviour is associated with the longitudinal vibration modes of the inclusions, namely their flexural and torsional modes, which allow a significant part of the energy to pass through and reach the receivers. To validate this statement, the dispersion curve for longitudinal bending waves has been computed for both material types and is represented in the plots by a dashed line. This new line divides the upper and lower parts of the plot, and below it, a completely different behaviour is seen when compared with the plots depicted in Figure 5.16 or Figure 5.17. For lower values of $\bar{k}$, the additional contribution of a torsional mode is seen, which also contributes to a reduced *IL* observed in Figure 5.18. To confirm that these are indeed the referred modes, the deformed configuration of the inclusions has been computed for $\bar{f}-\bar{k}$ pairs located over the corresponding dispersion curves and is depicted in Figure 5.19. To facilitate the interpretation, only two inclusions are plotted. Observing these plots it can be seen that a clear bending behaviour is observed in Figure 5.19 (a), while a torsional behaviour is seen in Figure 5.19 (b), thus confirming the described effects.

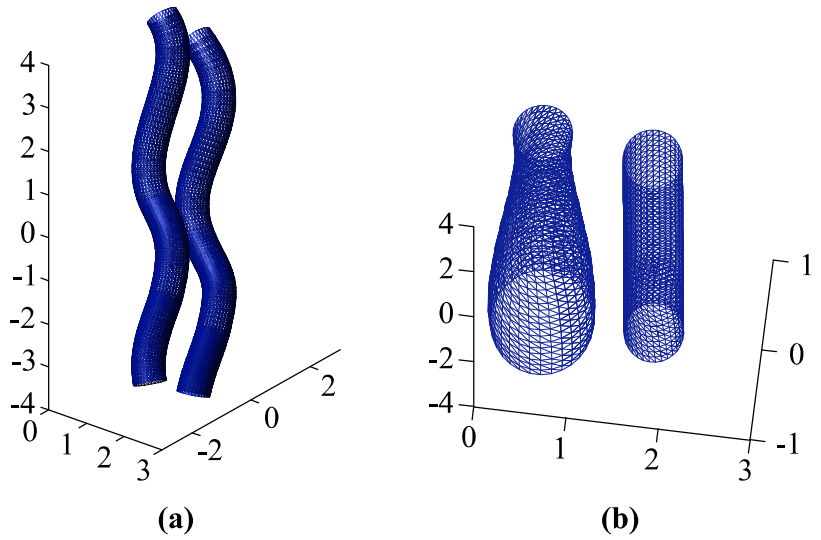

Figure 5.19 – Deformed configuration of elastic inclusions computed for $\bar{f}-\bar{k}$ pairs corresponding to (a) the bending wave and (b) torsional wave dispersion curves.

The observations made above about elastic inclusions allow inferring that accounting for the correct elastic behaviour of the inclusions is essential, since the global behaviour is very different from that seen in the case of rigid inclusions. The elastic behaviour of the inclusions clearly decreases the attenuation efficiency of the periodic structures, mainly for lower values of the normalized slowness.

5.2.5 Conclusion

In this section, a study regarding the simulation of the dynamic behaviour of an elastic sonic-crystal-like structure accounting for its 3D behaviour was made. The proposed model is based in a 2.5D elastodynamic formulation, making use of an improved version of the MFS specifically tailored for periodic structures. It was shown that the proposed model is quite adequate and very efficient for the analysis of such structures and allows simulations to be performed even for quite large systems. With the proposed improvement, efficiency is greater than 20 % when compared to traditional MFS.

From the presented application examples, some interesting conclusions can be drawn. It can be said that the simulated arrays of rigid cylinders essentially present the expected behaviour of a sonic crystal, exhibiting a clear band gap. The position of this band gap can be approximately

estimated, similar to that used for acoustic problems, considering the S wave velocity. When square and triangular lattices were compared, the latter seems to exhibit a smoother and cleaner behaviour, with a very well-defined band gap region, although affecting a narrower frequency band. Finally, it was observed that when elastic inclusions are considered, a dramatic change occurs, and the vibrational behaviour of the inclusions introduces a very significant degradation of the *IL*, particularly for low values of the normalized slowness ($\bar{k}$), below the dispersion curve associated with the bending waves of the inclusions. This behaviour represents a significant issue that must be addressed in order to efficiently use this concept for vibration mitigation.

6 3D FEM ANALYSIS OF VIBRATION MITIGATION

In the previous chapter the existence of attenuating properties of arrays of elastic scatterers was demonstrated in a 2.5D scenario, although also identifying possible limitations related to the propagation of bending waves along the scatterers. However, it has been found that the new concept of vibration protection based on buried periodic structures may constitute a powerful future solution that deserves further investigation. To achieve this objective, in this chapter, a 3D time domain finite element method was implemented for simulating ground wave propagation in the presence of buried periodic structures. For this purpose, a generic scenario such as the one schematically represented in Figure 6.1 is carefully defined and used for all cases of interest. In this scenario, an initial simplification in the loading pattern introduced by the train passage is assumed by taking the dynamic load to be invariant along one direction, which allows its representation using a line load. The load imposed by the train passage in reality is complex and governed by the train-track dynamic interaction (Alves-Costa *et al*., 2012b; Colaço *et al*., 2016), being similar to moving point load. However, due to the track bending stiffness, point loads are distributed along the track-ground interface and, in the context of the present study, this can be assumed as a line loading condition to save computational effort. The specific type of mitigation device studied consists of a buried periodic structure, made of a sequence of vertical (or slightly tilted) inclusions with square cross-section in the horizontal plane, periodically repeated along one direction, allowing to create a buried barrier between the line load and sensible receivers (see Figure 6.1). Thus, since the propagation domain is infinite, only a slice of the model needs to be considered containing the set of inclusions to be repeated in one direction. The effect of the line load and receivers is also included in the considered slice. Since slices are infinitely repeated along the longitudinal direction of the line load, their global effect can be reproduced by the simulation of a single slice of the host environment with boundary condition of zero displacement in the direction orthogonal to the slice faces (y direction in Figure 6.1).

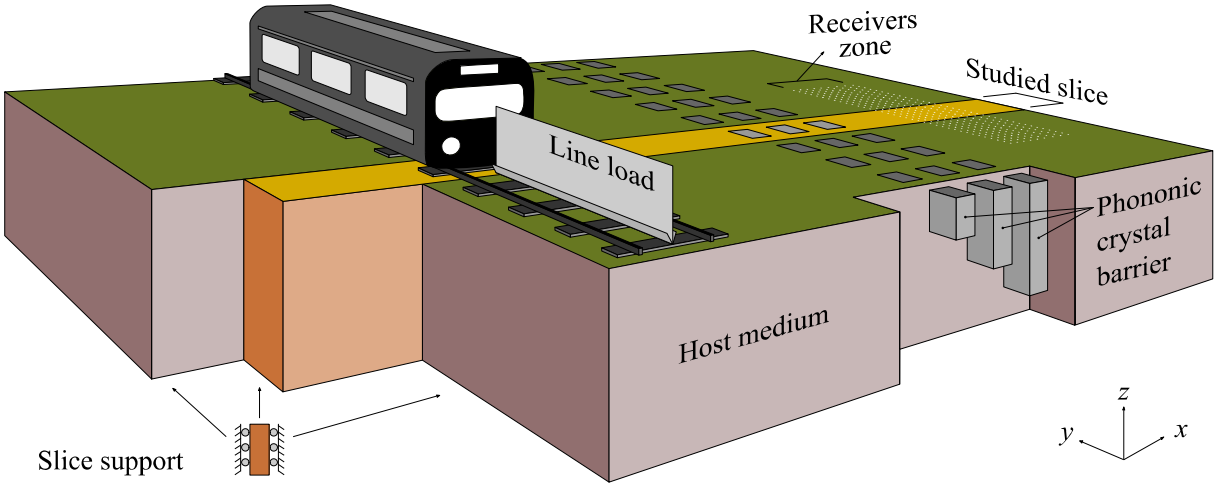

Figure 6.1 – Schematic representation of the model used for 3D wave propagation analyses.

6.1 Definition of studied scenarios

Extensive analyses were performed to understand the behaviour of a phononic crystal in different environments. Bearing in mind the presented general scenario, the study here presented was carried out in four complementary stages and results are grouped taking these stages into account. The first set of analyses considered a homogeneous soil medium, and simulations were performed to compare the performance with classical buried walls, for structures with different depths, materials and cross-sections. A second set of analyses considered the same homogeneous soil medium but simulated the effect of inclusions with different depths in the same phononic crystal. A third set of analyses aims at understanding more realistic scenarios in the performance of the same devices, with the presence of layered host ground media. Finally, a fourth set of analyses was done to evaluate the effect of the inclusions tilt in a homogeneous soil medium.

For all cases, the basic structure adopted for the phononic crystal device consists of three rows of inclusions with the same geometric and material characteristics. Next, the main properties and features of the studied scenarios are presented.

6.1.1 Phononic crystal buried in a homogeneous medium

The proposed phononic crystal device and a classical buried wall solution were initially studied. For both mitigation devices, three depths, three widths and two different material characteristics of the inclusions were considered. For comparison purposes, the buried wall was positioned at the same distance from the source as the closest inclusion. The host medium had a density $\rho_m = 2000\ \mathrm{kg/m^3}$, Young's modulus $E_m = 50 \times 10^6$ Pa and Poisson's ratio $\nu_m = 0.35$, properties of a soft soil.

A first set of analysis was performed for thirty-seven cases: the case without any type of mitigation devices plus the thirty-six summarised in Table 6.1, where the material properties of mitigation devices are also defined. In this context, the designation of "poor" is used for devices with the lower Young's modulus and "stiff" for devices with the higher Young's modulus. In practice, stiffer devices have properties close to those of concrete, while the so-designated "poor" inclusions and walls have properties closer to a soil-cement mixture (with a Young's modulus around ten times smaller than concrete).

Table 6.1 – Summary of test cases in the first set.

	Mitigation devices											
Type	Phononic crystal						Wall					
Cross-section in horizontal plane	0.2×0.2, 0.4×0.4 and 0.6×0.6 [$\mathrm{m^2}$]						Thickness [m] of 0.2, 0.4 and 0.6					
Depth [m]	1.5	3.0	5.0	1.5	3.0	5.0	1.5	3.0	5.0	1.5	3.0	5.0
Density [$\mathrm{kg/m^3}$]	2100			2400			2100			2400		
Poisson's ratio	0.25			0.20			0.25			0.20		
Young's modulus [Pa]	2.7×10^9			27×10^9			2.7×10^9			27×10^9		
Designation	"poor"			"stiff"			"poor"			"stiff"		

Figure 6.2 illustrates the 1.2 m wide slice which was modelled and that is infinitely repeated along y direction. In this figure, an absorption layer is shown, which is necessary to simulate the effect of an infinite medium in x and z (depth) directions. This layer, which has the width of at least one wavelength (considering the dominant wavelength of the emitted pulse), is responsible for absorbing all incoming energy, thus avoiding unwanted reflections from returning to the physical domain. The system is excited by a Ricker pulse, emitted from a line

source located 10 m to the right of the origin of the axes. The mitigation device has the centre of its first inclusion placed 10.3 m to the right of the excitation line load. The phononic crystal is composed of a set of three inclusions (along the x direction), spaced 1.2 m between centres, and infinitely repeated along the y axis with the same spacing. Three sets of inclusions were considered, with different depths of (1.5, 3.0 and 5.0) m and, for each depth, the horizontal cross-sections of $(0.2 \times 0.2, 0.4 \times 0.4$ and $0.6 \times 0.6)$ m^2 were tested. In addition, the two above described different materials were considered for the inclusions (see Table 6.1 and Figure 6.2). To benchmark the efficiency of these devices, the effect of a buried wall, also with its centreline placed 10.3 m from the source of excitation, was also studied. Similarly to the three sets of inclusions, three wall depths and three wall widths were considered with the same materials used in the inclusions. Finally, a line of receivers was placed on the ground surface, throughout the total width of the slice, at 15 m from the source (downstream, after the mitigation devices).

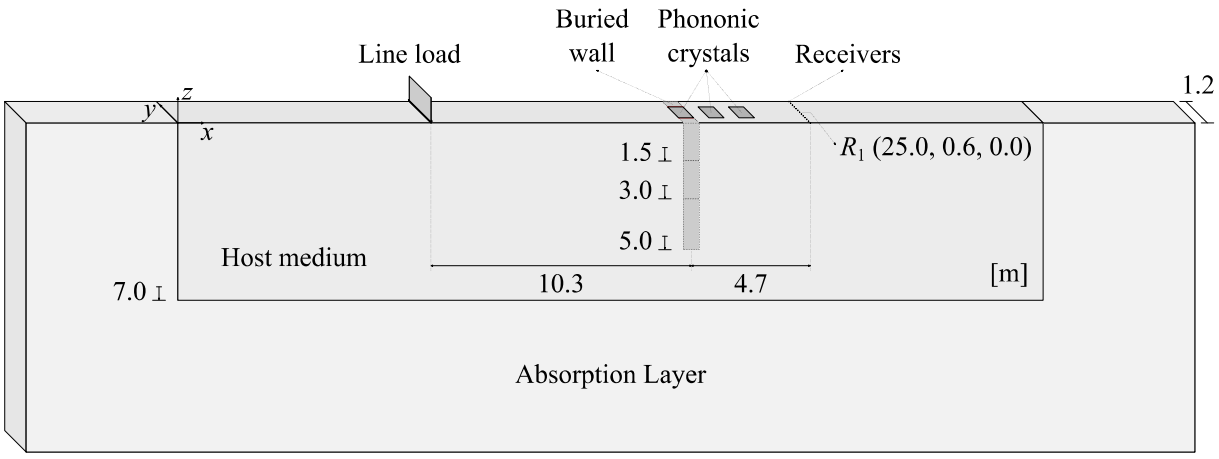

Figure 6.2 – Schematic representation of the slice model used for the numerical analysis of wave propagation.

6.1.2 Phononic crystal composed of inclusions with different depths

The same model described in the previous section is used to perform a second set of analyses on the effect of inclusions with different depths in the same phononic crystal. For these analyses, the phononic crystal is still composed of three rows of inclusions, each row with a constant depth. Thus, the model is schematically represented in Figure 6.2, and the only change made corresponds to the depth of the inclusions. The five cases summarised in Table 6.2, are analysed. The two sets of material properties, designated by “stiff” and “poor”, are again used.

Table 6.2 – Configurations of phononic crystals with varying inclusion depth.

Designation	Depth of row 1	Depth of row 2	Depth of row 3
{5.0, 5.0, 5.0} m	5.0 m	5.0 m	5.0 m
{5.0, 3.0, 5.0} m	5.0 m	3.0 m	5.0 m
{3.0, 5.0, 3.0} m	3.0 m	5.0 m	3.0 m
{1.5, 3.0, 5.0} m	1.5 m	3.0 m	5.0 m
{5.0, 3.0, 1.5} m	5.0 m	3.0 m	1.5 m

6.1.3 Phononic crystal buried in stratified media

For engineering purposes, natural grounds can be seen as layered domains of constant properties inside each layer. Thus, this variable – the effect of the soil stratification – is introduced into the model, with changes in wave propagation patterns and the response produced by the phononic crystals being expected.

As in previous cases, mitigation devices correspond to phononic crystals composed by a set of three parallelepipedic inclusions with quadrangular horizontal cross-section. As in the initial scenarios presented in 6.1.1, three sets of inclusions with distinct depths, (1.5, 3.0 and 5.0) m are studied, and, for each case, three configurations of the stratified host medium (S1, S2 and S3) are analysed, as summarised in Table 6.3.

Table 6.3 – Summary of the studies carried out in the third set of analyses.

				Mitigation devices depth [m]								
Host medium	(No mitigating devices)			1.5			3.0			5.0		
Stratification	S1	S2	S3	S1	S2	S3	S1	S2	S3	S1	S2	S3
Layer 1	RHM	RHM	RHM	RHM	RHM	RHM	RHM	RHM	RHM	RHM	RHM	RHM
Layer 2	RHM	SHM	SHM	RHM	SHM	SHM	RHM	SHM	SHM	RHM	SHM	SHM
Layer 3	RHM	SHM	R	RHM	SHM	R	RHM	SHM	R	RHM	SHM	R

RHM – Reference host medium; SHM – Stiffer host medium; R – Rock.

S1 – Only the reference soil; S2 – Reference soil in the surface layer and stiffer soil in the remaining layers; S3 – Reference soil in the surface layer, stiffer soil in the intermediate layer and rock in the deepest layer.

The layers referred in Table 6.3 are schematically defined in Figure 6.3, showing the modelled slice with the stratified soil, inclusion set, loading and receivers line. As in the previous model, the represented slice is infinitely repeated along the *y* direction, and adequate boundary conditions are used to simulate the infinite nature of the problem. The characteristics of the absorbent layer are the same as those considered in the previous model where, in the same way,

the energy absorption is based on the material damping to avoid unwanted reflections in the system being studied. The system is excited by a Ricker pulse with source located 10 m to the right of the system origin. The phononic crystal has its first element centre placed at a distance of 10.3 m to the right of the excitation point. This mitigation device consists of a periodic set of three inclusions spaced 1.2 m from their centres. Finally, a set of receivers is placed on the surface, along the total width of the slice, at 15 m from the source.

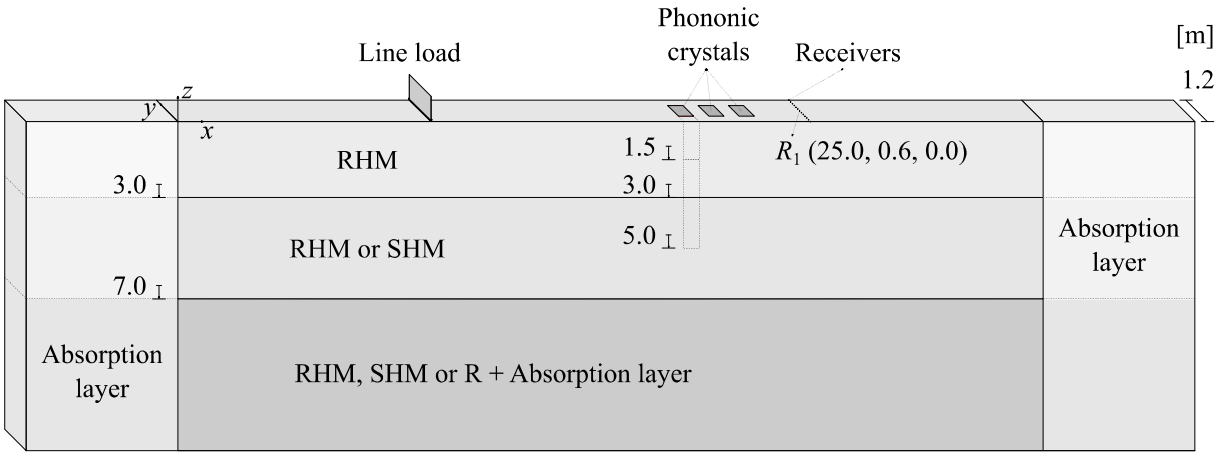

Figure 6.3 – Schematic representation of the slice model used for stratified soil cases.

For this set of analyses, only the "stiff" phononic crystal structures are considered. The material properties of both inclusions and of the different soil types are defined in Table 6.4.

Table 6.4 – Material properties used in the third set of analyses.

Materials	Density [kg/m^3]	Poisson's ratio	Young's modulus [Pa]	Wave velocities [m/s]		
				P	S	R
RHM	2000	0.35	50×10^6	200.31	96.23	89.95
SHM	2000	0.35	200×10^6	400.62	192.45	179.91
Rock	2312	0.23	32×10^9	4005.69	2371.99	2174.52
Mitigation devices	2400	0.20	27×10^9	3535.53	2165.06	1973.82

6.1.4 Phononic crystal with tilted scatterers buried in a homogeneous medium

This model is similar to the first model scenario. In this case, the soil has the same material properties and only the "Stiff" quadrangular inclusions 5 m deep and 0.6 m wide whose material

characteristics are defined in the Table 6.1 were considered. The angles, α, of 0° (reference angle), 5° and 10° (see Figure 6.4) where analysed.

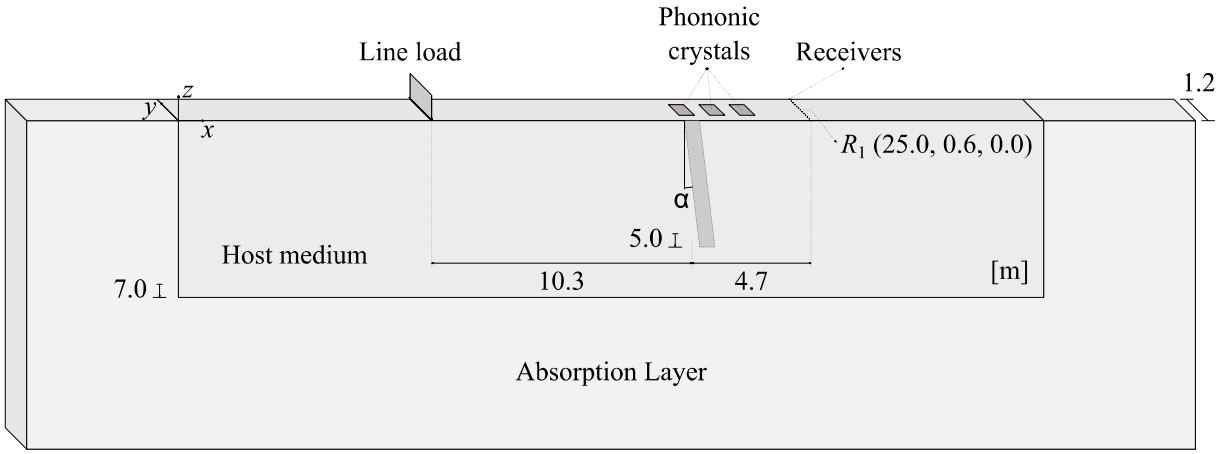

Figure 6.4 – Schematic representation of the slice model used for tilted scatterers.

6.2 Results and discussion

Numerical simulations were performed using the 3D FEM-TD model. The geometry depicted in Figure 6.2 and in Figure 6.3 was discretised using a mesh of 2 162 160 regular tetrahedral elements; this mesh is generated considering a regular grid of nodes, equally spaced 0.1 m along the three spatial directions. A propagating Ricker pulse with a central frequency of 60 Hz was considered in all studied cases. Due to the spectral content of this type of pulse, the chosen central frequency of 60 Hz allows to simulate propagation scenarios in which significant energy content exists in the $40 - 100$ Hz range: the relevant frequency range for transportation-induced vibrations. In the numerical process, a damping factor is taken equal to 1 % for all materials; the damping factor of the absorbent layer varied from 1 % near the Analysis zone to 100 % in the limit of the layer furthest from that zone.

The required time-steps for the different scenarios without the phononic crystal are 5.9×10^{-4} s, 3.0×10^{-4} s and 3.0×10^{-5} s, respectively for S1, S2 and S3. When the stiffer inclusions are considered, the time-step for S1 and S2 scenarios becomes lower, assuming the value of 3.5×10^{-5} s. In all cases, the critical time-step is conditioned by the stiffer medium, which may either be the inclusion or the rock layer (for S3 configuration).

6.2.1 Phononic crystals versus buried walls

This section presents the comparative results of the response in the Downstream zone due to the existence of vibration mitigation devices, namely in the presence of the phononic crystals and buried walls. To evaluate the differences due to the presence of both devices, the same materials were used for the two mitigation measures. Both results were, then, compared to the results without any type of mitigation devices to determine the respective insertion loss values.

Figure 6.5 shows the vertical amplitudes over time registered in receiver R_1 (see Figure 6.2) placed at the surface of the host medium, 15 m from the source, aligned with the centre of the inclusions. These results are obtained when a set of three rows of inclusions or a buried wall, both with 5 m depth and 0.6 m width, are considered. These responses are compared to homogeneous medium propagation considering devices with different material properties: (a) a softer material and (b) a stiffer material. Observing the depicted plots, the arrival of a first pulse is clearly visible for both cases, corresponding to P waves travelling in the soil. For the homogeneous medium, a set of pulses arrives later and well separated from the first, corresponding to S and R waves, which travel at lower velocities and, after that, no additional pulses are registered. This is the expected response for a homogeneous medium, in which, besides the interaction with the surface, no additional interferences with the propagation of the incident wave occur. The result is markedly different when the periodic inclusions are considered. Note that for the first pulse (P wave), there is no significant difference in the response with respect to the homogeneous medium. However, right after that a set of other pulses arrive at the receiver, corresponding to multiple interactions with the buried structures. The surface and S waves also suffer significant influence from the buried structures, and the strong pulse observed before, associated with these wave types, is now replaced by a sequence of pulses resulting again from interaction phenomena. It can be noted, for all types of buried structures, that the very strong peak (S and surface waves) is very much attenuated by the presence of either the phononic crystal or the wall, even when smaller stiff properties are considered. Observing L_1, L_2 and L_3 lines (see Figure 6.5), related to the maximum amplitudes registered for each case, there also seems to be some additional benefit when the phononic crystals are used. This will be studied in more detail later in this work.

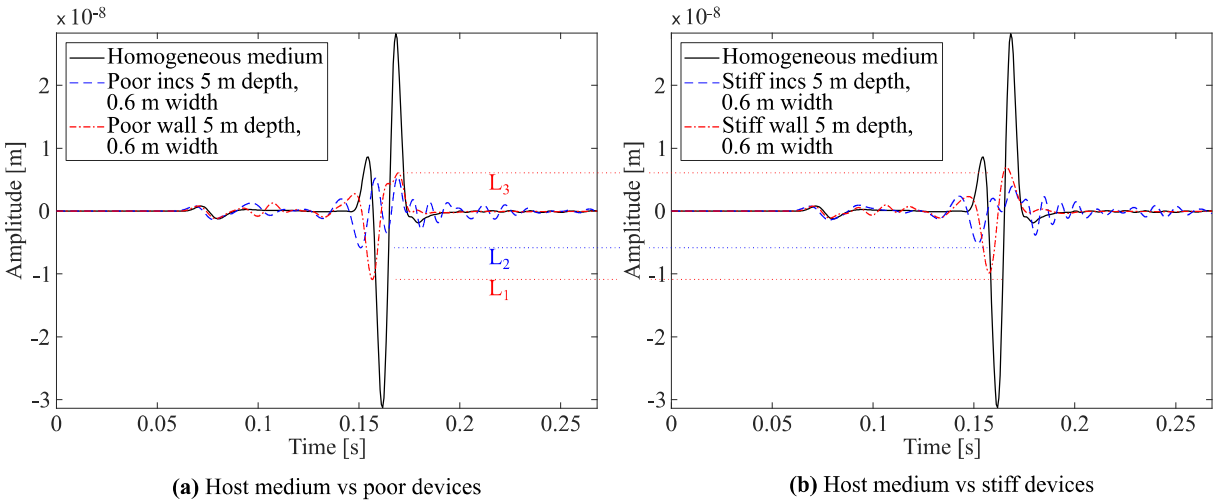

(a) Host medium vs poor devices

(b) Host medium vs stiff devices

Figure 6.5 – Comparison between mitigation device types and their stiffness: (a) poor and (b) stiff.

Figure 6.6 illustrates snapshots of the wave field in the Analysis zone, in terms of vertical displacements, computed in the presence of sets of 5 m depth stiff inclusions with differently sized square cross-sections: (a) 0.2 m, (b) 0.4 m and (c) 0.6 m.

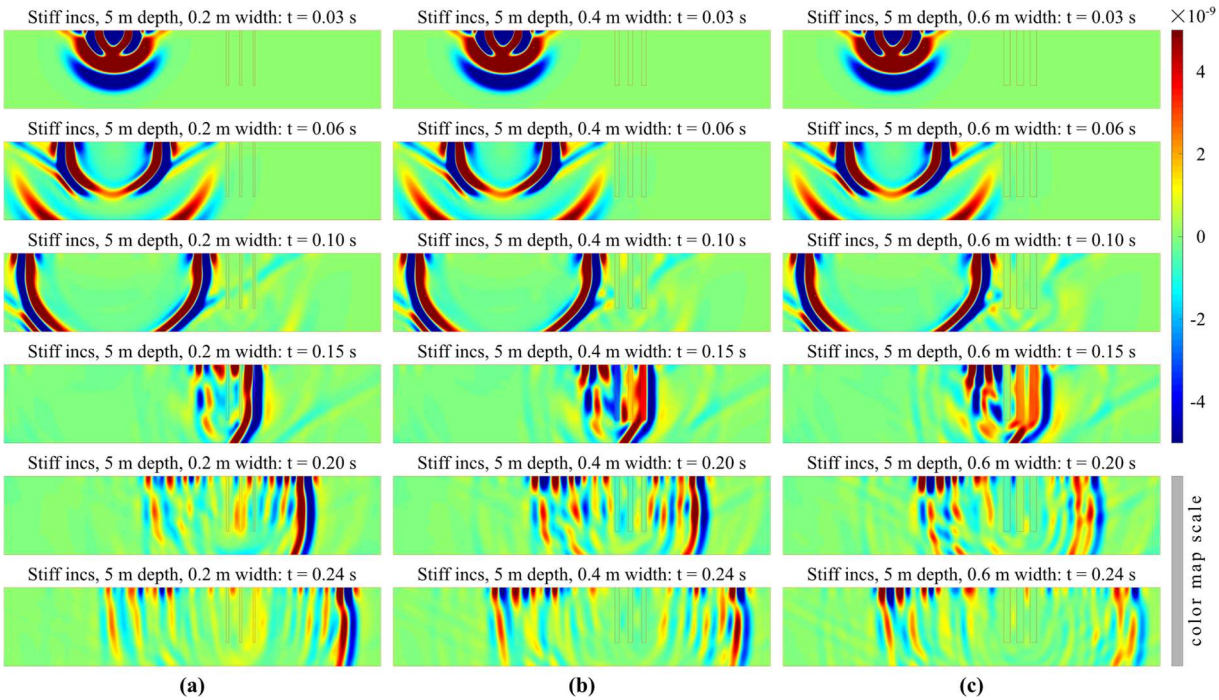

Figure 6.6 – Time evolution of 5 m depth stiff inclusions: (0.2, 0.4 and 0.6) m width, (a), (b) and (c) respectively.

Note that the distance between centres of inclusions is 1.2 m in all situations. One first remark that should be made is that no spurious reflections from the artificial absorption layer seem to occur. As for the wave propagation patterns, the interference of the buried devices is clear, with a more complex pattern being visible when multiple inclusions are considered – which becomes particularly evident for later times. These snapshots also evidence a considerable fraction of energy being reflected back by all inclusions, showing the intended shielding effect which, over time, is most evident in the inclusions with larger cross-sections. Additionally, from these snapshots can be seen that surface waves have a strong importance, as expected, since the geometric attenuation of this waves is null due to the loading characteristics (infinite line loading).

Figure 6.7 shows the average vertical vibration levels detected on surface receivers located 15 m from the source, beyond the sets of 5 m deep inclusions with "poor" and "stiff" material. The vibration levels, at each frequency band, correspond to the various widths, in the longitudinal direction, of the studied inclusions. These levels are computed in the frequency domain, after application of a fast Fourier-transform to the time signals obtained using the TD-FEM algorithm. To better observe the global behaviour, the response is grouped in frequencies of one-third octave bands, in the range from (10 to 160) Hz. The same total duration of the time signal was always considered (0.35 s) to allow for a correct comparison between the different scenarios, thus leading to the same frequency domain discretisation and to one-third octave band levels that are directly comparable. It should be noted, however, that the absolute vibration levels will always depend on the frequency content of the load. Therefore, they must be used only for comparison of different scenarios when the same excitation load is considered. Figure 6.7 shows that all sets of mitigation devices (although with different widths) allow a reduction of the vibration levels, despite acting differently throughout the frequency range. It is important to note that different reduction levels can be identified between the stiffer and softer ("poor") inclusions, and clearly the use of a stiffer material to build these phononic crystals leads to a better overall efficiency of the solution. The higher contrast between the propagation medium and the elastic material of the embedded scatterers allows a larger portion of the incident energy to be reflected and thus enhances the visible effect of the structure. An additional point that must be stated is related with the effect of the dimension of the scatterers, which, for both

materials, is a dominant factor; for both cases, as larger scatterers are modelled, a higher reduction in the vibration levels occurs indicating that, as expected, larger filling fractions of the matrix have a beneficial effect.

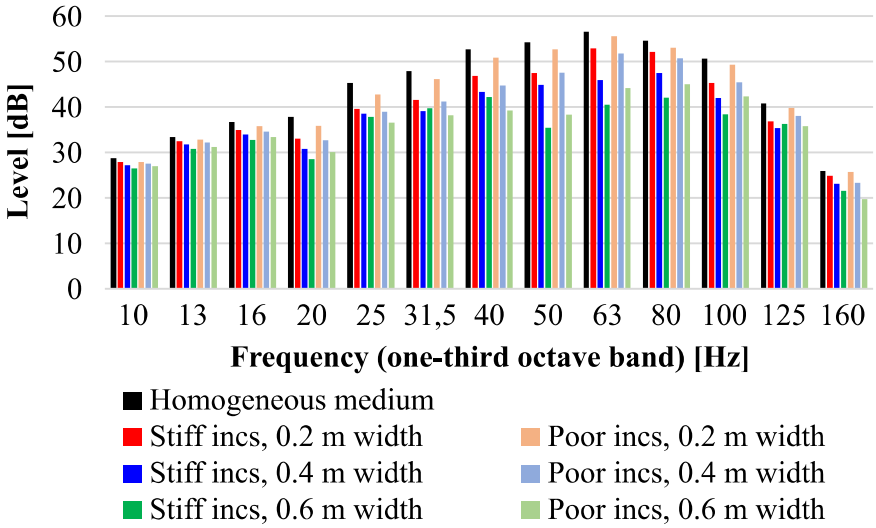

Figure 6.7 – Vertical vibration levels of 5 m deep, poor and stiff inclusions with several widths.

Although the analyses presented focus on the vertical displacements, an illustrative plot is presented in Figure 6.8 for horizontal displacements. In that case, the reduction is not so clear and in the lower frequency bands, (10 – 20) Hz, the effect is null or even negative.

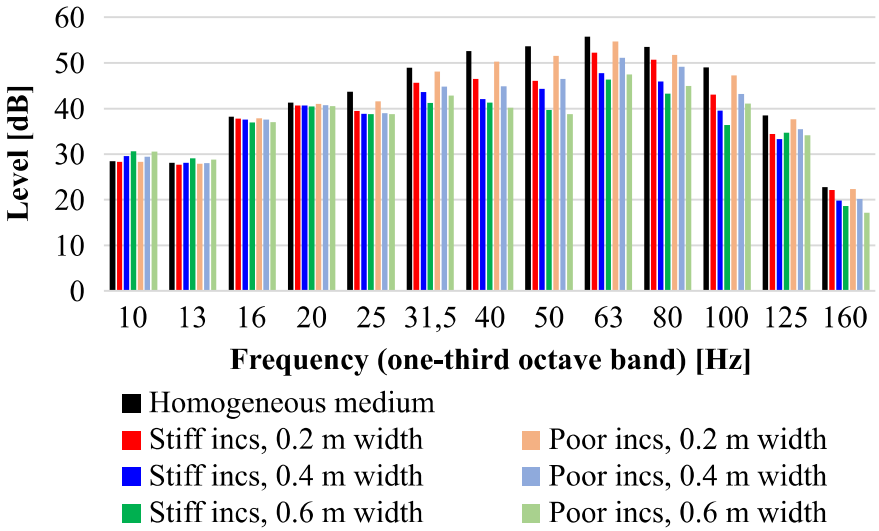

Figure 6.8 – Horizontal vibration levels of 5 m deep, poor and stiff inclusions with several widths.

Figure 6.9 presents the vertical vibration levels detected in the previously mentioned receivers, now comparing the various depths of inclusions and buried walls, in all cases with the same stiffer material and with 0.6×0.6 m^2 horizontal cross-section and 0.6 m thickness, respectively. A qualitative comparison between plots immediately allows identifying an important difference between the behaviour of both types of device. When the discrete set of periodically spaced inclusions is considered, a larger vibration reduction is registered at intermediate frequencies, while the continuous walls provide better vibration reduction at higher frequencies.

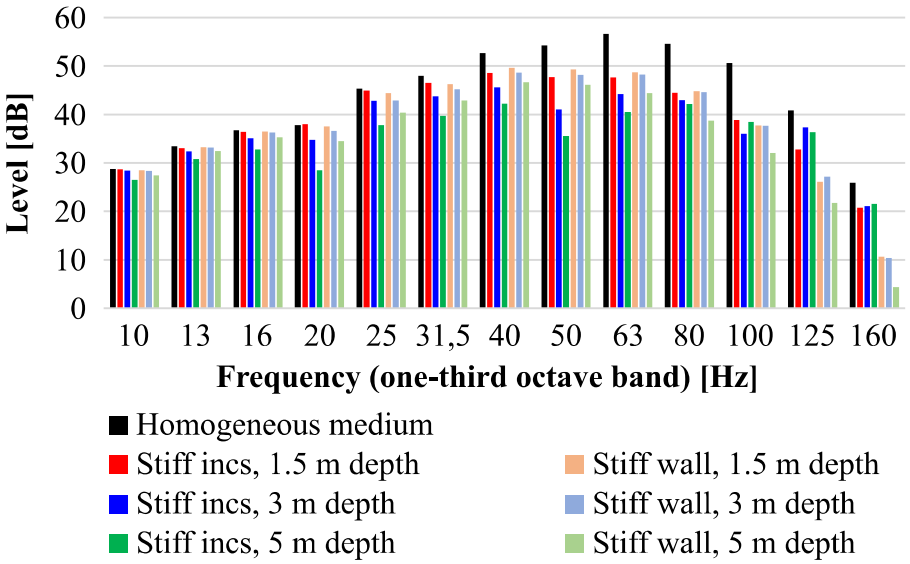

Figure 6.9 – Vertical vibration levels: both stiff inclusions and buried wall with 0.6 m width.

To better understand these results, Figure 6.10 represents the calculated reduction levels of vertical vibration estimated for each scenario, for the three depths studied, and for the two types of elastic material composing the mitigation devices. To evaluate the effect of the presence of mitigation devices in the vibrations registered in the previously mentioned receivers, the reduction is computed in terms of insertion loss level, *IL*, which was already defined at the beginning of the previous chapter – Equation (5.1).

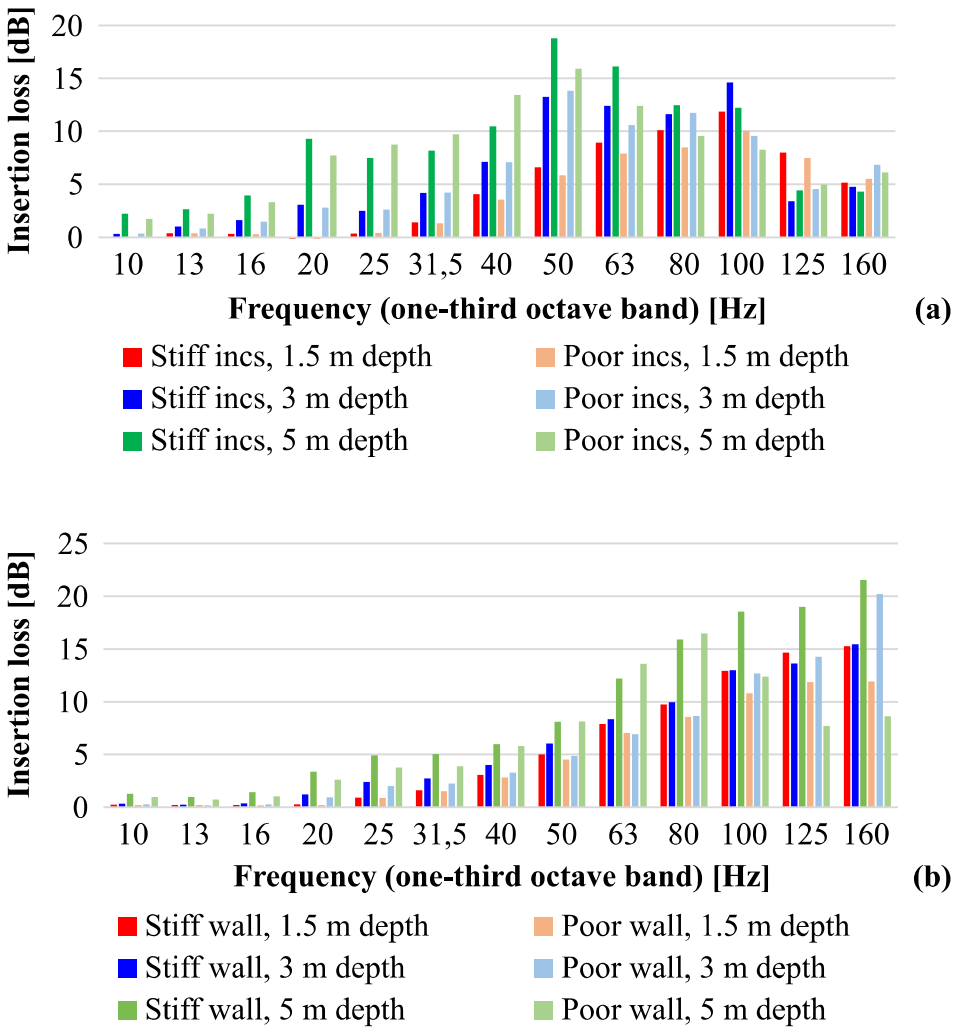

Figure 6.10 – Vertical insertion loss of mitigation devices of 0.6 m width: (a) set of inclusions and (b) buried wall.

Regarding the material type used in the protection devices, as expected and as previously commented for Figure 6.7, using a stiffer material generally leads to a better global performance for all tested depths, with higher values of insertion loss being reached. For this case, a sharper contrast of properties between the soil and the devices exists and allows stronger energy reflections to occur.

When comparing the horizontal cross-sectional dimensions of the buried devices (see Figure 6.11), it can be concluded that *IL* has an approximately linear relation with the cross-section (or with the filling fraction in the case of phononic crystals) in the frequency range of interest; in

other words, taking into account the cases studied and the frequency bands between (20 and 100) Hz, it can be stated that the greater the width, the higher *IL*.

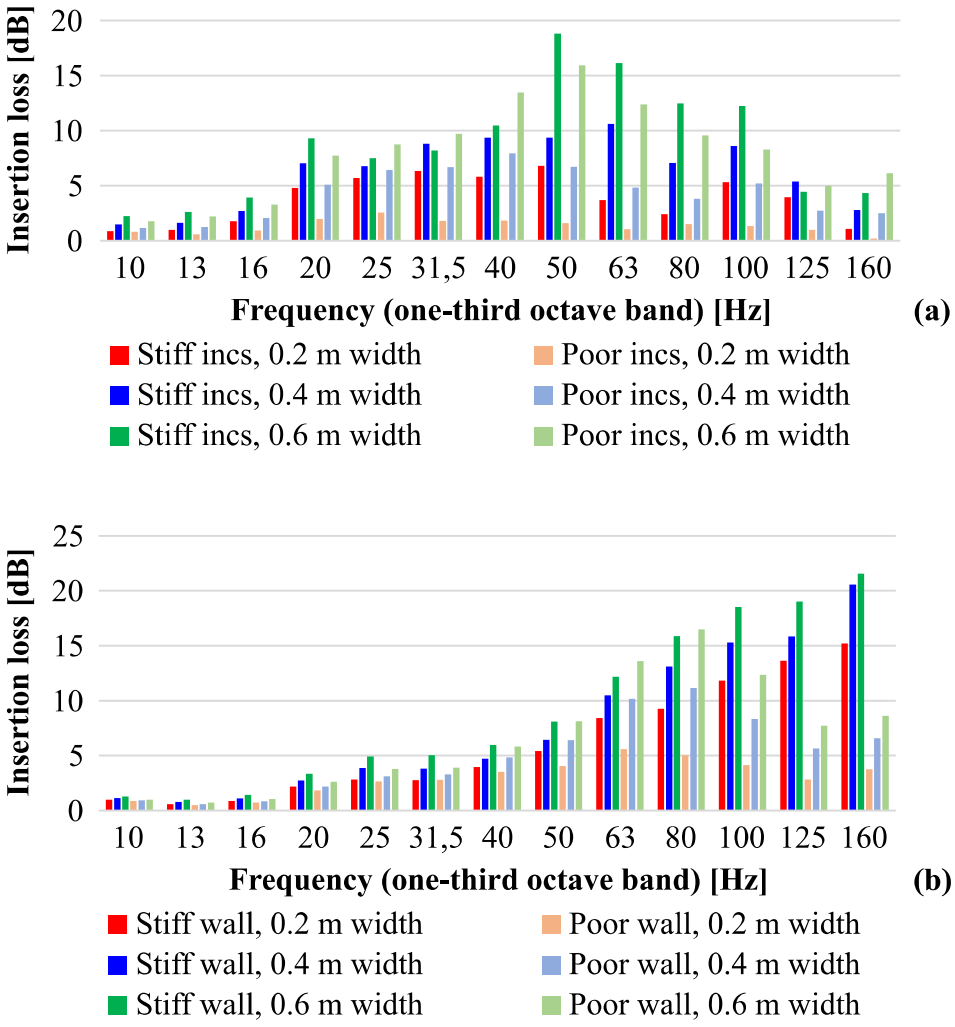

Figure 6.11 – Vertical insertion loss of mitigation devices 5 m deep: (a) set of inclusions and (b) buried wall.

Finally, Figure 6.12 displays results computed for distances between inclusions of 1.2 m (analysed in the previous cases) and 0.8 m. In these cases, the cross-section of the inclusion was considered square, with side dimensions being half the distance between inclusions (i.e. $0.6 \times 0.6\ \text{m}^2$ for a distance of 1.2 m, and $0.4 \times 0.4\ \text{m}^2$ for a distance of 0.8 m). Observing the presented plot, it becomes clear that a shift to higher frequencies occurs when a smaller spacing between inclusions is considered, confirming the behaviour identified earlier, and also the observations from (Castanheira-Pinto *et al.*, 2017) for horizontally placed scatterers.

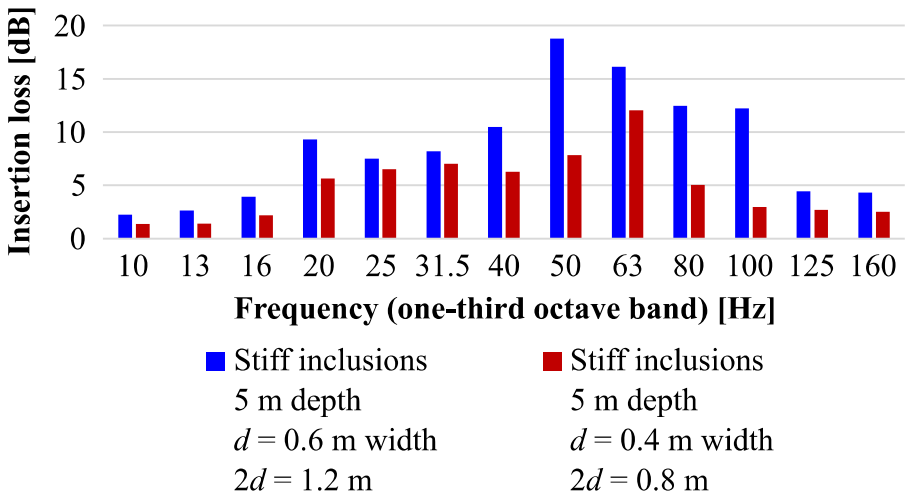

Figure 6.12 – Vertical insertion loss of mitigation devices 5 m deep comparing for square (d×d) inclusions spaced by 2d.

6.2.2 Phononic crystals using scatterers with different depths

Although in the previous section only sets of inclusions with the same depth have been analysed, it may be interesting to verify the behaviour of the periodic device when scatterers with different depths are considered. Thus, in this section, the analysis presented before is extended to the case in which each row of the phononic crystal may have a different depth (see Figure 6.1 where a possible configuration scheme of inclusions is represented). The model is the same as that shown in Figure 6.2 and the properties of the materials are the ones indicated in Table 6.1. In this section, only the study carried out with inclusions of 0.6×0.6 m^2 horizontal cross-section is presented, and the results compared with a reference for the case with all inclusions 5 m deep. The tested cases are the ones depicted in Table 6.2.

Figure 6.13 shows the comparison between the vertical amplitudes, in time domain, resulting from sets of multiple-depth inclusions with (a) poor and (b) stiff materials and the original set with a depth of 5 m. From the presented plots it is observed that, when inclusions 1.5 m deep are included, less favourable results are observed, while the remaining combinations seem to result in better performance; however, these time plots do not allow accurately detecting differences between the presented cases in detail. Regarding the type of material for the inclusions as expected and previously commented, using a stiffer material leads to a better global performance for all tested depths, with smaller amplitudes being reached (see line L). It

can be further added that the combination $\{5.0, 3.0\ 5.0\}$ m depths has practically the same performance as the reference combination (set of all inclusions width 5 m depth).

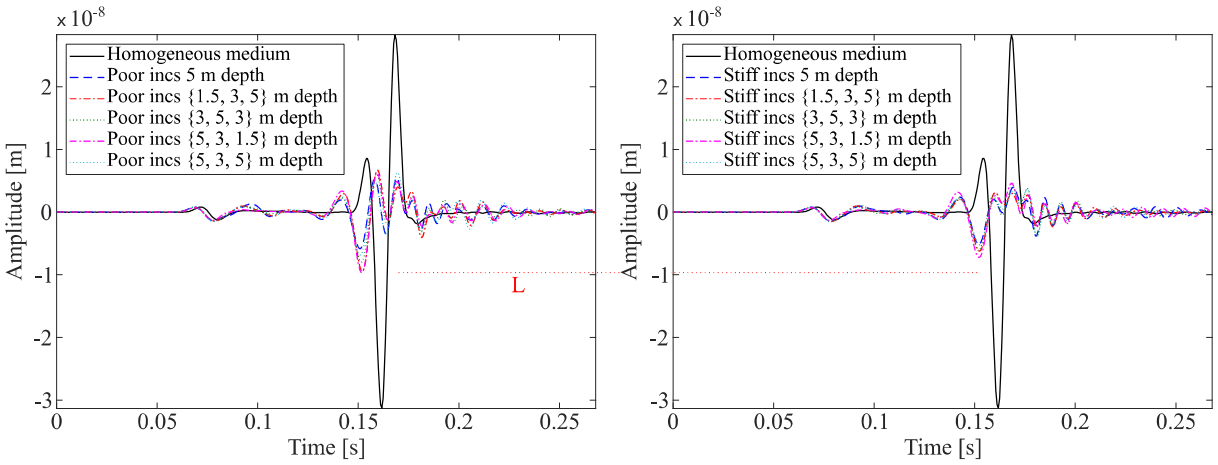

(a) Host medium vs poor devices **(b)** Host medium vs stiff devices

Figure 6.13 – Comparison between different configurations of phononic crystals: (a) poor and (b) stiff material.

A more detailed comparison can be performed by analysing results in the frequency domain, presented in Figure 6.14, which shows the insertion loss values registered on surface receivers 15 m from the source. From these charts, some conclusions may be drawn. The reference configuration outperforms all the remaining ones at lower frequencies, particularly when the softer material – see Figure 6.14 (a) – is used. Additionally, for configurations that include inclusions 1.5 m deep, this reduced performance is even more evident. For the higher frequencies, the combinations of different depths in the same phononic crystal produce better results. Looking at only this type of crystals, the solution $\{5.0, 3.0, 5.0)$ m produces, in almost all the frequency bands above 50 Hz, a better result.

Generally, the results presented in this section seem to indicate that some improved performance at higher frequencies may be obtained by using inclusions with different depths, although at the cost of losing part of the performance at lower frequencies. However, this gain is only visible when stiffer inclusions are used.

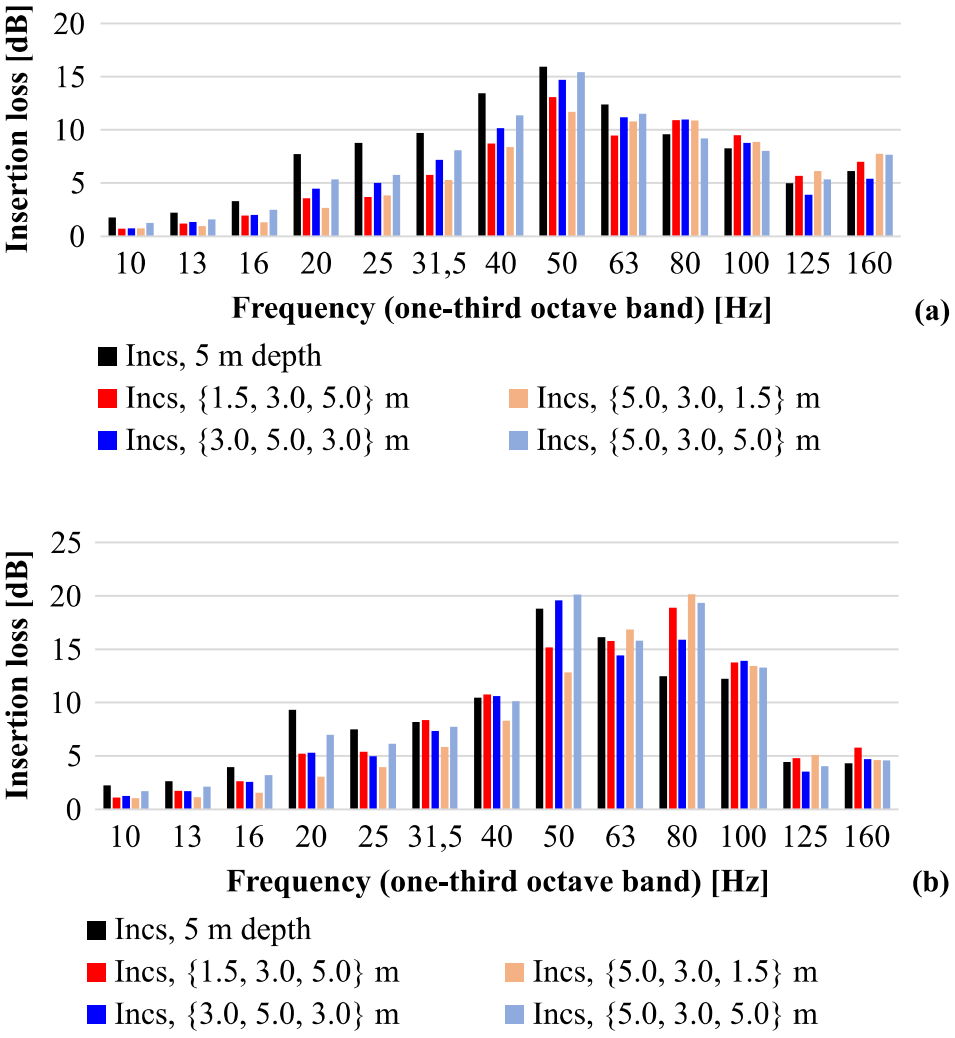

Figure 6.14 – Vertical insertion loss of sets of 3 inclusions with a (a) poor and a (b) stiff material.

6.2.3 Applications in layered ground

To understand the performance of the phononic crystal solutions when embedded in a stratified medium, several simulations were performed. Figure 6.15 displays the vertical amplitude over time, registered in the receiver R_1 (see Figure 6.3) and placed at the surface of the medium, 15 m away from the source, in the alignment of the centre of the inclusions. These results are obtained by taking into account three distinct stratification levels (see Table 6.3): S1, where only the reference soil is considered for all layers; S2, in which reference soil in the surface layer and stiffer soil in the remaining layers are considered; S3 wherein reference soil in the surface layer, stiffer soil in the intermediate layer and rock in the deepest layer are considered.

One should note that, for S2 and S3 cases, the highly dispersive character of the surface waves originates a quite different propagation pattern when compared to the S1 case.

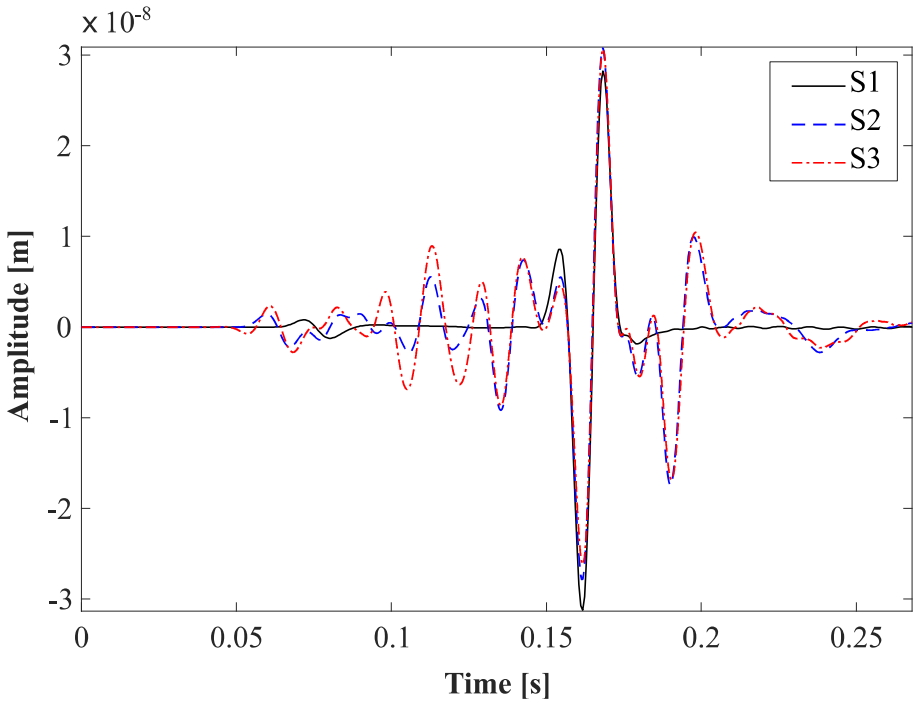

Figure 6.15 – Vertical displacement time history in the scenario with stratified media.

Figure 6.16 presents snapshots at different time instants of the wave field corresponding to the vertical displacements in the tested cases: (a) only the reference host medium, (b) a 3 m reference host medium layer and a stiffer soil below and, finally, (c) the 3 m reference soil layer, followed by a 4 m stiffer soil layer, followed by a bedrock. It is evident that, as time progresses, the interference of the progressively stiffer deeper layers leads, at higher frequencies, to the energy being trapped in the top soil, resulting from the lower layers' reflexion, originating a wave guiding effect, and thus a more complex wave pattern for the elastic waves in the layered media. For lower frequencies, a different effect is observed, with part of the energy travelling through the bottom layer, at much higher velocities, and then being again radiated to the top layer. It can also be seen that no spurious reflections from the artificial absorption layer occur.

Regarding now the phononic crystal with three inclusions 5 m deep, with $0.6 \times 0.6\ \mathrm{m}^2$ horizontal cross-section, Figure 6.17 shows the average vibration levels registered at surface

receivers; the reference levels obtained for each case without the phononic crystal are also included for comparison. From this figure, it can be concluded that the presence of the phononic crystals leads, again, to a decrease in surface vibration levels at all frequencies, although varying efficiency occurs with frequency and configuration of the layered ground.

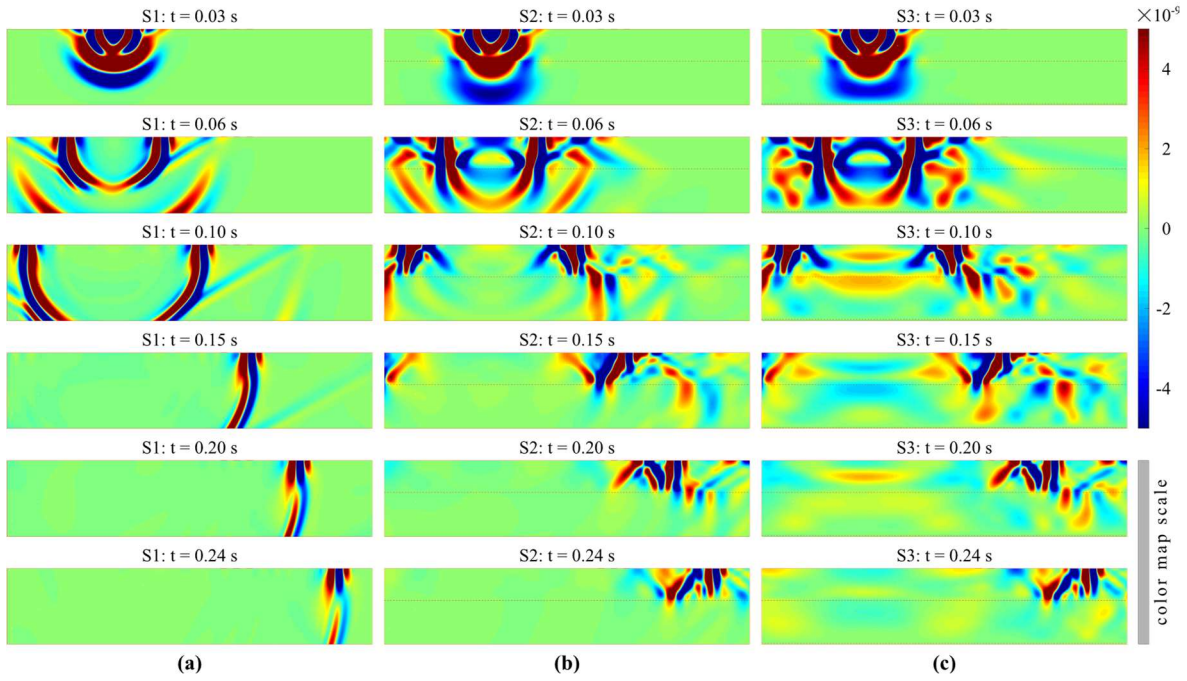

Figure 6.16 – Vertical displacements propagation over time in (a) S1, (b) S2 and (c) S3 stratification scenarios.

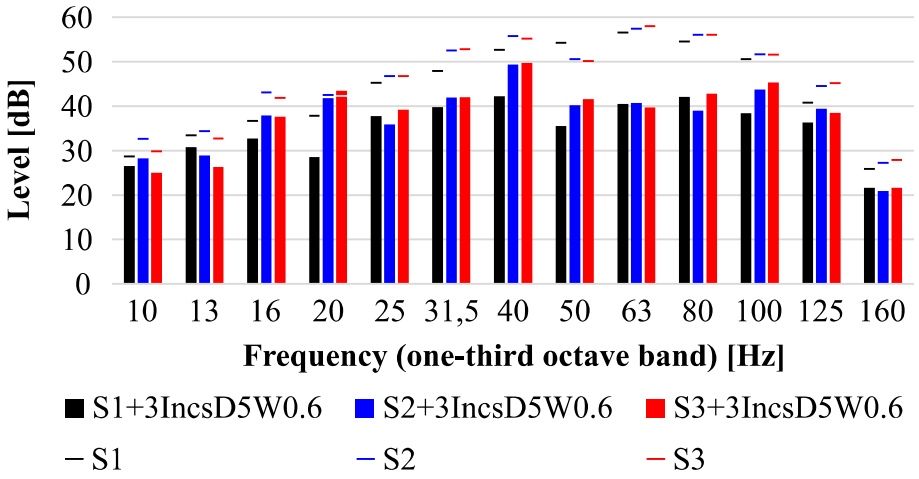

Figure 6.17 – Vertical vibration levels with and without inclusions for the S1, S2 and S3 scenarios.

To better evaluate and understand the effect of the presence of the phononic crystal in the vibrations registered in the previously mentioned receivers, the efficiency is computed in terms of insertion loss as defined before. In Figure 6.18, a significant reduction of vibration is observed in all stratified media scenarios – the same is to say, with good performance –, in the original propagation central frequency of 60 Hz. It is also verified that, as the soil is more stratified, with the host environment composed of stiffer lower layers, the vibration attenuation becomes smaller.

The aim of this study is to converge to mitigation devices that may be a future practical solution. Inclusions longer than 5 m may not be very interesting for technical and economic standpoints. However, an additional study with 7 m depth inclusions was done. In the case of homogeneous ground, there is a tendency for attenuation of vibration levels with the increase of inclusions length, i.e., as longer the inclusions are, the larger is their efficiency. In the case of layered ground, this efficiency is not so evident, being very similar to inclusions with 5 m depth.

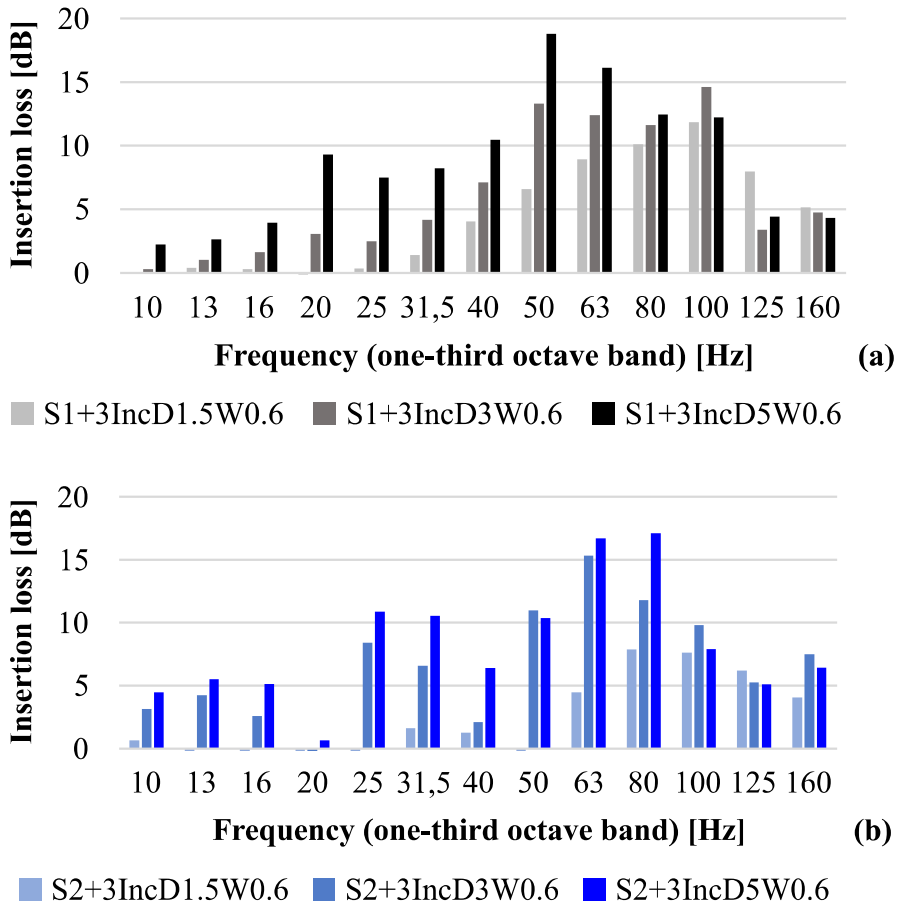

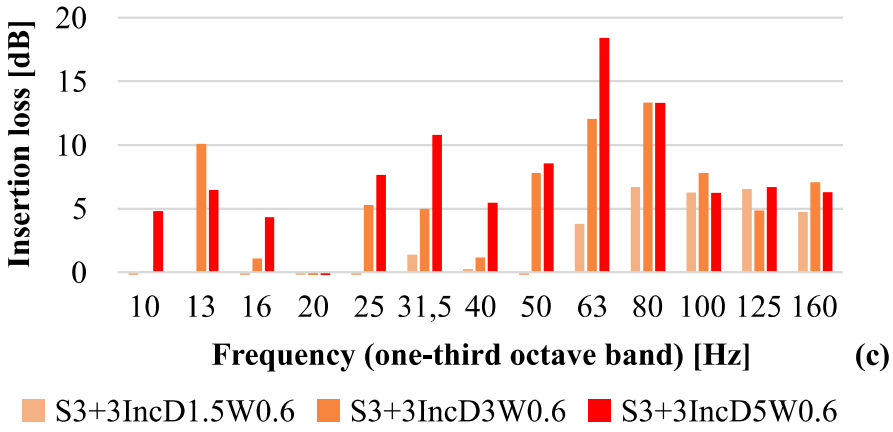

Figure 6.18 – Vertical vibrations insertion loss by phononic crystal mitigation devices in different stratified media: (a) S1; (b) S2; (c) S3 scenarios.

6.2.4 Phononic crystals using scatterers with a tilt angle

Finally, the results considering the influence of inclusions positioned with a tilt angle is presented. Figure 6.19 presents snapshots at different time instants of the wave field corresponding to the vertical displacements in the tested cases: (a) 0° reference angle, (b) angle of 5° and (c) angle of 10°. This figure shows that, for the studied angles, the influence of the inclination is minimal. However, some energy is reflected to the lower parts of the soil to the left of the tilted inclusions. This is visible mainly in later times.

Figure 6.20 shows the insertion loss average computed from the vertical vibration levels detected in the receivers line located 15 m from de load line, as defined in Figure 6.4. A qualitative comparison between plotted columns immediately allows identifying a benefit of tilted inclusions at low frequencies where the more tilted the more insertion loss. However, between central frequencies of (25 and 50) Hz the opposite is true. Between the central frequencies of (63 and 100) Hz, tilted inclusions perform better again. Although this is a quite complex phenomenon, it should be noted that the small tilt angle introduced will have some influence in the propagation pattern and can introduce changes in the expected behaviour. Indeed, the described Bragg effect will be influenced, and the reduction peak may be somewhat smoothed. This is, in fact, seen in Figure 6.20, in which the pronounced peak at 50 Hz is reduced and higher attenuations are obtained at (63 and 80) Hz.

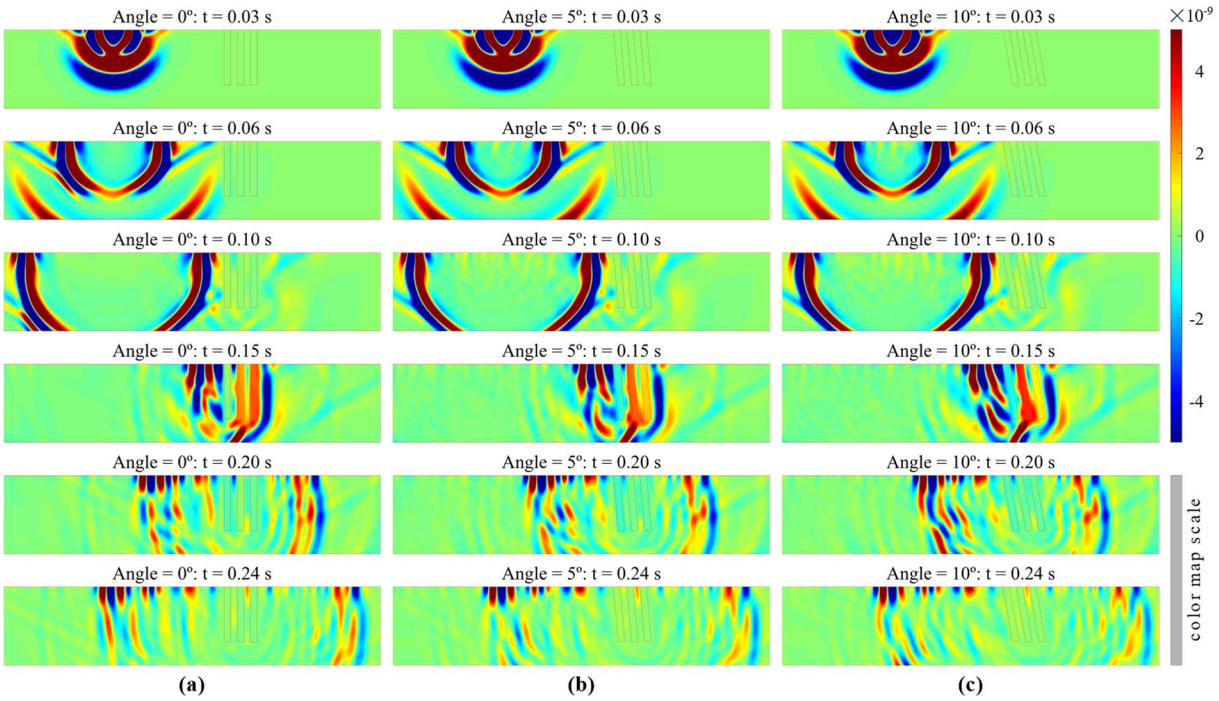

Figure 6.19 – Vertical displacements propagation over time with inclusions tilt angle of (a) 0°, (b) 5° and (c) 10° to the vertical.

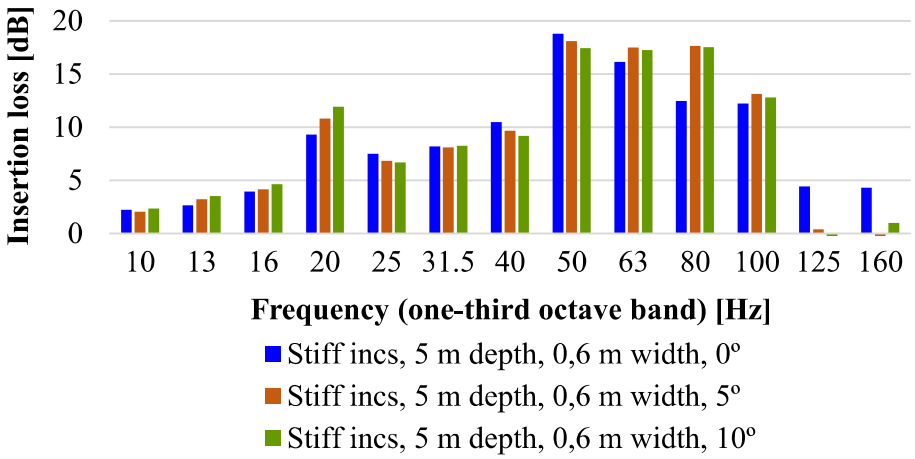

Figure 6.20 – Vertical vibrations insertion loss in the presence of inclusions with different tilt angles.

6.2.5 Conclusion

From the study here presented it can be concluded that it may be possible to mitigate the effect of the vibrations caused by the passage of trains in sensitive constructions to achieve human comfort and well-being. That mitigation is achieved by transposing the "phononic" crystals and

metamaterial concepts to the vibration protection based on buried structures periodically arranged located between the source and the receiver. Different geometries, materials and tilt angles were studied and compared with results of current mitigation solutions, in this case, with buried walls. It was verified that the studied concept allows quite interesting results in a range of frequencies that may be adjusted by changing the spacing and properties of the buried scatterers. Only in very specific frequency bands it can be seen, in the insertion loss graphs of Figure 6.10 a), that the soil without inclusions has better behavior, especially at lower frequencies. It should, however, be noted that traditional buried wall systems may provide better results at higher frequencies. In a generic way, the stiffer materials, relatively to the stiffness of the propagation medium, lead to better results. The behaviour of the structures in a more natural environment, as in the case of a stratified soil, was also efficient and showed a good performance, although a more complex response was observed. Regarding the geometry (horizontal cross-section and spatial arrangement) and material characteristics of the inclusions, it can finally be concluded that an optimal and tuned system depends widely on the properties of the host medium and the frequency band to be mitigated, since each configuration has its efficiency zone very much enhanced in the band gap frequency range.

A final aspect that is worth mentioning is that the time-marching 3D finite element model used here allowed to carry out this study in a more efficient manner, providing accurate results and a reduced computational effort.

7 NUMERICAL SIMULATION OF ULTRASONIC WAVE PROPAGATION

The propagation of ultrasonic waves is used in some applications in civil engineering, such as measurements and detection of structural damage. Ultrasonic damage detection techniques are increasingly being used because of their non-destructive characteristics and because they allow the detection of damage in the initial stage. In this chapter, numerical simulations based on the Time of Flight Diffraction method are presented to analyse elastic wave propagation in cracked concrete structures. The FEM-TD algorithm described in section 3.3 of this thesis will be used, since it is more adequate for the analysis of complex geometries.

7.1 Preliminary analysis

The purpose of this section is to evaluate the numerical model ability to detect damage in concrete structures and also as a first approach to interpreting the outputs. The accuracy of the computations of the distances travelled by the P waves is shown in a first case, presented in a 2D analysis. Next, a three-dimensional analysis is made in which the more complex patterns due to multiple reflections and wave types can be observed.

7.1.1 2D analysis

The 2D analysis allows evaluating the wave propagation and studying the results accurately and without excessive computational effort. This first analysis was made considering a 400×100 mm^2 concrete beam with a small rectangular defect, with 50×10 mm^2, at its centre, as shown in Figure 7.1. The geometric model was defined by a finite element mesh with a maximum element size of 0.001 m. The corresponding concrete properties are: density $\rho = 2500$ kg/m^3, Young's modulus $E = 35\,000$ N/mm^2 and Poisson's ratio $\nu = 0.15$.

This analysis scans the upper surface of the beam with a transducer that emits a vertical signal (a Ricker pulse) at each point, with a certain frequency, and acquires the response over time (t) – see the sources and receivers in Figure 7.1. Then, the distance ($t \times v$) travelled by the waves

is plotted considering the P waves velocity ($v = v_p = 3845$ m/s). A first set of results is shown in Figure 7.2 for different central frequencies of the emitted pulse, namely (a) 100 kHz, (b) 150 kHz, (c) 200 kHz and (d) 250 kHz. These figures show that the lower frequency exhibits wider pulses, which make it more difficult to interpret the different reflections in the system. This is particularly clear for higher order reflections. As higher frequencies are considered, the signals become progressively sharper, revealing more distinctly separate reflections. Among the presented results, those computed for 200 kHz seem to be a good compromise, which adequately evidence the main features of the wave propagation, while avoiding the drawbacks of higher frequency numerical simulations (such as finer meshes and consequently smaller time steps).

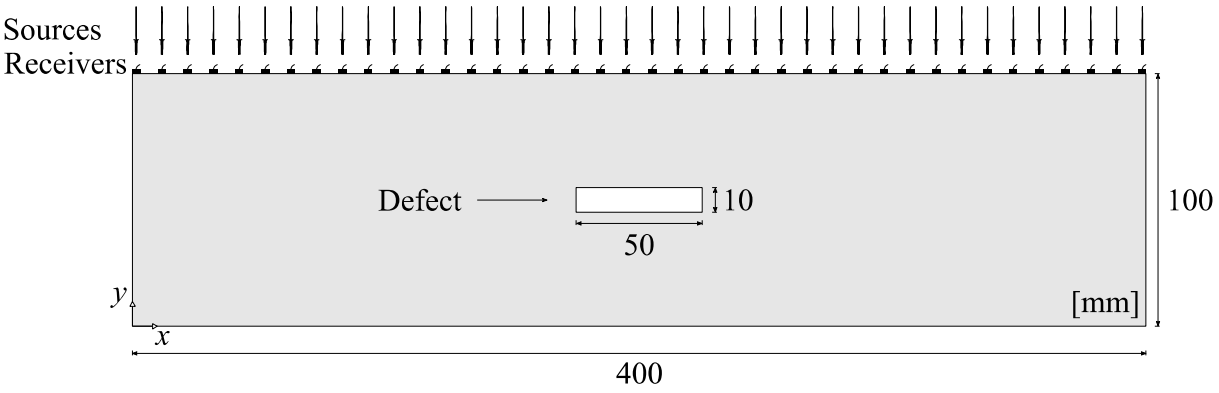

Figure 7.1 – Schematic representation of the analysed beam with a centred defect.

Figure 7.3 – magnification of Figure 7.2 (c) – shows the distance travelled by the P waves on the beam without defect, at each receiver placed at the top of the beam along its length. From this figure, it is clear that the distance travelled by the wave (0.2 m) is twice the height of the beam and the sum of two equal portions: the distance travelled on the outward flight and the distance travelled on the return flight. The colour map in the figure corresponds to the absolute value of the displacement amplitude at each receiver.

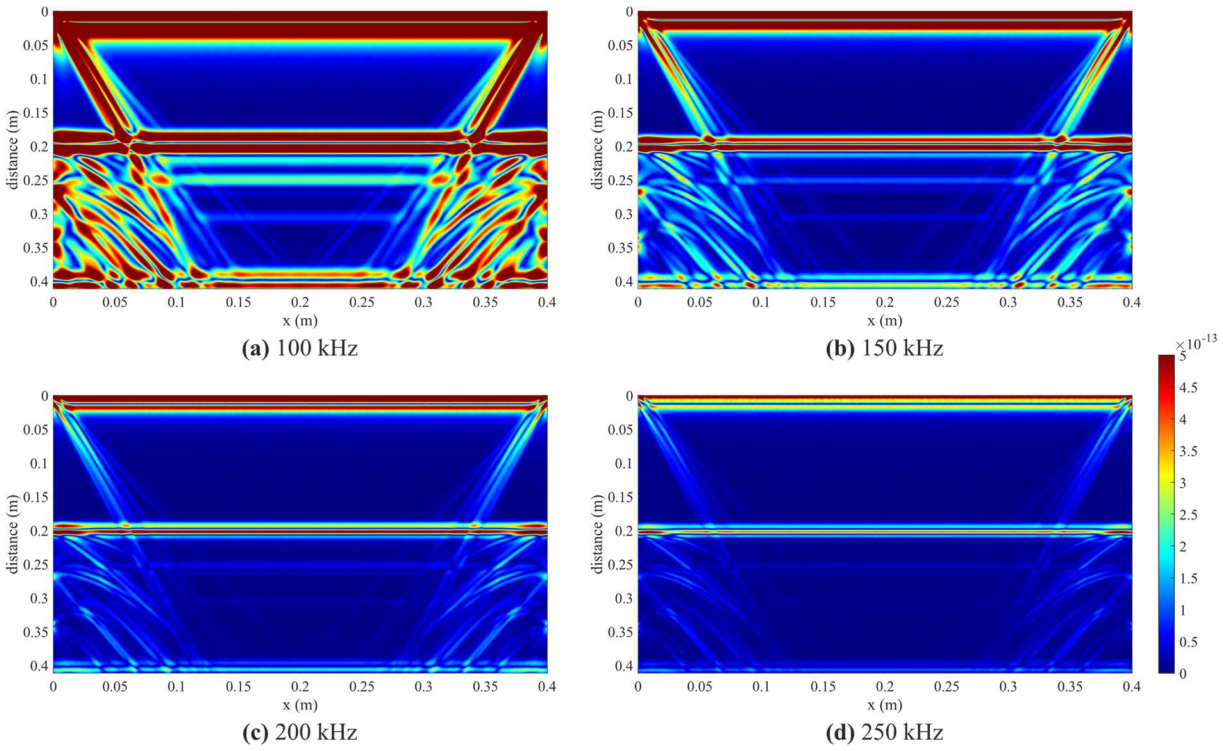

Figure 7.2 – Beam without defect, regarding a Ricker pulse with a central frequency of (a) 100 kHz, (b) 150 kHz, (c) 200 kHz and (d) 250 kHz.

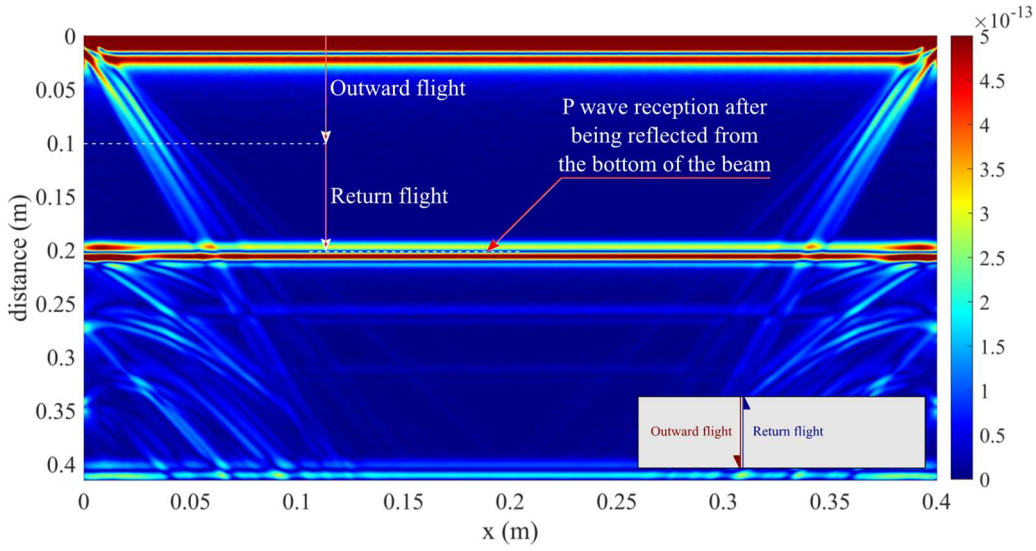

Figure 7.3 – Distance computed from data obtained on the receivers line, on the beam without defect, regarding a Ricker pulse with a central frequency of 200 kHz.

In the presence of the defect, and considering a frequency of 200 kHz, the plot shown in the Figure 7.4 is obtained. The distance travelled by the P waves is accurately obtained and thus

the distance of the top of the defect to the top of the beam ($0.09/2 = 0.045$ m) is well defined. Indeed, for this case, the performed analysis allows an excellent reconstruction of the propagation medium, clearly evidencing the presence and position of the defect. This is, in fact, a classical example of application of ultrasonic techniques to obtain images of the interior of a structure.

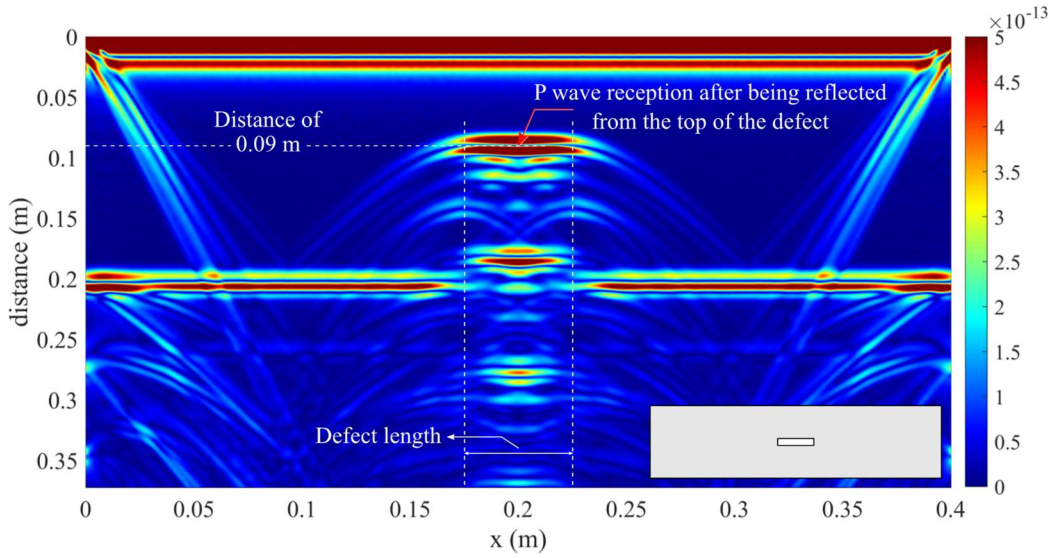

Figure 7.4 – Distance computed from data obtained on the receivers line, on the defected beam, regarding a Ricker pulse with a central frequency of 200 kHz.

To better understand the behaviour of the reflection of propagated waves over time, the two models represented in the Figure 7.5 are analysed where the defect is centred on the beam with the same dimensions and rotated 15º (a) to the left and (b) to the right. The beam has the same dimensions and material properties as before and the frequency of the wave propagation impulse is 200 kHz.

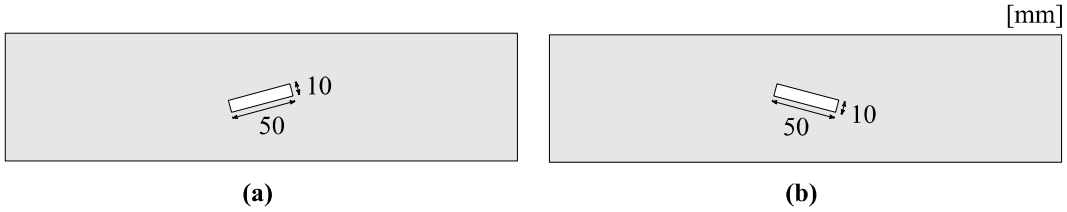

Figure 7.5 – Schematic representation of the beam with centred defects: rotated 15° (a) to the left and (b) to the right.

Observing the Figure 7.6, it is concluded that the evaluation of the rotated defect position is less clear; however, its presence and rotation is evident. In the Figure 7.6 (a), it can be seen that the reception of the left part of the defect occurs before its real location. The opposite is seen in the Figure 7.6 (b) where the reception of the left part is represented after its real position and extends beyond the defect, in the right part.

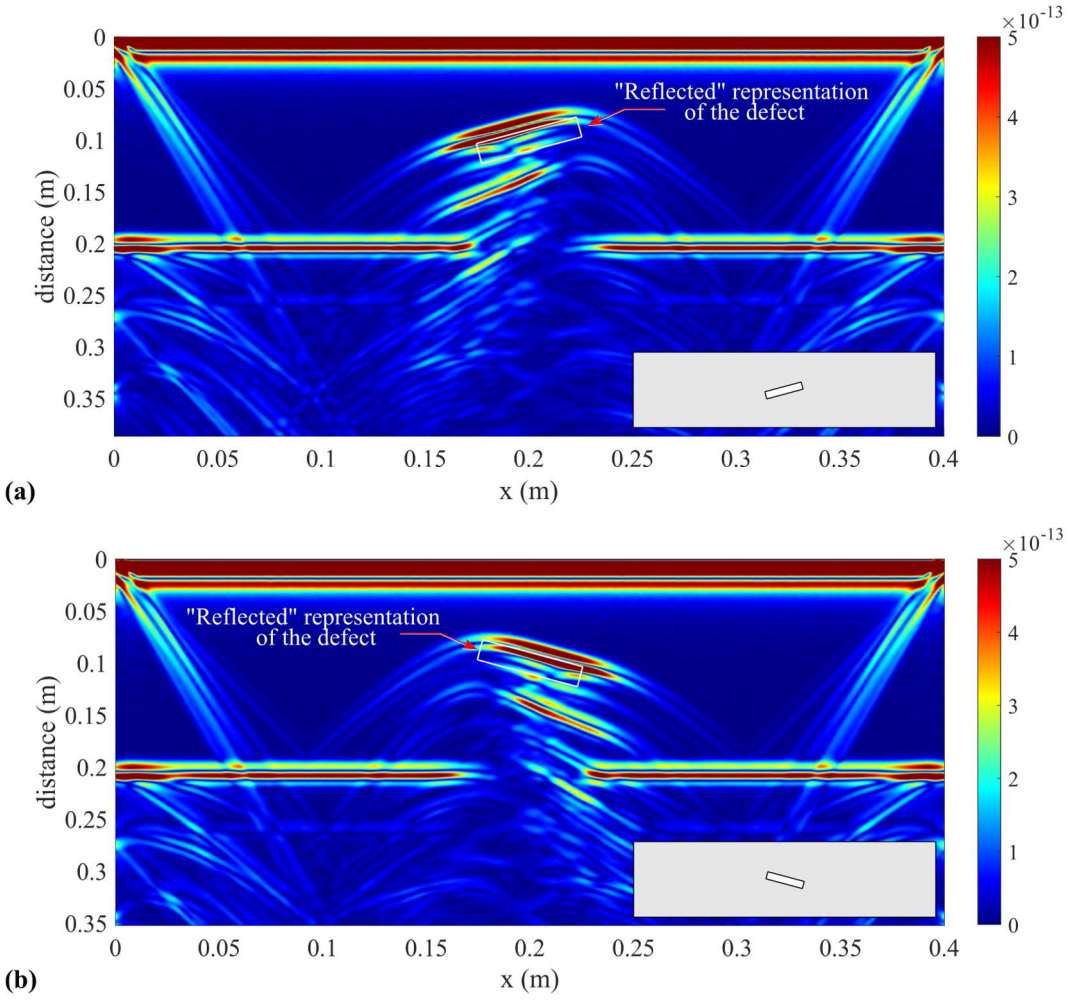

Figure 7.6 – Detection of the defect from data obtained on the receivers line, on the beam with defected rotated 15° (a) to the left and (b) to the right, regarding a Ricker pulse with a central frequency of 200 kHz.

This differential between the real position and the position inferred from the wave patterns is due to the effect represented in the Figure 7.7. The load acting in the system is vertical and creates a curved wavefront which, in the case of the defect rotated to the left, is reflected before the vertically propagating impulse reaches the defect, causing it to be identified before its real

position – see Figure 7.6 (a). Horizontally flipping the Figure 7.7, a similar scheme is obtained for the defect rotated to the right and, likewise, the shift to the right – see Figure 7.6 (b) – of the data read at the receivers relative to the real position of the defect is justified.

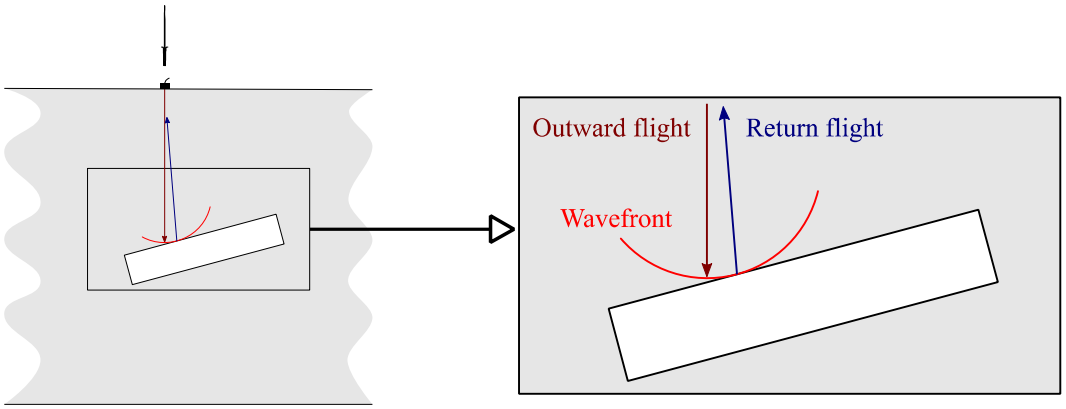

Figure 7.7 – Scheme of wave reflection in the rotated defect.

7.1.2 3D analysis

Analysis using a three-dimensional FEM-TD numerical model is next performed on a concrete beam of small size. For this analysis, beams with $400 \times 100 \times 100$ mm^3 were considered. The corresponding concrete properties are: density $\rho = 2500$ kg/m^3, Young's modulus $E = 35\,000$ N/mm^2 and Poisson's ratio $\nu = 0.15$. The models used are outlined in Figure 7.8 where the beam: (a) has no damage, (b) has a spherical hole in its centre, (c) has a semi-spherical hole in the centre of the upper face and, (d) has a semi-spherical hole in the centre of the front face. The spherical hole configurations have a diameter of 30 mm.

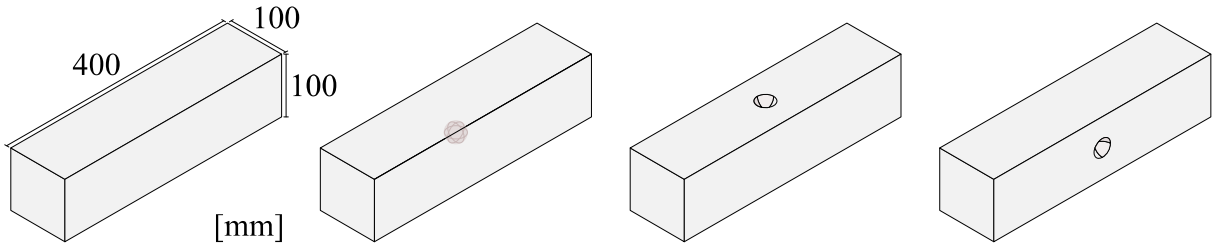

Figure 7.8 – Schematic representation of the analysed beam models.

All the beams were excited by a vertical Ricker pulse with a central frequency of 150 kHz, using a damping factor of 1 %, and located at S $(100, 50, 100)$ mm, as shown in Figure 7.9. Isolated receivers were placed in the positions R_1 $(300, 50, 100)$ mm and R_2 $(300, 0, 100)$ mm.

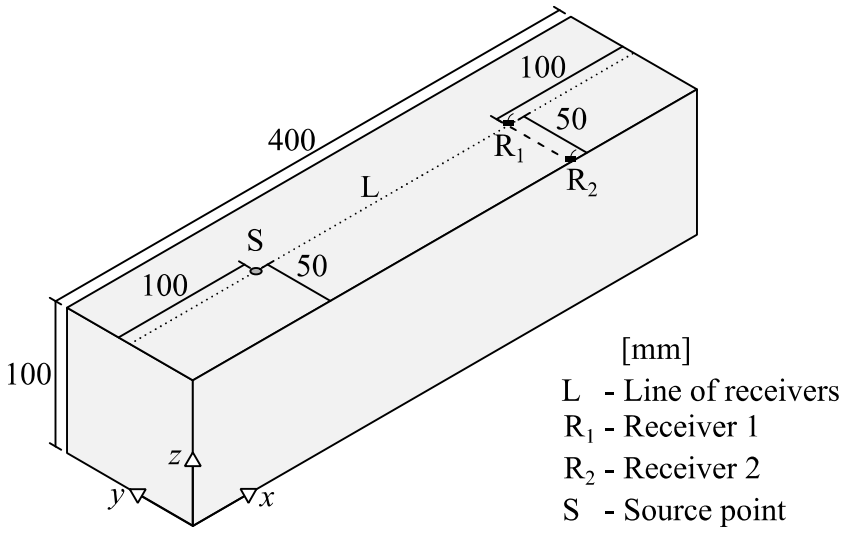

Figure 7.9 – Schematic representation of the source and receivers location.

Figure 7.10 shows plots of the computed horizontal amplitudes in the window time $[4, 16] \times 10^{-5}$ s, at the two receivers, (a) R_1 and (b) R_2, for all beam models. Comparing the two plots, it can be seen that amplitudes are higher in receiver R_2. This is due to reflections coming from the front face of the beam, which, in this case, amplify the signal at that point. In receiver R_1 there is a delay in signal arrival for the beam with the top face hole. This delay was expected, as well as the smaller amplitude with which it was detected. As the hole is in the straight wave path, there are reflections in the opposite direction to the propagation and the energy passing beyond the hole is smaller. It is further noted that the presence of the other holes (inward and front face holes) are not easily detected under the defined conditions. For example, between those models and the no hole beam model and taking receiver R_1 as reference, both the amplitude and the time-of-flight of the wave are similar in the first arrival. However, later there are small differences in amplitude.

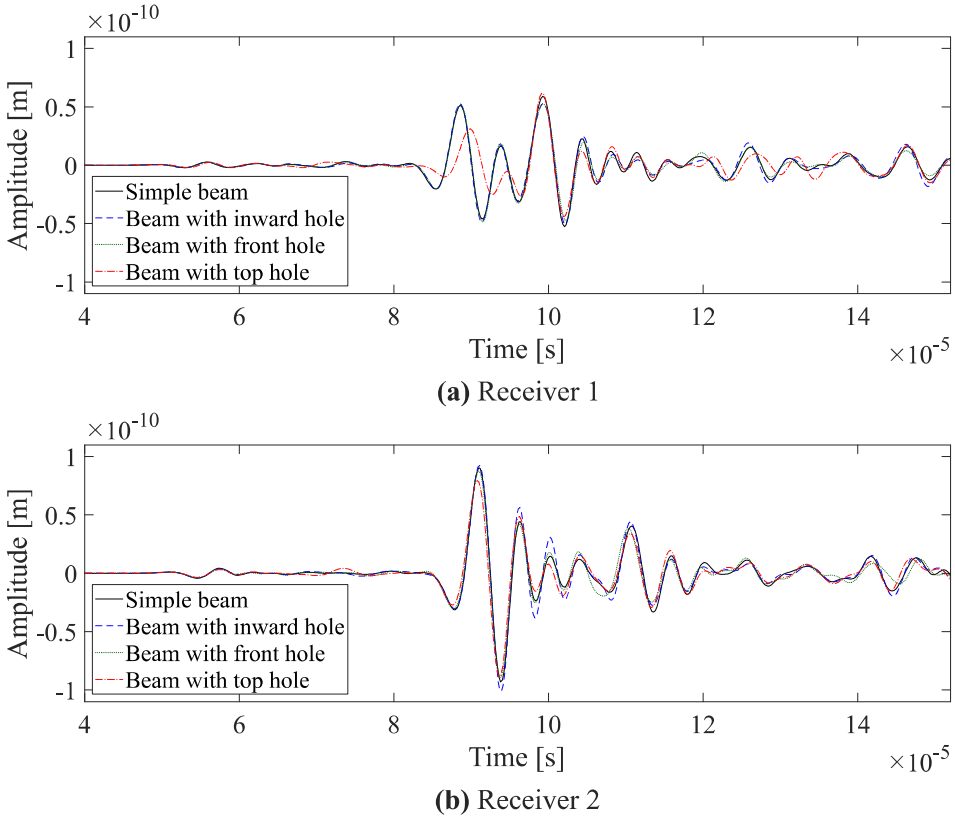

Figure 7.10 – Horizontal response computed at receivers (a) R_1 and (b) R_2, for all beam models.

In Figure 7.11 it is possible visualize the time responses on the receivers line positioned in the centre of the top face of the beam, along its length. From the plots, it can be seen the propagation over time is very similar except for the graph corresponding to the beam with the top face hole – Figure 7.11 (b).

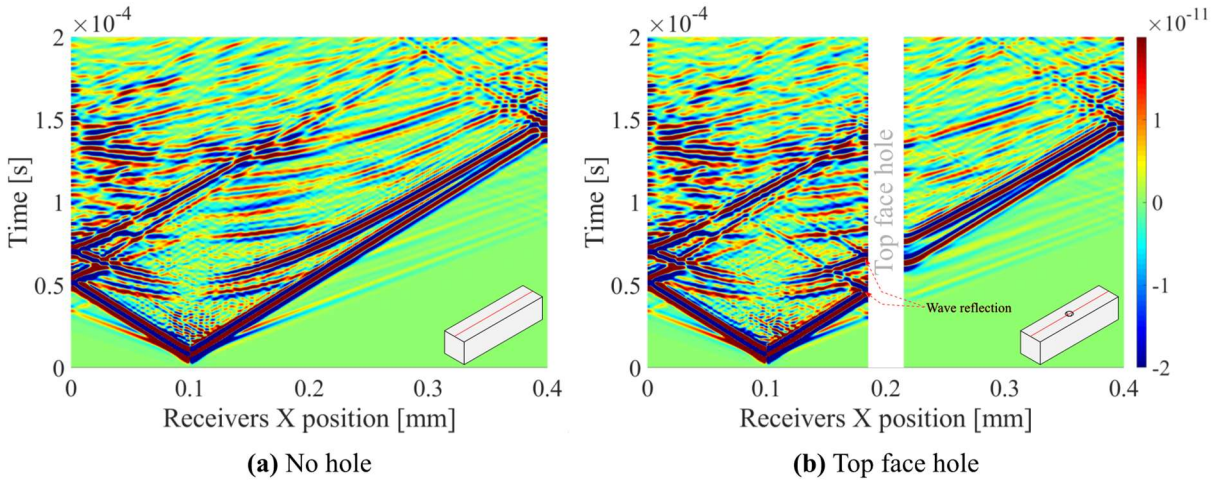

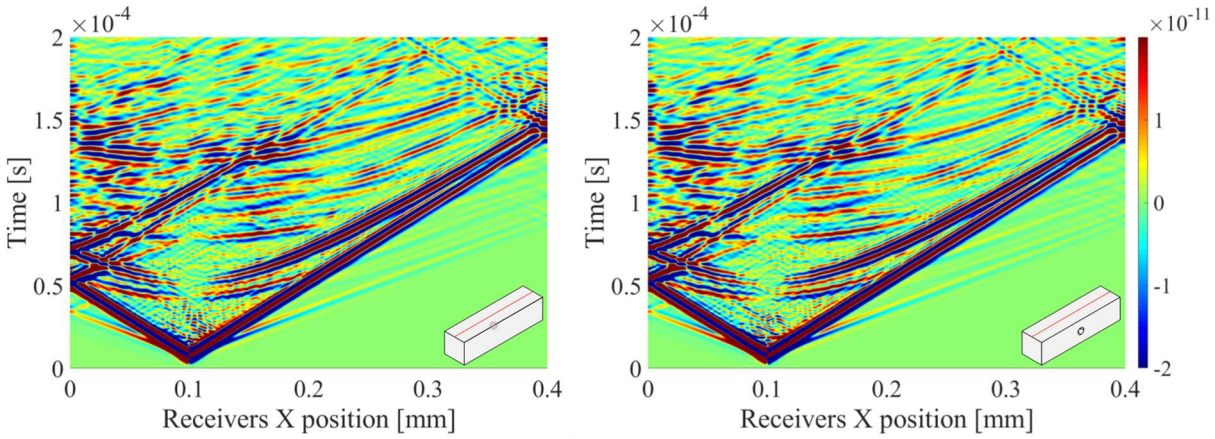

(c) Inward hole **(d)** Front face hole

Figure 7.11 – Time responses determined for the receivers positioned at (x, 0.05, 0.1), for (a) simple beam, and beams with (b) top face, (c) inward and (d) front face holes, for frequency of 150 kHz.

The propagation velocity of P waves in the specified concrete beam is $3845\,\mathrm{m/s}$ and its wavelength, for the induced frequency, is $26\,\mathrm{mm}$. This wavelength is very close to the hole dimensions. This is why the inward and front holes are not evident in the time-amplitude analysis. The top hole is evident on receiver R_1 because it is in the wave path, causing it to deflect – see Figure 7.11 (b) – and thus changing its amplitude and the time-of-flight. To highlight the effect of perturbations on that analysis, the wavelength must be significantly shorter than them, i.e., the frequency must be increased. Next, it is presented the same model with some configuration differences: both the frequency and the size of the inward spherical hole have been increased.

Figure 7.12 shows plots of the computed horizontal amplitudes in the window time $[4, 16] \times 10^{-5}\,\mathrm{s}$, at receiver R_1 for simple beam and for beam with $70\,\mathrm{mm}$ diameter spherical inward hole. The Ricker pulse excites the beam with a central frequency of 190 kHz at the same source point as before. In this configuration it is already possible to identify a time difference in wave arrival, a delay due to hole interference.

Figure 7.13 (b) shows that over time, energy increases before the centre of the beam ($x = 0.2\,\mathrm{m}$) due to the reflection caused by the inward hole.

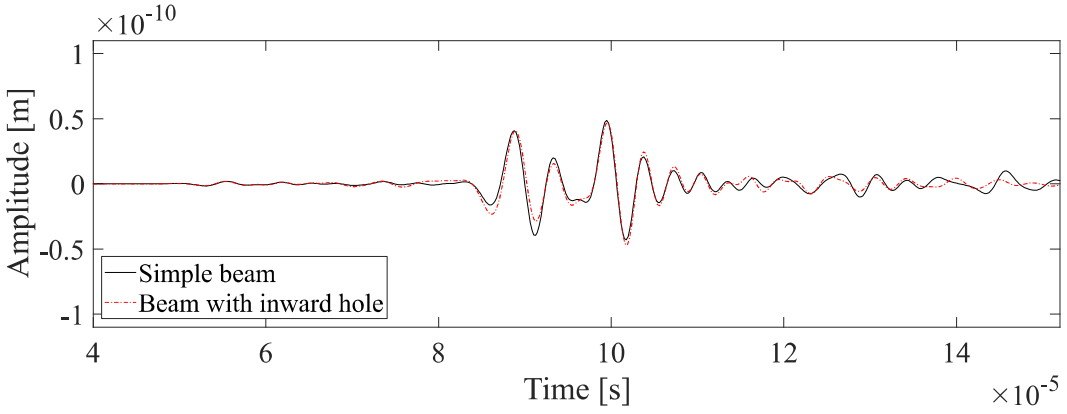

Figure 7.12 – Horizontal response computed at receiver R_1 for simple beam and for beam with 70 mm diameter spherical hole due to frequency of 190 kHz.

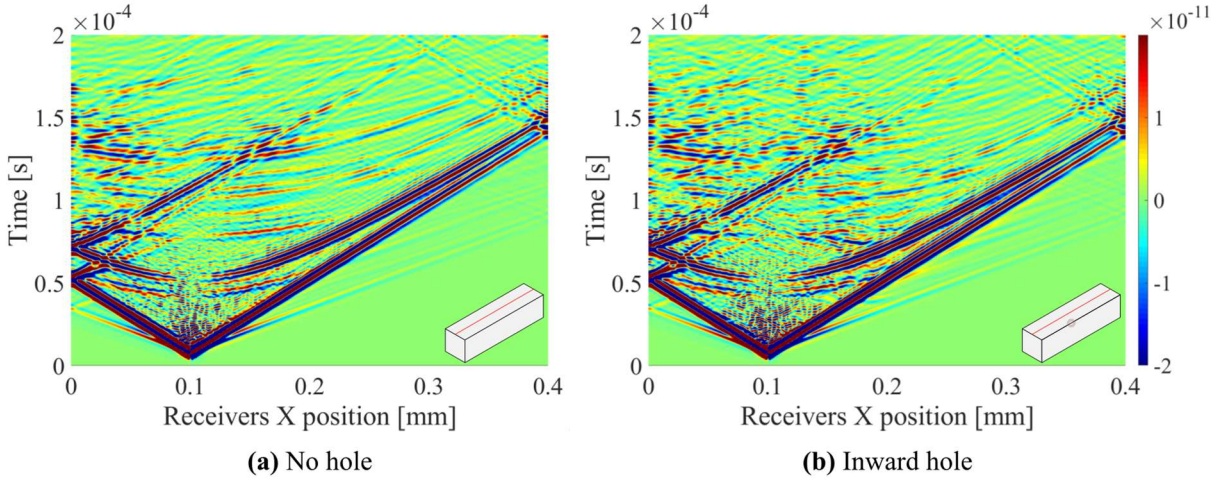

Figure 7.13 – Time responses determined for the receivers positioned at (x, 0.05, 0.1), for (a) simple beam and (b) beam with inward hole, for frequency of 190 kHz.

This example showed that by using the three-dimensional FEM in time domain, it is possible to simulate the damage detection in concrete beams, using ultrasound wave propagation. However, the propagation frequency is related to the detection rate; for example, to detect a particular damage, the propagated wavelength must be lower the size than this damage. The position of the transducer and receivers is also important. If they were placed on the front face of the beam, damage of that face would be detected and damage of the upper face would not be visible. At the computational level, this example requires significant effort in terms of memory and runtime. Thus, limitations such as the mesh size (number of degrees of freedom) hindered

the definition of the maximum frequency used to study this case. A higher frequency would be expected to provide better definition of the damage.

7.2 Application to analysis of a beam structure

FEM-TD is applied to a single edge notched concrete beam of small size, with maximum aggregate size of 8 mm – see experimental details in (Schlangen, 1993). The beam measures $400 \times 100 \times 100\ \text{mm}^3$ and has a $5 \times 20 \times 100\ \text{mm}^3$ notch, located at the middle of the top as shown in Figure 7.14.

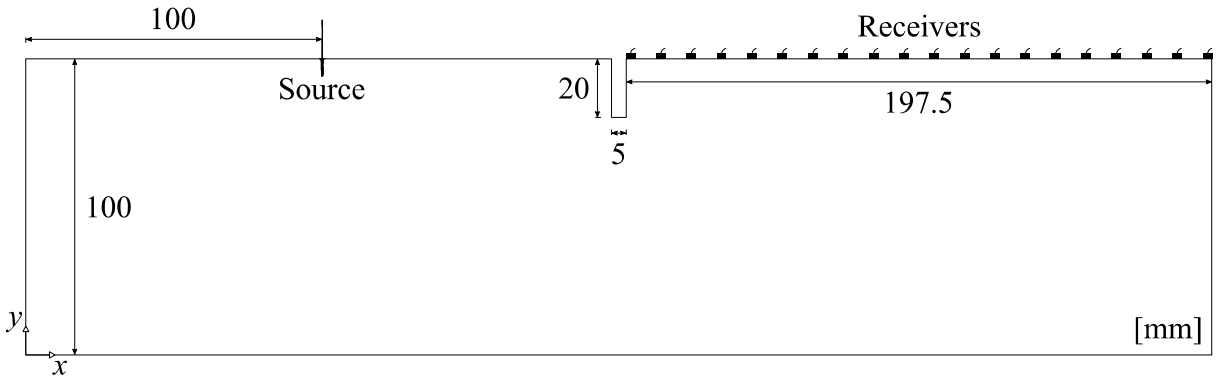

Figure 7.14 – Schematic representation of uncracked notched beam.

The corresponding material parameters are: density $\rho = 2500\ \text{kg/m}^3$; Young's modulus $E = 35\ 000\ \text{N/mm}^2$; Poisson's ratio $\nu = 0.15$; tensile strength $f_{t0} = 3.0\ \text{N/mm}^2$; and fracture energy $G_F = 0.1\ \text{N/mm}$. A constitutive law described in (Wells and Sluys, 2001) is used, with normal stiffness $k_n = 10^5\ \text{N/mm}^3$ and shear stiffness $k_s = 4{\times}10^2\ \text{N/mm}^3$. The study presented in this thesis focuses on two cracking stages. The crack paths presented in Figure 7.15 are obtained from numerical simulations with a strong embedded discrete crack approach (DSDA) using enriched finite elements. This variational consistent formulation is detailed in (Godinho, Dias-da-Costa, *et al*., 2013) and are in agreement with the experimental crack (Schlangen, 1993). After the computation of the crack pattern for the different stages, the FEM cracked model is used as geometry input data for the FEM-TD model. For the presented test case a 2D model of the beam and three distinct crack stages are considered: the initial defect-free beam (Figure

7.14); the beam in the cracked stage, first with the crack tip at 57 mm, Figure 7.15 (a), and next at 40 mm, Figure 7.15 (b), above the bottom of the beam.

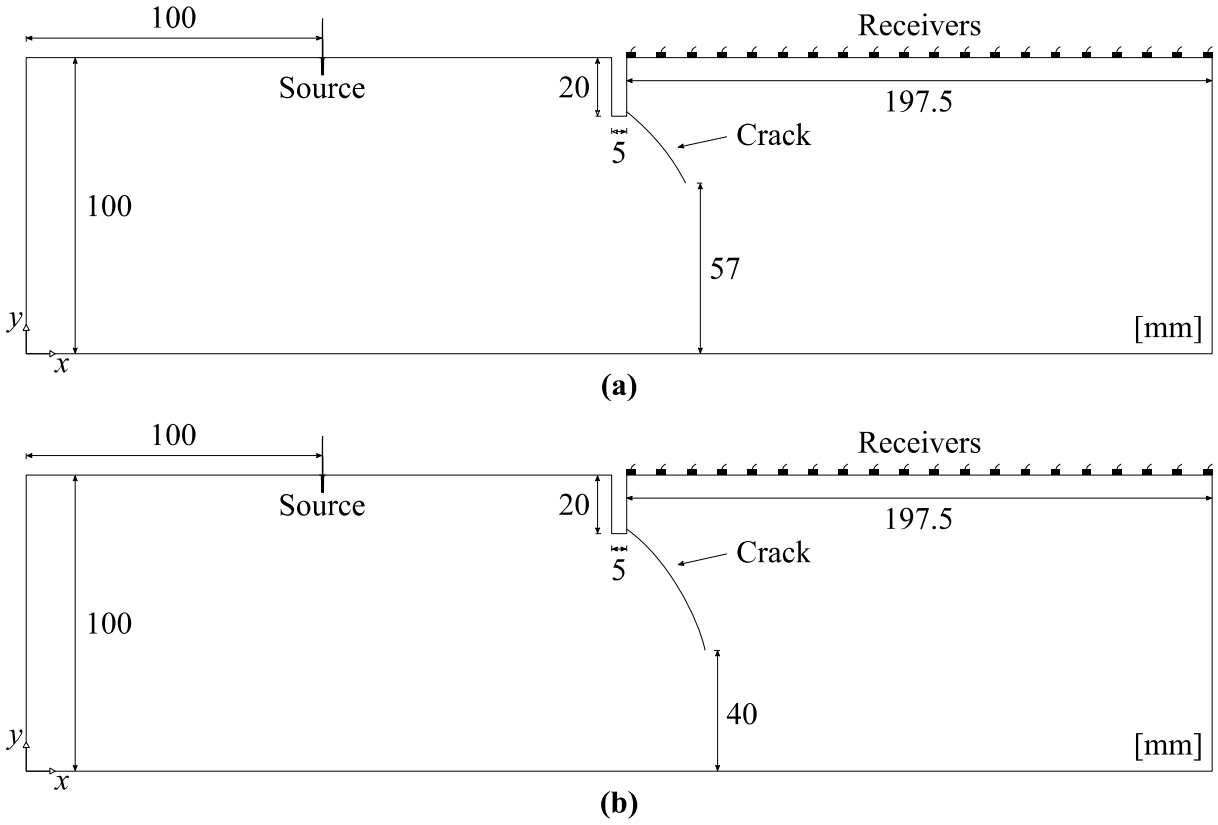

Figure 7.15 – Schematic representation of beam with crack tip at (a) 57 mm and (b) 40 mm above the bottom.

The analysis of this beam is carried out by two approaches: firstly, the beam is scanned on a surface with an emitter/receiver transducer (Pulse-Echo scanning) and then, only one source and the receivers (as indicated in Figure 7.14 and Figure 7.19) are positioned on a surface (Single Pulse-Echo).

7.2.1 Pulse-Echo scanning

In this approach, only a descriptive analysis of the phenomena involved is made. This analysis consists in scanning the upper surface of the beam with a transducer as previously done in section 7.1.1, where a pulse is emitted with a frequency of 200 kHz. Then, the distance ($t \times v$) travelled by the waves is plotted considering the P waves velocity ($v = 3845$ m/s). Figure 7.16

shows the evolution of wave propagation in the three crack stages: (a) uncracked notched beam and beam with crack tip at (b) 57 mm and (c) 40 mm above the bottom. In Figure 7.16 (a) it can be seen that, despite the small relative amplitude, the reading of the P wave (PP wave) in the receiver positioned at x = 0.1 m is translated by a distance of 0.2 m, perfectly corresponding to the sum of the distance travelled on the outward flight and the distance travelled on the return flight, which is twice the height of the beam. The same image shows, at same position (x = 0.1 m), the distances travelled by other "pure" waves, the S (S-S wave) and R (R-R wave) waves, and the distance travelled by combined waves which, due to their high relative amplitude, may have a negative impact on the identification the actual positioning of the crack. This is the case of P waves combined with S waves (P-S waves) and P waves combined with R waves (P-R waves). In Figure 7.16 (b) and Figure 7.16 (c), the presence of the crack is evident, both by the early reception of reflected wave to the right of the notch, and by the lack of reflections from the lower surface of the beam (see the lack of the reflected signal at the distance of 0.2 m just to the right of the notch). The shift to the right of the wave reflection is due to the effect already described and represented in the Figure 7.7.

Figure 7.17 shows the wave propagation when the right surface of the beam is scanned. Note that the plots are horizontally flipped because it is assumed that time (or, in this case, the distance) is easier to read when the timeline is represented from left to right. Unlike the previous figure, here the reading is more complex due to the multiple reflections at the upper and lower boundaries of the beam before the signal reaches the crack. Still, the presence of the crack is evident. It is verified, however, that the arrival of the corresponding reflection at the receiver is seen at a later time (distance). This is due to the wave taking a different direction when reflected by the crack and can be reflected multiple times at the edges of the beam until the signal returns to the receiver (see Figure 7.18). There is still, at an even later time ($t = 1.4 \times 10^4$ s, distance of 0.538 m), a large amount of energy that is trapped behind the crack and increases as the crack becomes larger.

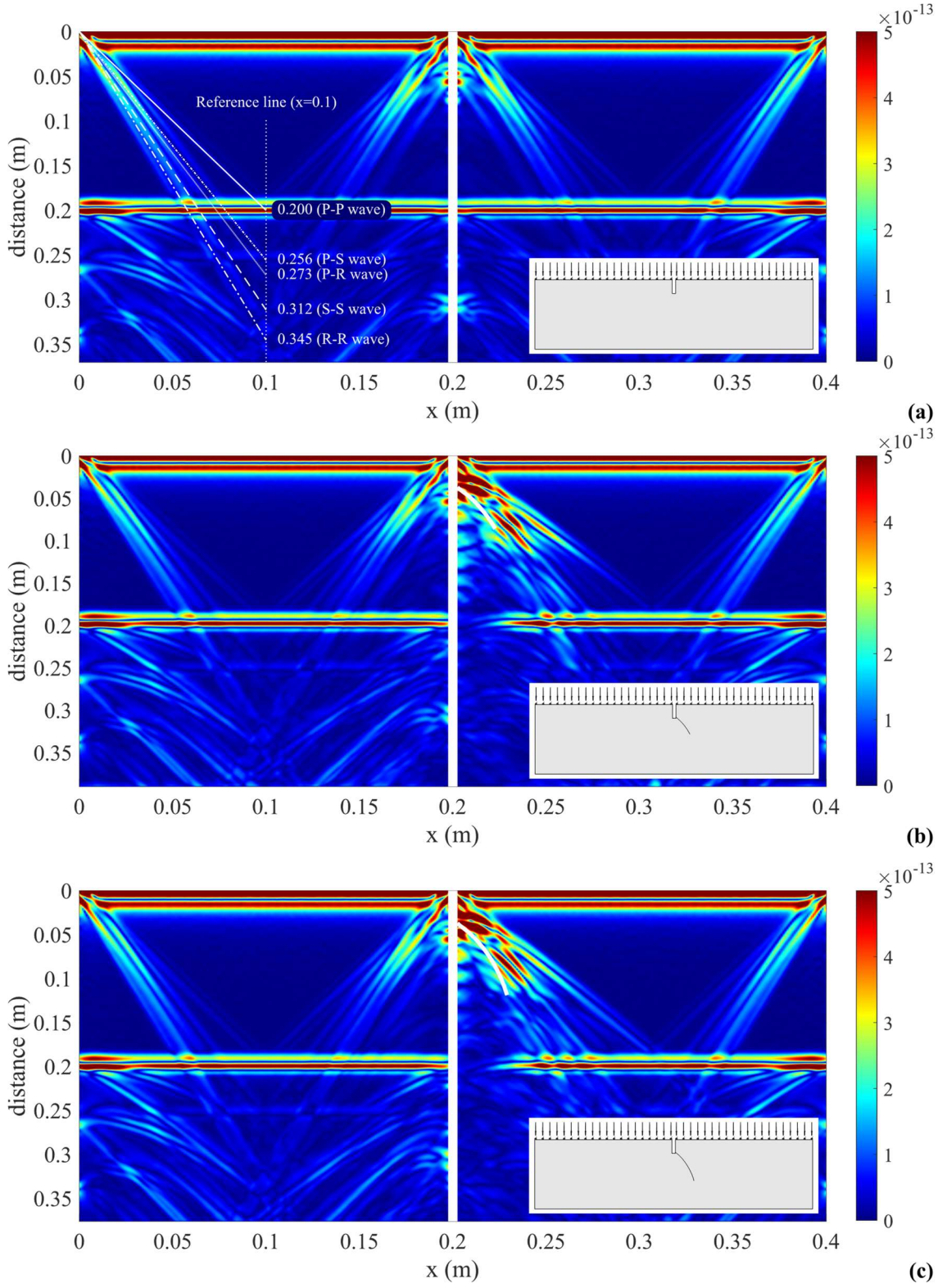

Figure 7.16 – Upper surface scan: (a) uncracked notched beam and beam with crack tip at (b) 57 mm and (c) 40 mm above the bottom.

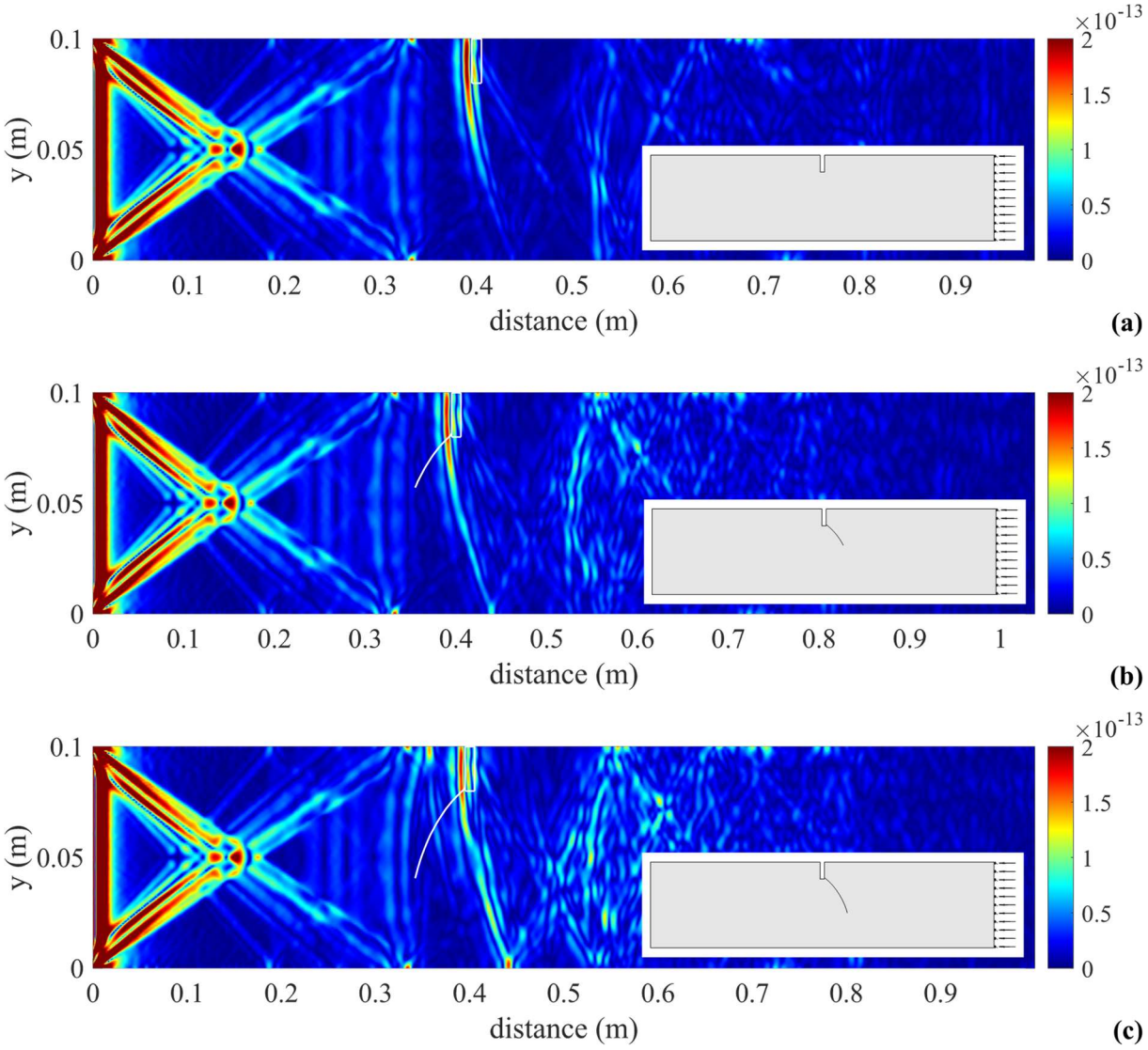

Figure 7.17 – Right surface scan: (a) uncracked notched beam and beam with crack tip at (b) 57 mm and (c) 40 mm above the bottom.

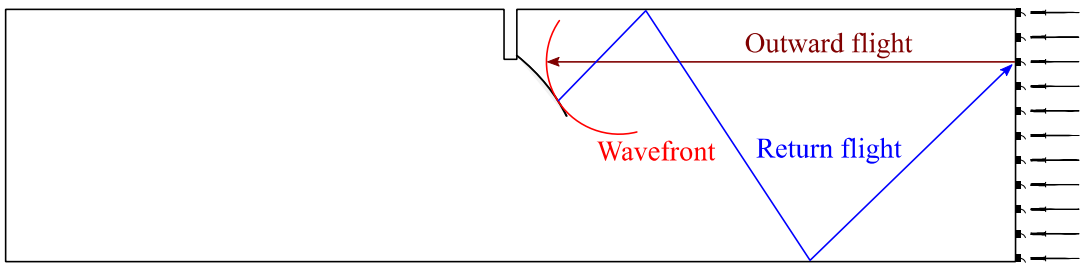

Figure 7.18 – Scheme of wave reflection in the cracked beam.

7.2.2 Single Pulse-Echo

In this second approach, the system is excited by a Ricker pulse whose source is located at $(100, 100)$ mm. The notch right side is the area of interest for ultrasound signal analysis. Therefore, the response is evaluated at a set of receivers placed along this area. For the reliability of the method, at least 8 mesh elements per wavelength are used to model the structural concrete beam.

For each of the proposed cracked beam geometries, a geometric ray analysis may be used to predict the most likely P-P and S-S wave paths for the earlier pulses reaching the receivers. In Figure 7.19 this geometrical analysis is schematically represented for the longer crack (tip at 40 mm from the bottom), considering two receiver positions, both placed to the right of the crack, at different distances along the x direction; the first is located half-way between the notch and the right end of the beam, A at $(300, 100)$ mm, and the second is located closer to the notch, at a quarter distance between the notch and the right end of the beam, B at $(250, 100)$ mm. For the first case, the expected first arrivals are originated by the diffraction of the incident wave by the crack tip, and by the back-wall echo effect at the bottom of the beam. These two paths are identified in the Figure 7.19 (a), respectively as Paths 1 and 2. When the receiver is positioned closer to the notch, the first arrival still corresponds to the pulse diffracted by the crack tip, but some changes occur for the second identified path. In this case, the propagation path is intercepted by the crack, and the diffraction by the crack tip also occurs after the reflection from the back-wall – see Figure 7.19 (b). It can be said that the receiver point is now shadowed by the presence of the crack, and the expected time of flight of this pulse should increase when compared to the uncracked configuration.

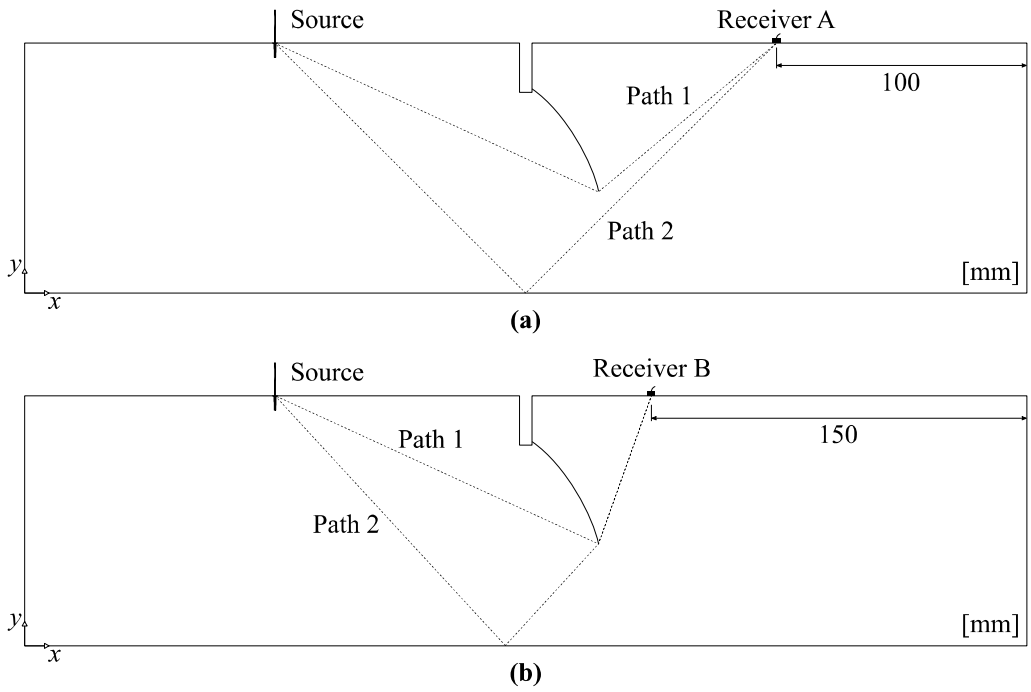

Figure 7.19 – Illustrative sketch of the waves paths.

The length of each path is defined in the Table 7.1.

Table 7.1 – Paths length.

Receiver	Path	Length [mm]
A	**1**	$142.037 + 92.496 = 234.533$
	2	$141.421 + 141.421 = 282.843$
B	**1**	$142.037 + 62.930 = 204.967$
	2	$135.709 + 55.180 + 62.930 = 253.819$

The wave propagation velocities considered for this case are $3844.8\ \mathrm{m/s}$ for P waves and $2467.2\ \mathrm{m/s}$ for S waves. Figure 7.20 illustrates the results computed for the propagating Ricker pulse with a central frequency of 100 kHz using damping factors of (a) 0.5 % and (b) 1 % while in Figure 7.21 the damping factors of (a) 2 % and (b) 5 % were used. The colour scale of the figures is intentionally different, so that the most significant pulses can be highlighted. The higher damping factor has an effect of cleaning the weaker pulses, transporting less energy, revealing the path of the most important pulses; in that case, as expected, later arrivals almost disappear, since their energy is progressively dissipated by the material damping.

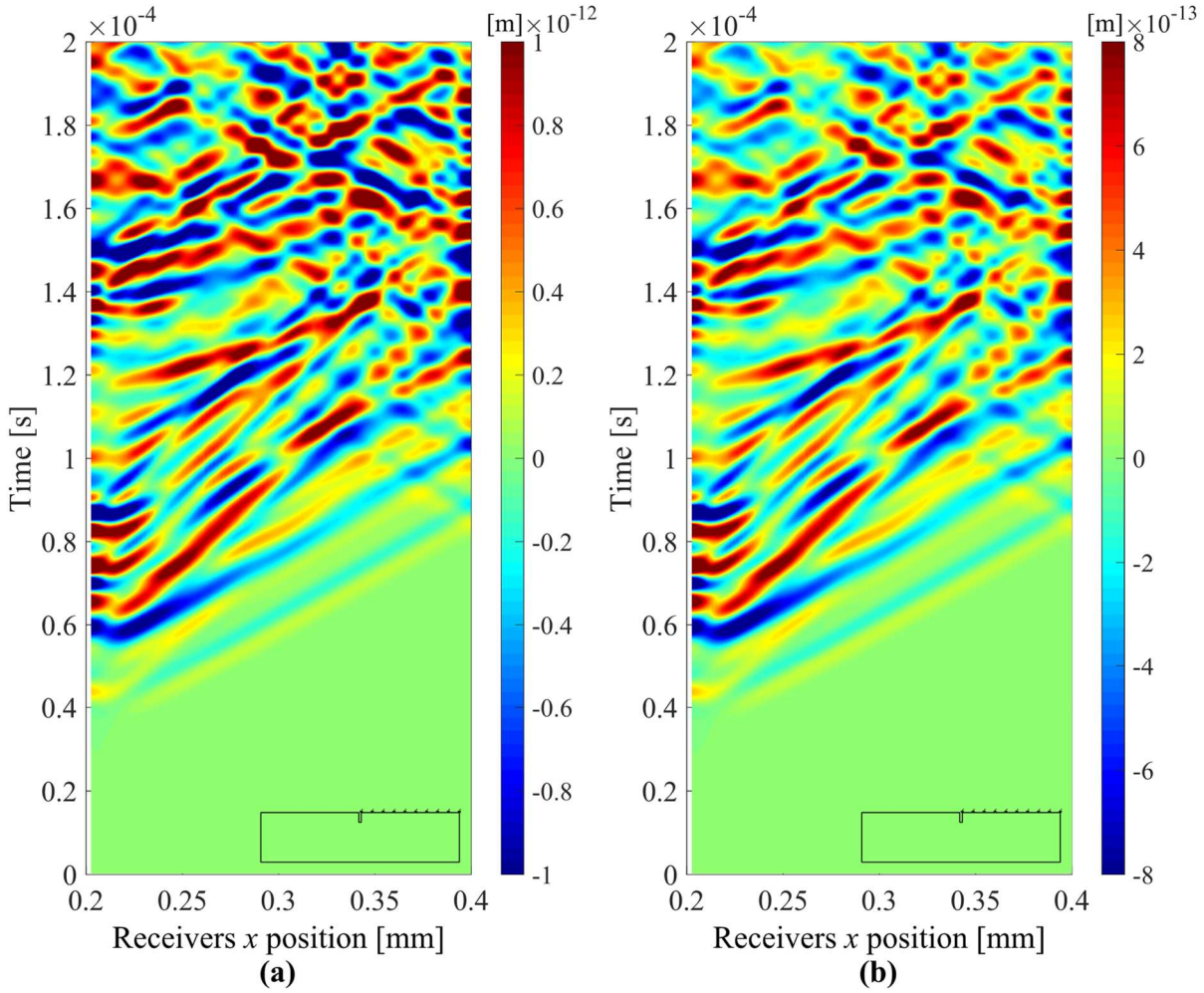

Figure 7.20 – Time responses determined for the receivers positioned at the top, for the uncracked beam using damping: (a) 0.5 % and (b) 1 %.

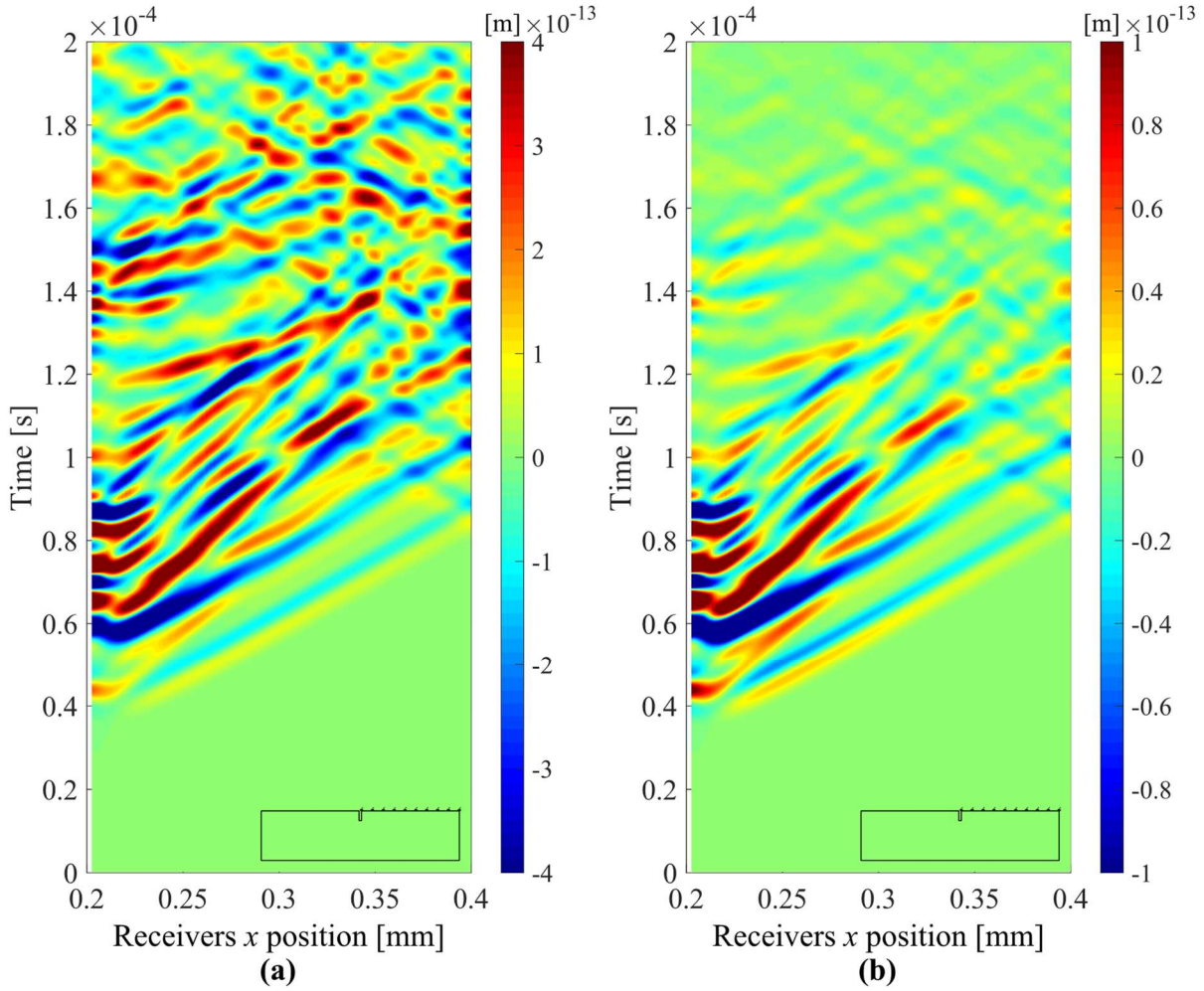

Figure 7.21 – Time responses determined for the receivers positioned at the top, for the uncracked beam using damping: (a) 2 % and (b) 5 %.

Figure 7.22 and Figure 7.23 show the time signals obtained for two different frequencies of the ultrasonic pulse: 100 kHz and 150 kHz, respectively. For this purpose, a damping factor of 2 % was used. For both frequencies, significant differences in the wave propagation pattern are registered for the two crack lengths with crack tips at (a) 57 mm and (b) 40 mm above the bottom. Comparing plots (a) and (b) it is verified that the arrival of the first wave to the receivers exposes relevant characteristics that can be used to infer the length of the crack. Indeed, this first arrival is generated by the diffraction effect at the crack tip (or at the bottom of the beam) as identified before, which tends to occur later as longer cracks are considered (see schematic representation in Figure 7.19). This variation in the arrival times is mostly visible at receivers placed closer to the notch (Receiver B). In addition, for longer cracks, this diffraction effect

originates a stronger deviation in the wave path and thus a lower amount of energy reaches the receivers; this effect is also clearly visible in plots (a) and (b).

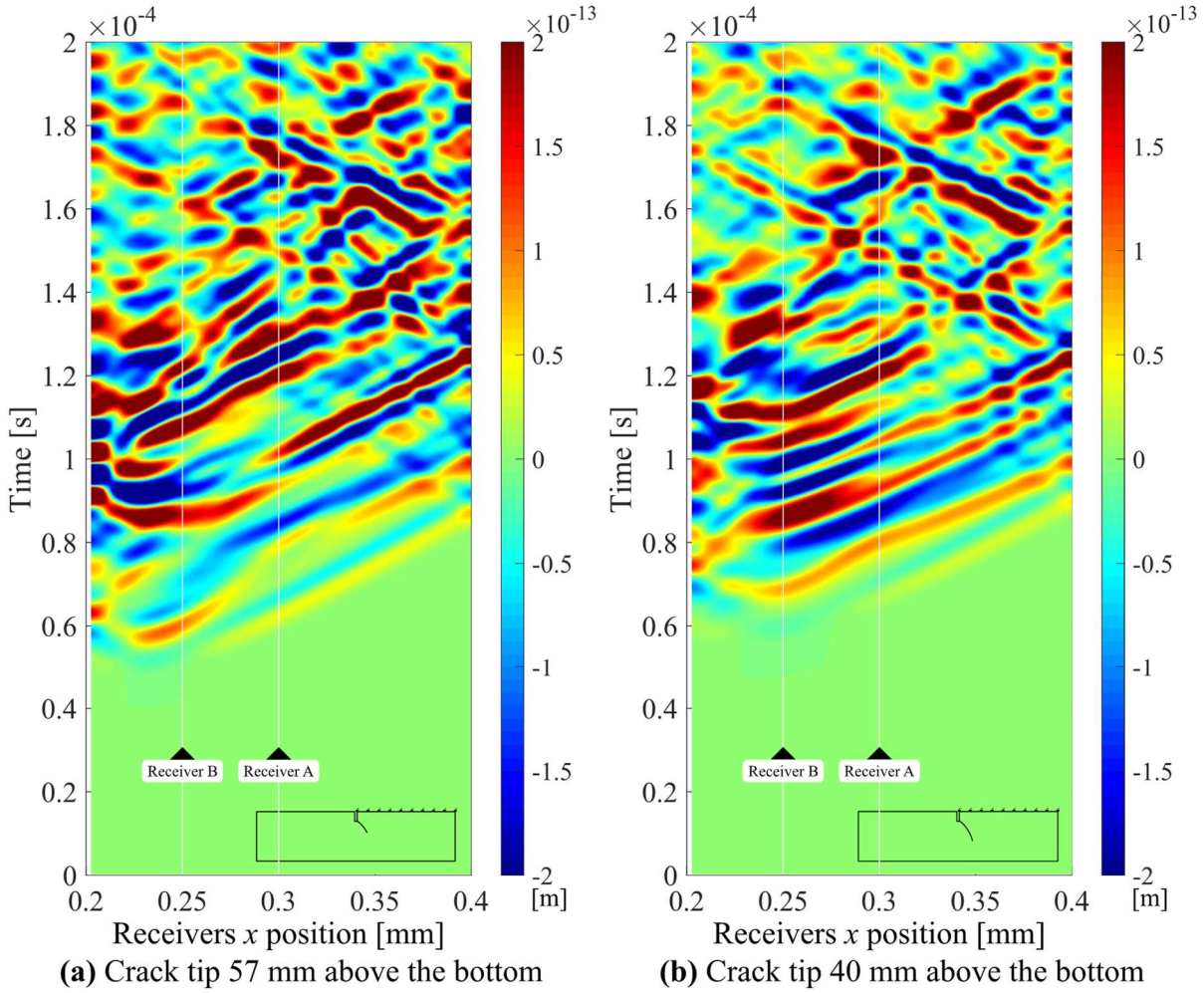

Figure 7.22 – Time responses for receivers at the top of the beam, for the cracked beam with crack tip at (a) 57 mm and (b) 40 mm above the bottom, for frequency of 100 kHz.

In Figure 7.23 (b) the computed times-of-flight using a geometrical ray analysis are identified for the two receivers (A and B) that will be later characterised in more detail. However, we can already make a descriptive and comparative analysis with Figure 7.22: for the frequency of 150 kHz, the pulses are thinner and easier to identify.

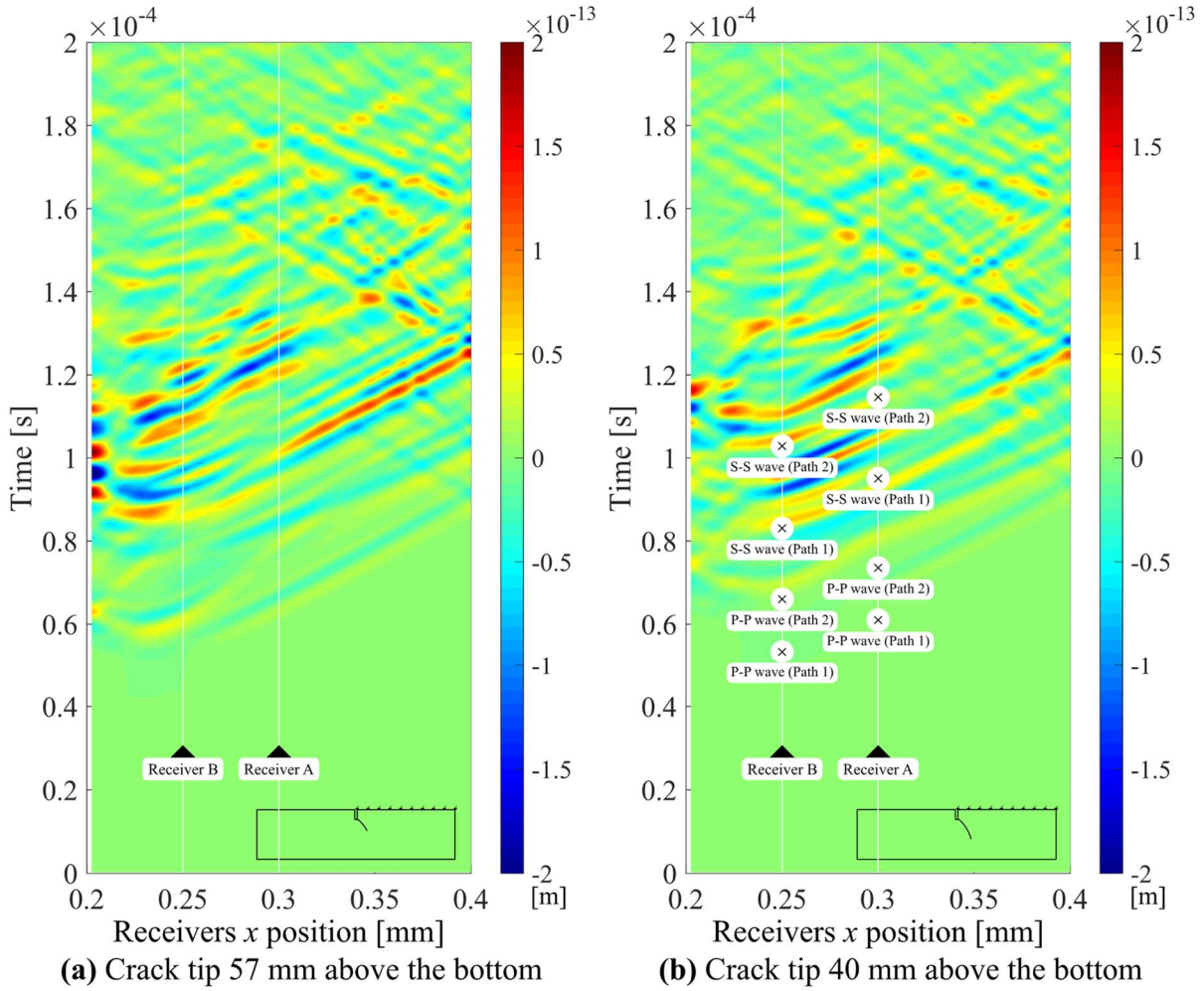

Figure 7.23 – Time responses for receivers at the top of the beam, for the cracked beam with crack tip at (a) 57 mm and (b) 40 mm above the bottom, for frequency of 150 kHz.

Figure 7.24 and Figure 7.25 show the time signals registered for all stages, uncracked and cracked beam, respectively: the first for the (a) perfect and (b) notched beam, and the second for the crack tip at (a) 57 mm and (b) 40 mm above the bottom. The source emitting the Ricker pulse with a frequency of 100 kHz, is located at the same location as before and the receivers are placed along the right-bottom edge of the beam: between (200 and 400) mm horizontal position. The damping factor is set to 2 %. It is observed that the arrival of the first wave is not influenced by the notch, nor by the two crack lengths defined in Figure 7.15. However, next to the notch x position the influence of the reflections of notch and crack is evident. In the lower right corner of the single beam there is a late concentration of energy resulting from the reflections at the boundaries of the beam, as shown in the upper right corner of Figure 7.24 (a).

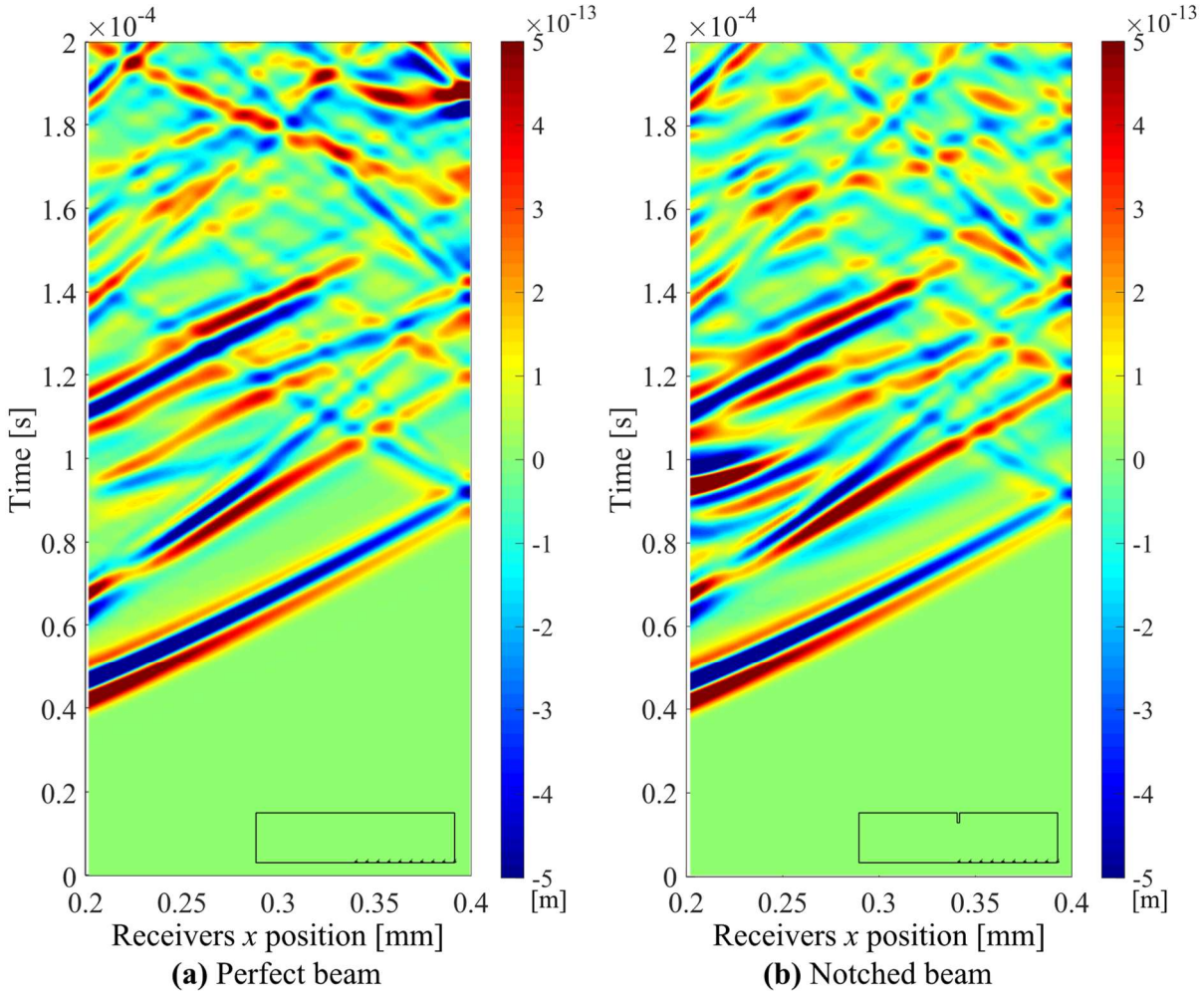

Figure 7.24 – Time responses for the receivers at the bottom of the uncracked beam: (a) perfect beam and (b) notched beam, for frequency of 100 kHz.

To have a more detailed insight of the presented results, analyses of the two individual receiver positions A and B, represented in Figure 7.19, are performed for the model with the longer crack path (crack tip at 40 mm above the bottom) by focusing on the expected arrival times of the earlier arriving pulses. For each receiver, it is possible to compute the time-of-flight (TOF) on the two paths, using a geometrical ray analysis (see Table 7.2). As expected, for each receiver and for each path, the first pulses are related to the P-P waves. Note that for receiver A, the crack does not interfere with Path 2.

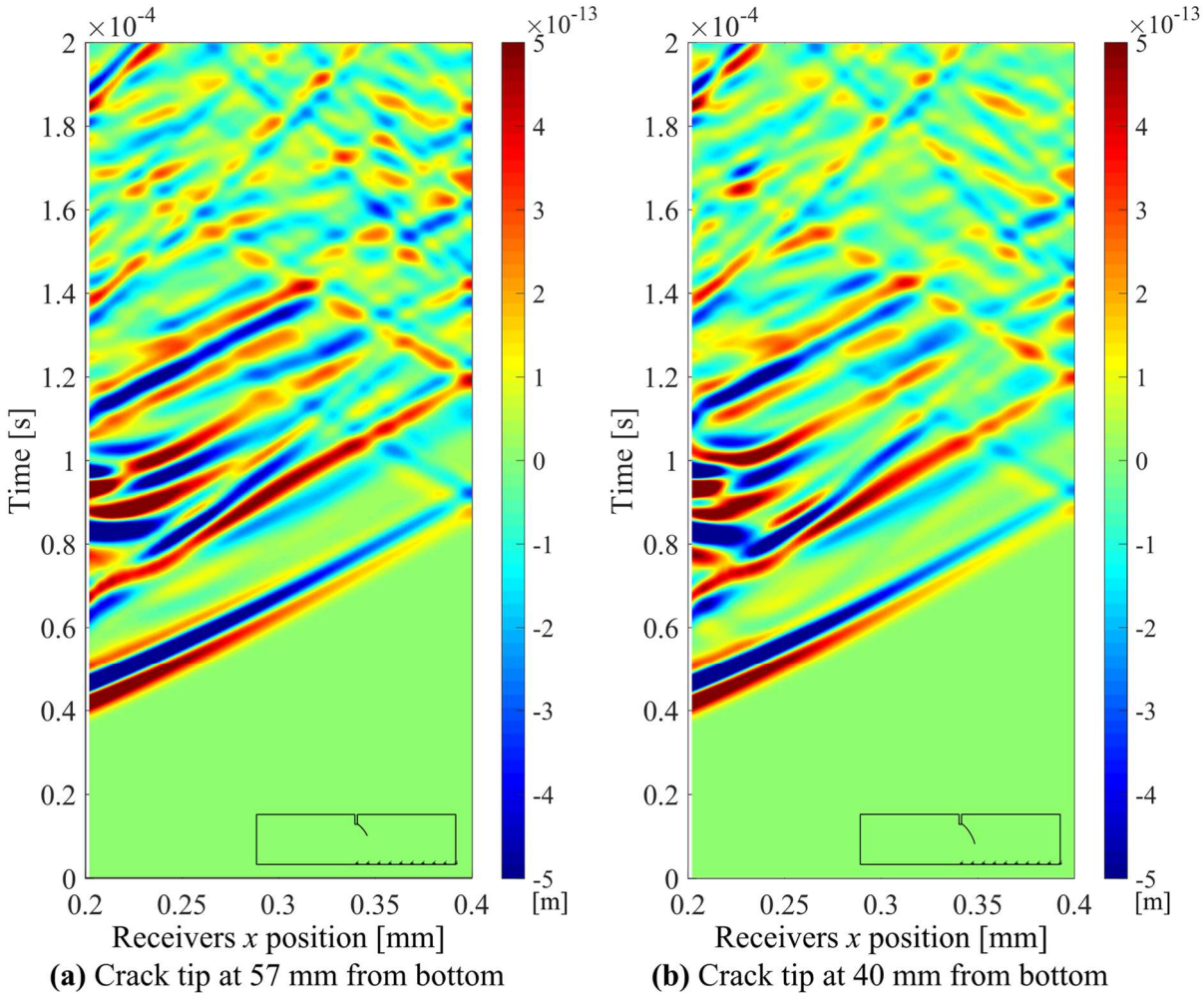

Figure 7.25 – Time responses for the receivers at the bottom of the cracked beam with crack tip at (a) 57 mm and (b) 40 mm above the bottom, for frequency of 100 kHz.

Table 7.2 – Time-of-flight to receivers A and B.

Time-of-flight [ms]	Receiver A		Receiver B	
	Path 1	Path 2	Path 1	Path 2
P-P waves	0.06100	0.07356	0.05331	0.06602
S-S waves	0.09506	0.11464	0.08308	0.10288

In Figure 7.26, two plots illustrate detailed views of the computed time responses (horizontal amplitudes) at the two receivers, (a) A and (b) B, for both cracked and uncracked beams, together with the estimated arrival times of the first two pulses induced by P-P and S-S waves, corresponding to Paths 1 and 2. The triangular marks depict the TOF estimated using

geometrical ray analysis. The presented results were computed for an ultrasonic frequency of 150 kHz (with a P wave wavelength of 25.6 mm and a S wave wavelength of 16.4 mm) and with a damping factor of 2 %.

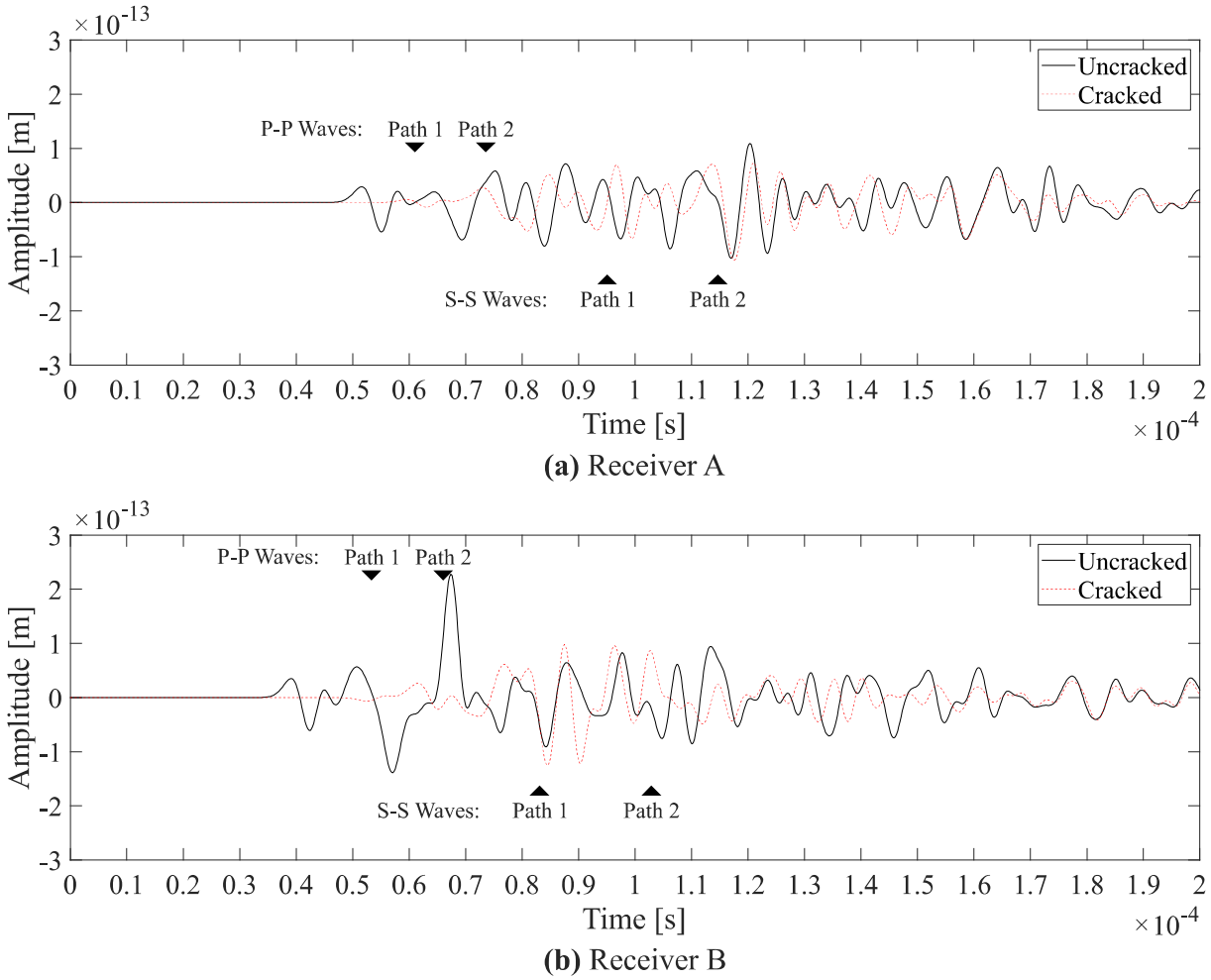

Figure 7.26 – Horizontal response computed at receivers (a) A and (b) B, for uncracked and cracked states, regarding a Ricker pulse with a central frequency of 150 kHz.

Observing the response computed for receiver A in Figure 7.26 (a), it is possible to identify the marked delay that occurs in the arrival times of the first pulse when the cracked beam is considered; this delay is directly related to the longer path that the P-P waves need to travel due to the presence of the crack. It may also be noted that the arrival time for this first pulse matches perfectly the predicted TOF presented above and identified with a triangular mark. As for the second arrival, the delay is much smaller and less noticeable, but a decrease of amplitude is

registered. Later, the arrival time of S-S waves through path 1 causes an increase in horizontal displacement amplitude which is again amplified by the arrival of the same type of waves coming from path 2. Again, the arrival times for these pulses match perfectly the estimated TOF. It is also noted that since Path 2 does not intercept the crack, the arrival time of the second pulse remains unchanged, and theses pulses appear almost overlapped at this receiver; it should be noted that there is not an exact match between the two curves at this point due to the influence of the many other energy paths connecting the source to the receiver. This is most noticeable in the arrival time of S-S waves.

The analysis of receiver B – Figure 7.26 (b) – shows similar features, with a very visible delay being registered for the first arrival of P-P waves. In the second arrival, the delay is much smaller and less noticeable. Indeed, since it now corresponds to a diffracted pulse, the energy of the pulse that travels along Path 2 is spread after reaching the crack tip, and thus the pulse is considerably attenuated. As before, the match between the TOF estimated using geometric ray analysis and the arrival times observed in the numerical response are excellent. After the analysis of the plotted results, it is possible to confirm that, for the studied configuration, the delay of the first arrival of P-P waves is the most relevant feature when trying to localise the presence and position of a possible embedded crack.

Figure 7.27 shows the vertical response in both receivers and, as before, the triangular marks depict the TOF estimated using geometrical ray analysis. By analysing vertical displacements, the same conclusions can be drawn.

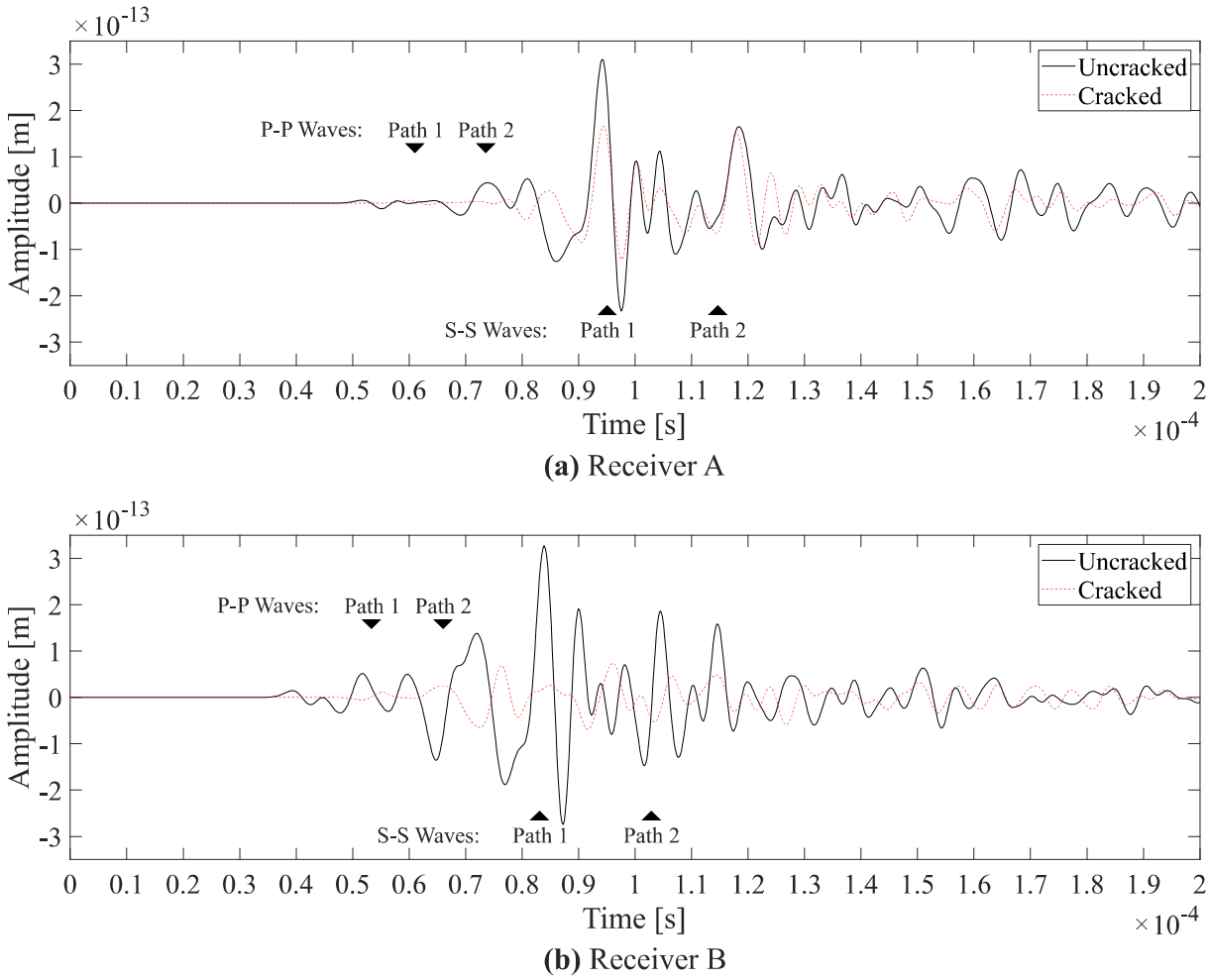

Figure 7.27 – Vertical response computed at receivers (a) A and (b) B, for uncracked and cracked states.

Given the described results, it may be stated that the P-P and S-S waves propagation patterns within the concrete beam are strongly influenced by the size of the crack, and that the responses registered at the receiver points may be of use for the evaluation of the damage within the beam. It is also important to note that concrete is, typically, a non-homogeneous material, and thus the propagation of high frequency waves may be significantly influenced by the small heterogeneities (e.g. aggregates, small voids, etc.). For this reason, it is common to make use of ultrasonic frequencies between 20 kHz and 150 kHz (International Atomic Energy Agency, 2002) for real sized concrete elements, or somewhat higher frequencies when small elements are to be analysed.

7.3 Conclusion

In this chapter the propagation of ultrasound waves was addressed as a means of detecting structural damage. The FEM-TD algorithm was used since it is the most suitable for the analysis of more complex geometries.

The preliminary 2D analysis allowed, without excessive computational effort, to reconstruct the propagation medium where the defect is clear. In this analysis, primary waves are used to measure distances and the time-of-flight in the concrete beam.

The preliminary 3D analysis shows that to have a good detection of the defect, both the source and the receiver must be well positioned in relation to the defect, otherwise it may not be detected. Also, the wavelength of the induced frequency must be significantly smaller than the size of the defect. In this case, limitations related to computational effort prevented from obtaining even better results in the detection of damage, since it was not possible to study higher frequencies.

From the analysis of a realistic beam structure, both through pulse-echo scanning and a single pulse-echo, it was concluded that the propagation pattern of P and S waves is strongly influenced by the size of the defect and that the response registered at the receivers may be used for the evaluation of the damage within a concrete beam. In both cases, but mainly in the case of the single pulse-echo, it is adequately demonstrated that the flight times computed using the numerical simulation coincide precisely with the flight times analytically computed. It was also demonstrated the possibility of studying P and S waves propagation patterns, making viable the evaluation of the integrity of the concrete, and the application of this type of analysis, in ultrasonic non-destructive techniques.

8 CLOSING REMARKS

The previous chapters have presented numerical simulations of elastic wave propagation in discontinuous media, namely applications in vibration control and ultrasonic crack detection. This chapter presents the contributions of the research to the field and the main conclusions in both application cases. Finally, some expected future developments are presented.

8.1 New contributions to the research field

This work contributed to the mitigation of vehicle-induced vibrations and expansion of knowledge in the area of damage detection in concrete structures. Both subjects are related to wave propagation in discontinuous media and its numerical simulation was carried out with the application of innovative models implemented for that purpose.

8.1.1 Mitigation of vehicle-induced vibrations

The technology associated with the concept of metamaterials has recently been applied in the field of acoustics, namely by its ability to interfere with wave propagation in a controlled and tuned manner, mitigating noises in a specific band, thus acting as an acoustic barrier for a given wave. The challenge of this work was to study the effect of buried barriers consisting of periodic arrangements of simple elements, forming large-scale crystalline patterns, in the protection of structures against traffic-induced vibrations. Geometry, arrangement and material properties were investigated. Comparisons with currently used devices were made to confirm the efficiency of the proposed phononic devices.

8.1.2 Damage detection

The damage detection in concrete structures was another subject addressed in this thesis. This work investigated P, S and surface waves whose pattern of propagation is more complex than the SH waves that are usually used for this purpose. The recognition of those patterns and the

comparison with the time-of-flight of the different waves, analytically computed, allowed determining the feasibility of their use in ultrasonic non-destructive techniques.

8.1.3 Numerical simulation tools

Two efficient algorithms for wave propagation were implemented: the method of fundamental solutions in the frequency domain for simple 2D and 2.5D geometries, and the finite element method in the time domain based on an innovative time march for complex 2D and 3D geometries. In other words, the MFS was used only to simulate the waves propagation in a semi-infinite medium with inclusions, to mitigate vibrations; while the FEM was used to simulate the propagation of waves in both finite and semi-infinite media. In the latter case, an absorbent layer was developed with the function of dissipating spurious reflections of the geometric model bounds that represent the infinite part of the modelled medium. Both versions of the algorithms have been validated and have proven to be efficient and accurate.

8.2 Main conclusions

The propagation of elastic waves has been studied since the first half of the nineteenth century. Currently, in civil engineering, the propagation of mechanical waves in elastic media is a relevant matter in research projects. The mitigation of seismic effects and vehicle-induced vibrations and the detection of discontinuities in concrete elements are the points of most interest. This thesis dealt with two distinct points: the mitigation of vehicle-induced vibrations, more specifically, railway vehicles, and the detection of damage in concrete structures.

For the case of vibration mitigation, the proposed phononic barriers have a significant effect on vibration levels reduction, mainly in the downstream zone. As a group of inclusions with the same characteristics, these barriers are only efficient in a certain frequency range. By changing some crystalline parameters, such as the distance between inclusions, their geometry, or their distribution within the phononic crystal, it is possible to move, reduce or enlarge the frequency range for which the barrier is most efficient. An optimal and tuned system depends widely on the properties of the host medium, the properties of the inclusions and the frequency band to be

mitigated. Each configuration has its efficiency zone very much enhanced in the band gap frequency range. In this work, a soft soil was used as the reference soil. In this sense, the performance of the phononic crystals discussed here are directly associated with this type of scenario.

A general MFS strategy, in frequency domain, was implemented to allow the analysis of wave propagation in the presence of buried inclusions in a half-space. The proposed strategy allows the simulation of any number of horizontally inclusions filled with distinct materials. 2D and 2.5D application examples were presented, which evidence the stability and convergence of solutions. The accuracy of the MFS is quite good, particularly when compared with BEM results.

To study vertical inclusions, a 3D FEM model in the time domain was developed in which the time integration was based on an innovative time-marching algorithm. In this case, an absorbent layer was developed to dissipating spurious reflections of the geometric model bounds that represent the infinite part of the modelled medium. This time-marching 3D finite element model allows to carry out the studies in a more efficient manner, providing accurate results and a reduced computational effort.

The FEM model in the time domain was also used for numerically simulating the process of crack detection in concrete elements using (P and S) waves based on ultrasound methods. An application example was presented, which allows to conclude that cracks can be identified by the propagation of (P and S) waves. The presented results also compared the effects of cracks of different lengths – i.e. corresponding to increasing damaged states – in the time signals registered at receiver points over the structure surface. Results are promising and confirm the feasibility of using (P and S) waves based ultrasonic equipment for on-site applications in the future.

8.3 Publications

As result of this thesis, several communications have been presented at national and international conferences. Furthermore, several papers have been published in international journals.

8.3.1 Conference communications

Carlos Albino, Luís Godinho, Daniel Dias-da-Costa, Paulo Amado-Mendes. "Numerical analysis of buried vibration protection devices using the MFS". Boundary Elements and other Mesh Reduction Methods XLII. WIT Press. Southampton. 2019. ISBN: 978-1-78466-341-4. Pp 225-236.

Luís Godinho, Carlos Albino, Pedro Alves-Costa, Paulo Amado-Mendes, Alexandre Castanheira-Pinto, Delfim Soares Jr. "A numerical study on the shielding performance of a periodic vibration protection device". International Conference on Noise and Vibration Engineering (ISMA 2018) and International Conference on Uncertainty in Structural Dynamics (USD 2018). Curran Associates, Inc. Conference Proceedings. Morehouse Lane. 2019. ISBN: 9781510876781.

Carlos Albino, Luís Godinho, Pedro Alves-Costa, Paulo Amado-Mendes. "Effect of buried phononic crystal barriers in stratified medium". 49th Spanish Congress on Acoustics (TECNIACUSTICA 2018). Cádiz. 24 to 26 October 2018. Pp 1033-1040. ISBN: 978-84-87985-30-4.

Paulo Amado-Mendes, Luís Godinho, Pedro Alves-Costa, Alexandre Castanheira-Pinto, Carlos Albino. "Numerical analysis of the shielding effect provided by periodic elastic scatterers". VETOMAC XIV. MATEC Web of Conferences. 2018, 211, 13005. DOI: https://doi.org/10.1051/matecconf/201821113005.

Luís Godinho, Carlos Albino, Pedro Alves-Costa, Paulo Amado-Mendes, Alexandre Pinto, Delfim Soares Jr. "Numerical study of a buried periodic device for vibration protection". 11th

European Congress and Exposition on Noise Control Engineering (EURONOISE 2018), Heraklion, Crete, Greece, 27-31 May 2018.

Carlos Albino, Luís Godinho, Daniel Dias-da-Costa and Delfim Soares Jr. "Ultrasonic wave propagation simulation to detect cracks in concrete structures using FEM". 48th Spanish Congress on Acoustics (TECNIACUSTICA 2017), A Coruña, 3 to 6 October 2017. Pp 1023-1031. ISBN: 978-84-87985-29-4.

Carlos Albino, Luís Godinho, Daniel Dias-da-Costa and Paulo Amado-Mendes. "The MFS as a tool for the numerical analysis of vibration protection devices". 22nd International Congress on Acoustics (ICA 2016). Buenos Aires, 5 to 9 September 2016.

8.3.2 International journal papers

Carlos Albino, Luís Godinho, Paulo Amado-Mendes, Pedro Alves-Costa, Daniel Dias-da-Costa, Delfim Soares Jr. "3D FEM analysis of the effect of buried phononic crystal barriers on vibration mitigation". Engineering Structures, 196, 2019 109340, 2019. DOI: https://doi.org/10.1016/j.engstruct.2019.109340.

Luís Godinho, Paulo Amado-Mendes, Pedro Alves-Costa, Carlos Albino. "MFS Analysis of the Vibration Filtering Effect of Periodic Structures in Elastic Media". International Journal of Computational Methods and Experimental Measurements, Vol.6, Issue 6 (2018), Pp 1108-1119. DOI:10.2495/CMEM-V6-N6-1108-1119.

8.4 Future developments

Regarding mitigation of vibrations induced by rail traffic through crystalline phononic devices, the following topics could be selected:

- It is true that the material properties of buried inclusions affect the propagation of waves in the host medium. The use of inclusions with different materials within the same

phononic crystal should be investigated to study its efficiency and the band gap frequency range.

- The efficiency of inclusions with different sections or of more compact solids (such as spheres or cubes) in the constitution of the phononic crystal is a theme that must be investigated.

- The use of metamaterials is having anti-noise application in different engineering fields. The same concept can be applied in the mitigation of vibrations, mainly in a certain range of frequencies. Thus, at the inclusion scale, the influence of the use of metamaterials should be investigated.

- The mitigating devices are made up of inclusions capable of filtering the mechanical waves. At the same time, the energy from these waves can be stored or converted to electrical energy. Currently, the paradigm related to sustainable energy production and harvesting is on the table, being this a topic of great relevance.

- For the implementation of such mitigation system, many variables have to be taken into account: the characteristics of the vehicle's circulation path, the distance between it and the sensitive object, the characteristics of the propagation medium, among others. As seen in the development of this work, the characteristics of mitigating devices can also be diverse, depending on the geometry of the section, distance between individual objects, material properties, etc. For these reasons, a solution for a specific case, results in a complex study of multiple variables. The development of an optimisation algorithm would be a great help to quickly reach a specific solution.

REFERENCES

Alagoz, B., and Alagoz, S. (2011). Towards earthquake shields: a numerical investigation of earthquake shielding with seismic crystals. *Open Journal of Acoustics*, *1*, 63–69.

Alves-Costa, P., Calçada, R. A. B., and Cardoso, A. S. (2012a). Ballast mats for the reduction of railway traffic vibrations. Numerical study. *Soil Dynamics and Earthquake Engineering*, *42*, 137–150. https://doi.org/https://doi.org/10.1016/j.soildyn.2012.06.014

Alves-Costa, P., Calçada, R. A. B., and Cardoso, A. S. (2012b). Influence of train dynamic modelling strategy on the prediction of track–ground vibrations induced by railway traffic. *Proceedings of the Institution of Mechanical Engineers, Part F: Journal of Rail and Rapid Transit*, *226*(4), 434–450. https://doi.org/10.1177/0954409711433686

Amado-Mendes, P., Alves-Costa, P., Godinho, L. M. C., and Lopes, P. A. (2015). 2.5D MFS–FEM model for the prediction of vibrations due to underground railway traffic. *Engineering Structures*, *104*, 141–154. https://doi.org/https://doi.org/10.1016/j.engstruct.2015.09.013

Amado-Mendes, P., and Godinho, L. M. C. (2013). Reduction of vibrations transmitted through the soil by multiple buried inclusions – numerical analysis. In Z. Dimitrovová, B. A, D. C, F. E, & H. G (Eds.), *11th International Conference on Vibration Problems*.

Amado-Mendes, P., Godinho, L. M. C., Santos, P. G., Dias, A. G., and Martins, M. (2016). Laboratory and full-scale experimental evaluation of the acoustic behaviour of sonic crystal noise barriers. *Phononic Crystals and Acoustic Metamaterials*.

Anderson, D. (2000). *Isolation of buildings from railway vibration: a case study*. Arup Acoustics.

Ang, W.-T. (2007). *A beginner's course in boundary element methods*. Universal Publishers.

APC International Ltd. (2015). *History of the development of ultrasound technology*. Piezo Applications. https://www.americanpiezo.com/blog/history-of-ultrasound-technology/

Argyris, J. H., Kelsey, S., and Kamel, H. (1964). *Matrix methods of structural analysis: a précis of recent developments* (Veubeke, B). Pergamon Press.

Barbosa, J. M. de O., Alves-Costa, P., and Calçada, R. A. B. (2015). Abatement of railway induced vibrations: numerical comparison of trench solutions. *Engineering Analysis with Boundary Elements*, *55*, 122–139. https://doi.org/https://doi.org/10.1016/j.enganabound.2014.11.029

Barros, R. M. de. (1996). *Elementos infinitos para tratamento de problemas da viscoelastodinâmica estacionária pelo método dos elementos finitos*. Universidade Estadual de Campinas.

Bathe, K.-J. (2014). *Finite element procedures* (2nd ed.). Klaus-Jurgen Bathe.

Bedford, A., and Drumheller, D. S. (1996). *Introduction to elastic wave propagation* (1st ed.).

Wiley.

Bongini, E., Lombaert, G., François, S., and Degrande, G. (2011). A parametric study of the impact of mitigation measures on ground borne vibration due to railway traffic. In G. De Roeck, G. Degrande, G. Lombaert, & G. Müller (Eds.), *EURODYN 2011* (pp. 663–670).

Bordón, J. D. R., Hoorickx, C. Van, Aznárez, J. J., Schevenels, M., Maeso, O. F., and Lombaert, G. (2018). Shape optimized inclined single and double wall wave barriers for ground vibration mitigation. *Soil Dynamics and Earthquake Engineering*, *112*, 215–231. https://doi.org/https://doi.org/10.1016/j.soildyn.2018.04.035

Brebbia, C. A., and Dominguez, J. (1977). Boundary element methods for potential problems. *Applied Mathematical Modelling*, *1*, 372–378. https://doi.org/http://dx.doi.org/10.1016/0307-904X(77)90046-4

Brûlé, S., Javelaud, E. H., Enoch, S., and Guenneau, S. (2014). Experiments on seismic metamaterials: molding surface waves. *Physical Review Letters*, *112*, 133901.

BSW-Berleburger. (2014). *Vibration isolation of buildings*. http://www.diemme.co.rs/wp-content/uploads/2011/02/Brochure-3.2-Vibration-Isolation-Buildings.pdf

Capineri, L., Tattersall, H. G., Silk, M. G., and Temple, J. A. G. (1992). Time-of-flight diffraction tomography for NDT applications. *Ultrasonics*, *30*, 275–288. https://doi.org/http:// dx.doi.org/10.1016/0041-624x(92)90001-3

Castanheira-Pinto, A., Alves-Costa, P., Godinho, L. M. C., and Amado-Mendes, P. (2018). On the application of continuous buried periodic inclusions on the filtering of traffic vibrations: a numerical study. *Soil Dynamics and Earthquake Engineering*, *113*, 391–405. https://doi.org/https://doi.org/10.1016/j.soildyn.2018.06.020

Castanheira-Pinto, A., Alves-Costa, P., Godinho, L. M. C., and Amado-Mendes, P. (2017). Mitigation of vibrations induced by railway traffic though soil burried inclusions: a numerical study. In A. Calvo-Manzano & A. Pérez-López (Eds.), *48º Congresso Español de Acústica (TECNIACÚSTICA 2017)* (pp. 1078–1086).

Chakraborty, J., Katunin, A., Klikowicz, P., and Salamak, M. (2019). Early crack detection of reinforced concrete structure using embedded sensors. *Sensors*, *19*(18). https://doi.org/10.3390/s19183879

Cheron, C., Walter, M., Sandor, J., and Wiebe, E. (2012). ERRAC Roadmap. Towards 2030: Energy, Noise and Vibration European Railway Roadmaps. *Procedia - Social and Behavioral Sciences*, *48*, 2221–2229. https://doi.org/https://doi.org/10.1016/j.sbspro.2012.06.1195

Colaço, A., Alves-Costa, P., Amado-Mendes, P., Godinho, L. M. C., and Calçada, R. (2017). Mitigation of vibrations and re-radiated noise in buildings generated by railway traffic: a parametric study. *Procedia Engineering*, *199*, 2627–2632. https://doi.org/https://doi.org/10.1016/j.proeng.2017.09.401

Colaço, A., Alves-Costa, P., and Connolly, D. P. (2016). The influence of train properties on railway ground vibrations. *Structure and Infrastructure Engineering*, *12*(5), 517–534. https://doi.org/10.1080/15732479.2015.1025291

Coulier, P., Cúellar, V., Degrande, G., and Lombaert, G. (2015). *Experimental and numerical evaluation of the efficiency of a stiff wave barrier in the soil*. 49–65. https://doi.org/10.7712/120115.3380.765

Coulier, P., Dijckmans, A., Cuéllar, V., Ekblad, A., Smekal, A., Degrande, G., and Lombaert, G. (2014). *Numerical and experimental study of stiff wave barriers for the mitigation of railway induced vibrations*.

Coulier, P., François, S., Degrande, G., and Lombaert, G. (2013). Subgrade stiffening next to the track as a wave impeding barrier for railway induced vibrations. *Soil Dynamics and Earthquake Engineering*, *48*, 119–131. https://doi.org/https://doi.org/10.1016/j.soildyn.2012.12.009

Coulier, P., and Hunt, H. E. M. (2014). Experimental study of a stiff wave barrier in gelatine. *Soil Dynamics and Earthquake Engineering*, *66*, 459–463. https://doi.org/https://doi.org/10.1016/j.soildyn.2014.08.011

Croy, I., Smith, M. G., and Waye, K. P. (2013). Effects of train noise and vibration on human heart rate during sleep: an experimental study. *BMJ Open*. https://doi.org/10.1136/bmjopen-2013-002655

D'Amato, M., Gigliotti, R., and Laguardia, R. (2019). Seismic isolation for protecting historical buildings: a case study. *Frontiers in Built Environment*, *5*, 87. https://doi.org/10.3389/fbuil.2019.00087

Dertimanis, V. K., Antoniadis, I. A., and Chatzi, E. N. (2016). Feasibility analysis on the attenuation of strong ground motions using finite periodic lattices of mass-in-mass barriers. *Journal of Engineering Mechanics*, *142*, 4016060.

Di Matteo, A., Masnata, C., and Pirrotta, A. (2019). Hybrid passive control strategies for reducing the displacements at the base of seismic isolated structures. *Frontiers in Built Environment*, *5*, 132. https://doi.org/10.3389/fbuil.2019.00132

Dias-da-Costa, D., Valença, J., Júlio, E., and Araújo, H. J. (2016). Crack propagation monitoring using an image deformation approach. *Structural Control and Health Monitoring*. https://doi.org/10.1002/stc.1973

Dihoru, L., Alexander, N., Taylor, C., Grumbar, H., and Newton, E. (2009). *A neural network approach for detection of damage in a vibrating beam* (Vol. 1504). https://doi.org/10.1063/1.4772143

Dijckmans, A., Coulier, P., Jiang, J., Toward, M. G. R., Thompson, D. J., Degrande, G., and Lombaert, G. (2015). Mitigation of railway induced ground vibration by heavy masses next to the track. *Soil Dynamics and Earthquake Engineering*, *75*, 158–170. https://doi.org/https://doi.org/10.1016/j.soildyn.2015.04.003

Dijckmans, A., Ekblad, A., Smekal, A., Degrande, G., and Lombaert, G. (2016). Efficacy of a sheet pile wall as a wave barrier for railway induced ground vibration. *Soil Dynamics and Earthquake Engineering*, *84*, 55–69. https://doi.org/https://doi.org/10.1016/j.soildyn.2016.02.001

dos Santos, N. C., Barbosa, J. M. de O., Calçada, R. A. B., and Delgado, R. M. (2017). Track-

ground vibrations induced by railway traffic: experimental validation of a 3D numerical model. *Soil Dynamics and Earthquake Engineering*, *97*, 324–344. https://doi.org/https://doi.org/10.1016/j.soildyn.2017.03.004

dos Santos, N. C., Colaço, A., Alves-Costa, P., and Calçada, R. A. B. (2016). Experimental analysis of track-ground vibrations on a stretch of the Portuguese railway network. *Soil Dynamics and Earthquake Engineering*, *90*, 358–380. https://doi.org/https://doi.org/10.1016/j.soildyn.2016.09.003

Drozdz, M. B. (2008). *Efficient finite element modelling of ultrasound waves in elastic media*. University of London.

European Commission. (2011). *White Paper: Roadmap to a Single European Transport Area – Towards a competitive and resource efficient transport system*.

European Commission. (2016). *The implementation of the 2011 White Paper on Transport «Roadmap to a Single European Transport Area – towards a competitive and resource-efficient transport system» five years after its publication: achievements and challenges*.

Fard, S. M. B., Kessissoglou, N., and Peters, H. (2015). Locally resonant sonic crystal barrier for low frequency noise control. *Acoustics 2015 Hunter Valley*.

Feng, S.-J., Zhang, X.-L., Zheng, Q.-T., and Wang, L. (2017). Simulation and mitigation analysis of ground vibrations induced by high-speed train with three dimensional FEM. *Soil Dynamics and Earthquake Engineering*, *94*, 204–214. https://doi.org/https://doi.org/10.1016/j.soildyn.2017.01.022

Fontara, I.-K., Schepers, W., Savidis, S., and Rackwitz, F. (2018). Finite element implementation of efficient absorbing layers for time harmonic elastodynamics of unbounded domains. *Soil Dynamics and Earthquake Engineering*, *114*, 625–638. https://doi.org/https://doi.org/10.1016/j.soildyn.2018.06.026

Fries, T.-P., and Matthies, H.-G. (2004). *Classification and overview of meshfree methods*. Institute of Scientific Computing, Technical University Braunschweig.

Galantucci, R. A., and Fatiguso, F. (2019). Advanced damage detection techniques in historical buildings using digital photogrammetry and 3D surface anlysis. *Journal of Cultural Heritage*, *36*, 51–62. https://doi.org/https://doi.org/10.1016/j.culher.2018.09.014

Germonpré, M., Degrande, G., and Lombaert, G. (2017). A track model for the prediction of ground-borne vibrations due to parametric excitation. *Procedia Engineering*, *199*, 2663–2668. https://doi.org/https://doi.org/10.1016/j.proeng.2017.09.538

Godinho, L. M. C., Amado-Mendes, P., Pereira, A., and Soares Jr., D. (2013). A coupled MFS–FEM model for 2-D dynamic soil–structure interaction in the frequency domain. *Computers & Structures*, *129*, 74–85. https://doi.org/http://dx.doi.org/10.1016/j.compstruc.2013.08.010

Godinho, L. M. C., Amado-Mendes, P., and Tadeu, A. J. B. (2015). Meshless analysis of soil–structure interaction using an MFS–MLPG coupled approach. *Engineering Analysis with Boundary Elements*, *55*, 80–92. https://doi.org/http://dx.doi.org/10.1016/j.enganabound.2014.10.016

Godinho, L. M. C., Costa, E. G. A., Pereira, A. S. C., and Santiago, J. A. F. (2012). Some observations on the behavior of the method of fundamental solutions in 3D acoustic problems. *International Journal of Computational Methods*, *09*(04), 1250049. https://doi.org/10.1142/S0219876212500491

Godinho, L. M. C., Dias-da-Costa, D., Areias, P., Júlio, E., and Soares Jr., D. (2013). Numerical study towards the use of a SH wave ultrasonic-based strategy for crack detection in concrete structures. *Engineering Structures*, *49*, 782–791. https://doi.org/http://dx.doi.org/10.1016/j.engstruct.2012.12.019

Godinho, L. M. C., Soares Jr., D., and Santos, P. G. (2015). An ACA-MFS approach for the analysis of sound propagation in sonic crystals. *Boundary Elements and Other Mesh Reduction Methods XXXVIII*, 23–34. https://doi.org/10.2495/BEM380021

Godinho, L. M. C., and Tadeu, A. J. B. (2002). The importance of a small wall deformation in the three-dimensional acoustic logging results. *Geophysical Journal International*, *151*(2), 403–415. https://doi.org/10.1046/j.1365-246X.2002.01792.x

Gomes, J. P. de C., Oliveira, L. A. P. de, Lanzinha, J. C. G., and Almeida, M. S. F. D. (2014). *Técnicas de inspecção e avaliação de estruturas de betão*.

Goszczyńska, B., Świt, G., Trąmpczyński, W., Krampikowska, A., Tworzewska, J., and Tworzewski, P. (2012). Experimental validation of concrete crack identification and location with acoustic emission method. *Archives of Civil and Mechanical Engineering*, *12*(1), 23–28. https://doi.org/https://doi.org/10.1016/j.acme.2012.03.004

Gradshteyn, I. S., and Ryzhik, I. M. (2007). *Table of integrals, series, and products* (A. Jeffrey & D. Zwillinger (eds.); 7th ed.). Elsevier Inc.

Gu, Y., Chen, W., Fu, Z.-J., and Zhang, B. (2014). The singular boundary method: mathematical background and application in orthotropic elastic problems. *Engineering Analysis with Boundary Elements*, *44*, 152–160. https://doi.org/http://dx.doi.org/10.1016/j.enganabound.2014.02.001

Gu, Y., Chen, W., and Zhang, C.-Z. (2011). Singular boundary method for solving plane strain elastostatic problems. *International Journal of Solids and Structures*, *48*, 2549–2556. https://doi.org/http://dx.doi.org/10.1016/j.ijsolstr.2011.05.007

Gu, Y., Hua, Q., Chen, W., and Zhang, C. (2016). Numerical evaluation of nearly hyper-singular integrals in the boundary element analysis. *Computers & Structures*, *167*, 15–23. https://doi.org/https://doi.org/10.1016/j.compstruc.2016.01.017

Gu, Y. T., and Zhang, L. C. (2008). Coupling of the meshfree and finite element methods for determination of the crack tip fields. *Engineering Fracture Mechanics*, *75*, 986–1004. https://doi.org/http://dx.doi.org/10.1016/j.engfracmech.2007.05.003

Hadikhan Tehrani, M. (2019). *Design and assessment of innovative dual-mode rolling isolation systems*.

Hall, L. (2003). Simulations and analyses of train-induced ground vibrations in finite element models. *Soil Dynamics and Earthquake Engineering*, *23*, 403–413. https://doi.org/https://doi.org/10.1016/S0267-7261(02)00209-9

Hemsworth, B. (2000). Reducing groundborne vibrations: state-of-the-art study. *Journal of Sound and Vibration*, *231*(3), 703–709. https://doi.org/https://doi.org/10.1006/jsvi.1999.2642

Honarvar, F., and Ledari, A. H. (2016). Three dimensional characterization of defects by ultrasonic time-of-flight diffraction (TOFD) technique. *19th World Conference on Non-Destructive Testing 2016*.

Hoorickx, C. Van, Schevenels, M., and Lombaert, G. (2017a). Double wall barriers as mitigation measures for ground vibration transmission. *Procedia Engineering*, *199*, 2735–2740. https://doi.org/https://doi.org/10.1016/j.proeng.2017.09.301

Hoorickx, C. Van, Schevenels, M., and Lombaert, G. (2017b). Double wall barriers for the reduction of ground vibration transmission. *Soil Dynamics and Earthquake Engineering*, *97*, 1–13. https://doi.org/https://doi.org/10.1016/j.soildyn.2017.02.006

Huang, J., Liu, W., and Shi, Z. (2017). Surface-wave attenuation zone of layered periodic structures and feasible application in ground vibration reduction. *Construction and Building Materials*, *141*, 1–11. https://doi.org/https://doi.org/10.1016/j.conbuildmat.2017.02.153

Huang, J., Liu, Y., and Li, Y. (2019). Trees as large-scale natural phononic crystals: simulation and experimental verification. *International Soil and Water Conservation Research*, *7*(2), 196–202. https://doi.org/https://doi.org/10.1016/j.iswcr.2019.03.004

Idelsohn, S. R., and Oñate, E. (2006). To mesh or not to mesh. That is the question…. *Computer Methods in Applied Mechanics and Engineering*, *195*, 4681–4696. https://doi.org/http://dx.doi.org/10.1016/j.cma.2005.11.006

International Atomic Energy Agency. (2002). *Guidebook on non-destructive testing of concrete structures: training course series* (17th ed.). International Atomic Energy Agency.

Jakubczyk-Gałczyńska, A., and Jankowski, R. (2014). *Traffic-induced vibrations. The impact on buildings and people*. https://doi.org/10.3846/enviro.2014.028

Jiang, J., Toward, M. G. R., Dijckmans, A., Thompson, D. J., Degrande, G., Lombaert, G., and Ryue, J. (2015). Reducing railway induced ground-borne vibration by using trenches and buried soft barriers. In J. C. O. Nielsen, D. Anderson, P.-E. Gautier, M. Iida, J. T. Nelson, D. Thompson, T. Tielkes, D. A. Towers, & P. de Vos (Eds.), *Noise and Vibration Mitigation for Rail Transportation Systems. Notes on Numerical Fluid Mechanics and Multidisciplinary Design*. Springer Berlin Heidelberg. https://doi.org/10.1007/978-3-662-44832-8_65

Jin, Q., Thompson, D. J., Lurcock, D. E. J., Toward, M. G. R., and Ntotsios, E. (2018). A 2.5D finite element and boundary element model for the ground vibration from trains in tunnels and validation using measurement data. *Journal of Sound and Vibration*, *422*, 373–389. https://doi.org/https://doi.org/10.1016/j.jsv.2018.02.019

Kaczmarek, M., Piwakowski, B., and Drelich, R. (2015). Non-contact ultrasonic non-destructive techniques: state of the art and their use in civil engineering. *International Symposium - Non-Destructive Testing in Civil Engineering (NDT-CE)*.

Kessler, S. S., Spearing, S. M., Atalla, M. J., Cesnik, C. E. S., and Soutis, C. (2002). Damage detection in composite materials using frequency response methods. *Composites Part B: Engineering*, *33*(1), 87–95. https://doi.org/https://doi.org/10.1016/S1359-8368(01)00050-6

Khazanovich, L., Freeseman, K., de Salles, L., and Asadollahi, A. (2016). *Damage detection techniques for concrete applications*.

Kim, S.-H., and Das, M. (2012). Artificial seismic shadow zone by acoustic metamaterials. *Modern Physics Letters B*, *27*.

Kimoto, K., Nakahata, K., and Saitoh, T. (2017). An elastodynamic computational time-reversal method for shape reconstruction of traction-free scatterers. *Wave Motion*, *72*, 23–40. https://doi.org/https://doi.org/10.1016/j.wavemoti.2016.12.007

Kouroussis, G., Connolly, D. P., Olivier, B., Laghrouche, O., and Alves-Costa, P. (2016). Railway cuttings and embankments: experimental and numerical studies of ground vibration. *Science of The Total Environment*, *557–558*, 110–122. https://doi.org/https://doi.org/10.1016/j.scitotenv.2016.03.016

Krödel, S., Thomé, N., and Daraio, C. (2015). Wide band-gap seismic metastructures. *Extreme Mechanics Letters*, *4*, 111–117. https://doi.org/https://doi.org/10.1016/j.eml.2015.05.004

Langer, P., Maeder, M., Guist, C., Krause, M., and Marburg, S. (2017). More than six elements per wavelength: the practical use of structural finite element models and their accuracy in comparison with experimental results. *Journal of Computational Acoustics*, *25*(04), 1750025. https://doi.org/10.1142/S0218396X17500254

Lee, B. C., and Staszewski, W. J. (2003). Modelling of Lamb waves for damage detection in metallic structures: part I. Wave propagation. *Smart Materials and Structures*, *12*, 804. https://doi.org/10.1088/0964-1726/12/5/018

Li, Y., Baker, E., Reissman, T., Sun, C., and Liu, W. K. (2017). Design of mechanical metamaterials for simultaneous vibration isolation and energy harvesting. *Applied Physics Letters*, *111*(25), 251903. https://doi.org/10.1063/1.5008674

Liu, G. R., and Lam, K. Y. (1996). Scattering of SH waves by flaws in sandwich plates and its use in flaw detection. *Composite Structures*, *34*, 251–261. https://doi.org/https://doi.org/10.1016/0263-8223(95)00143-3

Lohith K. S., M. (2009). *Ultrasonic non destructive testing* (p. 4).

Lopes, P. A., Alves-Costa, P., Calçada, R., and Cardoso, A. (2013). Numerical modeling of vibrations induced in tunnels: a 2.5D FEM-PML approach. *Traffic Induced Environmental Vibrations and Controls: Theory and Application*, *144*, 133–166. https://doi.org/10.24849/j.geot.2018.144.08

Lopes, P. A., Alves-Costa, P., Ferraz, M., Calçada, R., and Cardoso, A. S. (2014). Numerical modeling of vibrations induced by railway traffic in tunnels: from the source to the nearby buildings. *Soil Dynamics and Earthquake Engineering*, *61–62*, 269–285. https://doi.org/https://doi.org/10.1016/j.soildyn.2014.02.013

Maia, R. A. (2016). *Detecção de dano estrutural em estruturas planas utilizando redes neurais*.

Universidade de Brasília.

Manjula, K., Vijayarekha, K., Venkatraman, B., and Karthik, D. (2012). Ultrasonic time of flight diffraction technique for weld defects: a review. *Res. J. Appl. Sci. Eng. Technol., 4*, 5525–5533.

Marburg, S. (2002). Six boundary elements per wavelength: is that enough? *Journal of Computational Acoustics*, *10*, 25–51. https://doi.org/10.1142/S0218396X02001401

Martínez-Sala, R., Rubio, C., García-Raffi, L. M., Sánchez-Pérez, J. V., Sánchez-Pérez, E. A., and Llinares, J. (2006). Control of noise by trees arranged like sonic crystals. *Journal of Sound and Vibration*, *291*(1), 100–106. https://doi.org/https://doi.org/10.1016/j.jsv.2005.05.030

Martins, M., Godinho, L. M. C., and Picado-Santos, L. (2013). Numerical evaluation of sound attenuation provided by periodic structures. *Archives of Acoustics*, *38*(4). http://acoustics.ippt.gov.pl/index.php/aa/article/view/314

Mazza, F., and Labernarda, R. (2018). Effects of nonlinear modelling of the base-isolation system on the seismic analysis of r.c. buildings. *Procedia Structural Integrity*, *11*, 226–233. https://doi.org/https://doi.org/10.1016/j.prostr.2018.11.030

Medeiros, A. (2007). *Aplicação do ultra-som na estimativa da profundidade de fendas superficiais e na avaliação da eficácia de injeções em elementos de comcreto armado*. Universidade Federal de Santa Catarina.

Miklowitz, J. (1978). *The theory of elastic waves and waveguides* (W. T. Lauwerier, H. A., Koiter (ed.)). North-Holland.

Milsom, J. (2003). *Field Geophysics - the geological field guide series* (3rd ed.). John Wiley & Sons Ltd.

Morandi, F., Miniaci, M., Guidorzi, P., Marzani, A., and Garai, M. (2015). Acoustic measurements on a sonic crystals barrier. *6th International Building Physics Conference, IBPC 2015*, 134–139. https://doi.org/10.1016/j.egypro.2015.11.128

Nobile, L., and Nobile, S. (2015). Some recent advances of ultrasonic diagnostic methods applied to materials and structures (including biological ones). *Physics Procedia*, *70*, 681–685. https://doi.org/https://doi.org/10.1016/j.phpro.2015.08.080

Ogilvy, J. A., and Temple, J. A. G. (1983). Diffraction of elastic waves by cracks: application to time-of-flight inspection. *Ultrasonics*, *21*, 259–269. https://doi.org/http://dx.doi.org/10.1016/0041-624x(83)90058-6

Ögren, M., Gidlöf-Gunnarsson, A., Smith, M., Gustavsson, S., and Persson Waye, K. (2017). Comparison of annoyance from railway noise and railway vibration. *International Journal of Environmental Research and Public Health*, *14*, 805. https://doi.org/10.3390/ijerph14070805

Persson, P., Persson, K., and Sandberg, G. E. (2016). Numerical study of reduction in ground vibrations by using barriers. *Engineering Structures*, *115*, 18–27. https://doi.org/https://doi.org/10.1016/j.engstruct.2016.02.025

Petcher, P. A., Burrows, S. E., and Dixon, S. (2014). Shear horizontal (SH) ultrasound wave propagation around smooth corners. *Ultrasonics*, *54*(4), 997–1004. https://doi.org/https://doi.org/10.1016/j.ultras.2013.11.011

Praveen, A., Vijayarekha, K., Abraham, S. T., and Venkatraman, B. (2013). Fourier analysis of ultrasonic TOFD signals for defect detection in austenitic stainless steel welds. *International Journal of Computer Applications*, *71*, 14–17.

Rao, B. N., and Rahman, S. (2001). A coupled meshless-finite element method for fracture analysis of cracks. *International Journal of Pressure Vessels and Piping*, *78*, 647–657. https://doi.org/http://dx.doi.org/10.1016/S0308-0161(01)00076-X

Saitta, F., Clemente, P., Buffarini, G., Bongiovanni, G., Salvatori, A., and Grossi, C. (2018). Base isolation of buildings with curved surface sliders: basic design criteria and critical issues. *Advances in Civil Engineering*, *2018*. https://doi.org/https://doi.org/10.1155/2018/1569683

Santos, P. G., Carbajo, J., Godinho, L. M. C., and Soriano, J. (2014). Sound propagation analysis on sonic crystal elastic structures using the method of fundamental solutions (MFS). *Computers, Materials and Continua*, *43*, 109–136. https://doi.org/10.3970/cmc.2014.043.109

Schlangen, E. (1993). *Experimental and numerical analysis of fracture processes in concrete*. Delft University of Technology.

Shih, J.-Y., Thompson, D. J., and Zervos, A. (2016). The effect of boundary conditions, model size and damping models in the finite element modelling of a moving load on a track/ground system. *Soil Dynamics and Earthquake Engineering*, *89*, 12–27. https://doi.org/https://doi.org/10.1016/j.soildyn.2016.07.004

Sinou, J.-J. (2009). A review of damage detection and health monitoring of mechanical systems from changes in the measurement of linear and non-linear vibrations. In R. C. Sapri (Ed.), *Mechanical Vibrations: Measurement, Effects and Control* (pp. 643–702). Nova Science Publishers, Inc.

Smith, M. G., Croy, I., Ögren, M., and Waye, K. P. (2013). On the influence of freight trains on humans: a laboratory investigation of the impact of nocturnal low frequency vibration and noise on sleep and heart rate. *PLoS ONE*, *8(2): e558*. https://doi.org/10.1371/journal.pone.0055829

Soares Jr., D. (2016). A novel family of explicit time marching techniques for structural dynamics and wave propagation models. *Computer Methods in Applied Mechanics and Engineering*, *311*, 838–855. https://doi.org/http://dx.doi.org/10.1016/j.cma.2016.09.021

Soares Jr., D., Mansur, W. J., and Lima, D. L. (2007). An explicit multi-level time-step algorithm to model the propagation of interacting acoustic-elastic waves using finite element/finite difference coupled procedures. *Computer Modeling in Engineering & Sciences*, *17*, 19–34.

Suhairy, S. Al. (2000). *Prediction of ground vibration from railways*.

Tadeu, A. J. B., António, J., and Godinho, L. M. C. (2001). Green's function for two-and-a-

half dimensional elastodynamic problems in a half-space. *Computational Mechanics*, *27*, 484–491.

Tadeu, A. J. B., António, J., and Godinho, L. M. C. (2009). Defining an accurate MFS solution for 2.5D acoustic and elastic wave propagation. *Engineering Analysis with Boundary Elements*, *33*, 1383–1395. https://doi.org/http://dx.doi.org/10.1016/j.enganabound.2009.06.007

Tadeu, A. J. B., and Kausel, E. (2000). Green's functions for two-and-a-half dimensional elastodynamic problems. *Journal of Engineering Mechanics*, *126*, 1093–1097.

Talbot, J. P. (2016). Base-isolated buildings: towards performance-based design. *Proceedings of the Institution of Civil Engineers: Structures and Buildings*, *168(8)*, 574–582.

Talbot, J. P., and Hunt, H. E. M. (2000). On the performance of base-isolated buildings. *Building Acoustics*, *7*, 163–178.

Talbot, J. P., and Hunt, H. E. M. (2003). Isolation of buildings from rail-tunnel vibration: a review. *Building Acoustics*, *10*, 177–192.

Telford, W. M., Geldart, L. P., and Sheriff, R. E. (1990). *Applied Geophysics* (2nd ed.). Cambridge University Press.

Thompson, D. J., Jiang, J., Toward, M. G. R., Hussein, M. F. M., Ntotsios, E., Dijckmans, A., Coulier, P., Lombaert, G., and Degrande, G. (2016). Reducing railway-induced ground-borne vibration by using open trenches and soft-filled barriers. *Soil Dynamics and Earthquake Engineering*, *88*, 45–59. https://doi.org/https://doi.org/10.1016/j.soildyn.2016.05.009

Toward, M. G. R., Jiang, J., Dijckmans, A., Coulier, P., Thompson, D. J., Degrande, G., Lombaert, G., and Hussein, M. F. M. (2014). *Mitigation of railway induced vibration by using subgrade stiffening and wave impeding blocks*.

Tsiatas, G. C., and Yiotis, A. J. (2013). A BEM-based meshless solution to buckling and vibration problems of orthotropic plates. *Engineering Analysis with Boundary Elements*, *37*, 579–584. https://doi.org/http://dx.doi.org/10.1016/j.enganabound.2013.01.007

Umnova, O., Attenborough, K., and Linton, C. (2006). Effects of covering on sound attenuation by periodic arrays of cylinders. *The Journal of the Acoustical Society of America*, *119*, 278–284.

Waddington, D., Woodcock, J., Smith, M. G., Janssen, S., and Waye, K. P. (2015). CargoVibes: human response to vibration due to freight rail traffic. *International Journal of Rail Transportation*, *3*(4), 233–248. https://doi.org/10.1080/23248378.2015.1076623

Wang, Y.-S., and Wang, D. (1996). Scattering of elastic waves by a rigid cylindrical inclusion partially debonded from its surrounding matrix—I. SH case. *International Journal of Solids and Structures*, *33*, 2789–2815. https://doi.org/https://doi.org/10.1016/0020-7683(95)00179-4

Wells, G. N., and Sluys, L. J. (2001). Three-dimensional embedded discontinuity model for brittle fracture. *International Journal of Solids and Structures*, *38*, 897–913. https://doi.org/http://dx.doi.org/10.1016/S0020-7683(00)00029-9

Woo, J. S. K. (n.d.). *A summary of the early development of ultrasonics prior to the 1950s leading to medical applications*. Retrieved April 1, 2019, from http://www.ob-ultrasound.net/ultrasonics_history.html

Xu, J., and Wei, H. (2019). Ultrasonic Testing Analysis of Concrete Structure Based on S Transform. *Shock and Vibration*, *2019*, 9. https://doi.org/https://doi.org/10.1155/2019/2693141

Yang, Y. B., and Hung, H. H. (2009). *Wave propagation for train-induced vibrations. A finite/infinite element approach*. World Scientific Publishing Co. Pte. Ltd.

Yarmohammadi, F., Rafiee-Dehkharghani, R., Behnia, C., and Aref, A. J. (2019). Design of wave barriers for mitigation of train–induced vibrations using a coupled genetic-algorithm/finite-element methodology. *Soil Dynamics and Earthquake Engineering*, *121*, 262–275. https://doi.org/https://doi.org/10.1016/j.soildyn.2019.03.007

Yeh, F. W. T., Lukomski, T., Haag, J., Clarke, T., Stepinski, T., and Strohaecker, T. R. (2018). An alternative ultrasonic time of flight diffraction (TOFD) method. *NDT & E International*, *100*. https://doi.org/10.1016/j.ndteint.2018.08.008

Zhao, G., Zhang, D., Zhang, L., and Wang, B. (2018). Detection of Defects in Reinforced Concrete Structures Using Ultrasonic Nondestructive Evaluation with Piezoceramic Transducers and the Time Reversal Method. *Sensors*, *18*, 4176. https://doi.org/10.3390/s18124176

Zienkiewicz, O. C., Taylor, R. L., Taylor, R. L., and Taylor, R. L. (2000). *The finite element method: solid mechanics* (Vol. 2). Butterworth-heinemann.